

ABSTRACT

WANG, RUOCUN. Improvement of Electrochemical Ion Insertion Kinetics in Tungsten Oxides with Structural Water and Trace Water in a Non-Aqueous Electrolyte. (Under the direction of Dr. Veronica Augustyn).

For ion-insertion based electrochemical energy storage devices, such as lithium-ion batteries, the power of the device is fundamentally limited by kinetics associated with electrochemical ion insertion. This dissertation utilizes synthesis and a variety of characterization methods, including in situ and operando techniques, to investigate two strategies to improve ion insertion kinetics in transition metal oxides. The first strategy is the incorporation of structural water in materials. Hydrated tungsten oxides ($\text{WO}_3 \cdot \text{H}_2\text{O}$ and $\text{WO}_3 \cdot 2\text{H}_2\text{O}$) exhibit significantly faster proton insertion kinetics than anhydrous WO_3 . We demonstrate that the proton insertion is linked to the electrode mechanical response by developing an operando atomic force microscopy method to study local electrochemomechanics. Our results show that structural water leads to lower and more reversible deformation during proton insertion. The benefit of structural water in this material system inspired us to apply it as a material design rule and to investigate the structure and electrochemical property relationships of $\text{H}_2\text{W}_2\text{O}_7$ (or $\text{W}_2\text{O}_6 \cdot \text{H}_2\text{O}$) derived via selective-ion etching of $\text{Bi}_2\text{W}_2\text{O}_9$. This synthesis enabled a more optimum structural water to transition metal ratio which enabled a higher specific capacity for $\text{H}_2\text{W}_2\text{O}_7$ as compared to $\text{WO}_3 \cdot \text{H}_2\text{O}$. The material could deliver more than 80% its full capacity in less than one minute and was stable for over 100,000 cycles, showcasing the applicability of structural water for both fast kinetics and cycling stability. The strategy of structural water incorporation was also investigated as a structural motif to increase the kinetics associated with Mg^{2+} ion insertion from non-aqueous electrolytes. In a related concept, the last study investigated the addition of water to a non-aqueous electrolyte as a means to improve Mg^{2+} insertion kinetics. The kinetics of Mg^{2+} ion insertion in WO_3 improved

upon the addition of trace amounts of water. A water-enhanced surface diffusion hypothesis was proposed to explain this phenomenon. Overall, this dissertation utilized materials synthesis and characterization to investigate structure-property relationships associated with the presence of structural water and trace water in non-aqueous electrolytes.

© Copyright 2020 by Ruocun (John) Wang

All Rights Reserved

Improvement of Electrochemical Ion Insertion Kinetics in Tungsten Oxides with Structural Water and Trace Water in a Non-Aqueous Electrolyte

by
Ruocun (John) Wang

A dissertation submitted to the Graduate Faculty of
North Carolina State University
in partial fulfillment of the
requirements for the degree of
Doctor of Philosophy

Materials Science and Engineering

Raleigh, North Carolina
2020

APPROVED BY:

Dr. Veronica Augustyn
Committee Chair

Dr. Elizabeth Dickey

Dr. Jacob Jones

Dr. Gregory Parsons

DEDICATION

To my parents, Ping Lv and Zhiguang Wang

BIOGRAPHY

I was born on August 4th, 1993, in Hangzhou, China, as the only child to the family. At age of 11, I was fortunate to attend Entel Foreign Language School and later Hangzhou Foreign Language School (HFLS) for my junior and senior high schools. At HFLS, I had the opportunity to receive a conditional admission to Purdue University, which eventually changed the course of my life and brought me to the U.S. At Purdue, I majored in Materials Engineering and minored in Global Engineering Studies. Since the summer of Freshman year at Purdue, I started research with Prof. John A. Howarter on the growth and characterization of polymer brushes. As part of the minor, I participated in a one-semester exchange program at Imperial College London in the U.K. There, I enjoyed the graduate-level courses on electroceramics and interface science, which encouraged me to pursue a Ph.D. degree. After graduating from Purdue with distinction, I joined the department of Materials Science and Engineering at NC State University in 2015, working with Prof. Veronica Augustyn. At NC State, I spent five fulfilling years studying the effect of structural water on the electrochemical insertion of ions in transition metal oxides.

ACKNOWLEDGMENTS

I would like to thank my advisor, Professor Veronica Augustyn, for all the mentorship, leadership, advice, opportunities, patience, and care she offered in the past five years. Doing a Ph.D. with her has been one of the most fortunate events in my life. I was fortunate to cultivate my interests in energy storage research with her careful guidance and later fulfilled lots of my curiosity in the research projects. She has created many opportunities to help me grow as a researcher. Without the opportunities she created, I would not have the chance to attend the conferences (including the ones in Botswana and Germany) and would not meet with some of the great minds in the field. If there were no SciBridge, I never knew I could step up as a leader. If it were not her encouragement, I might not have taken on the leadership in the Energy Frontier Research Center. Just to name a few. There were countless lessons I learned from her throughout the years of interactions. These are treasures that I will value in my lifetime.

I want to thank Professor Beth Dickey for co-advising in my first year and the continued mentorship afterwards. The opportunities from MSA, CDP and SEAS program have enriched my graduate experience. Her care for students and high academic standards have been an inspiration.

I would like to thank Prof. Beth Dickey, Prof. Jacob Jones, and Prof. Greg Parsons for serving on my dissertation committee. I appreciate your time assessing my prelim and dissertation.

I would like to thank my collaborators at NC State: Ching-Chang Chung, Prof. Jacob Jones, Dr. Yang Liu, Dr. James S. Daubert, Prof. Greg Parsons, Tim Eldred, Prof. Wenpei Gao; at Oak Ridge National Lab: Dr. Wan-Yu Tsai, Dr. Gao Qiang, Dr. Nina Balke, Dr. Peter V. Bonnesen, Dr. Alexander Brady, Dr. Hsiu-Wen Wang; at UC Riverside: Yangyunli Sun, Prof. De-en Jiang; at AMES lab: Dr. Takeshi Kobayashi.

I thank my labmates in the Augustyn lab who have made the five years much more enjoyable: Shelby Boyd, James Mitchell, Mike Spencer, Dr. Simon Fleischmann, Saeed Saeed, Matthew Chagnot, and Ishita Kamboj. I enjoy their accompanying and appreciate their humor, kindness, and understanding. I thank Dr. Brian Lynch for the chitchat and slang.

I would like to thank my friends: Dr. Xiaotian Fang, Dr. Yingying Yu, and Dr. Changhao Zhang, Dr. Xiaolong Ma, Boyu Guo, Dr. Hanhan Zhou, Dr. Jianwei Zhao, Dr. Seunghyun Yoo, Juanqin Jin, Dr. Gao Qiang, Dr. Chen Dong, Dr. Xueping Yi for enriching my time in Raleigh.

I want to thank my parents: Zhiguang Wang and Ping Lv for their love, education, and support. I cannot make it here without them.

Chapter 3, “Operando Atomic Force Microscopy (AFM) Dilatometry of the Electrochemo-mechanics of Ion Insertion Materials,” is a modified version of the published work “Operando Atomic Force Microscopy Reveals Mechanics of Structural Water Driven Battery-to-Pseudocapacitor Transition” by myself, James Mitchell, Qiang Gao, Wan-Yu Tsai, Shelby Boyd, Matt Pharr, Nina Balke, and Veronica Augustyn in *ACS Nano*, 12, 2018. AFM data collection were performed by James Mitchell, Qiang Gao, Wan-Yu Tsai, and myself. Ex situ X-ray diffraction (XRD) was performed by James Mitchell. Scanning electron microscopy images were taken by Shelby Boyd.

Chapter 4, “Electrochemical Proton storage in Metastable $H_2W_2O_7$,” is a modified version of a manuscript in preparation, tentatively titled “High Power Energy Storage and Multicolor Electrochromism via Selective Etching of $Bi_2W_2O_9$.” The density functional theory results were calculated by Yangyunli Sun. The XRD refinement and deuterated $D_2W_2O_7$ were prepared by Dr. Alexander Brady. The neutron PDF refinement was performed by Dr. Hsiu-Wen Wang. In situ Raman and ex situ XRD were taken by Dr. Simon Fleischmann. The atomic-resolution scanning

transmission electron microscopy images were taken by Tim Eldred. The SEM images were taken by Shelby Boyd and Mike Spencer.

Chapter 6, “Electrochemical Mg^{2+} Insertion in WO_3 and $\text{WO}_3 \cdot \text{H}_2\text{O}$,” is a modified version of published work “Electrochemical Intercalation of Mg^{2+} into Anhydrous and Hydrated Crystalline Tungsten Oxides” by myself, Ching-Chang Chung, Yang Liu, Jacob Jones, and Veronica Augustyn in *Langmuir*, 33, 2017. The ex situ X-ray diffraction patterns were taken by Dr. Ching-Chang Chung. The ex situ scanning transmission electron microscopy images were taken by Dr. Yang Liu.

Chapter 7, “Effect of Water in a Non-aqueous Electrolyte on Electrochemical Mg^{2+} Insertion into WO_3 ,” is a modified version of a manuscript under revision, “Effect of Water in a Non-Aqueous Electrolyte on Electrochemical Mg^{2+} Insertion into WO_3 ,” by myself, Shelby Boyd, Peter V. Bonnesen, and Veronica Augustyn. The scanning electron microscopy images and energy dispersive X-ray spectroscopy were taken by Shelby Boyd. The nuclear magnetic resonance spectra were taken by Dr. Peter V. Bonnesen.

Appendix A contains derivation of ambipolar diffusivity and conductivity for electrochemical ion insertion processes that was modified from Prof. Sossina Haile’s Solid-State Electrochemistry course at Northwestern University.

This dissertation was supported by NC State startup funds, the Ralph E. Powe Junior Faculty Enhancement Award, and the Fluid Interface Reactions, Structures and Transport (FIRST) Center, an Energy Frontier Research Center funded by the U.S. Department of Energy, Office of Science, Office of Basic Energy Sciences. Most materials characterization at NC State was performed at the NCSU Nanofabrication Facility (NNF) and the Analytical Instrumentation Facility (AIF), which are supported by the State of North Carolina and the National Science

Foundation (award number ECCS-1542015). AIF and NNF are members of the North Carolina Research Triangle Nanotechnology Network (RTNN), a site in the National Nanotechnology Coordinated Infrastructure (NNCI). A portion of this research used resources at the Spallation Neutron Source, a DOE Office of Science User Facility operated by the Oak Ridge National Laboratory. Oak Ridge National Laboratory is managed by UT-Battelle, LLC, for the U.S. DOE under Contract No. DEAC05-00OR22725. Operando AFM and ^1H NMR were conducted at the Center for Nanophase Materials Sciences, which is a DOE Office of Science User Facility.

TABLE OF CONTENTS

LIST OF TABLES	x
LIST OF FIGURES	xi
Chapter 1: Introduction	1
Chapter 2: Fundamentals of Electrochemical Energy Storage	7
Thermodynamics.....	8
Kinetics	12
Physical Picture of Ion Insertion.....	20
Electrical Double Layer	22
Surface Ion Adsorption	24
Surface Diffusion	27
Bulk Diffusion	29
Material Deformation During Electrochemical Energy Storage	32
Chapter 3: Operando AFM Dilatometry of the Electro-Chemo-Mechanics of Ion Insertion Materials	37
Introduction.....	37
Experimental Methods	39
Results & Discussions.....	42
Conclusions.....	64
Chapter 4: Electrochemical Proton Storage in Metastable H₂W₂O₇	65
Introduction.....	65
Experimental Methods	67
Results & Discussions.....	73
Conclusions.....	100
Chapter 5: Cathode Materials for Rechargeable Magnesium Batteries	101
Chapter 6: Electrochemical Mg²⁺ Insertion in WO₃ and WO₃·H₂O	110
Introduction.....	110
Experimental Methods	112
Results & Discussions.....	116
Conclusions.....	138

Chapter 7: Effect of Water in a Non-Aqueous Electrolyte on Electrochemical Mg²⁺

Insertion into WO₃	139
Introduction.....	139
Experimental Methods.....	141
Results & Discussions.....	145
Conclusions.....	170
Chapter 8: Conclusions	172
REFERENCES	175
Appendix A – Derivation of Ambipolar Diffusivity and Conductivity for Ion Insertion Processes.....	203
Appendix B – Matlab Code for Performance Analysis of Cyclic Voltammograms.....	207
Appendix C – Matlab Code for <i>b</i> -Value Analysis of Cyclic Voltammograms	210
Appendix D – Matlab Code for Cyclability Analysis of Cyclic Voltammetry Experiments	214
Appendix E – Matlab Code for Single-Spot Operando AFM Dilatometry Analysis	217

LIST OF TABLES

Table 2.1	Volume change of selected materials operated by insertion with phase transformation mechanism at the corresponding intercalant concentration or specific capacity.	33
Table 3.1	Ranges of low, medium, and high deformation rates in WO_3 and $\text{WO}_3 \cdot 2\text{H}_2\text{O}$ used for Figure 3.12. To generate these ranges, the deformation rates at each spot at the cathodic peak potential were grouped together and analyzed with a histogram.	58
Table 5.1	Comparisons of magnesium and lithium ion for energy storage applications in the areas of ionic radius, voltage vs. standard hydrogen electrode, abundance, and volumetric and gravimetric capacity.	102
Table 5.2	A compilation of the operating voltage, specific capacity, and quantitative cycle life of orthorhombic V_2O_5 , MoS_2 , orthorhombic MoO_3 , and birnessite MnO_2	108
Table 6.1	Half-wave potentials of ferrocene/ferrocenium (Fc/Fc^+ ; $E_{1/2}$, Fc/Fc^+) measured in non-aqueous electrolytes and referenced to Mg/Mg^{2+} . To convert $E_{1/2}$, Fc/Fc^+ to its potential vs. Mg/Mg^{2+} , an average value of 2.61 V was utilized.	115
Table 7.1	The ICDD PDF numbers of the M_xWO_3 used in Figure 7.11	159

LIST OF FIGURES

Figure 1.1	Classification of electrochemical energy storage mechanisms as a function of their characteristic capacity and the associated degree of structural changes of the electrodes, reaction overpotential, and kinetic limitations. Adapted from reference 1.....	3
Figure 2.1	Characteristic electrochemical signatures of the relationship between potential and charge for an ideal battery and an ideal capacitor measured under constant current charge/discharge conditions. Adapted from reference 2.....	9
Figure 2.2	Schematics of simplified energy diagrams of $\text{Li}_{0.6}\text{CoO}_2$ and LiCoO_2 . E_f is the Fermi level of the electrode. e_g and t_{2g} stand for the doubly and triply degenerate states in the crystal field theory. The energy diagram of LiCoO_2 is adapted from reference 3	12
Figure 2.3	Typical discharge curve for a battery electrode measured under constant current charge/discharge conditions. The three types of polarization are labeled in the graph. Adapted from reference 4	14
Figure 2.4	Examples of how electrochemical characterization can be utilized to identify charge storage mechanisms. Schematic cyclic voltammograms (a, b, d, e, g, h) and corresponding galvanostatic profiles (c, f, i) representing various types of charge storage. The pseudocapacitive types presented here include (b) surface redox pseudocapacitance (e.g., hydrated RuO_2 in acidic aqueous electrolytes), (d) intercalation pseudocapacitance (e.g., $T\text{-Nb}_2\text{O}_5$ in a Li^+ non-aqueous electrolyte), and (e) combination of intercalation and surface redox pseudocapacitance (e.g., $\text{Ti}_3\text{C}_2\text{T}_x$ MXene in an acidic aqueous electrolyte). Reprinted from reference 5	16
Figure 2.5	(a) Cyclic voltammograms of nanostructured anatase TiO_2 films at 0.5 mV s^{-1} in a non-aqueous Li^+ electrolyte. The surface-controlled currents (shaded regions) are determined with k1, k2 analysis using Equation 2.22. (b) Charge storage of the same three TiO_2 thin films at 0.5 mV s^{-1} contributed from surface-controlled (“capacitance”) and diffusion-controlled current (“intercalation capacity”). Adapted from reference 6.	20
Figure 2.6	A step-wise schematic illustration of an ion insertion process from a non-aqueous electrolyte into an insertion electrode. Reproduced from reference 7	21

Figure 2.7	Voltage profile inside the electrolyte of batteries or EDLCs. The double layers at anode and cathode interfaces have different structure and compositions. Reproduced from reference 4.....	22
Figure 2.8	Schematic of the electrical double layer model at the interface between an electrolyte and a metal. The sphere with the arrow sign indicates solvent molecules. Reproduced from reference 8.....	23
Figure 2.9	Schematic of sublattice structures of OH adsorbed on the (100) or (111) surface of Pt. Adapted from reference 9.....	25
Figure 2.10	a) The variation of pseudocapacitance, C_{ϕ} , and surface coverage, θ , for ideal Langmuir electrosorption ($g=0$, solid curves) and Frumkin-type electrosorption that involves attractive lateral interactions between surface adsorbates ($g>0$, dashed curves). The outcome of this is that pseudocapacitance, as originally defined, is strongly potential dependent. The addition of the lateral interaction parameter broadens the peak but does not eliminate the potential dependence. Adapted from reference 10. b) Illustration of how three redox processes ($C_{\phi,1}$, $C_{\phi,2}$, and $C_{\phi,3}$) could overlap to form an almost-constant overall capacitance over an appreciable potential range in electrochemically formed RuO_2 thin films. Q (dashed curve) is the charge accumulated over the potential range and $\sum C_{\phi}$ (short dashed curve) are the summed capacitance of the three redox processes. Adapted from reference 11.....	27
Figure 2.11	Schematic showing Li^+ transport routes in a Li_xFePO_4 crystal with the [010] fast Li^+ conducting channel perpendicular to the surface. The three possible routes are bulk diffusion along the nominally non-conductive directions, surface diffusion, and electrolyte diffusion that require de-insertion and re-insertion of Li^+ . The relative resistances (R_{bulk} , R_{surfD} , and R_{rxn}) determine which route Li^+ would take during the phase segregation due to immersion in the electrolyte. Adapted from reference 12.....	28
Figure 2.12	Schematics showing a) the inhomogeneous distribution of intercalated ions due to fast charging and b) homogeneous distributions of intercalated ions when the rate of intercalation is low. Adapted from reference 13.....	33
Figure 3.1	Scanning electron micrographs of $\text{WO}_3 \cdot 2\text{H}_2\text{O}$ and WO_3 thin films on glassy carbon used in the operando AFM dilatometry experiments. a, c, Top-down micrographs depicting the random particle orientation of $\text{WO}_3 \cdot 2\text{H}_2\text{O}$ (a) and	

	WO ₃ (c) thin films. b, d, Cross-sectional micrographs used to determine average thickness of WO ₃ ·2H ₂ O (b) and WO ₃ (d) thin films.	43
Figure 3.2	Surface morphology and electrochemical characterization of WO ₃ and WO ₃ ·2H ₂ O electrodes obtained from the in situ electrochemical AFM cell. (a, c) Deflection images of the thin film electrode surface of WO ₃ ·2H ₂ O (a) and WO ₃ (c). (b, d) Cyclic voltammograms of WO ₃ ·2H ₂ O (b) and WO ₃ (d) electrodes in 0.5 M H ₂ SO ₄ at sweep rates ranging from 10 – 200 mV s ⁻¹	44
Figure 3.3	Top-down illustration of the commercial in situ electrochemical AFM cell used during the operando AFM dilatometry experiments. The design allows for the AFM cantilever to approach the working electrode submerged in electrolyte solution (0.5 M H ₂ SO ₄). A chemically inert polyether ether ketone (PEEK) housing electronically insulates the counter and working electrodes, while a manufactured hole in the side allows for the insertion of a reference electrode into the solution.....	45
Figure 3.4	Specific capacitance of WO ₃ ·2H ₂ O and WO ₃ in the in situ electrochemical AFM cell. a, b, Specific capacitance versus cycle number at various sweep rates for WO ₃ ·2H ₂ O (a) and WO ₃ (b). The capacity retention as a function of sweep rate observed for the WO ₃ ·2H ₂ O thin film electrodes is characteristic of this hydrated phase, as reported previously for slurry electrodes in reference 14.....	46
Figure 3.5	Local deformation of WO ₃ and WO ₃ ·2H ₂ O electrodes as a function of potential and capacity. (a, b) Deformation <i>versus</i> potential at different cyclic voltammetry sweep rates of WO ₃ ·2H ₂ O (a) and WO ₃ (b); Error bars indicate the standard deviations of the deformation at specific potentials for 18 cycles. (c, d) Deformation <i>versus</i> number of electrons per formula unit of WO ₃ and WO ₃ ·2H ₂ O at sweep rates of 20 mV s ⁻¹ (c) and 200 mV s ⁻¹ (d); Error bars indicate the standard deviations of the deformation at specific numbers of electrons per formula unit. Negative number of electrons represent the anodic cycle and positive number of electrons represent the cathodic cycle.	48
Figure 3.6	Correlation between the local deformation rate and the global electrode current. (a, b) Average deformation rate (solid line) and current (dashed line) <i>versus</i> potential at a sweep rate of 200 mV s ⁻¹ for WO ₃ ·2H ₂ O (a) and WO ₃ (b). Error bars indicate the standard deviations of the deformation rate at specific potentials. The shaded area indicates the regions of potential where the hydrogen evolution reaction contributes to the total current.....	49
Figure 3.7	Comparison of the deformation rate of redox-active materials to the glassy carbon substrate. a, b, Average deformation rate versus potential at a sweep rate of 10 mV s ⁻¹ for WO ₃ ·2H ₂ O (a) and WO ₃ (b). The response from the glassy carbon substrate is overlaid to show that deformation only occurs for the redox-active materials	50

Figure 3.8	Kinetic analysis of the local deformation rate of WO_3 and $\text{WO}_3 \cdot 2\text{H}_2\text{O}$. (a, b) Deformation rate versus potential at sweep rates from 10 to 200 mV s^{-1} for $\text{WO}_3 \cdot 2\text{H}_2\text{O}$ (a) and WO_3 (b). The circles indicate the deformation rate peak values used for b -value determination. Error bars indicate the standard deviations of the deformation rate at specific potentials. (c, d) b -value determination of the peak cathodic (c) and anodic (d) deformation rate for WO_3 (■) and $\text{WO}_3 \cdot 2\text{H}_2\text{O}$ (▲); markers indicate the cathodic and anodic deformation rate peak values at specific sweep rates and the dashed lines indicate the best linear fit	52
Figure 3.9	Correlation of the average local deformation rate to the global electrode current. a, b, Deformation rate (solid line) and current (dashed line) averaged across an 11×20 grid of points versus potential at a sweep rate of 200 mV s^{-1} for $\text{WO}_3 \cdot 2\text{H}_2\text{O}$ (a) and WO_3 (b). Error bars indicate the standard deviations of the deformation rate at specific potentials	54
Figure 3.10	Spatial variation of the local deformation rate of WO_3 and $\text{WO}_3 \cdot 2\text{H}_2\text{O}$ electrodes at the cathodic and anodic peak current potentials. (a, b) Local deformation rate at cathodic peak current potential for $\text{WO}_3 \cdot 2\text{H}_2\text{O}$ (a) and WO_3 (b). (c, d) Local deformation rate at anodic peak current potential for $\text{WO}_3 \cdot 2\text{H}_2\text{O}$ (c) and WO_3 (d).....	55
Figure 3.11	Cyclic voltammograms indicating the peak potentials of Figure 3.10. a, b, Cyclic voltammograms of $\text{WO}_3 \cdot 2\text{H}_2\text{O}$ (a) and WO_3 (b) thin film electrodes in 0.5 M H_2SO_4 collected in the <i>in situ</i> electrochemical AFM cell at sweep rate of 200 mV s^{-1}	56
Figure 3.12	Representative response of regions with low, medium, and high deformation rates. (a, b) Deformation rate versus potential of $\text{WO}_3 \cdot 2\text{H}_2\text{O}$ (a) and WO_3 (b) extracted from regions with low, medium, and high deformation rates. Error bars indicate the standard deviations of the deformation rate at specific potentials. (c, d) Maps of the locations of regions with low, medium, and high deformation rates in $\text{WO}_3 \cdot 2\text{H}_2\text{O}$ (c) and WO_3 (d).....	57
Figure 3.13	Ex situ X-ray diffraction of WO_3 . a, Electrochemical response of the cathodic and anodic linear sweep voltammograms at 5 mV s^{-1} for the slurry electrode. The asterisks indicate the various potentials at which <i>ex situ</i> diffraction patterns were obtained. b, Inset of the diffraction patterns obtained during the cathodic sweep from open-circuit voltage to -200 mV ($\text{H}_{0.12}\text{WO}_3$), depicting the structural evolution as a function of proton insertion. The 23.6° (020) and 24.3° (200) peaks merge, indicating a monoclinic to tetragonal phase transition upon proton insertion. c, Inset of the diffraction patterns obtained during the anodic sweep from -200 mV back to open-circuit voltage, depicting the reversibility of the monoclinic to tetragonal phase transition as protons are de-intercalated.....	59

- Figure 3.14 Indexing of $\text{H}_{0.12}\text{WO}_3$ (a) and pristine WO_3 (b) X-ray diffraction patterns. The X-ray diffraction pattern (red) of $\text{H}_{0.12}\text{WO}_3$ matches the peak positions of tetragonal $\text{H}_{0.1}\text{WO}_3$ (ICDD PDF 023-1448). The X-ray diffraction pattern (blue) of WO_3 matches with monoclinic δ - and ϵ - WO_3 (ICDD PDF 01-083-0950 and 01-087-2402), as we stated in our previous publication.² We attribute some peak broadenings in (a) to the presence of the ϵ phase. The reflection at $\sim 40^\circ 2\theta$ indicates the (111)-peak position of the platinum substrate..... 61
- Figure 3.15 Ex situ X-ray diffraction of $\text{WO}_3 \cdot 2\text{H}_2\text{O}$. a, Electrochemical response of the cathodic and anodic linear sweep voltammograms at 5 mV s^{-1} for the slurry electrode. The asterisks indicate the various potentials at which ex situ diffraction patterns were obtained. b, Inset of the diffraction patterns obtained during the cathodic sweep from open-circuit voltage to -200 mV ($\text{H}_{0.1}\text{WO}_3 \cdot 2\text{H}_2\text{O}$), depicting the structural evolution as a function of proton intercalation. The interlayer spacing for the dihydrate phase is not affected as protons are intercalated into the structure as indicated by the absence of change in the scattering angle of the (010) plane at $\sim 13^\circ 2\theta$. The two doublet peaks each merge into one single peak, indicating a shift in the tilted octahedra of the a-c plane toward higher symmetry. c, Inset of the diffraction patterns obtained during the anodic sweep from -200 mV back to open-circuit voltage, depicting the reversibility of the phase transition as protons are de-intercalated. A marker has been included to indicate the small impurity peak at $\sim 16^\circ 2\theta$ which correlates to the (010) plane of the monohydrate phase (ICDD PDF 043-0679)..... 62
- Figure 3.16 Crystallographic structures of $\text{WO}_3 \cdot n\text{H}_2\text{O}$. a, b, Monoclinic $\text{WO}_3 \cdot 2\text{H}_2\text{O}$ and (c) monoclinic $\gamma\text{-WO}_3$. a, (00 l)-orientation of monoclinic $\text{WO}_3 \cdot 2\text{H}_2\text{O}$ depicting the interlayer spacing and structural water of the layered, hydrated structure. b, Top-down orientation in the [0 k 0] direction, depicting the octahedral interstitial sites formed by the bridging oxygens of the corner-sharing WO_6 octahedra with water molecules above and below the plane. Complete dehydration of the hydrated, layered compound yields the anhydrous structure (c)..... 64
- Figure 4.1 Setup of electrochemical characterization of the cyclability of $\text{H}_2\text{W}_2\text{O}_7$ slurry electrode. The working and counter electrodes were held by alligator clips soldered to tin-plated copper wires. To prevent rust, the tin-plated copper wires were protected by Kapton tape and the connection between the alligator clips and electrodes were wrapped by Parafilm. A tube was inserted from the side to prevent accumulation of any in situ formed oxygen or hydrogen gases. (The tube might have caused electrolyte evaporation overtime.) 70
- Figure 4.2 Scanning electron micrographs of a,b) $\text{H}_2\text{W}_2\text{O}_7$ and c,d) WO_3 that is obtained from heat treatment of $\text{H}_2\text{W}_2\text{O}_7$. e) SEM-EDS spectrum of $\text{H}_2\text{W}_2\text{O}_7$ showing

	that the acid exchange is complete, and no bismuth was detectable at 2.419 keV (Bi M edge).....	74
Figure 4.3	TGA of a) $\text{H}_2\text{W}_2\text{O}_7$ and b) $\text{WO}_3 \cdot \text{H}_2\text{O}$ in air showing the dehydration process to form WO_3 , the mass loss is equivalent to 1.01 water loss per $\text{H}_2\text{W}_2\text{O}_7$ and 0.96 water loss per $\text{WO}_3 \cdot \text{H}_2\text{O}$	74
Figure 4.4	XRD pattern of WO_3 obtained from heat treating $\text{H}_2\text{W}_2\text{O}_7$. The intensity is plotted in the log scale due to the strong preferred orientation of 002 plane. The black ticks represent a reference pattern of $\gamma\text{-WO}_3$ (ICDD-PDF 04-005-4272).....	75
Figure 4.5	Raman spectra comparison of $\text{H}_2\text{W}_2\text{O}_7$ with $\text{WO}_3 \cdot \text{H}_2\text{O}$	76
Figure 4.6	Powder XRD of $\text{H}_2\text{W}_2\text{O}_7$ from experiment and comparison with calculated fit from Rietveld refinement.....	77
Figure 4.7	Neutron PDF of $\text{D}_2\text{W}_2\text{O}_7$ and comparison with calculated fit from real space refinement. The fit distance range is up to a) $r = 10 \text{ \AA}$, b) $r = 20 \text{ \AA}$, and c) $r = 40 \text{ \AA}$	78
Figure 4.8	Refined crystal structure of $\text{H}_2\text{W}_2\text{O}_7$. $\text{O}_{\text{b-}yz}$, O_t , and $\text{O}_{\text{b-}x}$ stand for equatorial bridging oxygen, terminal oxygen, and axial bridging oxygen, respectively. The unconventional axis is due to the $P112_1/n$ space group.	79
Figure 4.9	Atomic-resolution HAADF-STEM micrograph of $\text{H}_2\text{W}_2\text{O}_7$. The yellow blocks indicate single-layer, tri-layer, and quad-layer planar defects as labeled in the graphs.....	80
Figure 4.10	Bond lengths obtained from real-space refinement of $\text{D}_2\text{W}_2\text{O}_7$ from neutron PDF. The double-bond was used to emphasize the exceptionally short bonds according to literature convention. ¹⁵	82
Figure 4.11	Correlation between the force constant and W–O bond length. The literature data are obtained from reference. ¹⁵ The solid curve is from equation 4.2. For $\text{H}_2\text{W}_2\text{O}_7$ data points, W–O bond lengths are obtained from neutron PDF refinement and force constants are calculated from the assigned Raman peak positions using equation 4.6.	83
Figure 4.12	Cyclic voltammograms of $\text{H}_2\text{W}_2\text{O}_7$ in 3 M H_2SO_4 from a) 1 – 20 mV s^{-1} and b) 50 – 1000 mV s^{-1}	84
Figure 4.13	Coulombic efficiency of $\text{H}_2\text{W}_2\text{O}_7$ in 3 M H_2SO_4 from 1 to 1,000 mV s^{-1} , corresponding to the cyclic voltammograms in Figures 4.12. Error bars represent the standard deviation obtained from measurements performed on three separate electrodes.....	85

Figure 4.14 Anodic specific capacity as a function of sweep rate and the corresponding discharging time, comparing $\text{H}_2\text{W}_2\text{O}_7$, $\text{WO}_3 \cdot \text{H}_2\text{O}$, and WO_3 . The average values and standard error are obtained from three electrodes of each composition.	86
Figure 4.15 Sweep rate dependence of the anodic peak current in log scale for b -value determination from 1 – 1000 mV s^{-1}	87
Figure 4.16 Cyclability test: a) cyclic voltammograms of $\text{H}_2\text{W}_2\text{O}_7$ at 20 mV s^{-1} to showcase the stability of this material against cycling. Presented is every 1,000 th cycle out of 100,000 cycles. b) Anodic capacity retention and Coulombic efficiency as a function of cycle number for 100,000 cycles. The asterisk symbol (*) indicates the first cycle after a two-month pause of experiment due to COVID-19 outbreak.	89
Figure 4.17 a) Ex situ XRD patterns of pristine, protonated, and cycled $\text{H}_2\text{W}_2\text{O}_7$ electrodes. * indicates $\text{WO}_3 \cdot \text{H}_2\text{O}$ impurities because of selectively etching a batch of $\text{Bi}_2\text{W}_2\text{O}_9$ that contained Bi_2WO_6 impurities. The cycled pattern was obtained from a different electrode. b) Linear sweep voltammogram of a $\text{H}_2\text{W}_2\text{O}_7$ slurry electrode in 1 M H_2SO_4 cycled at 5 mV s^{-1} to -0.5 V vs. Ag/AgCl	91
Figure 4.18 DFT-calculated proton absorption energy at various oxygen sites in $\text{H}_{2+x}\text{W}_2\text{O}_7$. $\text{O}_{\text{b-yz}}$, O_{t} , and $\text{O}_{\text{b-x}}$ stand for equatorial bridging oxygen, terminal oxygen, and axial bridging oxygen, respectively. The integer before oxygen indicates the number of sites absorbed by proton per 8 W atoms	92
Figure 4.19 Comparison of 200 XRD peak calculated from the DFT-calculated structures to the ex situ experimental data for $\text{H}_{2+x}\text{W}_2\text{O}_7$ at various proton concentrations. a) $x = 0.25$, b) $x = 0.5$, c) $x = 0.75$, and d) $x = 1$. In the figures, “sim.” and “exp.” stand for simulated and experimental, respectively. A gaussian function was used for the shape of the simulated pattern.....	94
Figure 4.20 Physical characterization of the proton insertion mechanism in $\text{H}_2\text{W}_2\text{O}_7$. a) Linear sweep voltammograms of a $\text{H}_2\text{W}_2\text{O}_7$ slurry electrode in 1 M H_2SO_4 cycled at 5 mV s^{-1} between -0.7 and 0.3 V vs. Ag pseudo-reference. b) In situ Raman spectra of $\text{H}_{2+x}\text{W}_2\text{O}_7$ as a function of proton insertion, x . The spectra were taken at the terminal potentials of the linear sweep voltammograms. c) Optical micrographs of the same electrode showing the multicolor electrochromism of $\text{H}_{2+x}\text{W}_2\text{O}_7$. Scale bar = 10 μm	95
Figure 4.21 Bond angle and length statistics of DFT-calculated structures of $\text{H}_{2+x}\text{W}_2\text{O}_7$ at various proton concentrations. a) four corner-sharing tungsten oxide octahedra with a few tungsten and oxygen atoms labeled for illustration purpose. The statistics for the following bond angles and lengths are presented: b) equatorial W–O–W bond angles [including W(1)–O(4)–W(3)	

	and W(2)–O(5)–W(4)], c) equatorial W–O bond lengths [including W(1)–O(4), W(3)–O(4), W(2)–O(5), W(4)–O(5),], d) axial O(1)–W(1)–O(2) bond angles, e) axial W(1)–O(1) and W(1)–O(2) bond lengths, f) axial W(1)–O(2)–W(2) bond angles, g) axial W(1)–O(2) and W(2)–O(2) bond lengths, h) axial O(2)–W(2)–O(3) bond angles, and i) W(2)–O(2) and W(2)–O(3) bond lengths. The error bars stand for standard deviations of the measurements performed on 8 tungsten-oxide octahedra. At $x = 0.25$, both the absorptions at O_t and O_{b-yz} sites are considered and at other concentrations only O_t absorption is considered	98
Figure 5.1	Voltage versus capacity for magnesium metal and cathode materials for magnesium ion under currently active investigations. ^{16–34}	103
Figure 5.2	a) Crystal structure of Chevrel phase Mo_6S_8 ; ³⁵ b) a performance summary of a Mg-rechargeable battery prototype using a Mo_6S_8 cathode and a magnesium metal anode. ³⁶	104
Figure 5.3	Framework structure of Prussian blue analogue. ³⁷	105
Figure 5.4	1D tunneled/olivine structures: a) hollandite MnO_2 , ³⁸ b) todorokite MnO_2 , ³⁹ and c) transition metal silicates. ⁴⁰	107
Figure 5.5	2D layered structures: a) orthorhombic V_2O_5 , ⁴¹ b) MoS_2 , ⁴² c) orthorhombic MoO_3 , ⁴³ and d) birnessite MnO_2 . ⁴⁴	107
Figure 6.1	Crystal structures of a) monoclinic WO_3 , b) orthorhombic $WO_3 \cdot H_2O$, and c) monoclinic $WO_3 \cdot 2H_2O$	111
Figure 6.2	CVs at 0.5 mV s^{-1} of WO_3 , $WO_3 \cdot H_2O$, and stainless steel in a 0.001 M ferrocene and 0.1 M $Mg(ClO_4)_2$ in acetonitrile (ACN) electrolyte. The pseudoreference electrode was an Ag wire and the counter electrode was activated carbon. The dashed line indicates the half-wave potential of Fc/Fc^+ ($E_{1/2, Fc/Fc^+}$) vs. Ag/Ag^+	114
Figure 6.3	SEM micrographs of thin film electrodes before (a, c, e) and after (b, d, f) cycling in 0.1 M $Mg(ClO_4)_2$ in ACN electrolyte: a & b) WO_3 , c & d) $WO_3 \cdot H_2O$, e & f) $WO_3 \cdot 2H_2O$. The particle morphology is similar for all materials before cycling and there is no apparent change in particle morphology after electrochemical cycling. Scale bar = 500 nm.....	118
Figure 6.4	Raman spectra of the as-synthesized $WO_3 \cdot 2H_2O$, $WO_3 \cdot H_2O$, and WO_3 powders showing the phase purity of each material as highlighted by the positions of the terminal and bridging oxygen stretching modes.....	119
Figure 6.5	CVs of thin film electrodes of WO_3 , $WO_3 \cdot H_2O$, and $WO_3 \cdot 2H_2O$ in 0.1 $Mg(ClO_4)_2$ in ACN at a) 0.5 mV s^{-1} and b) 10 mV s^{-1} . All materials undergo reversible storage of Mg^{2+} , with the highest capacity observed in WO_3 .	

However, the rate capability of the hydrated phases is better, as evidence by their higher current at 10 mV s⁻¹. The numbers in (a) are the redox peak pair positions whose ΔE_{peak} is noted in the main text..... 122

Figure 6.6 Capacity and Coulombic efficiency of Mg²⁺ storage in thin film electrodes of WO₃, WO₃·H₂O, and WO₃·2H₂O: a) capacity and number of e⁻ per WO₃ vs. sweep rate and b) Coulombic efficiency vs. sweep rate. The high capacity of WO₃ quickly declines as the sweep rate is increased above 0.1 mV s⁻¹ from 75 mAh g⁻¹ to less than 10 mAh g⁻¹ at 20 mV s⁻¹. The Coulombic efficiency tends to improve as the sweep rate increases likely due to decreasing effects of parasitic reactions..... 124

Figure 6.7 Ex situ Raman spectra of a thin film electrode of WO₃ at three different stages: as-synthesized (pristine), magnesiated, and cycled. There is no change in the structure after Mg²⁺ storage. The optical images of the thin film electrodes in the inset show the reversible electrochromism of the WO₃ with Mg²⁺ 125

Figure 6.8 Ex situ Raman spectra of the thin film electrodes of WO₃·H₂O at three different stages: as-synthesized (pristine), magnesiated, and cycled. There is no change in the local structure after Mg²⁺ storage. The optical images of the thin film electrodes in the inset show the reversible electrochromism of the WO₃·H₂O with Mg²⁺ 126

Figure 6.9 Ex situ Raman spectra of the thin film electrodes of WO₃·2H₂O at three different stages: as-synthesized (pristine), magnesiated, and cycled. After Mg²⁺ storage, the structure transforms to WO₃·H₂O as indicated by the shift of the W=O and O-W-O stretching modes to lower wavenumbers. The optical images of the thin film electrodes in the inset show the reversible electrochromism of the WO₃·2H₂O with Mg²⁺ 127

Figure 6.10 Raman spectra of a WO₃·2H₂O thin film electrode before and after immersion in 0.1 M Mg(ClO₄)₂ in ACN electrolyte for 10 hours. The shift of the bridging and terminal oxygen stretching and deformation modes to lower wavenumbers indicates the formation of WO₃·H₂O and the removal of interlayer water from the structure 129

Figure 6.11 Ex situ XRD patterns of WO₃ slurry electrodes at three different stages: as-synthesized (pristine), magnesiated, and cycled. The asterisk symbol indicates the diffraction peak of the stainless steel substrate, which also served as an internal reference. The *m*-WO₃ reference pattern at the bottom corresponds to ICDD PDF 04-005-4272 (monoclinic γ -WO₃) and the *c*-WO₃ reference pattern corresponds to ICDD PDF 00-041-0905 (cubic WO₃) 130

Figure 6.12 HAADF images overlaid with EDS patterns of WO₃ at three different stages: a) as-synthesized (pristine), b) magnesiated (Mg_{0.18}WO₃), and c) cycled. The

HAADF images represent the regions where the EDS patterns were collected. The Cu and C signals came from the carbon-coated Cu TEM grid.....	131
Figure 6.13 CVs at 0.5 mV s^{-1} and the cathodic capacity of thin film and slurry electrodes cycled in non-aqueous Mg^{2+} and Li^+ electrolytes, respectively: a, b) WO_3 and c, d) $\text{WO}_3 \cdot \text{H}_2\text{O}$	133
Figure 6.14 Determination of the sweep rate dependence of the anodic peak current (b value) from 0.1 to 20 mV s^{-1} for WO_3 and $\text{WO}_3 \cdot \text{H}_2\text{O}$ a) thin film electrodes in Mg^{2+} and b) slurry electrodes in Li^+ non-aqueous electrolytes. The CVs for these data points are shown in Figures 6.15 and 6.16	134
Figure 6.15 CVs from $0.1 - 20 \text{ mV s}^{-1}$ for a) WO_3 and b) $\text{WO}_3 \cdot \text{H}_2\text{O}$ in $0.1 \text{ M Mg}(\text{ClO}_4)_2$ in ACN electrolyte. The * indicates the variation of the peak current with sweep rate utilized to determine the “ b -value” in Figure 6.14a	135
Figure 6.16 CVs from $0.1 - 100 \text{ mV s}^{-1}$ for a) WO_3 and b) $\text{WO}_3 \cdot \text{H}_2\text{O}$ in 1 M LiClO_4 in PC electrolyte. Only anodic peaks from $0.1 - 20 \text{ mV s}^{-1}$ were used for kinetics analysis. The * indicates the variation of the peak current with sweep rate utilized to determine the “ b -value” in Figure 6.14b	135
Figure 6.17 Performance of a slurry electrode of WO_3 in Mg^{2+} electrolyte: a) cyclic voltammetry at 0.1 mV s^{-1} with color gradually changing from black to red as the cycle number increases and b) capacity vs. cycle number (after cycle 36, the working electrode was adjusted to immerse the entire active area into the electrolyte), and c) Raman spectra of the electrode before and after 50 cycles at 0.1 mV s^{-1}	137
Figure 7.1 CVs at 0.5 mV s^{-1} and galvanostatic discharge curves at 1C of WO_3 electrodes in $0.1 \text{ M Mg}(\text{ClO}_4)_2$ in CH_3CN with various water concentrations for ex situ physical characterization. a) CVs of 5 mg cm^{-2} electrodes on stainless steel substrates for ex situ SEM, b) CV of a $100 \text{ }\mu\text{g cm}^{-2}$ thin film electrode for ex situ TEM, c) CVs of $200 \text{ }\mu\text{g cm}^{-2}$ electrodes on gold-plated glass substrate for ex situ XPS, d) CVs of slurry electrodes (mass between 1 and 3 mg cm^{-2}) on stainless steel substrates cycled just below the first redox for ex situ XRD, and e) galvanostatic discharge curves of slurry electrodes (mass between 1 and 3 mg cm^{-2}) on stainless steel substrates to obtain 60 mAh g^{-1} in both electrodes, which is equivalent to cycling beyond the second redox peak in cyclic voltammetry. Note that the potential ranges in the CVs shifted from one to another. This was caused by the potential shift of the Ag pseudoreference electrode.	144
Figure 7.2 Cyclic voltammograms of WO_3 in $0.1 \text{ M Mg}(\text{ClO}_4)_2$ in CH_3CN with various added water concentrations in the electrolyte at a sweep rate of 1 mV s^{-1} . Arrows indicate the direction of redox peak shift with increased water concentration. $1/1'$ and $2/2'$ represent two sets of redox peaks associated with	

the energy storage process in WO ₃ . A fresh WO ₃ electrode was used for each water concentration	147
Figure 7.3 Photographs of 25 mg WO ₃ dropcast on 2.5 cm × 3 cm stainless steel substrate in the a) pristine state and b) after reduction in 0.1 M Mg(ClO ₄) ₂ in CH ₃ CN with 0 [H ₂ O]:[Mg ²⁺] at 20 mV s ⁻¹	147
Figure 7.4 CVs of WO ₃ ·H ₂ O at 1 mV s ⁻¹ in 0.1 M Mg(ClO ₄) ₂ in CH ₃ CN with various added concentrations of water	148
Figure 7.5 Anodic capacity as a function of sweep rate for selected cyclic voltammograms in Figure 7.2	149
Figure 7.6 Cyclic voltammograms (CVs) of WO ₃ at 0.1 and 0.5 mV s ⁻¹ in 0.1 M Mg(ClO ₄) ₂ in acetonitrile (CH ₃ CN) with various concentrations of added water for [H ₂ O]:[Mg ²⁺] of a) 0, b) 2, c) 4, d) 6, e) 8, and f) 20. In the figures, 1/1', 2/2', 3/3', and 4/4' indicate the likely electrochemical redox couples. Each cyclic voltammetry experiment was conducted in a fresh electrolyte with a fresh WO ₃ electrode	150
Figure 7.7 Integrated capacity of the cathodic cycle versus time calculated from the CVs in Figure 7.2	151
Scheme 7.1 Illustration of the electrochemical system in this study and the potential mechanisms by which water in the non-aqueous electrolyte could improve electrochemical insertion kinetics	152
Figure 7.8 Ex situ XRD patterns of WO ₃ slurry electrodes, comparing the pristine electrode to the ones reduced in electrolytes with different water concentrations. The asterisk (*) indicates peaks from the stainless-steel substrates. <i>m</i> -WO ₃ reference pattern is from PDF 04-005-4272 (monoclinic γ -WO ₃); <i>t</i> -WO ₃ reference pattern is from PDF 00-050-1750 (tetragonal Na _{0.1} WO ₃); the <i>c</i> -WO ₃ reference pattern is from PDF 01-075-0293 (cubic Na _{0.3} WO ₃). ⁴⁵	154
Figure 7.9 a) ¹ H-NMR spectra of 0.1 M Mg(ClO ₄) ₂ in CD ₃ CN with various concentrations of added water. b) ¹ H-NMR spectra of CD ₃ CN with various concentrations of added water	156
Figure 7.10 Single-peak fitting of the 200 reflection in the XRD patterns of <i>e</i> _{0.52} WO ₃ shown in Figure 7.8, for a) 0 [H ₂ O]:[Mg ²⁺] and b) 20 [H ₂ O]:[Mg ²⁺]. The data was fitted with Line-Profile Analysis Software (LIPRAS). ⁴⁶ The fit was performed with a combination of Cu-K α ₁ and Cu-K α ₂ using Pseudo-Voigt peak shape function. The background was fit with a polynomial function and refined during the peak fitting process	157

Figure 7.11 Lattice parameter comparison of cubic Mg_xWO_3 to published data (Table 7.1) on cubic M_xWO_3 ($M = H, Li, Na, \text{ and } Ca$). Assuming pure Mg^{2+} insertion, x in Mg_xWO_3 was assumed as half of the stored charge	158
Figure 7.12 Electron trajectory and X-ray intensity simulation of a 20 kV electron beam on a Mg_xWO_3 film. a) Electron trajectory as a function of depth and width. The red trajectories represent back-scattered electrons and the blue trajectories are for electrons that did not back scatter. b) The intensity of the Mg K-edge X-ray generated as a function of depth	161
Figure 7.13 a) EDS of WO_3 thin film electrodes, comparing a control sample immersed in the dry Mg electrolyte to the ones reduced in electrolytes with different water concentrations. b) Bar charts comparing the fraction of Mg^{2+} obtained from EDS and cyclic voltammetry (calculated) assuming that all charge storage was only due to Mg^{2+} insertion.....	161
Figure 7.14 Survey and high resolution XPS spectra of WO_3 reduced in Mg electrolytes with 0 and 20 $[H_2O]:[Mg^{2+}]$. a,b) survey scans. c,d) O 1s spectra, the fitted peaks are $H_2O/C-O/ClO_4^-$ (533.2 eV), OH^- or $C=O$ (531.9 eV), and WO_3 (530.1 eV). e,f) C 1s spectra, the fitted peaks are C-C (285 eV), C-O (286.5 eV), and COOR (289 eV). g,h) Mg 2p spectra, the fitted peaks are Mg in WO_3 (50.8 eV) and Mg-OH (49.9 eV). i,j) W 4f spectra, the fitted peaks are W(V) $4f_{7/2}$ (34.1 eV), W(V) $4f_{5/2}$ (36.5 eV), W(VI) $4f_{7/2}$ (35.9 eV), and W(VI) $4f_{5/2}$ (38.1 eV)	164
Figure 7.15 a) HRTEM micrograph of a WO_3 particle reduced in Mg electrolytes with 20 $[H_2O]:[Mg^{2+}]$. The inset shows the FFT results and the corresponding regions in yellow boxes. b) HAADF-STEM micrograph and STEM-EDS mapping of a group of WO_3 particles “on edge” reduced in Mg electrolyte with 20 $[H_2O]:[Mg^{2+}]$. The white box indicates the region of STEM-EDS mapping	167

Chapter 1: Introduction

The last decade has seen great progress in electrochemical energy storage (EES) mainly through the large-scale mass production of Li-ion batteries (LIBs). The economy of scale has significantly reduced the cost of batteries and led to the proliferation of technologies ranging from portable electronics, cell phones, laptops, to electric vehicles. The impact is reflected not only by the number of technologies available today that are powered by batteries, but also by the depth of market penetration. In developing countries like Ghana, the mobile phone ownership has increased from 8% in 2002 to 83% in 2015, with a steady increasing market share of smartphones.⁴⁷ Since developing countries account for 80% of the world's population and >95% of the population growth,⁴⁸ the battery-powered technologies are shaping the way of communication among almost the entire upcoming generation on earth. In addition, EES is expected to play an important role in the large-scale adoption of renewable technologies like solar and wind power, which will help achieve the goal of global greenhouse gas net-zero emissions in the long-term future.⁴⁹ Because of the profound impact of Li-ion batteries, three of the inventors, John Goodenough, Stanley Whittingham, and Akira Yoshino, were honored with the 2019 Nobel Prize in Chemistry.

The broad applications of EES technologies demand their continued development to include options for improved energy and power density. Due to the fundamental energy storage mechanisms (**Figure 1.1**), there are tradeoffs between these two merits. In general, the mechanisms that involve less material structural or volume change will have faster kinetics and smaller overpotential (to be introduced in §2.2). The highest power density ($\sim 15 \text{ kW kg}^{-1}$) is achieved in electrical double-layer capacitors (EDLCs), which typically have relatively low energy densities between $1 - 10 \text{ Wh kg}^{-1}$.⁵⁰ On the other extreme, advanced materials based on conversion mechanisms can reach up to two-to-five times the capacity as the materials used for commercial

LIBs, achieving energy densities over 2000 Wh kg^{-1} .⁵¹ However, the fundamental kinetic hinderance requires charging time over few hours to achieve this capacity. Electrochemical ion insertion or intercalation (*note: intercalation was originally defined as a special case of insertion in layered materials; the use of “intercalation” is now broadened to describe insertion in other materials, and this term will be used interchangeably in the dissertation*) remains as the most promising mechanism to achieve simultaneous high power and high energy density EES. The commercial LIBs based on intercalation mechanisms with phase changes have a power density of $\sim 1 \text{ kW kg}^{-1}$ and an energy density of $\sim 200 \text{ Wh kg}^{-1}$.⁵² Due to the diffusion-limited kinetics, they typically require charging times from tens of minutes to hours. When the kinetics are no longer limited by diffusion and no phase transformation takes place, the mechanism is termed insertion or intercalation pseudocapacitance (because the electrochemical behavior begins to approximate a capacitor), which allows for charging time of less than 10 mins. The research in this dissertation was based on the electrochemical ion insertion mechanism, with a primary objective of improving the kinetics of ion insertion for protons and multivalent cations.

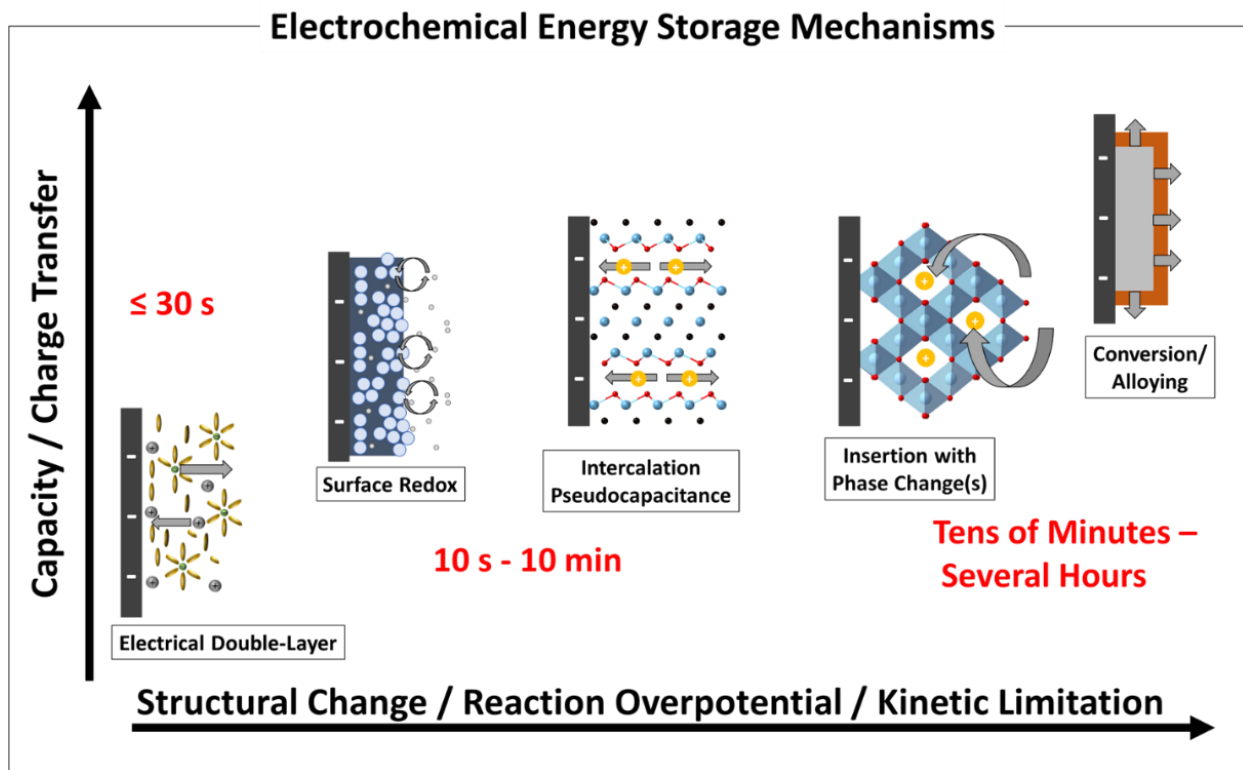


Figure 1.1. Classification of electrochemical energy storage mechanisms as a function of their characteristic capacity and the associated degree of structural changes of the electrodes, reaction overpotential, and kinetic limitations. Adapted from reference 1.

We identified two areas where the improvement of insertion kinetics could be particularly helpful. The first area is the search for materials and mechanisms that could enable simultaneous high-power and high energy density, what has been termed the “holy grail” of EES.⁵³ This research area aims to help EES meet the ever specialized and diverse needs of new applications. The other area is the improvement of cathode materials for rechargeable magnesium-ion batteries. Magnesium-ion batteries expand energy storage chemistry beyond Li-ion and are one alternative for high energy density as the performance of LIBs approaches their theoretical limit. One bottleneck of magnesium batteries is the lack of cathode materials with fast Mg^{2+} insertion kinetics.^{36,54}

During the search for high-power and high energy density materials, we identified structural water as an interesting structure motif that could improve the ion insertion kinetics in tungsten oxides.¹⁴ To shed light on the relationship between structural water and kinetic improvement, in the first study (Chapter 3) we probed the mechanical deformation of WO_3 and $\text{WO}_3 \cdot 2\text{H}_2\text{O}$ during electrochemical insertion of protons at different rates using operando atomic force microscopy dilatometry. The mechanical behavior helped us propose a structural origin of the fast kinetics in $\text{WO}_3 \cdot 2\text{H}_2\text{O}$; that is, the presence of structural water reduces the deformation and extent of structural reorganization during ion insertion. We also discovered a direct relationship between the electrochemical current associated with ion insertion and the rate of electrode deformation, which allowed for indirect measurement of local electrochemical behavior using mechanical deformation.

In the second study (Chapter 4), we applied the knowledge of structural water as a motif for fast insertion kinetics to synthesize materials with higher energy storage performance. $\text{WO}_3 \cdot \text{H}_2\text{O}$ had fast ion insertion kinetics but suffered from a relatively low capacity. We identified a metastable material, $\text{H}_2\text{W}_2\text{O}_7$ ($\text{W}_2\text{O}_6 \cdot \text{H}_2\text{O}$), which could be obtained from selective etching of $\text{Bi}_2\text{W}_2\text{O}_9$. It had the same structural water motif as $\text{WO}_3 \cdot \text{H}_2\text{O}$ but with less water content. While we expected a slight capacity increase, $\text{H}_2\text{W}_2\text{O}_7$ stored 100% more capacity than $\text{WO}_3 \cdot \text{H}_2\text{O}$ and could deliver almost all of its theoretical capacity within a minute. To understand the energy storage mechanism, we resolved all atom positions using X-ray diffraction, neutron pair distribution function, and scanning transmission electron microscopy, and studied the ion insertion mechanism in $\text{H}_2\text{W}_2\text{O}_7$ using density functional theory, ex situ X-ray diffraction, and in situ Raman spectroscopy. We found the increase in capacity in $\text{H}_2\text{W}_2\text{O}_7$ as compared to $\text{WO}_3 \cdot \text{H}_2\text{O}$ was likely

due to a change of ion insertion site. $\text{H}_2\text{W}_2\text{O}_7$ also exhibited multi-color electrochromism during proton insertion.

In the third study (Chapter 6), we examined the role of structural water during multivalent ion insertion in a non-aqueous electrolyte. We tested WO_3 , $\text{WO}_3 \cdot \text{H}_2\text{O}$, and $\text{WO}_3 \cdot 2\text{H}_2\text{O}$ in a Mg^{2+} containing non-aqueous electrolyte to examine whether these materials could insert Mg^{2+} and if structural water could improve the kinetics of Mg^{2+} insertion. Both hypotheses were supported by ex situ characterization.

In the previous study, we could not exclude the role of trace amounts of water from the electrolyte salt on ion insertion kinetics in non-aqueous electrolyte. In the literature, the presence of this water was attributed to several mechanisms, including water co-insertion, proton co-insertion, or formation of a beneficial interphase. In the final study (Chapter 7), we systematically varied the water concentration in the Mg^{2+} -containing non-aqueous electrolyte and performed a series of electrochemical and ex situ physical characterizations. The experimental evidence did not support any of the existing hypotheses in the literature and led us to propose a water-enhanced surface diffusion mechanism to explain the improvement of Mg^{2+} insertion kinetics.

This dissertation used tungsten oxides as model structures to explore the effect of structural water and trace water in a non-aqueous electrolyte on the kinetics of electrochemical proton and Mg^{2+} insertion. Structural water improved proton insertion kinetics by dampening the structural transformation and was applied to identify novel materials with high-power energy storage capabilities. This effect was not specific to protons and also improved Mg^{2+} insertion kinetics in a non-aqueous electrolyte. Trace water in the non-aqueous Mg electrolyte could improve Mg^{2+} ion insertion in tungsten oxide. The mechanism was hypothesized to be water-enhanced surface diffusion. In addition to the materials insights, this dissertation extended the capability of an

operando atomic force microscopy dilatometry technique to measure local electrochemical behavior of redox-active electrodes.

Chapter 2: Fundamentals of Electrochemical Energy Storage

This chapter aims to provide a brief introduction to materials research for electrochemical energy storage with a special focus on the ion insertion mechanism. The sections below dive into the thermodynamics and kinetics of EES and the individual processes that happen during an ion insertion reaction.

§2.1 (thermodynamics) shows how to calculate energy, capacity, and voltage of EES systems at equilibrium and explains how an ion insertion reaction occurs at the electrode.

§2.2 (kinetics) demonstrates the factors that lead to the deviations of performance from the equilibrium conditions and describe basic analytical tools to analyze the kinetics of electrodes.

§2.3 (physical picture of ion insertion) provides an overview of the processes during ion insertion and serves as a prelude to the following sections on each individual process.

§2.4 (electrical double layer) describes how the electric double layer affects energy storage and provides a modern model of double layer.

§2.5 (surface ion adsorption) elaborates on the adsorption isotherms and how they affect the modeling of pseudocapacitive and ion insertion behaviors.

§2.6 (surface diffusion) discusses surface ion diffusion and how it can affect the kinetics of ion insertion.

§2.7 (bulk diffusion) draws implications from ambipolar diffusion of ions in materials, mentions a few experimental techniques for measuring diffusivity in energy storage research, and reviews the connection between activation energy barrier, diffusivity, and conductivity.

§2.8 (material deformation during electrochemical energy storage) discusses deformation of materials as a response to ion insertion and how applying forces to materials may affect ion insertion.

2.1 Thermodynamics

The maximum energy of an EES system is determined by the thermodynamics. For a reversible electrochemical reaction, the available electrical energy is the Gibbs free energy (ΔG) with electrical terms:

$$\Delta G = nFV \quad (2.1)$$

where, n is the number of electrons transferred per mol of reactants, F is the Faraday's constant or the charge per mole of electrons, V is the voltage of the EES system or the electromotive force of the reaction. Because both charge and voltage vary in EES systems under operation, we use the integration form to calculate the energy (E):

$$E = \int QdV \quad (2.2)$$

where, Q is the total charge generated by the electrochemical reaction usually normalized by mass or volume. **Figure 2.1** demonstrates the characteristic relationship between potential and charge for an ideal battery and an ideal capacitor. In an ideal capacitor, charge has a linear relationship with potential, and this slope is defined as the capacitance (C):

$$Q = CV \quad (2.3)$$

The energy equation for an ideal capacitor is then:

$$E = \frac{1}{2} CV^2 \quad (2.4)$$

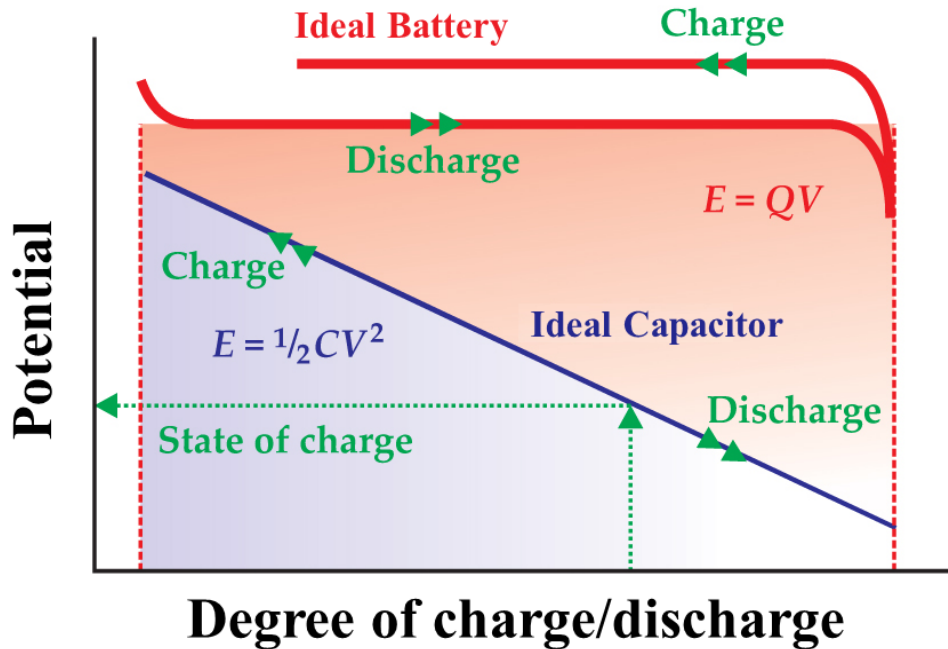


Figure 2.1 Characteristic electrochemical signatures of the relationship between potential and charge for an ideal battery and an ideal capacitor measured under constant current charge/discharge conditions. Adapted from reference 2.

An ideal battery has a constant voltage profile across the whole range of operation and the energy equation may be simplified as:

$$E = QV \quad (2.5)$$

The fundamental explanation for the voltage plateau is the Gibbs phase rule at constant temperature and pressure conditions:

$$f = C_n - p \quad (2.6)$$

where, f is the degree of freedom, C_n is the number of components participating in the reaction, and p is the number of phases. In battery systems, the electrochemical reactions at both the anode and cathode are usually two-phase and involve solid components. The two-phase reaction leaves zero degrees of freedom, so voltage has to be invariant until a reaction limit is reached. For solid-

solution reactions that involve only one phase, as in many pseudocapacitive materials, the voltage will change with the degree of charge/discharge enabling the calculation of capacitance as in Equation 2.3. Note that there is a hysteresis between the charge and discharge voltage plateaus due to kinetic effects, termed polarization, which will be introduced in the next section.

The charge of faradaic reactions can be calculated via Faraday's law of electrolysis:

$$Q = \frac{mFn}{M} \quad (2.7)$$

where, m is the mass of the reactant and M is the molar mass of the reactant. It provides an assessment of the capacity of a material.

Since this dissertation focuses on ion-insertion type materials, a generalized ion-insertion reaction is analyzed below. Assume a transition metal oxide MO_2 (M = transition metal) can undergoes reversible electrochemical insertion of cations (A^{n+}):



The Gibbs free energy under standard state of this reaction is the difference in the formation energy (G) of MO_2 and AMO_2 :

$$\Delta G_{rxn}^\circ = G(AMO_2) - G(MO_2) \quad (2.9)$$

The standard potential of this reaction with respect to the standard electrode potential of the A^{n+}/A redox couple can be calculated using equation 2.1.

$$V^\circ = \frac{\Delta G_{rxn}^\circ}{nF} \quad (2.10)$$

In actual systems, ΔG_{rxn}° and V° are affected by the temperature and activity (approximated by concentration) according to the Nernst equation:

$$\Delta G_{rxn} = \Delta G_{rxn}^\circ + RT \ln \frac{1}{[A^{n+}]} \quad (2.11)$$

$$V = V^\circ - \frac{RT}{nF} \ln \frac{1}{[A^{n+}]} \quad (2.12)$$

where, R is ideal gas constant, T is temperature, and $[A^{n+}]$ is the concentration of A^{n+} in the electrolyte. Equation 2.12 indicates the higher the electrolyte concentration, the higher the redox potential. In an EES system, materials with higher potential are usually used as the cathode and the ones with lower potential are anodes. The bigger the potential difference, the more energy we can extract out of the system. However, both potentials should be within the electrolyte stability window for long cycle life and avoid electrolyte breakdown / the need for interface stabilization.

The redox reaction during an electrochemical ion insertion can be illustrated using the simplified energy diagram shown in **Figure 2.2**, using LiCoO_2 as an example. When the reaction is thermodynamically favorable, adding more electrons or lowering the electrode potential will increase the Fermi level (E_f), cause reduction of Co^{4+} to Co^{3+} , and simultaneously lead to Li^+ intercalation to balance the charge. The potential where this reaction occurs is determined by equation 2.12. As the t_{2g} band is filled up, almost all accessible Co^{4+} is reduced. This is where the reversible insertion reaction stops and further reduction to element Co^0 will lead to conversion reactions of the material.

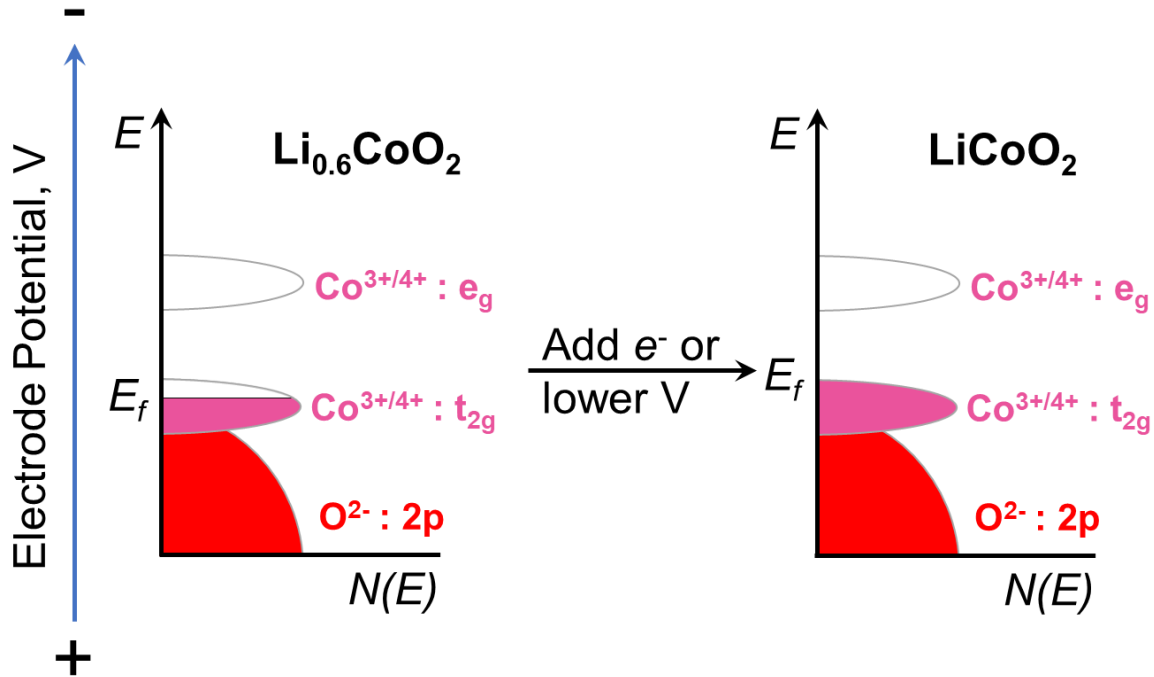


Figure 2.2. Simplified energy diagrams of $\text{Li}_{0.6}\text{CoO}_2$ and LiCoO_2 . E_f is the Fermi level of the electrode. e_g and t_{2g} stand for the doubly and triply degenerate states of the octahedrally-coordinated Co from crystal field theory. The energy diagram of LiCoO_2 is adapted from reference 3.

2.2 Kinetics

Thermodynamics help us determine the maximum energy extractable at equilibrium conditions and kinetics govern the power capability of EES systems. When we increase the rate of reaction by applying greater current or faster potential ramp, the capacity of the electrode will decrease and the voltage hysteresis in Figure 2.1 will increase, leading to poorer energy efficiency. Both changes are the result of three types of polarizations or overpotentials. In this section, we elaborate on the effect of kinetics on potential and capacity of ion-insertion type materials.

While the thermodynamics of an electrochemical reaction were introduced in the last section, the detailed mechanism usually involves a series of physical, chemical, and electrochemical steps. The rates of these individual steps determine the kinetics of the energy storage processes. Three most pronounced kinetics effect for polarization are: (1) activation polarization, which is associated with the kinetics of the charge-transfer reaction, (2) ohmic polarization, which is due to the resistance of the electrochemical cell, especially the resistance of the electrode, and (3) concentration polarization, which is usually due to the diffusion limitation in the electrode.⁴ The polarizations (sometimes named overpotential), η , manifest themselves as deviations from the standard potential:

$$\eta = E_{OCV} - E_T \quad (2.13)$$

where, E_{OCV} is the open-circuit voltage, like what will be measured in Figure 2.2a, and E_T is the cell voltage upon current application.

As shown in **Figure 2.3**, when a constant current is applied, initially when there are enough reactive sites on the surface, the reaction is limited by the charge transfer reaction. The activation polarization follows the Tafel equation:

$$\eta = a - b \log (I/I_o) \quad (2.14)$$

where, a and b are constants, I is current, and I_o is exchange current. The Ohmic polarization occurs throughout the electrochemical reaction and follows Ohm's law:

$$\eta = IR_e \quad (2.15)$$

where, R_e is the electrical resistance. Concentration polarization arises after the surface sites are mostly reacted and the kinetics of the reaction are limited by the diffusion of the inserted ions (as ion diffuse into the bulk, the originally reacted surface site is reactivated). The concentration polarization due to solid-state diffusion is dependent on the intrinsic ionic conductivity of the

material and the diffusion length (size of the particles constituting the electrode material). The diffusion limitation is discussed below for the capacity retention at higher rate of charge/discharge.

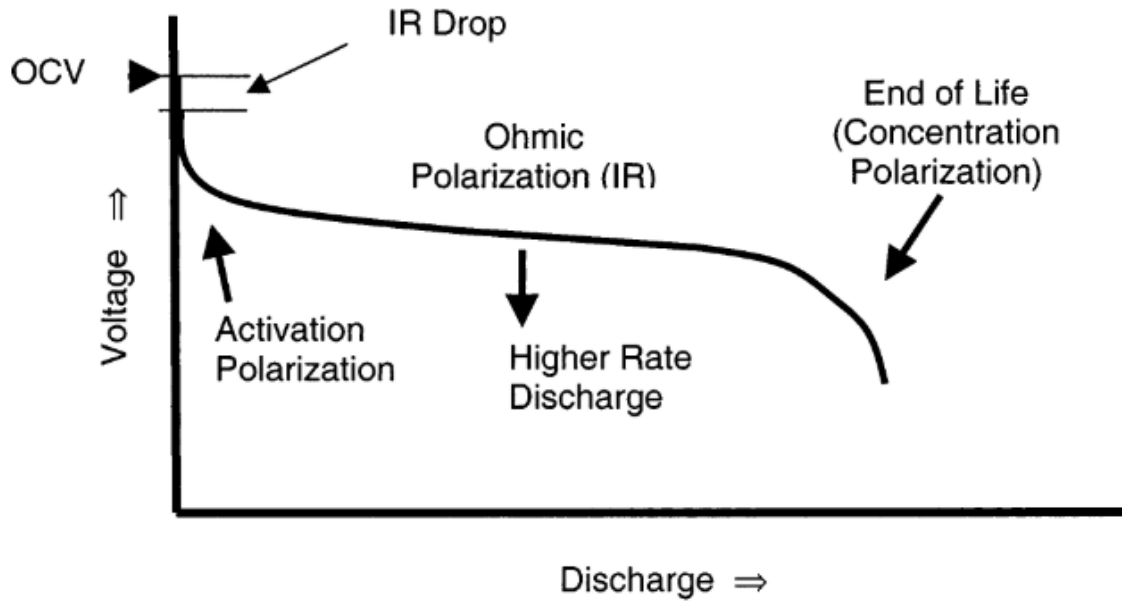


Figure 2.3. Typical discharge curve for a battery electrode measured under constant current charge/discharge conditions. The three types of polarization are labeled in the graph. Adapted from reference 4.

The decrease in capacity at higher rates is largely due to concentration polarization. As the potential where ion insertion happens deviates further from the standard potential, the reaction will not be able to complete before the breakdown of electrolyte starts to happen. Fundamentally, concentration polarization occurs because the diffusion length in the active material (l) is greater than how far the ion can diffuse in the given time frame:

$$l > \sqrt{Dt_d} \quad (2.16)$$

where D is the diffusion coefficient of the ion and t_d is the diffusion time. To reduce the concentration polarization, significant efforts have been made to engineer existing materials and

to find new materials with high intrinsic ionic and electronic conductivity. It should be noted that in thick electrodes (hundreds of microns), concentration polarization can also arise from the electrolyte in pores.⁵⁵

In a more simplified manner, kinetics can be broadly classified by whether the charge storage is surface-limited or diffusion-limited. Kinetics manifest themselves in determining the power of EES devices. EES based on electrical double-layer formation, surface redox, or intercalation pseudocapacitance is fundamentally surface-limited, and this enables an operation time typically less than 10 mins. EES operating by intercalation with phase changes or conversion mechanisms are typically diffusion-limited and usually require an hour or longer charging times.

One popular electrochemical analytical tool to investigate the rate-limiting behavior of EES materials is cyclic voltammetry. In contrast to the constant current (also known as galvanostatic) method, cyclic voltammetry changes the potential of an electrode at a constant rate. A comparison of the cyclic voltammograms to the discharge curves for various types of EES materials can be found in **Figure 2.4**. In this categorization, Type B pseudocapacitive is Faradaic in nature, while Type C Faradaic is not capacitive in nature. Cyclic voltammetry is a common characterization technique for the study of pseudocapacitive materials because the relationship between current and sweep rate can readily be used to identify the presence of diffusion limitations.

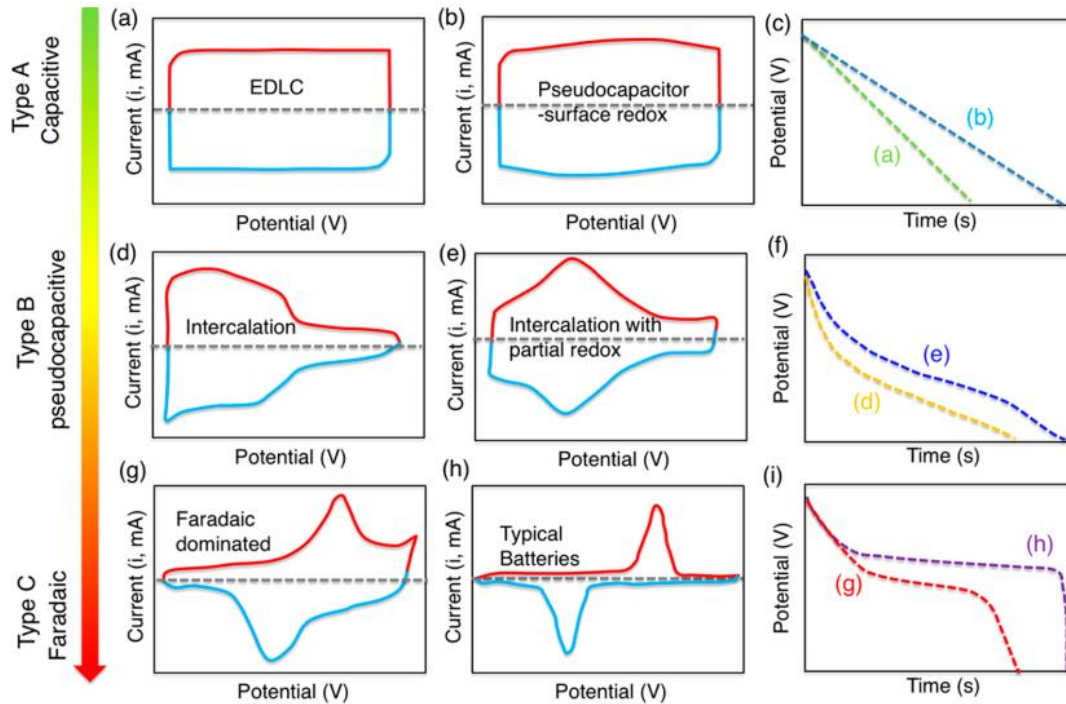


Figure 2.4. Examples of how electrochemical characterization can be utilized to identify charge storage mechanisms. Schematic cyclic voltammograms (a, b, d, e, g, h) and corresponding galvanostatic profiles (c, f, i) representing various types of charge storage. The pseudocapacitive types presented here include (b) surface redox pseudocapacitance (e.g., hydrated RuO_2 in acidic aqueous electrolytes), (d) intercalation pseudocapacitance (e.g., $T\text{-Nb}_2\text{O}_5$ in a Li^+ non-aqueous electrolyte), and (e) combination of intercalation and surface redox pseudocapacitance (e.g., $\text{Ti}_3\text{C}_2\text{T}_x$ MXene in an acidic aqueous electrolyte). Reprinted from reference 5.

Lindström *et al.* proposed a simple relationship between the applied sweep rate and observed electrochemical current, and used it to study Li^+ insertion into nanoporous anatase TiO_2 films. This relationship can be used as a first-line tool (referred to as *b*-value analysis) to determine the presence of surface-controlled or capacitive (vs. semi-infinite diffusion-controlled) kinetics:

$$I(V) = av^b \quad (2.17)$$

where $i(V)$ is the current at a specific potential, a and b are adjustable parameters, and b can be determined as the slope of $\log(i)$ vs. $\log(v)$ for various sweep rates, v . Kinetic limitations can be estimated from the limiting cases of the b -value, $b = 1$ and 0.5 . When the current is directly proportional to the sweep rate, $b = 1$, the process is surface-controlled. There are two possibilities for the mechanism behind such a response: the current is due to the formation of the electrical double-layer:

$$I = C_{DL}Av \quad (2.18)$$

where C_{DL} is the double-layer capacitance per surface area, and A is the electrochemically active surface area of the electrode. The other option is that the current is due to redox processes not limited by diffusion, what some electrochemical literature terms “modified [thin film] electrodes”.⁵⁶

$$I = \frac{n^2F^2}{4RT} A\Gamma^*v \quad (2.19)$$

where Γ^* is the amount of redox-active adsorbed species at the surface (mol cm^{-2}). Whether the mechanism is ascribed to double-layer capacitance or redox processes not limited by diffusion, the relationship between current and sweep rate is the same, with $b = 1$. Therefore, to distinguish between those two processes, other techniques need to be utilized. One of the most common approaches has been to determine the electrochemically active surface area and then calculate the double-layer capacitance assuming a constant value of $10\text{-}40 \mu\text{F cm}^{-2}$.^{57,58} While this approach may provide a good estimate, determining the electrochemical surface area is often challenging, and the double-layer capacitance of most materials is not clearly established.⁵⁹ This is particularly problematic for pseudocapacitive materials, such as hydrous RuO_2 , that exhibit hydrated grain boundaries or interlayers. The electrochemically active surface area of such materials may be much larger than what is typically measured with, for example, physical adsorption of gas molecules.

Therefore, distinguishing between Faradaic and non-Faradaic processes often requires the combination of electrochemical characterization with techniques that can detect a charge transfer event, such as changes in the optical and electronic properties or bond length, ideally in an operando setting.

When $b = 0.5$, the reaction is semi-infinite diffusion-controlled, and the current follows the irreversible form of Randles-Ševčík equation:

$$I = 0.4958n \cdot FAC^* \cdot D^{1/2} \left(\frac{\alpha n F}{RT} \right)^{1/2} \nu^{1/2} \quad (2.20)$$

where C^* is the maximum concentration of the reduced species in the structure, and α is the transfer coefficient. The Randles-Ševčík equation was developed to determine the diffusion coefficient of a redox-active species in the electrolyte and adapted for the case of redox-active electrodes for semi-infinite diffusion control, for example, when the diffusion distance is much larger than the theoretical diffusion length.⁶⁰

When the b -value falls between 0.5 and 1, the mechanism is attributed to either mixed control (a linear combination of diffusion and capacitive contributions)⁶¹ or finite-length diffusion (where the diffusion distance is no longer much greater than $\sqrt{Dt_d}$).^{62,63} Under the mixed control assumption, Liu *et al.* proposed the following linear combination of surface- and diffusion-controlled currents:⁶¹

$$i(V, \nu) = k_1(V)\nu + k_2(V)\nu^{1/2} \quad (2.21)$$

Dunn *et al.* utilized this concept to deconvolute capacitive vs. diffusive contributions to the total current for many types of nanostructured transition metal oxides.^{64–66} To do this, **equation 2.21** is rearranged to obtain:

$$i(V, \nu)/\nu^{1/2} = k_1(V)\nu^{1/2} + k_2(V) \quad (2.22)$$

Solving for k_1 and k_2 at specific potentials across multiple sweep rates gives the quantitative fraction of the current due to surface- and diffusion-controlled processes. The method allows for the separation of the cyclic voltammograms into surface-controlled and diffusion-controlled regions, as shown in **Figure 2.5a**. The charge stored due to surface- and diffusion-controlled current contributions can then be quantified at different sweep rates, such as in **Figure 2.5b**. One major limitation of this approach is that it does not account for the shift of potential with higher sweep rates due to increased polarization processes, such as Ohmic losses.^{67,68} While equation 2.21 is simplistic, it has provided a critical and quantifiable understanding of how nanoscale materials develop pseudocapacitive features. Automated Matlab programs for calculating capacity, b -value, and cycle life analyses based on cyclic voltammetry data generated by BioLogic potentiostats are provided in Appendices B, C, and D.

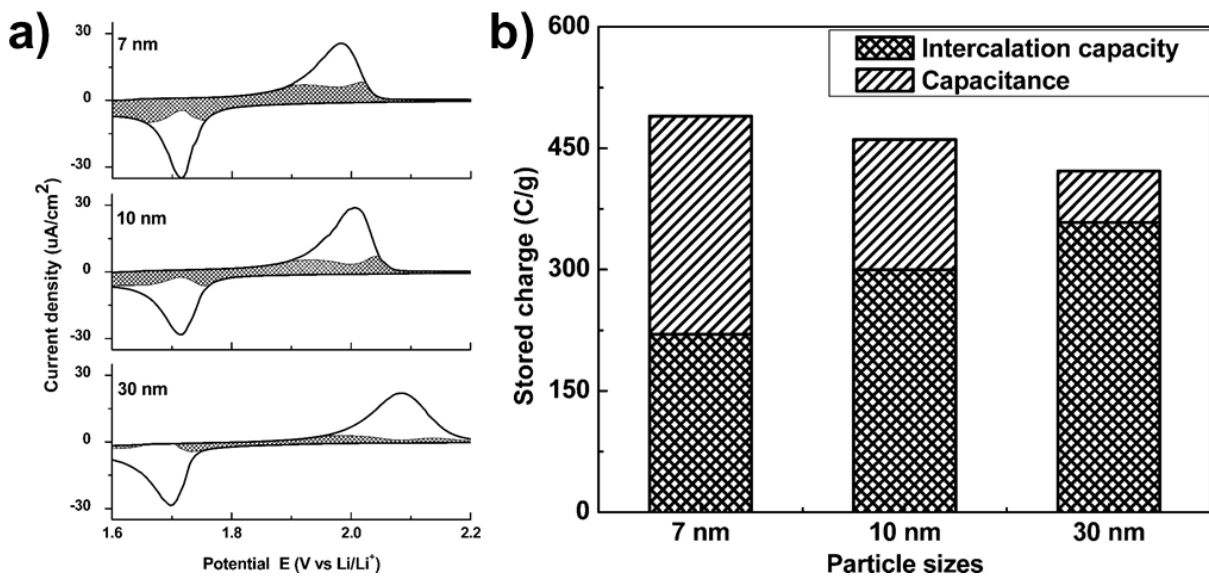


Figure 2.5. (a) Cyclic voltammograms of nanostructured anatase TiO_2 films at 0.5 mV s^{-1} in a non-aqueous Li^+ electrolyte. The surface-controlled currents (shaded regions) are determined with k_1, k_2 analysis using Equation 2.22. (b) Charge storage of the same three TiO_2 thin films at 0.5 mV s^{-1} contributed from surface-controlled (“capacitance”) and diffusion-controlled current (“intercalation capacity”). Adapted from reference 6.

2.3 Physical Picture of Ion Insertion

As discussed in the last section, the detailed mechanism of electrochemical reactions at the electrode involve a series of steps. In this section, the individual steps for ion insertion processes are introduced. More detailed discussions of the individual steps are provided in the subsequent sections. An atomistic view of an ion insertion process is shown **Figure 2.6**. In this model, when an adequate potential or current is applied to the electrode and the ion insertion reaction becomes thermodynamically favorable, ion insertion proceeds with the following steps. In the electrolyte, due to the potential gradient at the electrode, cations are attracted to the electrode/electrolyte interface with their solvation shells. Near the interface, they participate in the formation of the

electrical double layer. At the interface, cations become partially desolvated and adsorb onto the surface of the electrode. As the reaction is thermodynamically favorable, cations will form chemical bonds to the surface while electrons from the external circuit inject into the electrode, effectively reducing the material. In transition metal oxides, depending on their electronic properties, these electrons are either in the conduction band or in the localized states within the band gap. Subsequently, the partially desolvated cations diffuse across the surface to intercalation sites, where they typically fully desolvate and insert into the material.⁶⁹ While this model does not include the effect of the solid-electrolyte interphase, which plays a major role in commercial Li-ion battery anodes, it provides a physical foundation for understanding the ion insertion processes.⁷⁰

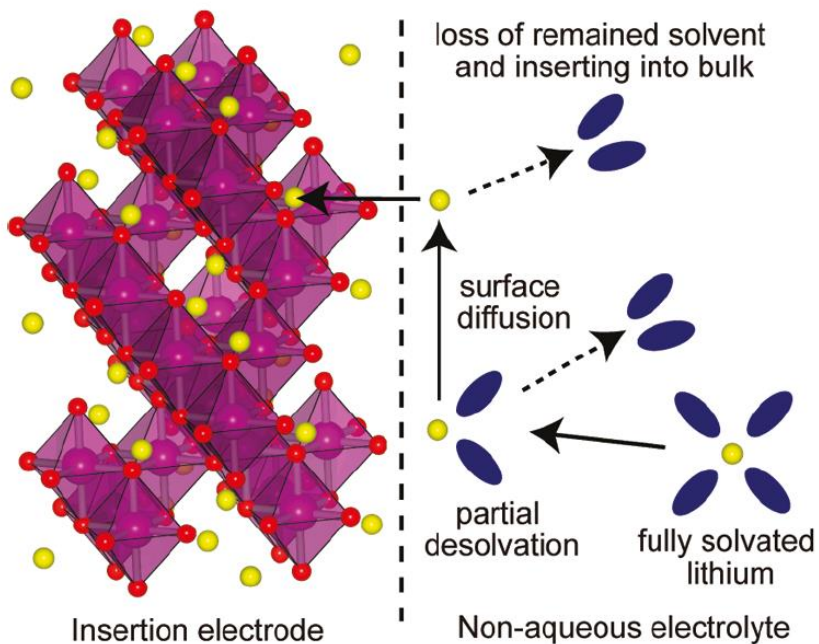


Figure 2.6. A step-wise schematic illustration of an ion insertion process from a non-aqueous electrolyte into an insertion electrode. Reproduced from reference 7.

2.4 Electrical Double Layer

Electrical double layers (EDLs) are space charge layers formed at the interface between the electrodes and the electrolyte to screen the surface charge, as shown in **Figure 2.7**. Electrical double layer is the mechanism by which EDLCs store energy. It is also present in ion insertion systems, but the contribution is usually ignored because it constitutes only a small fraction of the total charge storage in micron-scale materials. In addition to charge storage, the double layer can affect the charge transfer rate of electrochemical redox reactions as it governs the concentration of ions at interfaces.⁷¹

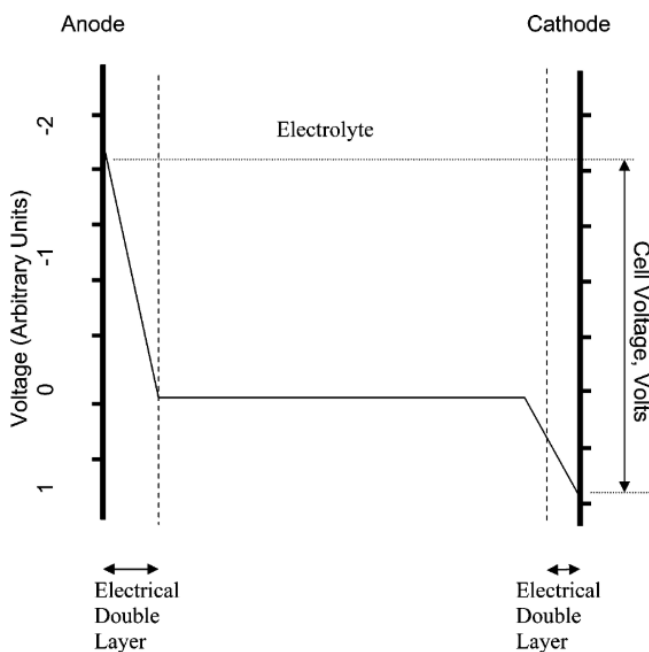


Figure 2.7. Voltage profile inside the electrolyte of batteries or EDLCs. The double layers at anode and cathode interfaces have different structure and compositions. Reproduced from reference 4.

The double layer is defined between the inner and outer Helmholtz layers, as depicted in **Figure 2.8**. The inner Helmholtz layer consists of surface charge, including the specifically adsorbed ions on the surface of the electrode. The outer Helmholtz layer is composed of solvated

ions that are closest to the electrode surface. The separation, d , between the centers of the inner and outer Helmholtz layers can be used to calculate a Helmholtz capacitance, C_H :

$$C_H = \frac{\epsilon A}{d} \quad (2.23)$$

where, ϵ is the electrolyte dielectric constant and A is the accessible surface area.

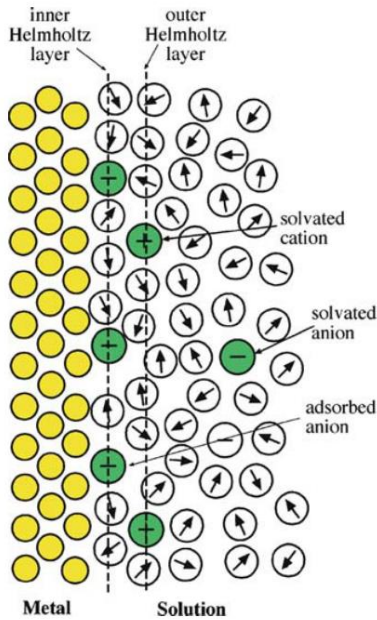


Figure 2.8. Schematic of the electrical double layer model at the interface between an electrolyte and a metal. The sphere with the arrow sign indicates solvent molecules. Reproduced from reference 8.

The region beyond the outer Helmholtz layer is termed the diffuse layer, where the ion distribution was statistically modeled by Gouy and Chapman using the Poisson-Boltzmann equation. This diffuse layer results in a capacitance, C_{GC} . In the Gouy-Chapman-Stern model, the total capacitance of this interface, C , can then be calculated:

$$\frac{1}{C} = \frac{1}{C_H} + \frac{1}{C_{GC}} \quad (2.24)$$

Later, Grahame introduced the concept of specifically adsorbed ions to the model and Bockris, Devanathan, and Müllen proposed the variation of dielectric constant of the solvent in the double layer.^{72,73} That is largely today's picture of electrical double layer. Understanding the detailed double layer structure, particularly under confinement by high surface area materials, is still at the frontier of electrochemical research using advanced experimental and computation methods.⁷⁴

2.5 Surface Ion Adsorption

After ions specifically adsorb on the electrode surface, the behavior may be described by various adsorption isotherms. The isotherms provide explanations for capacitance associated with electrochemical adsorption (adsorption pseudocapacitance) of species on the electrode surface (e.g., H on Pt shown in **Figure 2.9**).⁷⁵ This model was also used as a hypothesis to explain the redox pseudocapacitance of hydrous RuO₂. Ion insertion processes into micron-scale materials that involve the entire bulk of the electrode material exhibit a small contribution from charge storage due to electrochemical adsorption on the surface. However, in certain scenarios, ion distribution in a solid-state lattice can be viewed as an adsorption process, and some adsorption isotherms like the Frumkin isotherm still find use in modeling bulk ion insertion.^{76,77}

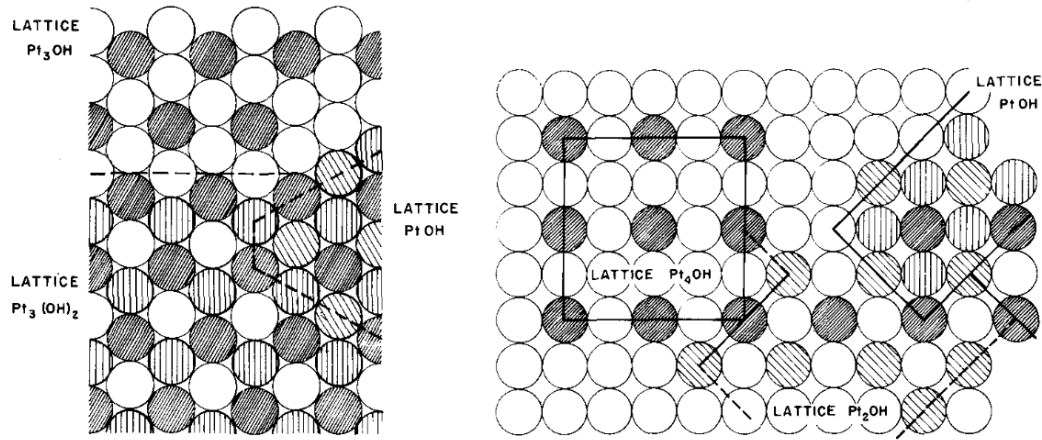


Figure 2.9. Schematic of sublattice structures of OH adsorbed on the (100) or (111) surface of Pt.

Adapted from reference 9.

The simplest isotherm for the adsorption of charged species on a surface is the Langmuir isotherm. Assume we have electrosorption of cation A^+ onto the surface of a conductive substrate M :⁷⁸



The Langmuir isotherm gives us

$$\frac{\theta}{1-\theta} = KC_A e^{\frac{VF}{RT}} \quad (2.26)$$

where the concentration of the cation in solution is C_A , the surface coverage of MA_{ads} is θ , the surface coverage of M is $1-\theta$, the ratio of the forward and reverse reaction rate constant is K , F is the Faraday constant, R is the ideal gas constant, V is the electrode potential, and T is the temperature. Rearrangement of **equation 2.26** leads to the following, which has the form of the Nernst equation except now the ratio of the reduced to oxidized species has been replaced by the extent of adsorbate surface coverage, θ :

$$E = E^0 + \frac{RT}{F} \ln \left[\frac{1}{KC_A} \frac{\theta}{1-\theta} \right] \quad (2.27)$$

where, E is the equilibrium potential of the redox couple and E^0 is the standard potential of the redox couple. Assuming the charge required to complete a monolayer coverage of A_{ads} is q , the pseudocapacitance C_ϕ can be defined as:⁷⁸

$$C_\phi = q \frac{d\theta}{dV} = \frac{qF}{RT} \cdot \frac{KC_A e^{\frac{VF}{RT}}}{\left(1 + KC_A e^{\frac{VF}{RT}}\right)^2} = \frac{qF}{RT} \theta(1 - \theta) \quad (2.28)$$

Equation 2.28 indicates that the maximum pseudocapacitance is reached when $\theta = 0.5$. As a result, for a purely Langmuir-type electrosorption process, the pseudocapacitance will be a function of the applied potential and surface coverage, as shown in the solid curves of **Figure 2.10a**. There are two factors that can substantially reduce the steepness of the isotherm, leading to a broadly distributed dependence of C_ϕ on potential. The first is deposition of adsorbates at distinguishable successive states of electrochemical adsorption with increasing coverage, giving rise to multiple peaks as illustrated in **Figure 2.10b**.^{9,11} This was one hypothesis for the formation of constant capacitance profile in redox pseudocapacitance of hydrous RuO_2 . The second factor is a lateral repulsive interaction between adsorbates as θ increases, increasing the dependence of C_ϕ on potential. This factor can be described by introducing a lateral interaction parameter, g , as a function of θ (Frumkin-type isotherm):

$$\frac{\theta}{1-\theta} = KC_A e^{\left(\frac{VF}{RT} - g\theta\right)} \quad (2.29)$$

$$C_\phi = \frac{qF}{RT} \frac{\theta(1-\theta)}{1+g\theta(1-\theta)} \quad (2.30)$$

The lateral interaction parameter g represents either attractive ($g > 0$) or repulsive ($g < 0$) interactions between the adsorbed species.⁷¹ When g is > 0 , the resultant pseudocapacitance has a broader peak shape and a lower maximum as compared to the Langmuir case (the solid curves in **Figure 2.10a**).

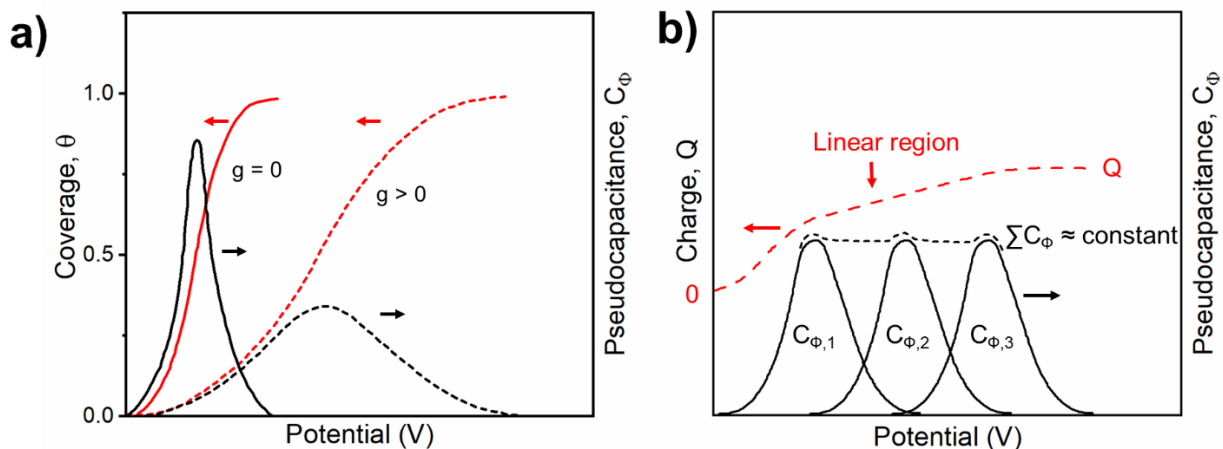


Figure 2.10. a) The variation of pseudocapacitance, C_ϕ , and surface coverage, θ , for ideal Langmuir electrosorption ($g = 0$, solid curves) and Frumkin-type electrosorption that involves attractive lateral interactions between surface adsorbates ($g > 0$, dashed curves). The outcome of this is that pseudocapacitance, as originally defined, is strongly potential dependent. The addition of the lateral interaction parameter broadens the peak but does not eliminate the potential dependence. Adapted from reference 10. b) Illustration of how three redox processes ($C_{\phi,1}$, $C_{\phi,2}$, and $C_{\phi,3}$) could overlap to form an almost-constant overall capacitance over an appreciable potential range in electrochemically formed RuO_2 thin films. Q (dashed curve) is the charge accumulated over the potential range and $\sum C_\phi$ (short dashed curve) are the summed capacitance of the three redox processes. Adapted from reference 11.

2.6 Surface Diffusion

The impact of surface diffusion of adsorbed ions is traditionally considered negligible in ion insertion systems due to the short distance required for ions to diffuse from an adsorption site to an insertion site.⁶⁹ However, in Li_xFePO_4 , a 1D ion conductor, Li, et al. found that the intraparticle Li^+ transport was dominated by surface diffusion instead of the other possible routes

shown in **Figure 2.11**.¹² It implies that in highly anisotropic systems, surface diffusion can play an important role in the kinetics of ion insertion. In addition, they found that different solvent molecules affect Li^+ surface diffusivity differently. For example, water is more effective at assisting surface diffusion of Li^+ than propylene carbonate. Because there is a lack of experimental techniques to measure surface diffusion at the solid-liquid interface, they reported a surface diffusivity of at least $10^{-12} \text{ cm}^2 \text{ s}^{-1}$ as estimated by phase field modeling. This is four magnitudes higher than the bulk diffusivity of Li^+ in Li_xFePO_4 .⁷⁹

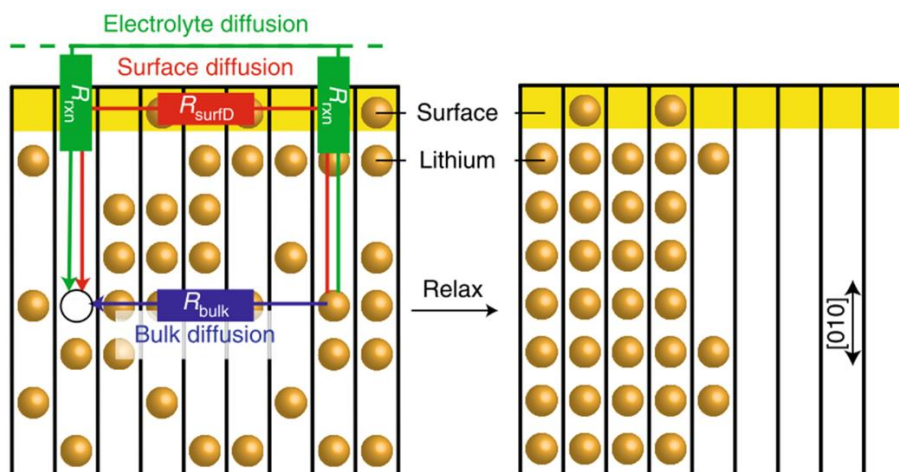


Figure 2.11. Schematic showing Li^+ transport routes in a Li_xFePO_4 crystal with the $[010]$ fast Li^+ conducting channel perpendicular to the surface. The three possible routes are bulk diffusion along the nominally non-conductive directions, surface diffusion, and electrolyte diffusion that requires de-insertion and re-insertion of Li^+ . The relative resistances (R_{bulk} , R_{surfD} , and R_{rxn}) determine which route Li^+ would take during the phase segregation due to immersion in the electrolyte. Adapted from reference 12.

One drawback of solvent-assisted surface diffusion is that if the interaction between the ion and the solvent is too strong, complete desolvation during the insertion may become the rate-limiting step. In the case of solvent-assisted surface diffusion of H^+ on WO_3 , it was found that the

overall reaction rate constant was inversely proportional to the proton affinity of the solvent.⁸⁰ For Mg^{2+} intercalation in V_2O_5 , dimethoxyethane was found to slow down the intercalation kinetics as compared to acetonitrile (ACN) due to its more stable solvate structure with Mg^{2+} .⁸¹ Therefore, the appropriate solvent that can take advantage of fast surface diffusion ideally needs to simultaneously possess low desolvation energy as well.

The lack of theory and characterization for solvent-assisted surface diffusion renders it an opportunity for future research. In Chapter 7, we tested out this hypothesis for Mg^{2+} insertion into WO_3 in a non-aqueous electrolyte with trace amount of water.

2.7 Bulk Diffusion

Bulk diffusion is frequently the rate-limiting step of EES based on ion insertion. In mixed conductors like most ion-insertion materials, the diffusion of ions is coupled with the diffusion of electrons in the material and is regarded as ambipolar diffusion (or chemical diffusion in broader sense). In this section, we discuss the implication of ambipolar diffusion and mention a few experimental and simulation techniques for measuring diffusivity used in energy storage research. Note that no conductivity or diffusivity were measured in this dissertation. This section is for background information only.

The derivation for ambipolar diffusion equations for ion insertion processes is detailed in **Appendix A**. For the diffusion of inserted ions, A^{n+} , in a solid-state lattice, the flux of ambipolar diffusion can be defined as

$$J_A = -\tilde{D} \frac{dc_A}{dx} \quad (2.31)$$

where, \tilde{D} is the ambipolar diffusivity, c_A is the concentration of A^{n+} , and x is distance. Equation 2.31 also implies that the measurement of diffusivity based on concentration gradient will give us the ambipolar diffusivity. At the dilute solution limit,

$$\tilde{D} = -\frac{RT\tilde{\sigma}}{(nF)^2} \left(\frac{1}{c_{A^{n+}}} + \frac{n^2}{c_{e^-}} \right) \quad (2.32)$$

where, c_{e^-} is the concentration of electrons. The ambipolar conductivity, $\tilde{\sigma}$, can be defined as

$$\tilde{\sigma} = \left(\frac{1}{\sigma_{e^-}} + \frac{1}{\sigma_{A^{n+}}} \right)^{-1} = \frac{\sigma_{e^-}\sigma_{A^{n+}}}{\sigma_{e^-} + \sigma_{A^{n+}}} \quad (2.33)$$

where, σ_{e^-} and $\sigma_{A^{n+}}$ are the electrical conductivity and ionic conductivity of A^{n+} , respectively.

Combining equations 2.32 and 2.33 gives us

$$\tilde{D} = -\frac{RT}{(nF)^2} \left(\frac{1}{\sigma_{e^-}} + \frac{1}{\sigma_{A^{n+}}} \right)^{-1} \left(\frac{1}{c_{A^{n+}}} + \frac{n^2}{c_{e^-}} \right) \quad (2.34)$$

Equation 2.34 allows us to discuss the ambipolar diffusivity of inserted ions in the context of carrier concentrations and ionic and electrical conductivities. When both electrical conductivity and electron density are much higher than the ionic counterparts, the ambipolar diffusivity will be approximately the same as the ionic diffusivity. This is probably the case for metallic conductors like MXenes. On the other hand, significantly higher ionic conductivity and ion concentration will lead to an ambipolar diffusivity equal to the electronic diffusivity, like in the case of electrolytes for fuel cells. Most ion insertion materials are in between these two extreme cases and need to be analyzed individually. As an example, assume we have a semiconducting material of which the band structure does not change significantly upon ion insertion. When ion insertion happens, electrons from the external circuit also start to populate the conduction band, so that we have a similar $c_{A^{n+}}$ and c_{e^-} . As the electrical conductivity of electrons in the conduction band is several orders of magnitude greater than the ionic conductivity, the ambipolar conductivity is equal to the ionic conductivity. In this case, Equation 2.34 is simplified as

$$\tilde{D} = -\frac{RT\sigma_{A^{n+}}}{(nF)^2} \left(\frac{1+n^2}{c_{A^{n+}}} \right) = -\frac{(1+n^2)RT}{(nF)^2} \left(\frac{\sigma_{A^{n+}}}{c_{A^{n+}}} \right) \quad (2.35)$$

According to the Nernst-Einstein equation, part of equation 2.35 can be substituted by $D_{A^{n+}}$,

$$\tilde{D} = (1 + n^2)D_{A^{n+}} \quad (2.36)$$

If A^{n+} is a monovalent ion like Li^+ , then

$$\tilde{D} = 2D_{\text{Li}^+} \quad (2.37)$$

If A^{n+} is a divalent ion like Mg^{2+} , then

$$\tilde{D} = 5D_{\text{Mg}^{2+}} \quad (2.38)$$

The ambipolar diffusivity illustrates the complex interplay between carrier concentrations and ionic and electrical conductivities and gives us a quantitative estimate of what happens if we improve the ionic and/or electrical conductivities of materials. Ultimately, we want materials with high ionic and electrical conductivity to achieve the ‘‘Holy Grail’’ of simultaneous high-energy and high-power EES. Note that here we used an example where ion insertion improved electrical conductivity. However, this is not always the case. For example, cubic ReO_3 was found to lose its metallic conductivity upon Li^+ insertion due to structural distortions.⁸²

The diffusivity of ions can be measured experimentally or estimated via simulation. The experimental methods include galvanostatic intermittent titration technique (GITT), AC impedance spectroscopy, nuclear magnetic resonance (NMR), isotope tracer diffusion, quasi-elastic neutron scattering (QENS), etc.^{83–85} Simulation methods mainly involve density functional theory (DFT). Among these methods, GITT and AC impedance spectroscopy measure the chemical diffusivity or ambipolar diffusivity. The diffusivity from NMR, isotope tracer diffusion, QENS and DFT is classified as self-diffusivity (D^*) due to lack of concentration gradient in the measurement. Self-diffusivity is related to the ionic diffusivity via the following relationship

$$D^* = D \frac{\partial \ln c}{\partial \ln a} \quad (2.39)$$

At the dilute solution limit, they are equivalent.

Many transport measurements will provide activation energy barrier, E_a . It can be used to calculate the ionic diffusivity via the random walk model,

$$D = \Gamma d^2 / 2n_i \quad (2.40)$$

where, d is the hopping distance between sites, n_i is the dimensionality of the random walk, and Γ is the hopping rate constant:

$$\Gamma = P_i v_D \exp\left(-\frac{E_a}{k_B T}\right) \quad (2.41)$$

where, P_i is the probability of the nearest site being available, v_D is the Debye frequency and k_B is the Boltzmann constant. This diffusivity can be converted to conductivity via the Nernst-Einstein equation:

$$D = \frac{RT}{(nF)^2} \frac{\sigma}{c} \quad (2.42)$$

2.8 Material Deformation During Electrochemical Energy Storage

As shown in Figure 1.1, a general relationship exists between capacity and structural change. In EDLCs, the charge storage occurs via the formation of the electric double layer and the electrode material does not experience any structural change apart from slight volume expansion or contraction (< 1%).⁸⁶ Conversion or alloying reactions involve major phase transformation(s) with large volume change (+300% for the lithiation of silicon, +130% for Cd/Cd(OH)₂ in Ni/Cd batteries, and +120% for Pb/PbSO₄ in lead-acid batteries).^{51,87} Compared to the conversion mechanism, intercalation with phase transformation results in much smaller volume changes as shown in **Table 2.1**. Strain develops during ion insertion due to change of molar volume as a

function of composition, leading to deformation,⁸⁸ phase separation,⁸⁹ and even fracture of active materials.¹³ As EES based on ion insertion operates by converting electrical energy into chemical energy, the change in electrode volume is part of the undesired work that causes inefficient energy storage. The negative impact of strain deteriorates at fast charging conditions as the inhomogeneous distribution of compositions (**Figure 2.12**) leads to the buildup of stress. In this section, we introduce the relationship between capacity and strain in ion insertion materials and how it can be used to characterize the deformation during electrochemical ion insertion processes.

Table 2.1. Volume change of selected materials operated by insertion with phase transformation mechanism at the corresponding intercalant concentration or specific capacity.

Materials	% Volume change	Concentration of inserted ions	Corresponding theoretical specific capacity (mAh g ⁻¹)	Ref.
graphite	14	0.17 Li ⁺ /C	372	90
LiCoO ₂	2	0.5 Li ⁺ /TM	137	91
LiMn ₂ O ₄	6 - 7	0.5 Li ⁺ /TM	74	92
Li ₄ Ti ₅ O ₁₂	0.2	0.6 Li ⁺ /TM	175	93,94
Nb ₁₆ W ₅ O ₅₅	5.5	1 Li ⁺ /TM	171	95
Nb ₁₈ W ₁₆ O ₉₃	2.8	1 Li ⁺ /TM	149	95

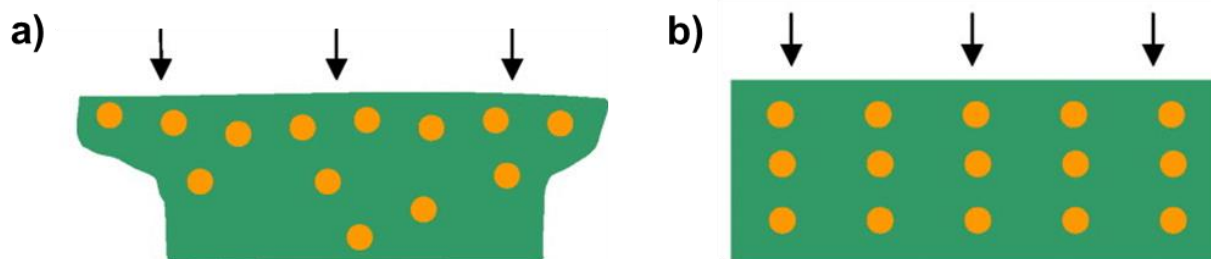


Figure 2.12. Schematics showing a) the inhomogeneous distribution of intercalated ions due to fast charging and b) homogeneous distributions of intercalated ions when the rate of intercalation is low. Adapted from reference 13.

Structural changes in an ion-insertion material induced by electrochemical reactions can lead to the development of strain (ε):

$$\varepsilon = \frac{\delta}{L_0} \quad (2.43)$$

where δ is deformation and L_0 is the original length of the active material. It is experimentally found that in a number of ion-insertion type materials there is direct proportionality between the total charge storage capacity and strain:^{88,96,97}

$$Q \propto \varepsilon \quad (2.44)$$

In simple terms, the deformation scales with the amount of charge storage. In the same manner, the rate of electrode elastic deformation is related to insertion current for cyclic voltammetry experiments with constant sweep rate (dV/dt):

$$\frac{dQ}{dt} = I \propto \frac{d\varepsilon}{dt} \quad (2.45)$$

where t is time and I is current. In constant current experiments, Schiffer et al. observed the following relationship:⁹⁷

$$\frac{dV}{dQ} \propto \frac{d^2\varepsilon}{dQ^2} \quad (2.46)$$

Since current is constant in this case, equation 2.46 is equivalent to

$$\frac{dV}{dt} \propto \frac{d^2\varepsilon}{dt^2} \quad (2.47)$$

These relationships allows for the operando measurement of mechanically-induced changes but also vice-versa: for the use of mechanical response as a proxy to electrochemical current in situations where the electrochemical intercalation current may be difficult to measure. This can be the case if there are multiple electrochemical processes occurring at the same time (e.g. electrolyte decomposition) or when the sample amount is small, as in single-particle electrochemistry.

In Chapter 3, we introduce operando dilatometry using AFM to measure the deformation of active materials during charge/discharge. As we land an AFM tip on the material surface to measure the strain, inevitably we introduce a local stress to the system. The effect of stress on capacity or the electrochemical potential of the system can be derived using the Gibbs-Duhem equation that includes the following intensive variables: chemical potential (μ), electrical potential (V), entropy (S), and pressure (P).

$$Nd\mu + nFNdV = -SdT + V_m dP \quad (2.48)$$

where, N is the amount of chemical species and V_m is the volume of the material. If we integrate it from $P = 0$ to P at constant T and N , we have:

$$N(\mu - \mu_0) + nFN(V - V_0) = V_m P \quad (2.49)$$

If we assume V_m follows:

$$V_m = N\Omega \quad (2.50)$$

where, Ω is the volume per atom, we will have:

$$\mu - \mu_0 + nF(V - V_0) = P\Omega \quad (2.51)$$

$$\mu + nFV = \mu_0 + nFV_0 + P\Omega \quad (2.52)$$

If we define electrochemical potential of the system $\tilde{\mu}$ as:

$$\tilde{\mu} = \mu + nFV \quad (2.53)$$

then equation 2.52 can be rearranged as

$$\tilde{\mu} = \tilde{\mu}_0 + P\Omega \quad (2.54)$$

Note that this derivation neglects volume change due to pressure, which could be a reasonable assumption in ceramic materials with high stiffness.

Because pressure is defined as positive for compressive stress and electrochemical potential is the free energy change per added atom, equation 2.54 implies that the pressure of the

AFM tip on the active material could make intercalation more difficult. Therefore, the force being applied by the AFM needs to be carefully controlled. This relationship may be also applicable to active materials operated under confined conditions, like in a core-shell structure.

Chapter 3: Operando AFM Dilatometry of the Electro-Chemo-Mechanics of Ion Insertion Materials

3.1 Introduction

Recently, we discovered that the presence of structural water leads to a transition from battery to pseudocapacitive behavior in crystalline tungsten oxides.¹⁴ The anhydrous, monoclinic WO_3 exhibits primarily diffusion-limited proton insertion, whereas the hydrated, monoclinic $\text{WO}_3 \cdot 2\text{H}_2\text{O}$ exhibits primarily surface-limited, or pseudocapacitive, proton intercalation. The rate capability and energy efficiency of the $\text{WO}_3 \cdot 2\text{H}_2\text{O}$ is improved over that of WO_3 despite similarity in particle morphology and surface area. The improvement in the kinetics of ion intercalation in hydrated tungsten oxides has been attributed to the presence of structural water.^{98–100} Structural water has also been shown to improve energy storage kinetics in transition metal oxides such MnO_2 and V_2O_5 ;^{101–103} in these materials has been hypothesized to decrease the activation energy required for interfacial charge transfer and/or ion diffusion.¹⁰⁴ An underexplored question is whether the presence of structural water mitigates the mechanical deformation during ion intercalation, thus leading to fast energy storage kinetics.

The different kinetic responses for proton insertion into $\text{WO}_3 \cdot 2\text{H}_2\text{O}$ and WO_3 bring into question whether the presence of structural water promotes different mechanical responses. For most materials, the electrochemical insertion of cations leads to a change in the unit cell dimensions and/or phase of the structure to accommodate both the ion and increased electron density.^{105,106} Since the current represents the change in capacity per time, a general relationship between the current and the rate of dimensional change may be written for a material undergoing deformation due to electrochemical ion insertion:

$$i(E) = \frac{dQ(E)}{dt} \propto \frac{d\delta(E)}{dt} \quad (3.1)$$

where $i(E)$ is the current at a particular potential, $Q(E)$ is the capacity at a particular potential, t is the time, and $\delta(E)$ is the deformation of the material at a particular potential.¹⁰⁷ Because the accumulation of electrons and cations in the electrode results in a mechanical deformation of the host material, it follows that measuring the mechanical deformation could provide additional understanding of the enhanced rate capability of $\text{WO}_3 \cdot 2\text{H}_2\text{O}$.

Here, we investigate the local mechanical response of WO_3 and $\text{WO}_3 \cdot 2\text{H}_2\text{O}$ to proton insertion using atomic force microscopy (AFM) dilatometry, where the uni-axial electrode deformation is measured through the AFM tip displacement.^{86,108} While several techniques are available to measure the total deformation of an electrode during energy storage,^{96,107} the methodology presented here provides a local and operando measurement with a temporal resolution as high as 100 μs (limited by AFM instrument electronics) and a lateral spatial resolution on the order of tens of nanometers (limited by the AFM tip dimension). This approach has been used to study purely capacitive and pseudocapacitive energy storage systems,⁸⁶ but has never been applied to battery-type materials. We show that the anhydrous, battery-type tungsten oxide exhibits a hysteresis in the electrode deformation as a function of potential, whereas the hydrated, pseudocapacitive tungsten oxide shows little-to-no hysteresis. The difference in the behavior of hysteresis was also observed in the results obtained by traditional in situ electrochemical dilatometry on battery-type and capacitor-type materials.^{109,110} In addition, the overall deformation of the hydrated tungsten oxide is smaller even when a greater number of electrons is stored per formula unit than in the anhydrous oxide. We also demonstrate that the deformation rate is directly proportional to the energy storage current in insertion-type oxides, and that it exhibits the same kinetic dependence as the current for diffusion and capacitive processes. This is a very important finding which connects the local mechanical signature (measured with nanoscale lateral and axial

resolution) to the electrochemical redox-process. It also provides an opportunity to study local electrochemical redox-processes that are not attainable with current-based techniques. The deformation is mapped as a function of position in the electrode to demonstrate the ability of operando AFM dilatometry to probe local changes in the electrode deformation as a function of ion storage. Together, these methods allow for local studies of mechanically coupled electrochemical processes since the deformation is measured with a lateral resolution of tens of nanometers with the AFM probe. Our results show that proton intercalation in hydrated tungsten oxides produces a highly reversible and homogenous mechanical response. In addition, these results suggest that the role of structural water in hydrated tungsten oxide may be to enable facile mechanical deformation by decreasing the number of primary bonds that deform during proton intercalation.

3.2 Experimental Methods

Materials Synthesis

WO₃·2H₂O was synthesized through a room temperature acid precipitation method as described by Freedman.¹¹¹ Briefly, a 1 M Na₂WO₄ (Sigma-Aldrich) aqueous solution was dripped into 3 M HCl (Fisher) under stirring. This led to the rapid precipitation of WO₃·2H₂O which was subsequently washed until pH ~7. Crystalline monoclinic WO₃ were obtained by heating WO₃·2H₂O at 350 °C in air overnight. All materials were ground to a powder with a mortar and pestle.

Electrode Preparation

WO₃·*n*H₂O thin films for the operando AFM dilatometry measurements were drop cast from N-methyl-2-pyrrolidone (NMP, Sigma Aldrich) onto circular glassy carbon substrates (HTW-Germany). The solutions consisted of 95 % w/w active material (WO₃·*n*H₂O) and 5 % w/w polyvinylidene fluoride binder (PVDF, Arkema). Substrates were air dried overnight before a final oven drying step for thirty minutes. Anhydrous WO₃ films were dried at 130 °C and WO₃·2H₂O films were dried at 75 °C to prevent dehydration. Resulting films had a total mass loading of 100 μg cm⁻².

For ex situ XRD, The anhydrous WO₃ slurry was made as described previously.¹⁴ WO₃·2H₂O electrodes were fabricated by mixing an aqueous solution of WO₃·2H₂O (16 % w/v) with a slurry consisting of acetylene black (4 % w/v) (Alfa Aesar) and PVDF (4 % w/v) in NMP. The resulting mixture had a composition of 80 % w/w WO₃·2H₂O, 10 % w/w acetylene black, and 10 % w/w PVDF. Electrodes for the ex situ studies were made by painting the slurry onto platinized silicon wafers (Radiant Technologies, Inc.) and drying at 50 °C. Mass loadings for ex situ measurements were controlled at 4 – 5 mg cm⁻².

Operando Atomic Force Microscopy Dilatometry

Operando AFM dilatometry measurements were conducted using a commercial in situ electrochemical AFM cell (**Figure 3.3**) and MFP-3D atomic force microscope (both from Asylum Research, USA) with Pt coated AFM tips (Nanosensors, PPP-EFM-50, $k = 0.5-9.5 \text{ N m}^{-1}$). Electrode deformation measurements were obtained using two methods. For deformation measurement on individual spots, a constant force mode was used. For the 20 × 20 point grid mapping with a spacing of 25 nm, at each spot the AFM cantilever performed a force-distance

curve at each spot and triggered the potentiostat to run cyclic voltammetry at 200 mV s^{-1} for 7 cycles during the contact part of the force distance curve. After the cyclic voltammetry was finished, the cantilever withdrew and moved to the next spot. The above procedure was repeated for all 400 points on the grid. The deformation was recorded by the deflection of the cantilever. Electrochemical characterization was performed with a Bio-Logic SP-300 potentiostat (Bio-Logic, USA) in a three-electrode configuration with Ag/AgCl reference and activated carbon counter electrodes in $0.5 \text{ M H}_2\text{SO}_4$ as the electrolyte. The EC-Lab software (Bio-Logic) recorded the time, potential of the working electrode, current, and deformation signal from the microscope in the unit of volts. The conversion of the deformation signal to the unit of length was obtained by taking the slope of the retraction part of the force-distance curve.

Ex situ X-ray Diffraction

X-ray diffraction was performed on a PANalytical Empyrean X-ray diffractometer in standard Bragg-Brentano geometry with Cu-K α radiation. Ex situ measurements for anhydrous WO_3 were performed in a nitrogen atmosphere with the Anton Paar TTK 450 chamber. Measurements for $\text{WO}_3 \cdot 2\text{H}_2\text{O}$ were conducted in an ambient atmosphere to prevent dehydration. Diffraction patterns were collected for both phases at various potentials as noted in the main text in order to determine the structural evolution as a function of potential. Electrochemical measurements were conducted in a three-electrode beaker cell with Ag/AgCl reference and platinum wire counter electrodes in $0.5 \text{ M H}_2\text{SO}_4$ electrolyte. The potential of the working electrode was controlled with a WaveNow^{xv} potentiostat (Pine Instruments) using linear sweep voltammetry (LSV) at a sweep rate of 5 mV s^{-1} . After the LSV scan finished, the electrode was immediately removed from solution, rinsed with deionized water, dried with compressed air, and

placed into the diffractometer. The same electrode was used throughout the ex situ experiment. After one XRD measurement and before the next LSV scan, the electrode was held at either the open circuit potential (cathodic scans) or -0.2 V (anodic scans).

Analysis of Operando AFM Deformation Data

To obtain the electrode deformation rate, a set of data smoothing procedures was applied to the original deformation data, $\delta(E)$. The high-frequency noise was smoothed by a Savitzky-Golay filter and then a background subtraction was applied to remove the low-frequency background variation. The derivative of the smoothed deformation data was taken with respect to time to obtain the deformation rate, $d\delta(E) dt^{-1}$. Due to the sensitivity of the derivative, the deformation rate data was smoothed with a second Savitzky-Golay filter. The negative deformation rate was used in the graphs to aid visual observation and in the main text was referred to as “deformation rate.” A negative deformation rate indicates expansion of the electrode, while a positive deformation rate indicates contraction. For the mapping data, note that, due to external interferences including reference potential drift during measurement for $\text{WO}_3 \cdot 2\text{H}_2\text{O}$ and software glitches for WO_3 , only the first 11×20 grid of points were used for quantitative analysis.

3.3 Results & Discussions

To determine the mechanical response of $\text{WO}_3 \cdot n\text{H}_2\text{O}$ ($n = 0$ or 2) during electrochemical proton intercalation, thin film electrodes were fabricated by drop-casting $\text{WO}_3 \cdot n\text{H}_2\text{O}$ particles onto a glassy carbon electrode. The morphology and thickness of the electrodes were measured with scanning electron microscopy (SEM) (**Figure 3.1**). The particle-based films of both oxides were $\sim 370 - 480$ nm thick, with larger and smaller aggregates throughout. The surface morphology of

the dry electrodes was measured using AFM and shown in **Figures 3.2a** and **3.2c**. From our prior results,¹⁴ the platelet-like particles of $\text{WO}_3 \cdot 2\text{H}_2\text{O}$ are oriented in the [010] direction.

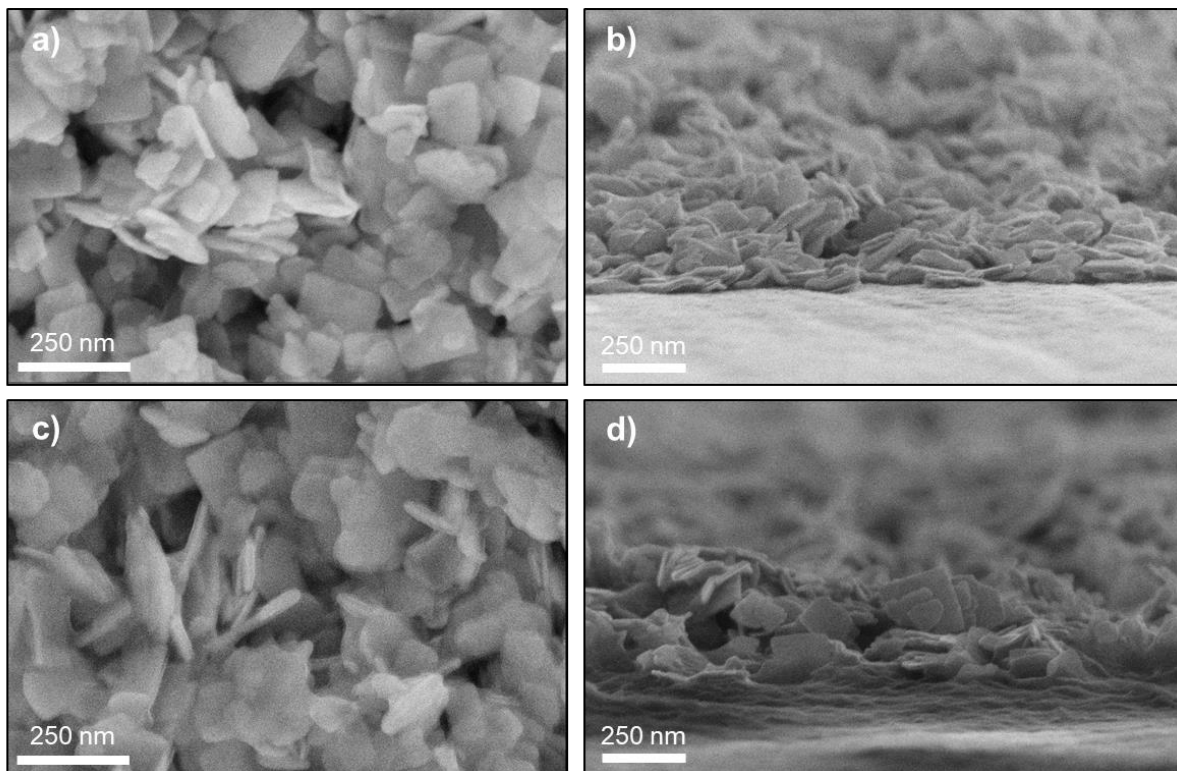


Figure 3.1. Scanning electron micrographs of $\text{WO}_3 \cdot 2\text{H}_2\text{O}$ and WO_3 thin films on glassy carbon used in the operando AFM dilatometry experiments. a, c, Top-down micrographs depicting the random particle orientation of $\text{WO}_3 \cdot 2\text{H}_2\text{O}$ (a) and WO_3 (c) thin films. b, d, Cross-sectional micrographs used to determine average thickness of $\text{WO}_3 \cdot 2\text{H}_2\text{O}$ (b) and WO_3 (d) thin films. SEM micrographs courtesy of Shelby Boyd.

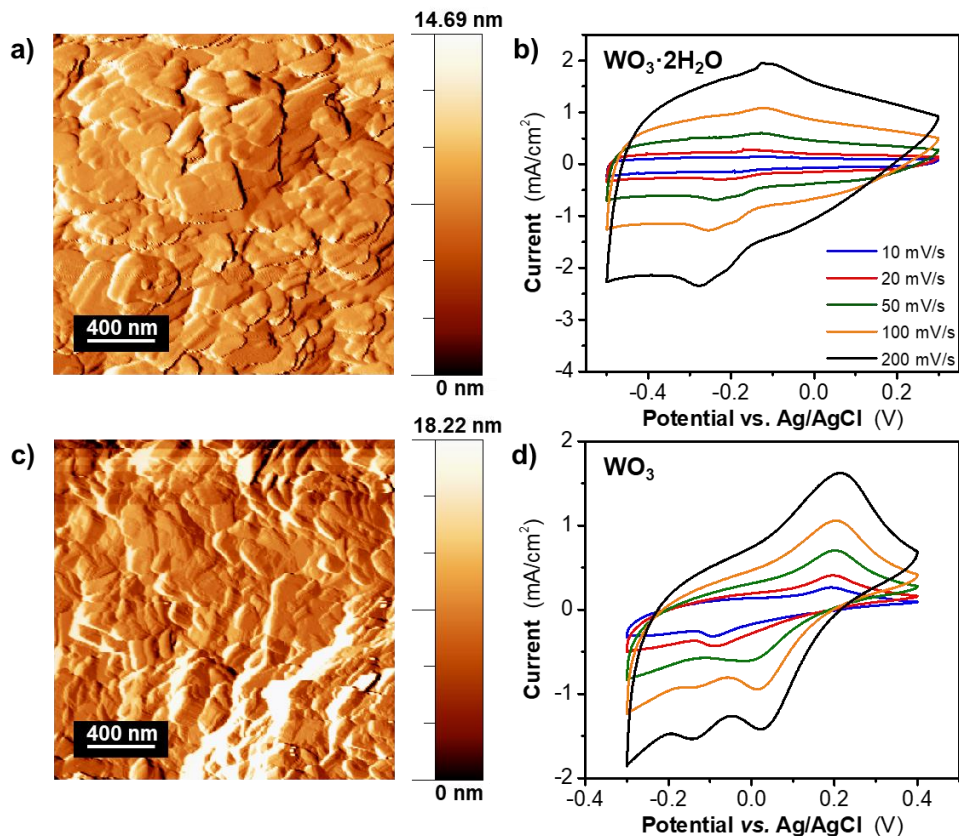


Figure 3.2. Surface morphology and electrochemical characterization of WO_3 and $\text{WO}_3 \cdot 2\text{H}_2\text{O}$ electrodes obtained from the in situ electrochemical AFM cell. (a, c) Deflection images of the thin film electrode surface of $\text{WO}_3 \cdot 2\text{H}_2\text{O}$ (a) and WO_3 (c). (b, d) Cyclic voltammograms of $\text{WO}_3 \cdot 2\text{H}_2\text{O}$ (b) and WO_3 (d) electrodes in 0.5 M H_2SO_4 at sweep rates ranging from 10 – 200 mV s^{-1} .

Proton insertion into $\text{WO}_3 \cdot n\text{H}_2\text{O}$ may be written as:



where the maximum amount of proton insertion (x) is typically < 1 ,¹¹² for a capacity of 417 C g^{-1} for WO_3 and 360 C g^{-1} for $\text{WO}_3 \cdot 2\text{H}_2\text{O}$. In aqueous acidic electrolytes, the maximum insertion capacity is not reached due to the onset of the hydrogen evolution reaction. **Figures 3.2b** and **3.2d** show the cyclic voltammograms of $\text{WO}_3 \cdot n\text{H}_2\text{O}$ in 0.5 M H_2SO_4 electrolyte from 10 to 200 mV s^{-1}

¹ ($t = 3.5 - 70$ s) in the in situ electrochemical AFM cell (**Figure 3.3**). The specific capacitance values at these sweep rates are presented in **Figure 3.4**. As in prior reports,¹⁴ the in situ AFM cell results demonstrate that proton storage in $\text{WO}_3 \cdot 2\text{H}_2\text{O}$ is a more reversible process than in WO_3 as observed from the increased symmetry of the cyclic voltammograms over all sweep rates. Due to the thin film architecture, the in situ cell results are limited to sweep rates $> 10 \text{ mV s}^{-1}$ as there is a significant current contribution from the hydrogen evolution reaction at slower rates.

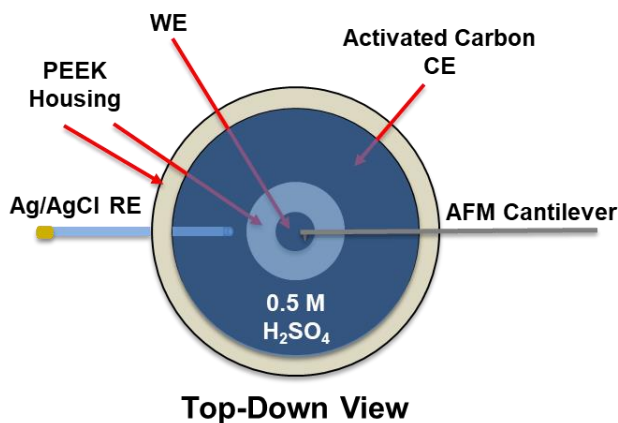


Figure 3.3. Top-down illustration of the commercial in situ electrochemical AFM cell used during the operando AFM dilatometry experiments. The design allows for the AFM cantilever to approach the working electrode submerged in electrolyte solution ($0.5 \text{ M H}_2\text{SO}_4$). A chemically inert polyether ether ketone (PEEK) housing electronically insulates the counter and working electrodes, while a manufactured hole in the side allows for the insertion of a reference electrode into the solution.

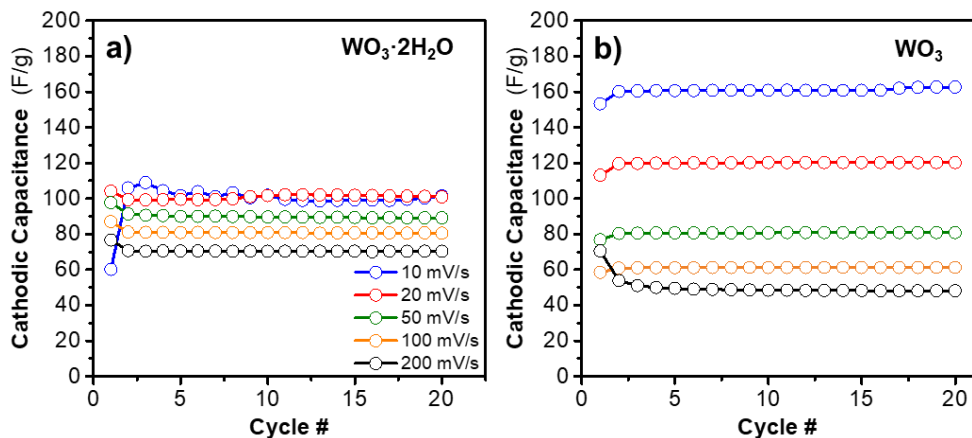


Figure 3.4. Specific capacitance of $\text{WO}_3 \cdot 2\text{H}_2\text{O}$ and WO_3 in the in situ electrochemical AFM cell. a, b, Specific capacitance versus cycle number at various sweep rates for $\text{WO}_3 \cdot 2\text{H}_2\text{O}$ (a) and WO_3 (b). The capacity retention as a function of sweep rate observed for the $\text{WO}_3 \cdot 2\text{H}_2\text{O}$ thin film electrodes is characteristic of this hydrated phase, as reported previously for slurry electrodes in reference 14.

The deformation (δ , in nm) of the thin film electrodes was measured as a function of applied potential and at different cyclic voltammetry sweep rates using the in situ AFM cell. **Figure 3.5a** and **3.5b** show the local deformation of each electrode as a function of potential from 10 to 200 mV s^{-1} . At all sweep rates, the $\text{WO}_3 \cdot 2\text{H}_2\text{O}$ exhibits a highly reversible and almost linear deformation for both the cathodic and anodic sweeps, indicating that the intercalation and de-intercalation processes occur at approximately the same potentials and are thus highly reversible. Such a response would be expected from the broad, symmetric shape of the CV for $\text{WO}_3 \cdot 2\text{H}_2\text{O}$. On the other hand, at all sweep rates, WO_3 exhibits nonlinear deformation and hysteresis between the anodic and cathodic sweeps. This hysteresis indicates that insertion and de-insertion deformation do not occur at the same potentials and are thus less reversible. The electrode deformation depends on the capacity, or number of electrons stored per formula unit. **Figures 3.5c**

and **3.5d** show that at both 20 and 200 mV s⁻¹, the overall deformation is smaller for WO₃·2H₂O even when the number of stored electrons is greater than in WO₃. Overall, these observations indicate differences in the mechanical response to insertion between WO₃·2H₂O and WO₃, similar to their differences in the current response to insertion.

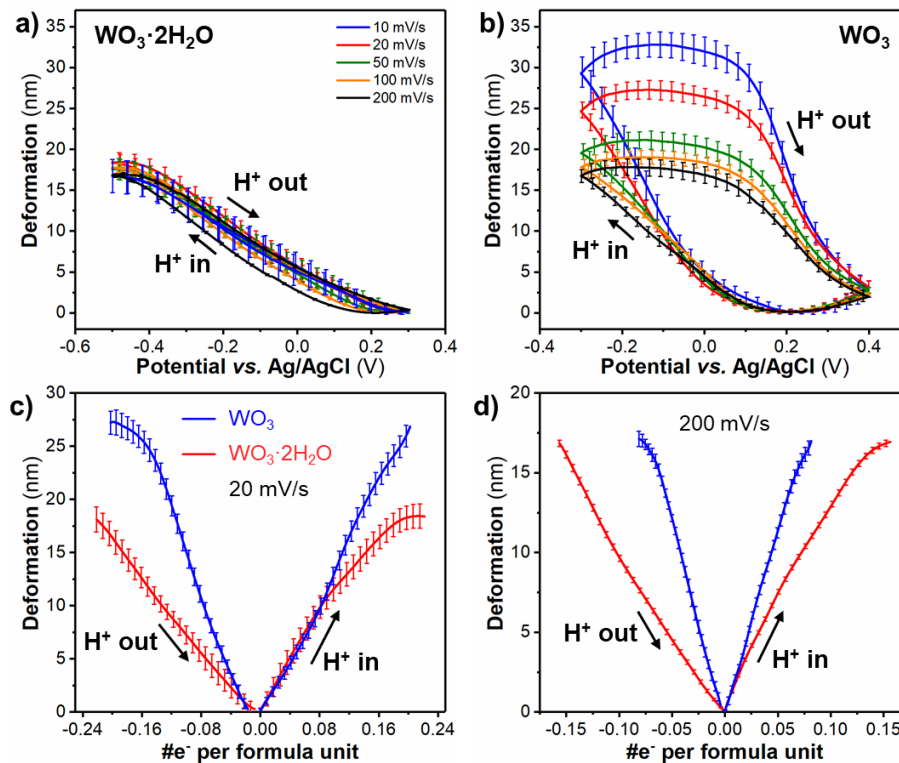


Figure 3.5. Local deformation of WO_3 and $\text{WO}_3 \cdot 2\text{H}_2\text{O}$ electrodes as a function of potential and capacity. (a, b) Deformation versus potential at different cyclic voltammetry sweep rates of $\text{WO}_3 \cdot 2\text{H}_2\text{O}$ (a) and WO_3 (b); Error bars indicate the standard deviations of the deformation at specific potentials for 18 cycles. (c, d) Deformation versus number of electrons per formula unit of WO_3 and $\text{WO}_3 \cdot 2\text{H}_2\text{O}$ at sweep rates of 20 mV s^{-1} (c) and 200 mV s^{-1} (d); Error bars indicate the standard deviations of the deformation at specific numbers of electrons per formula unit. Negative number of electrons represent the anodic cycle and positive number of electrons represent the cathodic cycle.

Since current (i) is the rate of change of the capacity (Q), the current can be expressed as $dQ dt^{-1}$ and a cyclic voltammogram is plotted as the “capacity rate” as a function of potential. We were interested in determining whether the deformation rate ($d\delta dt^{-1}$) also depends upon potential.

Interestingly, as shown in **Figure 3.6**, we found that the deformation rate exhibits almost the same dependence on the potential as the capacity rate, that is, the insertion rate was closely tied to the deformation rate at a particular potential. The deformation rate of the glassy carbon substrate as a function of potential is shown in **Figure 3.7** along with the response of the redox-active tungsten oxides. As expected, glassy carbon exhibits no significant deformation rate since this non-porous electrode exhibits no change in volume during to the formation of the electric double layer at its surface.

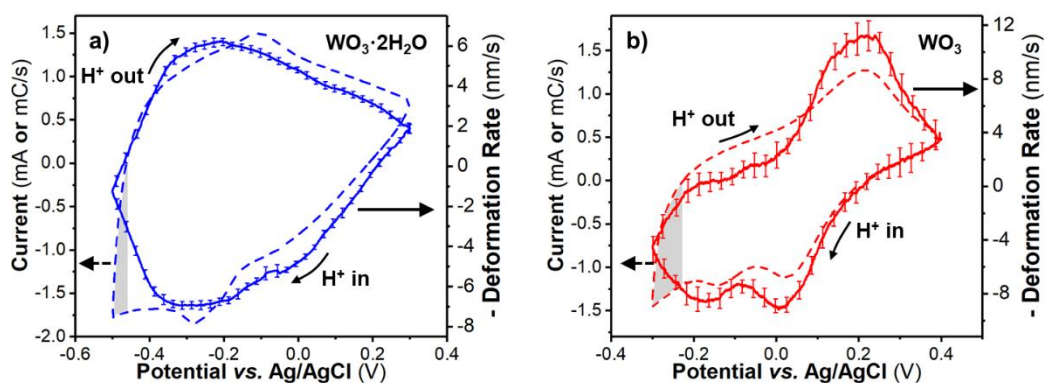


Figure 3.6. Correlation between the local deformation rate and the global electrode current. (a, b) Average deformation rate (solid line) and current (dashed line) versus potential at a sweep rate of 200 mV s^{-1} for $\text{WO}_3 \cdot 2\text{H}_2\text{O}$ (a) and WO_3 (b). Error bars indicate the standard deviations of the deformation rate at specific potentials. The shaded area indicates the regions of potential where the hydrogen evolution reaction contributes to the total current.

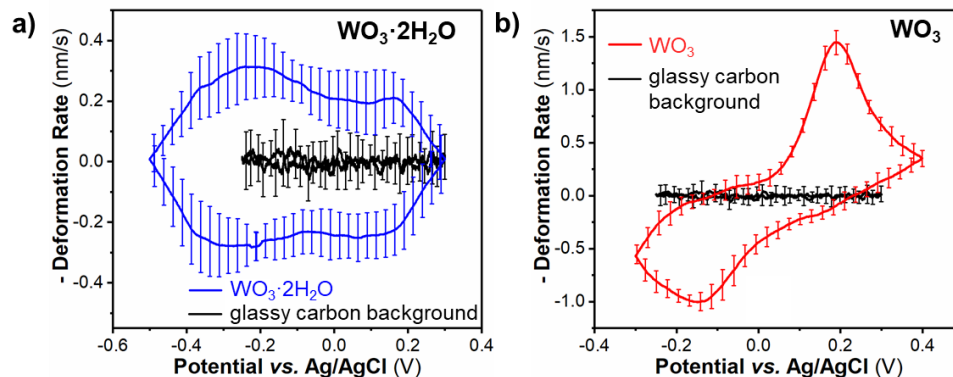


Figure 3.7. Comparison of the deformation rate of redox-active materials to the glassy carbon substrate. a, b, Average deformation rate versus potential at a sweep rate of 10 mV s^{-1} for $\text{WO}_3 \cdot 2\text{H}_2\text{O}$ (a) and WO_3 (b). The response from the glassy carbon substrate is overlaid to show that deformation only occurs for the redox-active materials.

The observation that the local deformation rate is related to the current is consistent with the report of Tavassol, *et al.*,⁹⁶ who found that in macroscopic mechanical measurements of the deformation of a graphite electrode during lithiation, the derivative of the strain of the entire electrode with respect to the voltage ($d\varepsilon dE^{-1}$) scaled with the current. The deformation rate of $\text{WO}_3 \cdot 2\text{H}_2\text{O}$ was smaller and more consistent as a function of potential than for WO_3 , mirroring its nearly symmetric, broad current response in the cyclic voltammogram. In the case of WO_3 , the deformation rate was greater and also asymmetric, similar to its current response. These “deformation rate voltammograms” are shown at 200 mV s^{-1} , where the $\text{WO}_3 \cdot 2\text{H}_2\text{O}$ stores more electrons per formula unit than WO_3 . A noteworthy feature of the deformation rate response is that it is only sensitive to energy storage processes that induce a local mechanical response from the electrode material. For instance, no deformation occurs at the cathodic turnover potential, during which the hydrogen evolution reaction occurs at the surface of the electrode (regions indicated by the shaded areas in Figure 3.6). In other words, the operando AFM dilatometry technique presented

here measures the local, nanoscale deformation response directly induced by electrochemical insertion with high temporal and spatial resolution.

The clear relationship between deformation and current led us to determine how the deformation rate varied as a function of sweep rate. In electrochemical systems, current that is directly proportional to the sweep rate is said to be surface-limited (capacitive), whereas current that is limited by semi-infinite diffusion will exhibit a square root dependence on the sweep rate.¹¹³ This relationship has been generalized and applied to numerous energy storage materials to determine the extent of capacitive vs. diffusion-controlled storage:

$$i(E) = av^b \tag{3.3}$$

Here, v is the cyclic voltammetry sweep rate and a and b are constants. The b -value (with limits of $0.5 \leq b \leq 1$) describes the dependence of the current on the sweep rate, where the limiting values are determined by the rate-limiting mechanisms described above. In a manner similar to Equation 3.3, **Figure 3.8** shows a logarithmic plot of the peak deformation rate as a function of sweep rate; in this type of plot, the slope gives the b -value. In the case of $\text{WO}_3 \cdot 2\text{H}_2\text{O}$, the peak deformation rate varies with a b -value ~ 1 during both proton intercalation and de-intercalation. For WO_3 , the peak deformation rate varies with a lower value of ~ 0.7 during both proton insertion and de-insertion. This relationship is very similar to what is obtained for the peak current dependence as a function of sweep rate in both $\text{WO}_3 \cdot 2\text{H}_2\text{O}$ and WO_3 ,¹⁴ again indicating the strong relationship between the mechanical deformation of the material and the proton insertion process.

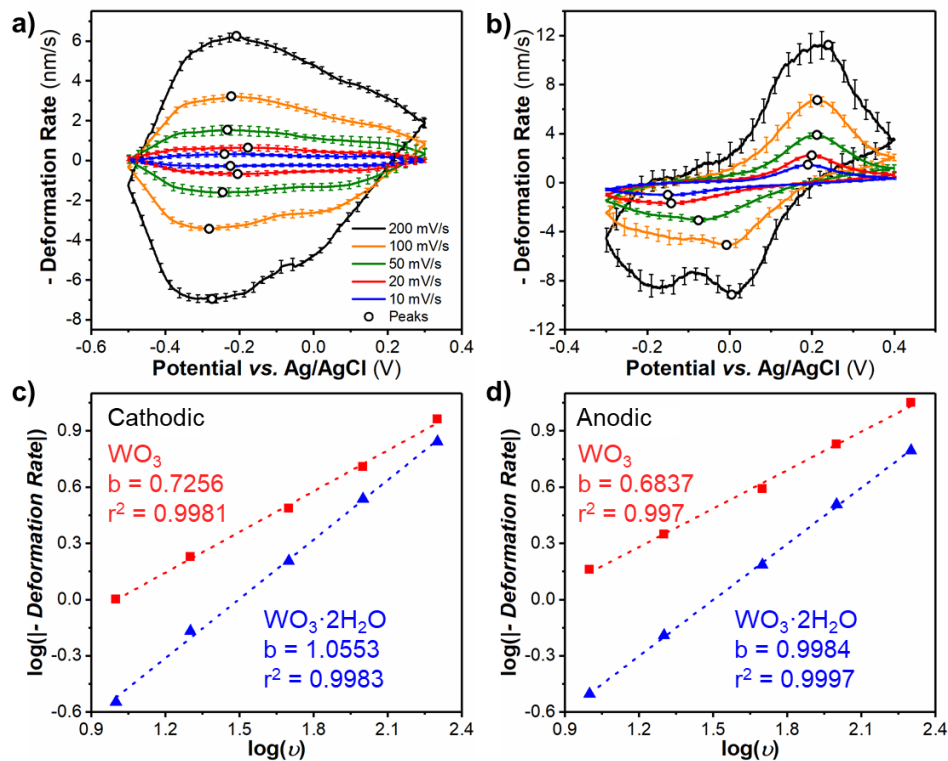


Figure 3.8. Kinetic analysis of the local deformation rate of WO_3 and $\text{WO}_3 \cdot 2\text{H}_2\text{O}$. (a, b) Deformation rate versus potential at sweep rates from 10 to 200 mV s^{-1} for $\text{WO}_3 \cdot 2\text{H}_2\text{O}$ (a) and WO_3 (b). The circles indicate the deformation rate peak values used for b -value determination. Error bars indicate the standard deviations of the deformation rate at specific potentials. (c, d) b -value determination of the peak cathodic (c) and anodic (d) deformation rate for WO_3 (■) and $\text{WO}_3 \cdot 2\text{H}_2\text{O}$ (▲); markers indicate the cathodic and anodic deformation rate peak values at specific sweep rates and the dashed lines indicate the best linear fit.

To determine whether the results obtained at a single spot on the electrode are representative of the local features of the material, we mapped a 20×20 grid of points with 25 nm spacing between each point on the electrodes (a 11×20 grid of points was used for quantitative analysis; details in Methods/Experimental). At each point, the local deformation of the electrode

was measured as a cyclic voltammetry sweep rate of 200 mV s^{-1} was applied to the entire electrode for 7 cycles. This experiment allowed for a correlation between the global current measurement and the local, nanoscale electrode deformation. Videos tracking the deformation rate and current as a function of potential at each point for WO_3 and $\text{WO}_3 \cdot 2\text{H}_2\text{O}$ are available at the journal website (link: https://pubs.acs.org/doi/suppl/10.1021/acsnano.8b02273/suppl_file/nn8b02273_si_002.avi and https://pubs.acs.org/doi/suppl/10.1021/acsnano.8b02273/suppl_file/nn8b02273_si_003.avi). The videos show that for both materials, the deformation rate as a function of potential at each point is qualitatively similar, and therefore the results obtained at a single point are representative of the overall material response.

Figure 3.9 shows the current and average deformation rate as a function of potential. Compared to the graphs obtained from a single point, the averaged graph shows better agreement between the deformation rate peak potentials and the current peak potentials and enhanced signal-to-noise ratio. **Figure 3.10** shows “maps” of the deformation rate and current for the cathodic and anodic peak potentials for WO_3 and $\text{WO}_3 \cdot 2\text{H}_2\text{O}$ (peak potentials are indicated in **Figure 3.11**). The deformation rate maps show that while single-point measurement results are qualitatively similar to each other, both electrodes exhibit spatial inhomogeneity.

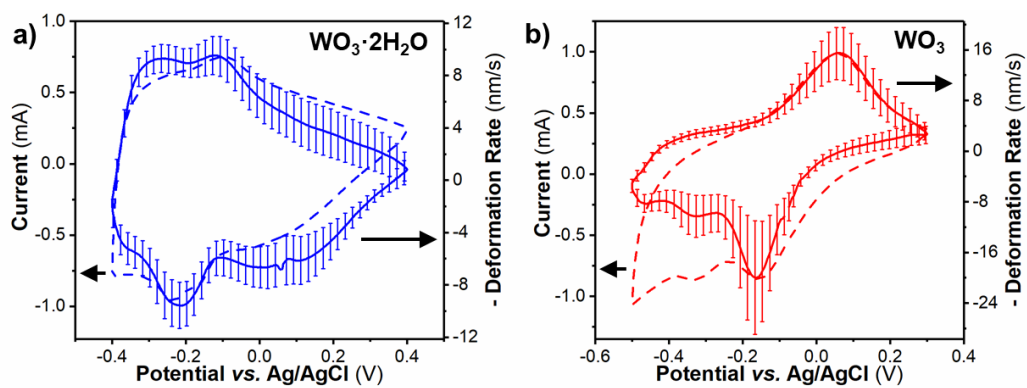


Figure 3.9. Correlation of the average local deformation rate to the global electrode current. a, b, Deformation rate (solid line) and current (dashed line) averaged across an 11×20 grid of points versus potential at a sweep rate of 200 mV s^{-1} for $\text{WO}_3 \cdot 2\text{H}_2\text{O}$ (a) and WO_3 (b). Error bars indicate the standard deviations of the deformation rate at specific potentials.

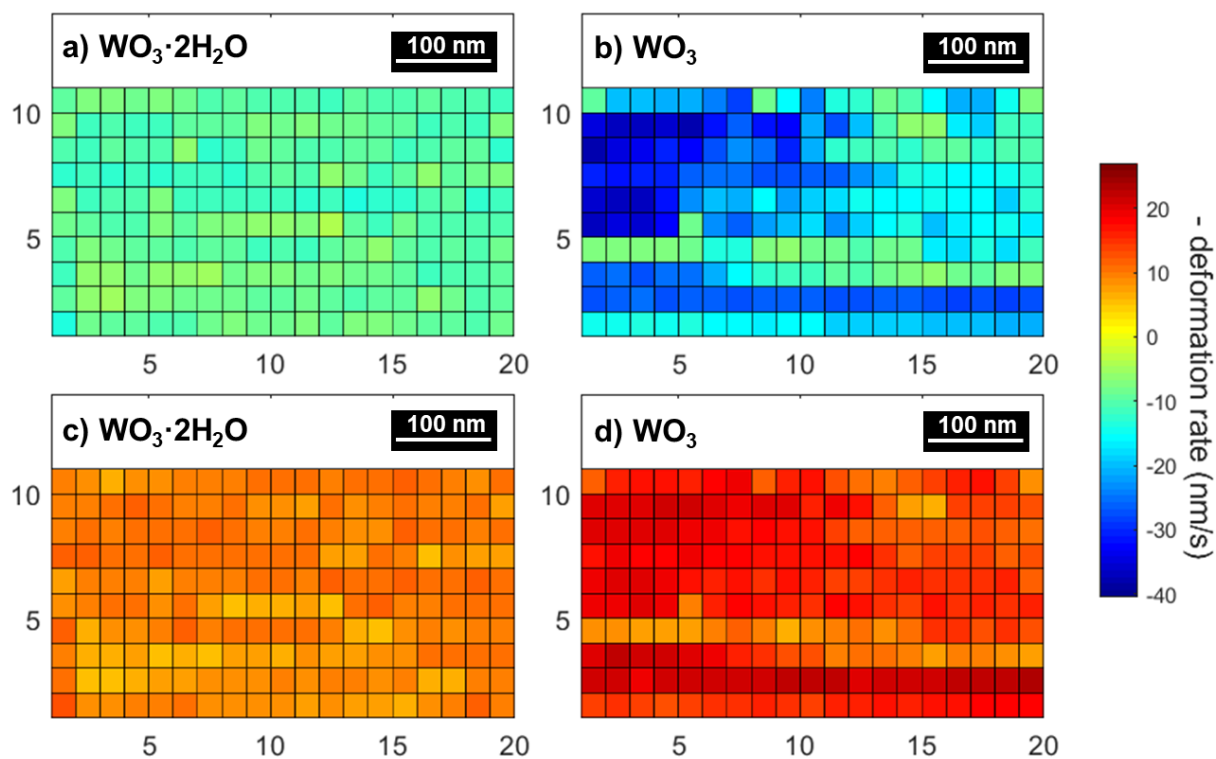


Figure 3.10. Spatial variation of the local deformation rate of WO_3 and $\text{WO}_3 \cdot 2\text{H}_2\text{O}$ electrodes at the cathodic and anodic peak current potentials. (a, b) Local deformation rate at cathodic peak current potential for $\text{WO}_3 \cdot 2\text{H}_2\text{O}$ (a) and WO_3 (b). (c, d) Local deformation rate at anodic peak current potential for $\text{WO}_3 \cdot 2\text{H}_2\text{O}$ (c) and WO_3 (d).

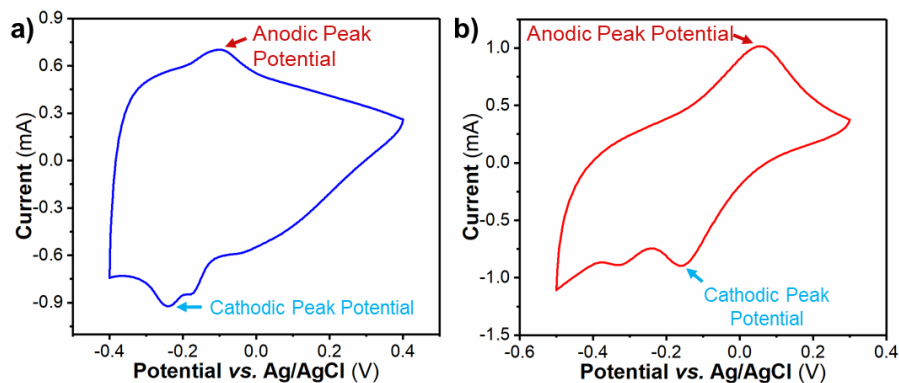


Figure 3.11. Cyclic voltammograms indicating the peak potentials of Figure 3.10. a, b, Cyclic voltammograms of $\text{WO}_3 \cdot 2\text{H}_2\text{O}$ (a) and WO_3 (b) thin film electrodes in 0.5 M H_2SO_4 collected in the *in situ* electrochemical AFM cell at sweep rate of 200 mV s^{-1} .

The inhomogeneity is visualized in **Figure 3.12**, which shows the average deformation rate vs. potential collected from regions with low, medium, and high deformation rates. The criteria for selecting regions with low, medium, and high deformation rates in WO_3 and $\text{WO}_3 \cdot 2\text{H}_2\text{O}$ are displayed in **Table 3.1**. The inhomogeneity can be attributed to the variation of the electrode thickness and particle orientation observed in the SEM micrographs in Figure 3.1. Overall, this technique presents a method to correlate global electrochemical measurements with local deformation in energy storage materials. The advantages of this technique include an indirect measurement of local electrochemical activity with an axial resolution of up to 0.1 nm, a lateral resolution of tens of nanometers, and a temporal resolution as high as 100 μs . There are several limitations to this method. The first limitation comes from AFM instrument. The scan size is usually limited to below $150 \times 150 \mu\text{m}$. The second limit may come from the time it takes to scan and perform dilatometry over a large area, as in the meantime the sample may undergo degradation or drift of position, or the electrochemical cell may change (due to electrolyte evaporation, reference electrode drift, etc.). Due to the nature of AFM probes, sample areas that contain steep

walls and overhangs should be avoided. While the ideal sample for AFM would be an epitaxial thin film with well-controlled crystallographic orientation and thickness, our results show the versatility of the technique in that good results are possible even with more disordered drop-cast and porous electrodes.

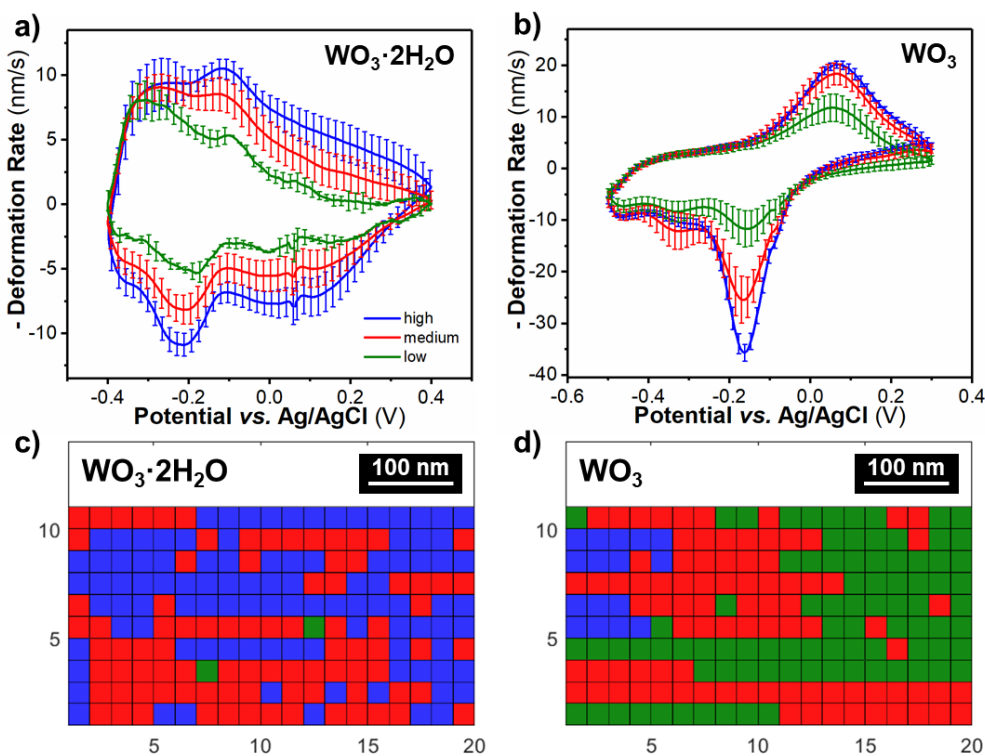


Figure 3.12. Representative response of regions with low, medium, and high deformation rates. (a, b) Deformation rate versus potential of $\text{WO}_3 \cdot 2\text{H}_2\text{O}$ (a) and WO_3 (b) extracted from regions with low, medium, and high deformation rates. Error bars indicate the standard deviations of the deformation rate at specific potentials. (c, d) Maps of the locations of regions with low, medium, and high deformation rates in $\text{WO}_3 \cdot 2\text{H}_2\text{O}$ (c) and WO_3 (d).

Table 3.1. Ranges of low, medium, and high deformation rates in WO_3 and $\text{WO}_3 \cdot 2\text{H}_2\text{O}$ used for Figure 3.12. To generate these ranges, the deformation rates at each spot at the cathodic peak potential were grouped together and analyzed with a histogram.

Electrodes	range of low deformation rate (nm s^{-1})	range of medium deformation rate (nm s^{-1})	range of high deformation rate (nm s^{-1})
WO_3	-0.13 – -0.02	-0.24 – -0.13	-0.35 – -0.24
$\text{WO}_3 \cdot 2\text{H}_2\text{O}$	-0.04 – -0.01	-0.07 – -0.04	-0.14 – -0.07

To understand the differences in the deformation of $\text{WO}_3 \cdot n\text{H}_2\text{O}$ electrodes during proton intercalation, we investigated the materials' structural evolution using ex situ X-ray diffraction (ex situ XRD). WO_3 (**Figure 3.13**) undergoes a reversible phase transition, whose onset and disappearance coincides with the cathodic and anodic redox peaks, respectively, of the cyclic voltammogram. Prior reports of H^+ and Li^+ insertion into monoclinic WO_3 have determined that at the level of insertion investigated here ($\text{H}_{0.12}\text{WO}_3$), there is an electrochemically reversible phase transition to the tetragonal structure,^{114,115,116} and at $\text{H}_{0.23}\text{WO}_3$, this transition leads to a volume expansion of 1.77%.¹¹⁷ This volume expansion of the unit cell is smaller than what we observed from the operando AFM dilatometry. The difference is attributed to the complexity of our drop-cast thin film electrodes, where orientation of the particles and porosity could contribute to the deformation magnitude.

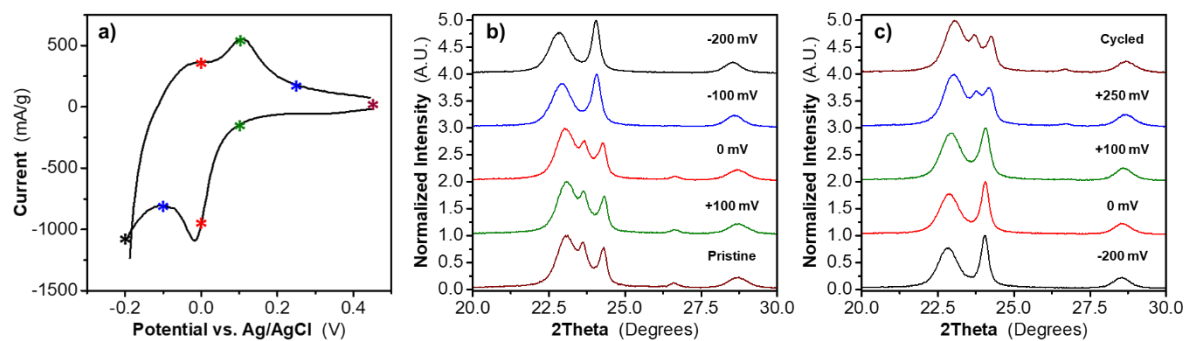


Figure 3.13. Ex situ X-ray diffraction of WO_3 . a, Electrochemical response of the cathodic and anodic linear sweep voltammograms at 5 mV s^{-1} for the slurry electrode. The asterisks indicate the various potentials at which ex situ diffraction patterns were obtained. b, Inset of the diffraction patterns obtained during the cathodic sweep from open-circuit voltage to -200 mV ($\text{H}_{0.12}\text{WO}_3$), depicting the structural evolution as a function of proton insertion. The 23.6° (020) and 24.3° (200) peaks merge, indicating a monoclinic to tetragonal phase transition upon proton insertion. c, Inset of the diffraction patterns obtained during the anodic sweep from -200 mV back to open-circuit voltage, depicting the reversibility of the monoclinic to tetragonal phase transition as protons are de-intercalated. *Ex situ* XRD courtesy of James Mitchell.

As shown in **Figure 3.14a**, the results presented here agree with these prior reports in that at a potential of -0.2 V ($\text{H}_{0.12}\text{WO}_3$) the structure can be indexed to that of tetragonal $\text{H}_{0.1}\text{WO}_3$.¹¹⁶ We noticed that the peak widths in Figure 3.14a are not all consistent and we attributed it to the presence of two phases in the pristine WO_3 as shown in **Figure 3.14b** and discussed in prior literatures.^{14,118} $\text{WO}_3 \cdot 2\text{H}_2\text{O}$ also undergoes a reversible phase transition whose existence is bound by the cathodic and anodic redox peaks (**Figure 3.15**). Importantly, these results show that for intercalation levels of up to $\text{H}_{0.1}\text{WO}_3 \cdot 2\text{H}_2\text{O}$ (-0.2 V), there is no visible change of the (010) interlayer spacing. This has been attributed to the absence of proton storage sites in the hydrated

interlayer of $\text{WO}_3 \cdot 2\text{H}_2\text{O}$.¹¹⁹ The primary structural differences before and after the phase transition are the merging of diffraction peaks between ~ 22.5 and 27.5° . Laurinavichute, *et al.*¹²⁰ also observed the merging of these peaks with chemical intercalation of protons into $\text{WO}_3 \cdot 2\text{H}_2\text{O}$. Prior reports indicate that the phase transition is likely due to a structural transformation toward a more symmetric crystal structure *via* increasing orthogonality of $\text{WO}_5(\text{OH}_2)$ octahedra^{120–122} due to the storage of protons in the octahedral tungsten oxide layer.^{122,123} The distortion of $\text{WO}_3 \cdot 2\text{H}_2\text{O}$ due to proton intercalation is therefore only two dimensional, whereas the distortion of WO_3 is three-dimensional. This difference in structural distortion between the WO_3 structure and $\text{WO}_3 \cdot 2\text{H}_2\text{O}$ may contribute to the more irreversible electrochemical insertion kinetics in the former, resulting in the previously reported transition from battery to pseudocapacitive behavior *via* structural water.¹⁴

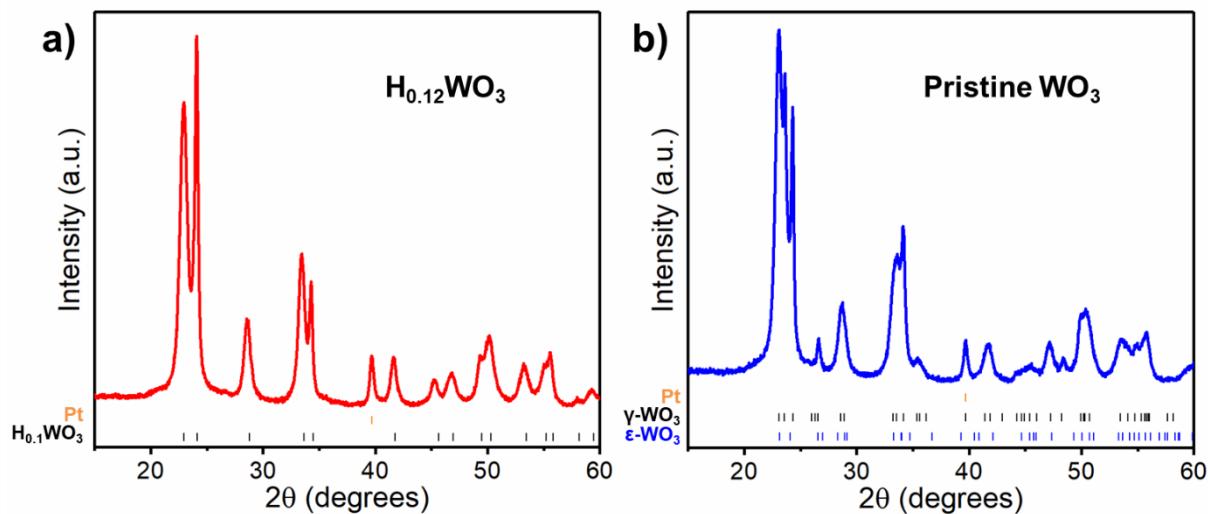


Figure 3.14. Indexing of $\text{H}_{0.12}\text{WO}_3$ (a) and pristine WO_3 (b) X-ray diffraction patterns. The X-ray diffraction pattern (red) of $\text{H}_{0.12}\text{WO}_3$ matches the peak positions of tetragonal $\text{H}_{0.1}\text{WO}_3$ (ICDD PDF 023-1448). The X-ray diffraction pattern (blue) of WO_3 matches with monoclinic δ - and ϵ - WO_3 (ICDD PDF 01-083-0950 and 01-087-2402), as we stated in our previous publication.² We attribute some peak broadenings in (a) to the presence of the ϵ phase. The reflection at $\sim 40^\circ$ 2θ indicates the (111)-peak position of the platinum substrate. *Ex situ* XRD courtesy of James Mitchell.

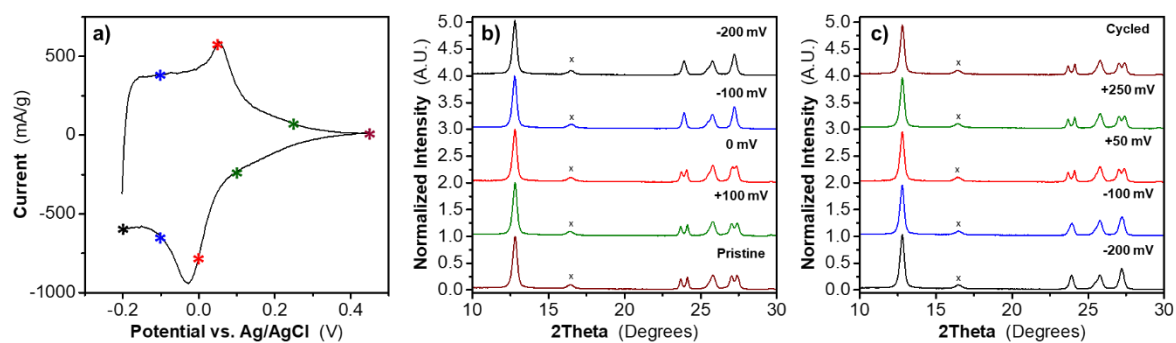


Figure 3.15. Ex situ X-ray diffraction of $\text{WO}_3 \cdot 2\text{H}_2\text{O}$. a, Electrochemical response of the cathodic and anodic linear sweep voltammograms at 5 mV s^{-1} for the slurry electrode. The asterisks indicate the various potentials at which ex situ diffraction patterns were obtained. b, Inset of the diffraction patterns obtained during the cathodic sweep from open-circuit voltage to -200 mV ($\text{H}_{0.1}\text{WO}_3 \cdot 2\text{H}_2\text{O}$), depicting the structural evolution as a function of proton intercalation. The interlayer spacing for the dihydrate phase is not affected as protons are intercalated into the structure as indicated by the absence of change in the scattering angle of the (010) plane at $\sim 13^\circ 2\theta$. The two doublet peaks each merge into one single peak, indicating a shift in the tilted octahedra of the a-c plane toward higher symmetry. c, Inset of the diffraction patterns obtained during the anodic sweep from -200 mV back to open-circuit voltage, depicting the reversibility of the phase transition as protons are de-intercalated. A marker has been included to indicate the small impurity peak at $\sim 16^\circ 2\theta$ which correlates to the (010) plane of the monohydrate phase (ICDD PDF 043-0679). *Ex situ* XRD courtesy of James Mitchell.

The results presented here demonstrate that $\text{WO}_3 \cdot 2\text{H}_2\text{O}$ and WO_3 exhibit different deformation behavior during the storage of protons. As indicated by the ex situ XRD results shown here and reported previously, both $\text{WO}_3 \cdot 2\text{H}_2\text{O}$ and WO_3 undergo phase transitions upon insertion of H^+ . However, in the material with structural water, the mechanism is kinetically surface-limited

and highly reversible, whereas in the anhydrous material, it is diffusion-limited and more irreversible. The differences in the mechanical response and kinetics between these two materials may be due to the difference in the number of primary bonds that undergo distortion during proton intercalation and de-intercalation and the role of interlayer structural water in confining distortion into only two dimensions.

WO_3 exhibits a distorted ReO_3 -type structure, where each WO_6 octahedra is corner sharing in three dimensions. $\text{WO}_3 \cdot 2\text{H}_2\text{O}$ is made up of $\text{WO}_5(\text{OH}_2)$ octahedra that are also corner sharing, but only in two dimensions; the corner sharing octahedra layers are separated from each other by structural water molecules (**Figure 3.16**). In both materials, the proton intercalation site has been hypothesized as the octahedral site between the bridging oxygens of tungsten octahedra.^{122,123} The primary structural differences in this site in $\text{WO}_3 \cdot 2\text{H}_2\text{O}$ are that there is an interlayer water molecule above and below the site, and that $\text{WO}_5(\text{OH}_2)$ octahedra are not connected to each other *via* primary bonds between layers. The separation of these two-dimensional layers by structural water may lead to much more facile and flexible mechanical deformation during proton insertion than in WO_3 , where the WO_6 octahedra effectively undergo three-dimensional distortion during ion insertion. The apparent lack of proton intercalation sites within the structural water layer in $\text{WO}_3 \cdot 2\text{H}_2\text{O}$ is also quite different from the intercalation behavior of other layered oxides with structural water, and may explain why the kinetic behavior of this material is particularly fast.

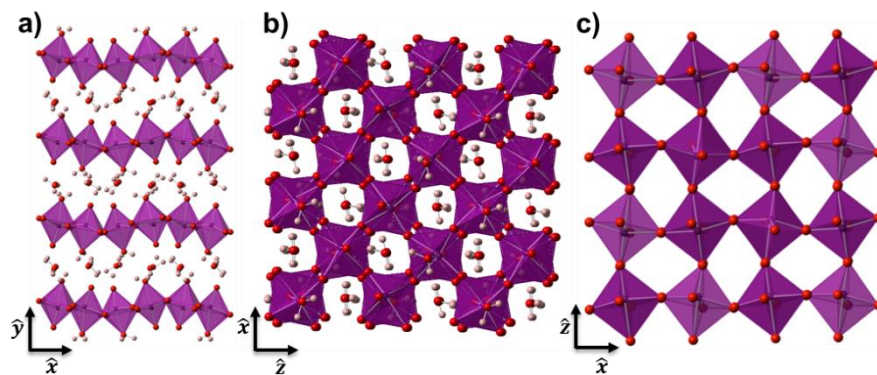


Figure 3.16. Crystallographic structures of $\text{WO}_3 \cdot n\text{H}_2\text{O}$. a, b, Monoclinic $\text{WO}_3 \cdot 2\text{H}_2\text{O}$ and (c) monoclinic $\gamma\text{-WO}_3$. a, (00l)-orientation of monoclinic $\text{WO}_3 \cdot 2\text{H}_2\text{O}$ depicting the interlayer spacing and structural water of the layered, hydrated structure. b, Top-down orientation in the $[0k0]$ direction, depicting the octahedral interstitial sites formed by the bridging oxygens of the corner-sharing WO_6 octahedra with water molecules above and below the plane. Complete dehydration of the hydrated, layered compound yields the anhydrous structure (c).

3.4 Conclusions

Our results imply that for a material to possess high rate capability, it not only needs high electronic and ionic conductivity, but also a flexible structure to accommodate the structural distortion due to ion storage. These results also demonstrate a powerful and versatile operando AFM technique for measuring local electro-chemo-mechanical coupling in materials, opening the door for improved understanding of mechanisms of energy storage in materials as well their degradation processes. In the future, this technique can be expanded to map out the details of local redox-processes or applied to single particle electrodes that cannot be measured with standard electrochemical techniques.

Chapter 4: Electrochemical Proton Storage in Metastable $\text{H}_2\text{W}_2\text{O}_7$

4.1 Introduction

The benefits of structural water on proton storage are evident as shown in the last Chapter. However, materials that can simultaneously satisfy the matrices of high energy, high power, low cost, and sustainability are rare. This scarcity of existing materials brings up the need to explore unconventional methods to synthesize materials that cannot be accessible via direct routes.

Topochemical reactions can be used to convert a thermodynamically stable phase into a related metastable phase by selectively etching away arrays of atoms while retaining much of the bonding in the precursor.^{124–126} The selective etching of MAX phases (where M is a transition metal, A is an element such as Al, Si, Sn, In, Ga, and X is C and/or N)^{127,128} into MXenes is a prominent example of soft chemistry used to prepare metastable 2D materials. In particular, Ti_3C_2 MXene shows pseudocapacitive proton storage in acidic electrolytes with high capacity retention up to sub-second charge/discharge timescales and cycling stability of over 10,000 cycles.^{129,130} MXenes are not the only example of highly efficient metastable materials for proton insertion. Perez, et al. utilized selective etching of Li from Li_3IrO_4 to synthesize a new protonated phase, $\text{H}_{3+x}\text{IrO}_4$. This material showed highly reversible proton insertion kinetics with up to $\sim 1.7 e^-$ stored per Ir.¹³¹ Later, Zhang, et al. extended this method to the Ruddlesden-Popper phase Sr_2IrO_4 and prepared $\text{H}_{3.6}\text{IrO}_4 \cdot 3.7\text{H}_2\text{O}$.¹³² These examples highlight that metastable materials derived from selective ion etching of high-temperature precursors open up a host of new structures and compositions for EES applications. In the case of transition metal oxides, those with layered perovskite structures such as Dion-Jacobson and Aurivillius phases that contain a soluble cation provide significant opportunities for creating novel metastable materials for proton insertion-based EES.^{124,125,133}

In this work, we demonstrate $\text{H}_2\text{W}_2\text{O}_7$, a metastable material synthesized via selective etching of the Aurivillius-related $\text{Bi}_2\text{W}_2\text{O}_9$, as an electrode for high power proton-based energy storage and multicolor electrochromism. In an Aurivillius phase, slabs of perovskite-like $[\text{A}_{n-1}\text{B}_n\text{O}_{3n+1}]^{2-}$, where A and B are cations and n is the number of perovskite blocks, are separated by layers of $[\text{Bi}_2\text{O}_2]^{2+}$.¹³⁴ In $\text{Bi}_2\text{W}_2\text{O}_9$, the perovskite A-sites are vacant and so the structure consists of $[\text{W}_2\text{O}_7]^{2-}$ layers separated by $[\text{Bi}_2\text{O}_2]^{2+}$. Schaak and Mallouk discovered $\text{H}_2\text{W}_2\text{O}_7$ via acid leaching of $\text{Bi}_2\text{W}_2\text{O}_9$,¹³⁵ the topochemical nature of the reaction was identified through electron microscopy.¹³⁶ Proton intercalation into $\text{H}_2\text{W}_2\text{O}_7$ was first reported by Kim, et al., with a specific capacity of $\sim 60 \text{ mAh g}^{-1}$ ($0.5 e^-$ per W) at a rate of 5C (12-min charge/discharge time) and almost 100% capacity retention after 1,000 cycles.¹³⁷ Despite this promising proton insertion behavior, relatively little is known about the structure or energy storage mechanism of $\text{H}_2\text{W}_2\text{O}_7$. Our prior investigations of proton insertion into layered $\text{WO}_3 \cdot 2\text{H}_2\text{O}$ (obtained via direct synthesis) showed the importance of structural water for fast kinetics.^{14,88,138} However, this material has a low theoretical specific capacity due to the large weight fraction of water (13%). Since structural water comprises only 4 wt% of $\text{H}_2\text{W}_2\text{O}_7$ (which can also be written as $\text{W}_2\text{O}_6 \cdot \text{H}_2\text{O}$), this material may enable both fast insertion kinetics and high capacity. Here, we perform comprehensive structural characterization to obtain a high-fidelity crystal structure of $\text{H}_2\text{W}_2\text{O}_7$ using an iterative approach that combines X-ray diffraction (XRD), neutron pair distribution function (neutron PDF), scanning transmission electron microscopy (STEM), Raman spectroscopy, and density functional theory (DFT) optimization. Electrochemical characterization using cyclic voltammetry in a sulfuric acid electrolyte showed a capacity retention of $\sim 80\%$ at $1,000 \text{ mV s}^{-1}$ (1.5-sec charge/discharge time) as compared to 1 mV s^{-1} (~ 16 -min charge/discharge time). Based on analysis of the cyclic voltammetry peak current, the proton intercalation kinetics in the micron-scale particles were

limited by finite-space diffusion. Cyclability at 20 mV s⁻¹ (~1-min charge/discharge time) showed capacity retention above 90% beyond 10,000 cycles. The intercalation mechanism was studied by ex situ XRD, in situ Raman spectroscopy, and DFT. These results indicated that proton storage occurs at the apex oxygen sites within the hydrated interlayer. Lastly, optical micrographs collected during in situ Raman spectroscopy showed reversible, multicolor electrochromism, with color changes from pale yellow to blue, purple, and lastly, orange as a function of proton content in H₂W₂O₇ in an aqueous electrolyte. These results highlight the use of selective etching of layered perovskites for the synthesis of high power, metastable transition metal oxide materials and the use of H₂W₂O₇ as an anode material for proton-based energy storage or aqueous electrochromic applications.

4.2 Experimental Methods

Synthesis of Tungsten Oxides

H₂W₂O₇ and WO₃ were prepared via selective etching of Bi₂W₂O₉ followed by heat treatment. Bi₂W₂O₉ was made by solid-state synthesis. In a typical synthesis, a 1:2 molar ratio of Bi₂O₃ (nanopowder, 99.9%, Alfa Aesar) and WO₃ (prepared as described below) was mixed in a mortar and pestle for 15 mins. The mixed powder was then suspended in 100 mL ethanol (Fisher Scientific) and magnetically stirred until all ethanol evaporated overnight. The well-mixed powder was put into a ceramic crucible and heat treated at 700 °C for 20 h. The obtained Bi₂W₂O₉ was a white powder with a green shade. A typical selective etching was performed by stirring 4 g of Bi₂W₂O₉ in 200 mL of 6 M HCl for three days. The obtained yellow powder was washed by centrifuging in deionized water multiple times until pH reached ~7 and then dried in the ambient. H₂W₂O₇ and the WO₃ were obtained by heat treating the yellow powder from selective etching at

120 °C overnight and at 650 °C for 3 h, respectively. $\text{WO}_3 \cdot \text{H}_2\text{O}$ was prepared by heat treating a $\text{WO}_3 \cdot 2\text{H}_2\text{O}$ powder synthesized using a precipitation method at 120 °C in air overnight.¹¹¹ WO_3 powder, which was used in the synthesis of $\text{Bi}_2\text{W}_2\text{O}_9$, was prepared by heating $\text{WO}_3 \cdot 2\text{H}_2\text{O}$ at 350 °C in air for 3 h. A deuterated sample was prepared in the same manner with additional precautions, including: (1) a glovebox was employed to prevent isotopic exchange with atmosphere H_2O and always flushed/backfilled with dry N_2 gas for the synthesis and sample handling; (2) DCl (Cambridge Isotope) and D_2O water (Cambridge Isotope, 99.96% D) were used to replace the chemicals containing H; and (3) $\text{D}_2\text{W}_2\text{O}_7$ was sealed and loaded in the appropriate sample holder for neutron experiments right after the heating step.

Electrode Preparation

Slurry electrodes were used for all electrochemical characterization, including in situ studies. The slurries consisted of 60 wt% active material ($\text{H}_2\text{W}_2\text{O}_7$, $\text{WO}_3 \cdot \text{H}_2\text{O}$, or WO_3), 10 wt% carbon black (acetylene black, Alfa Aesar), and 30 wt% Nafion (5 wt% Nafion in ethanol, Fuel Cell Earth). The slurries were cast onto 1×2 cm glassy carbon current collectors with active material mass loadings of $0.5 - 2 \text{ mg cm}^{-2}$. All electrodes were heat treated at 120 °C overnight prior to use. Glassy carbon substrates were used for their corrosion resistance in acidic electrolytes. A carbon screen-printed electrode with a carbon counter electrode and a Ag pseudoreference electrode (RRPE1002C, Pine Research Instrumentation) was used for in situ electrochemical Raman spectroscopy. For ex situ electrochemical X-ray diffraction (XRD), $1 \text{ cm} \times 2 \text{ cm}$ gold-plated glass substrates were used to minimize background peaks. The gold-plated glass was prepared by sputtering a 50 nm gold layer onto a 15 nm chromium adhesion layer on soda-lime glass (University Wafer).

Electrochemical Characterization

Electrochemical characterization was conducted in a 50 mL three-neck round-bottom glass cell (Sigma-Aldrich) with a three-electrode setup. Ag/AgCl in saturated KCl solution (Pine Research Instrumentation) served as the reference electrode. The counter electrode was a Pt wire (99.997%, Alfa Aesar) in all cyclic voltammetry experiments except for the cyclability tests. For the cyclability tests, the counter electrode was another $\text{H}_2\text{W}_2\text{O}_7$ slurry electrode on glassy carbon because the occurrence of oxygen evolution reactions at the Pt wire led to rust of alligator clips and eventually lost of electrical connection over time. Extra precautions were taken to prevent the rust issue for the cyclability test. The setup can be found in **Figure 4.1**. The electrolyte was 1 M or 3 M H_2SO_4 (Certified ACS Plus, Fisher Scientific). Cyclic voltammetry was performed with a potentiostat (MPG2, BioLogic).

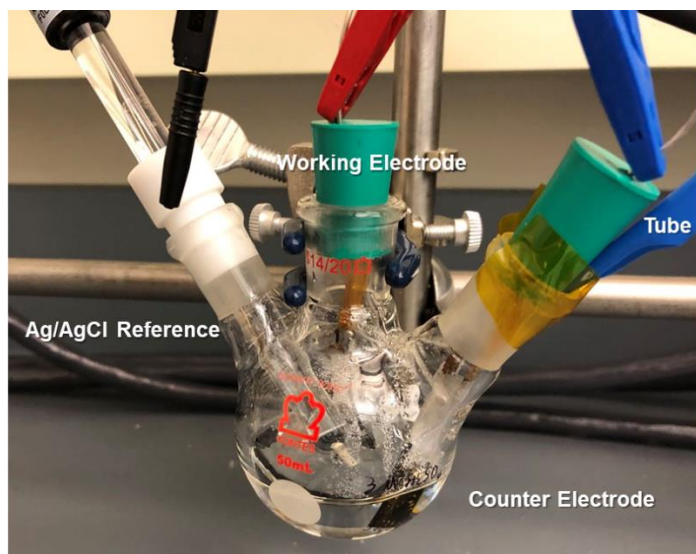


Figure 4.1. Setup of electrochemical characterization of the cyclability of $\text{H}_2\text{W}_2\text{O}_7$ slurry electrode. The working and counter electrodes were held by alligator clips soldered to tin-plated copper wires. To prevent rust, the tin-plated copper wires were protected by Kapton tape and the connection between the alligator clips and electrodes were wrapped by Parafilm. A tube was inserted from the side to prevent accumulation of any in situ formed oxygen or hydrogen gases. (The tube might have caused electrolyte evaporation overtime.)

Physical Characterization

Thermogravimetric analysis (TGA) was performed on a Seiko Exstar TG/DTA6200 in air with a ramp rate of $5\text{ }^\circ\text{C min}^{-1}$. Scanning electron microscopy (SEM) and energy dispersive spectrometry (EDS) was collected on a FEI Verios 460L field-emission scanning electron microscope with an Oxford X-Max 50 mm^2 Silicon Drift Detector. Scanning transmission electron microscopy (STEM) was performed on a FEI Titan 80-300 aberration-corrected scanning transmission electron microscope with an electron microscope pixel array detector (EMPAD).

Neutron pair distribution function of $\text{D}_2\text{W}_2\text{O}_7$ was performed at Nanoscale Ordered Materials Diffractometer (NOMAD) at the Spallation Neutron Source, Oak Ridge National

Laboratory. The $\text{D}_2\text{W}_2\text{O}_7$ sample was loaded/sealed in 3 mm quartz capillary inside a N_2 -filled glove box and transported to the beamline for neutron total scattering measurements. The capillary tube was loaded in the sample shifter carousel at the NOMAD (BL-1B) instrument, as described by Neufeind et al.¹³⁹ Scattering data were collected in 24 minute frames at room temperature in an Argon atmosphere for a total of ~2.8 hours at 60 Hz setting. The beamline's Interactive Data Language codes¹³⁹ developed for the NOMAD instrument data reduction was used to normalize data, subtract background and container scattering signals, and produce histograms appropriate for PDF analysis. Inelastic-incoherent effects resulting from D-atoms (comprised a weak sample-dependent background) were removed by subtracting real space intensity less than 0.7 \AA through Fourier filter methods.^{140,141} The experimental PDF was obtained by a Fourier transform of the total scattering structure function $S(Q)$ up to Q_{max} of 25 \AA^{-1} , and was analyzed using the software package PDFgui.¹⁴² Instrument resolution parameters, $Q_{\text{damp}} = 0.0177$ and $Q_{\text{broad}} = 0.0192$, were determined with Ni bulk powder (99.99%, Sigma Aldrich) measured under similar conditions.

XRD of WO_3 was conducted on a Rigaku SmartLab diffractometer and XRD of $\text{H}_2\text{W}_2\text{O}_7$ was conducted on a PANalytical Empyrean diffractometer. Both diffractometers operated with $\text{Cu K}\alpha$ radiation ($\lambda = 1.54 \text{ \AA}$) in a Bragg-Brentano geometry. Rietveld refinement of the powder XRD data of $\text{W}_2\text{O}_6 \cdot \text{H}_2\text{O}$ was performed with GSAS II software package.¹⁴³ Ex situ electrochemical XRD of $\text{H}_2\text{W}_2\text{O}_7$ was performed on a slurry electrode coated on gold-plated glass. The electrochemical setup was the same as described in the previous section except that cycling was performed with linear sweep voltammetry using a portable potentiostat (WaveNow^{XV}, Pine Research Instrumentation). The $\text{H}_2\text{W}_2\text{O}_7$ electrode was cycled to -500 mV vs. Ag/AgCl at 5 mV s^{-1} in $1 \text{ M H}_2\text{SO}_4$. The electrochemically reduced electrode was removed from the electrolyte,

rinsed with deionized water, and covered with a thin Mylar film (M-2358, TECHREF) to prevent oxidation in the ambient.

Raman spectroscopy was measured with a WITec alpha300 M confocal Raman microscope with a frequency-doubled Nd:YAG laser with a wavelength of 532 nm. Raman spectra of powders were collected through a 100× objective (spot size of 0.41 μm²) and the in situ spectra were collected through a 63× water dipping objective (spot size of 0.33 μm²). The working electrode was cycled at 5 mV s⁻¹ to desired potentials and then held at these potentials during collection of the Raman spectra.

Density Functional Theory Calculations

DFT calculations were performed using the Vienna Ab initio Simulation Package (VASP)¹⁴⁴ with generalized gradient approximation (GGA) for electron exchange and correlation in the form of the Perdew-Burke-Ernzerhof (PBE) functional.¹⁴⁵ The projector augmented wave (PAW) potentials were adopted to describe the electron-nuclei interaction.¹⁴⁶ An energy cutoff of 700 eV was used for plane wave basis sets and the Brillouin zone were sampled by 4×4×1 *k*-point mesh. The van der Waals interaction were described by DFT-D3 correction.¹⁴⁷ The structure of H_{2+x}W₂O₇ was modeled by a supercell containing 4 formula units. All degrees of freedom were relaxed until the residual force were below 0.01 eV Å⁻¹. To simulate the proton insertion energetics during the electrochemical process, hydrogen atoms (H⁺+e⁻) were added to the unit cell. The hydrogen absorption energy was calculated as $E_{ab} = \frac{E_{H_{2+x}W_2O_7} - E_{H_2W_2O_7} - \frac{x}{2}E_{H_2}}{x}$, where $E_{H_{2+x}W_2O_7}$, $E_{H_2W_2O_7}$ and E_{H_2} are the total energy of protonated H_{2+x}W₂O₇, pure H₂W₂O₇, and H₂ molecule, respectively.

4.3 Results & Discussions

Structural characterization

Selective etching of the Aurivillius-related $\text{Bi}_2\text{W}_2\text{O}_9$ in an aqueous acidic environment proceeds via the topotactic exchange of BiO^+ with H^+ :¹³⁵



While the bilayer $[\text{W}_2\text{O}_7]^{2-}$ structure of $\text{H}_2\text{W}_2\text{O}_7$ and its dehydration behavior were investigated by Kudo et al,¹³⁶ a refined structure and positions of the light elements have not yet been resolved. Here, an iterative approach was adopted to obtain a high-fidelity crystal structure using DFT optimization and multi-modal characterization.¹⁴⁸ We first created a $\text{H}_2\text{W}_2\text{O}_7$ structure based on the structure of the parent $\text{Bi}_2\text{W}_2\text{O}_9$. The structure was then optimized with DFT and refined with X-ray diffraction (XRD) to obtain the long-range structure. The short-range structure was obtained by combining knowledge from neutron PDF, Raman spectroscopy, and DFT. Atomic-resolution STEM imaging further verified the structure.

The $\text{H}_2\text{W}_2\text{O}_7$ is a pale-yellow powder composed of platelets with a flake-like morphology (300 nm – 3 μm in lateral dimensions and 50 – 300 nm in thickness), as shown in **Figures 4.2a and 4.2b**. EDS indicates no residual bismuth in $\text{H}_2\text{W}_2\text{O}_7$ (**Figure 4.2e**). The concentration and characteristics of the water in $\text{H}_2\text{W}_2\text{O}_7$ was investigated with thermogravimetric analysis (TGA, **Figure 4.3a**). $\text{H}_2\text{W}_2\text{O}_7$ experiences a phase transformation between 170 °C and 350 °C and loses 3.72% mass (~ 1 water per formula unit, in agreement with the theoretical water content from **equation 4.1**). The dehydrated product was identified as $\gamma\text{-WO}_3$ by XRD (**Figure 4.4**). The characteristics of $\text{H}_2\text{W}_2\text{O}_7$ dehydration resemble that of $\text{WO}_3 \cdot \text{H}_2\text{O}$ (**Figure 4.3b**), which also loses one water per formula unit above 130 °C to form $\gamma\text{-WO}_3$.

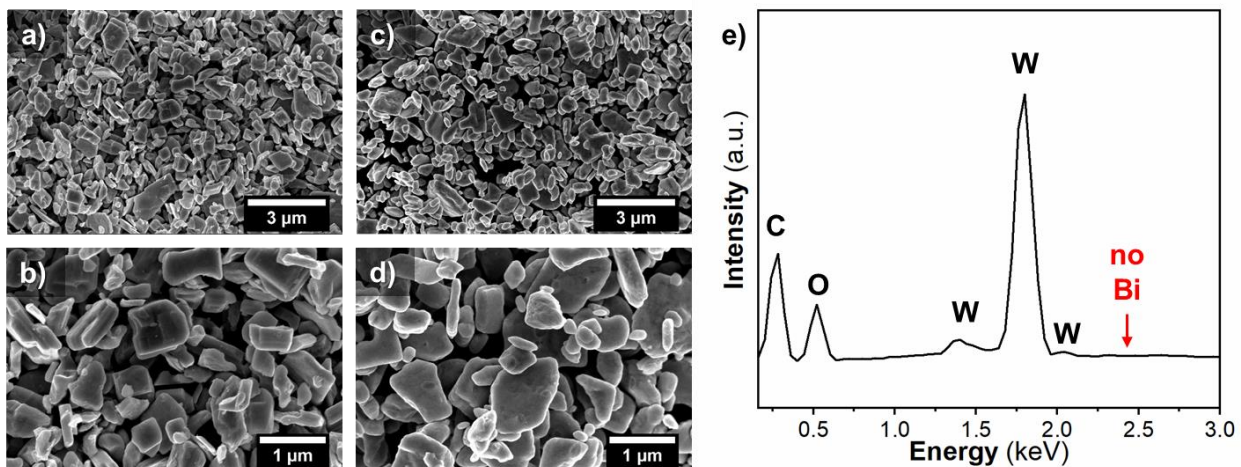


Figure 4.2. Scanning electron micrographs of a,b) $\text{H}_2\text{W}_2\text{O}_7$ and c,d) WO_3 that is obtained from heat treatment of $\text{H}_2\text{W}_2\text{O}_7$. e) SEM-EDS spectrum of $\text{H}_2\text{W}_2\text{O}_7$ showing that the acid exchange is complete, and no bismuth was detectable at 2.419 keV (Bi M edge). SEM-EDS courtesy of Shelby Boyd and Mike Spencer.

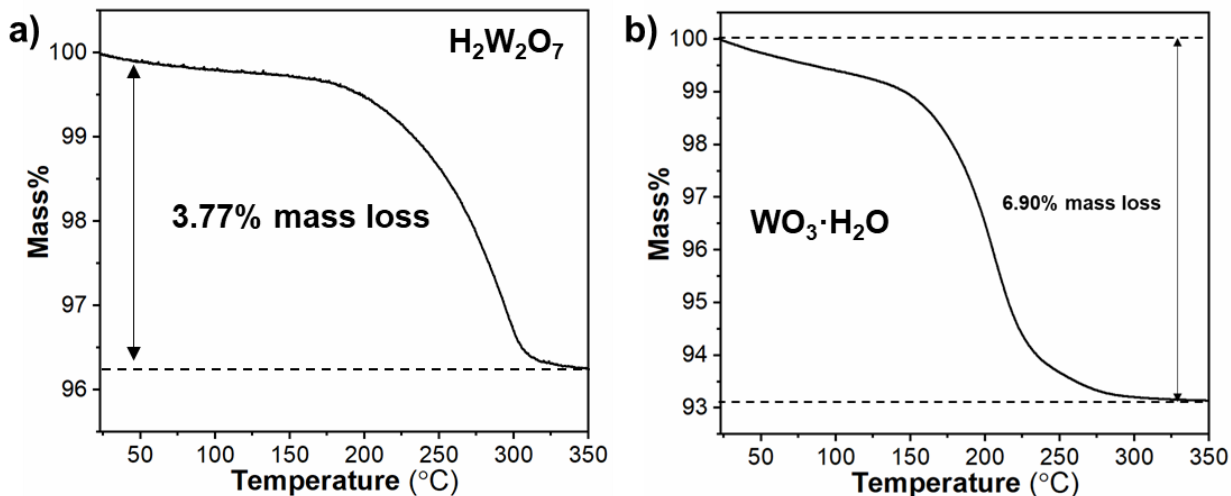


Figure 4.3. TGA of a) $\text{H}_2\text{W}_2\text{O}_7$ and b) $\text{WO}_3 \cdot \text{H}_2\text{O}$ in air showing the dehydration process to form WO_3 , the mass loss is equivalent to 1.01 water loss per $\text{H}_2\text{W}_2\text{O}_7$ and 0.96 water loss per $\text{WO}_3 \cdot \text{H}_2\text{O}$.

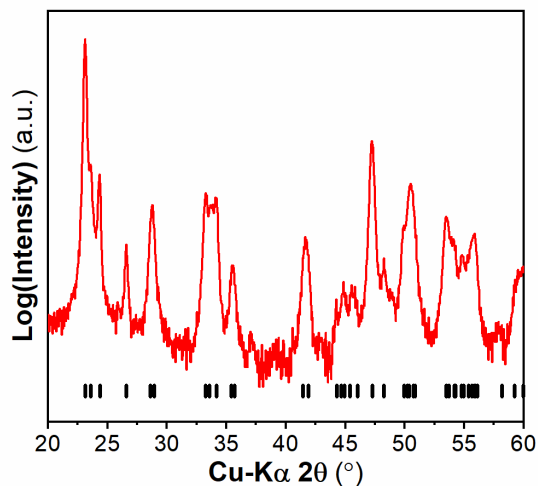


Figure 4.4. XRD pattern of WO_3 obtained from heat treating $\text{H}_2\text{W}_2\text{O}_7$. The intensity is plotted in the log scale due to the strong preferred orientation of 002 plane. The black ticks represent a reference pattern of $\gamma\text{-WO}_3$ (ICDD-PDF 04-005-4272).

Another indication of the water environment comes from comparison of the Raman spectra of $\text{H}_2\text{W}_2\text{O}_7$ and $\text{WO}_3 \cdot \text{H}_2\text{O}$. As shown in **Figure 4.5**, both materials exhibit a peak at $\sim 950 \text{ cm}^{-1}$. In $\text{WO}_3 \cdot \text{H}_2\text{O}$, this peak corresponds to the stretching mode of terminal $\text{W}=\text{O}$ [$\nu(\text{W}=\text{O})$],¹⁴⁹ which occurs due to the presence of a $\text{W}-\text{OH}_2$ bond on the opposite end of a $\text{WO}_5(\text{OH}_2)$ octahedron.¹⁵⁰ Based on the TGA and Raman results, water in $\text{H}_2\text{W}_2\text{O}_7$ is also likely to exist as a covalent $\text{W}-\text{OH}_2$ bond. This information helped us create a crystal structure of $\text{H}_2\text{W}_2\text{O}_7$, which was then optimized with DFT and refined with powder XRD and neutron PDF data.

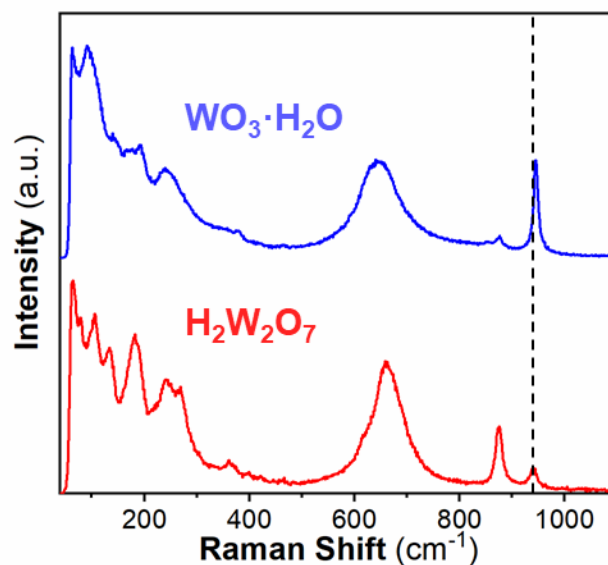


Figure 4.5. Raman spectra comparison of $\text{H}_2\text{W}_2\text{O}_7$ with $\text{WO}_3 \cdot \text{H}_2\text{O}$.

The long-range structure was determined by the refinement of powder XRD. The experimental powder XRD data and their comparison to calculated fits are presented in **Figure 4.6**. Rietveld refinement found the best fit achieved with the space group $P112_1/n$. The refined structure confirms our prediction of the water environment and shows that $\text{H}_2\text{W}_2\text{O}_7$ is a layered material with a spacing of 9.4 Å between (200) planes. The bilayers, which consist of ReO_3 -type corner-sharing octahedra of alternating WO_6 and $\text{WO}_5(\text{OH}_2)$, stack in an ABAB sequence and are translated by $\frac{1}{2}$ unit cell in the b axis from layer A to layer B.

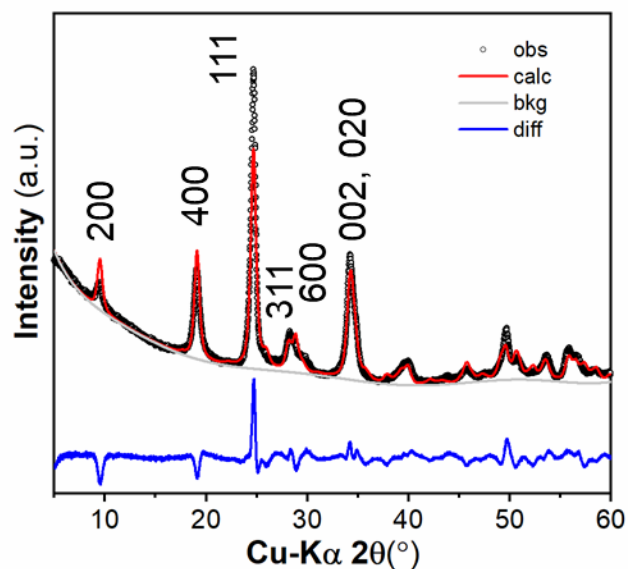


Figure 4.6. Powder XRD of $\text{H}_2\text{W}_2\text{O}_7$ from experiment and comparison with calculated fit from Rietveld refinement. XRD refinement courtesy of Alexander Brady.

The local octahedral distortion and position of proton and oxygen were obtained from the refinement of neutron PDF. **Figure 4.7** shows the experimental neutron PDF of $\text{D}_2\text{W}_2\text{O}_7$ sample, and its comparison to the calculated PDF obtained from real-space structure refinements. The presence of water species (here terminal D_2O molecules) is clearly seen for the covalent O–D bond observed at ~ 0.95 Å and a weak signal for the intramolecular D–D distance (~ 1.6 Å) in the PDF pattern. The third peak centered at ~ 1.85 Å is W–O bond for WO_6 and $\text{WO}_5(\text{OD}_2)$ octahedra. Note that the width of this peak is much wider than the O–D peak observed at ~ 0.95 Å. It is because this peak also contains D-bonding for the interactions among the adjacent W_2O_6 layers. The fourth primarily corresponds to the O–O distances in WO_6 and $\text{WO}_5(\text{OD}_2)$ octahedra. To further interpret PDF data and resolve the structural details of $\text{D}_2\text{W}_2\text{O}_7$, a trial-and-error approach was attempted. Here, structural parameters were adopted from our own DFT simulation as starting point in PDF data refinements. During the fit we varied the scale factor, the unit-cell, the atomic coordinates,

and the isotropic thermal displacements (U_{iso}) for of W, O, and D atoms in $\text{D}_2\text{W}_2\text{O}_7$ phase (all constrained by the $P112_1/n$ space group, which was found to best describe the experimental observation in both real and reciprocal spaces). The r -dependence of the PDF peak width due to correlated thermal motions was refined using the variable delta1 (δ_1). A spherical envelope function, involving the shape damping parameter (spdiameter), was included to account for the observed finite coherent-domain size effect, but was fixed to 54 Å during the fits. After several refinement cycles (with $P112_1/n$ symmetry constrain), a suitable fit was obtained. Here we did not observe any r -dependent residual errors (in the difference curves) when the fit r -range progressively changed from 0-10 Å to 0-40 Å. A goodness-of-fit of 13% was achieved at $r = 10$ Å. The refined structure shows that the structural water forms a hydrogen bond to the oxygen across the gallery with a bond length of ~ 1.9 Å, resulting in an interlayer held together by a hydrogen-bonding network. The final structure is shown in **Figure 4.8**.

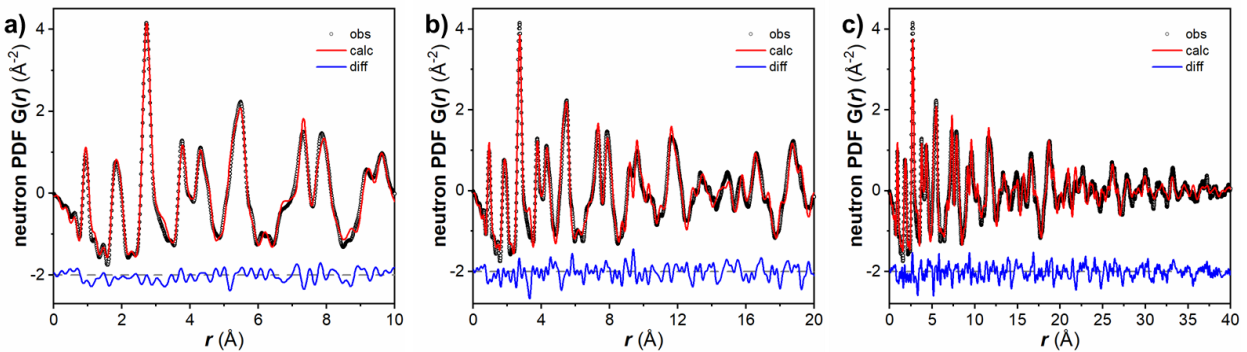


Figure 4.7. Neutron PDF of $\text{D}_2\text{W}_2\text{O}_7$ and comparison with calculated fit from real space refinement. The fit distance range is up to a) $r = 10$ Å, b) $r = 20$ Å, and c) $r = 40$ Å. Neutron PDF and refinement courtesy of Alexander Brady and Hsiu-Wen Wang.

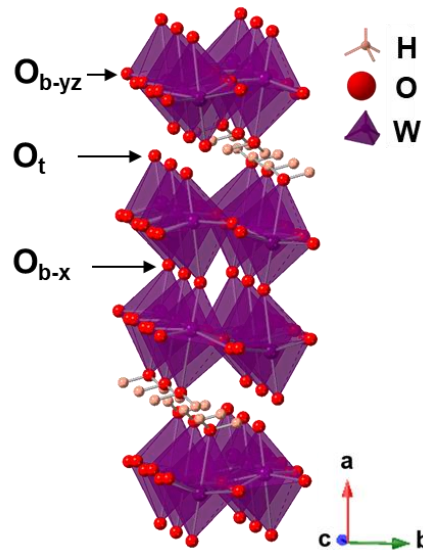


Figure 4.8. Refined crystal structure of $\text{H}_2\text{W}_2\text{O}_7$. O_{b-yz} , O_t , and O_{b-x} stand for equatorial bridging oxygen, terminal oxygen, and axial bridging oxygen, respectively. The unconventional axis is due to the $P112_1/n$ space group. DFT courtesy of Yangyunli Sun and De-en Jiang.

One interesting finding from neutron PDF refinement is a coherent domain size of 54 \AA , equivalent to ~ 6 bilayers of $\text{H}_2\text{W}_2\text{O}_7$, in contrast to the micron-scale particle size. To investigate how well the long-range order is preserved in the individual particles, we employed atomic-resolution STEM imaging. The high-angle annular dark-field (HAADF) micrograph in **Figure 4.9a** visualizes the tungsten atoms in the crystal structure at the $[011]$ zone axis. The distance between the tungsten slabs across the gallery is $\sim 4.6 \text{ \AA}$, agreeing with the refinement results. The micrograph shows that while the individual particle maintains the same tungsten slab direction, there are tri-layer tungsten oxide planar defects present in the material. More HAADF micrographs in **Figure 4.9** indicate the additional presence of single-layer and quad-layer defects. An accounting of defects in the micrographs shows that 12.1% of the slabs are planar defects, which correspond to an average domain size of $\sim 63 \text{ \AA}$. Since this is close to what is observed in neutron

PDF, we hypothesize that the small domain size is due to the single-layer, tri-layer, and quad-layer tungsten oxide slabs taking the place of regular bilayer tungsten oxide slabs. According to the neutron PDF results, ~15% of the layers deviated from the ideal bilayer in the $\text{H}_2\text{W}_2\text{O}_7$ we synthesized. Since no bismuth remains in the structure after selective etching, the presence of these defects is likely from the solid-state synthesis of the parent $\text{Bi}_2\text{W}_2\text{O}_9$.¹⁵¹

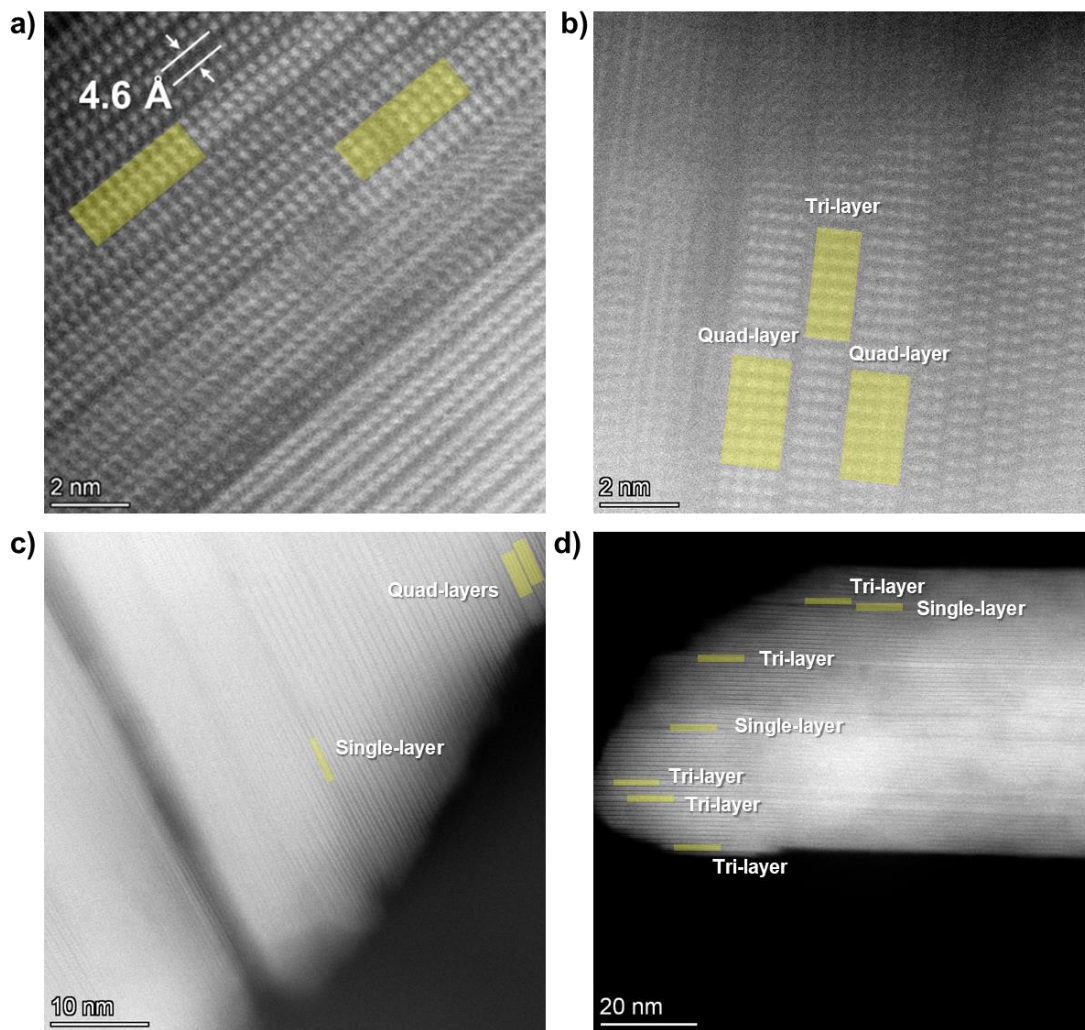


Figure 4.9. Atomic-resolution HAADF-STEM micrograph of $\text{H}_2\text{W}_2\text{O}_7$. The yellow blocks indicate single-layer, tri-layer, and quad-layer planar defects as labeled in the graphs. HAADF-STEM courtesy of Tim Eldred.

The W–O bond lengths obtained from neutron PDF also help confirm the Raman spectrum assignment using the classical theory. Based on the empirical relationships in the literature and Hooke’s law, we derived the relationship between the Raman shift (ν_R) of the stretching modes and W–O bond length (d in Å):^{152,153}

It was found in transition metal oxides that the force constant (k) of a metal-oxide bond can be related to bond order (s) and bond length (d) using the following relationship:

$$k(N/m) = 400s(W-O) \quad (4.2)^{152}$$

$$s(W-O) = (d/1.904)^{-6} \quad (4.3)^{153}$$

Since the force constant is related to the Raman frequency (ν_R) of stretching modes using Hooke’s law, we have:

$$\nu_R(cm^{-1}) = \frac{1}{2\pi c} \sqrt{\frac{k}{\mu}} \quad (4.4)$$

where, c is the speed of light, μ is the reduced mass:

$$\mu = \frac{m_1 \times m_2}{m_1 + m_2} \quad (4.5)$$

In the case of W–O bond, $m_W = 183.84 \text{ amu} = 3.05 \times 10^{-22} \text{ g}$ and $m_O = 16 \text{ amu} = 2.66 \times 10^{-23} \text{ g}$.

Introducing the reduced mass into equation 4.4 gives:

$$\nu_R (cm^{-1}) = 1.0729\sqrt{k} = 4683.71 \times d^{-3} \quad (4.6)^{15}$$

Equation 4.6 indicates that shorter W–O bonds will have higher Raman shifts. Given the W–O bond lengths in **Figure 4.10** and based on this relationship and interpretation of the $WO_3 \cdot H_2O$ Raman spectrum,¹⁵ we assign the peak at 941.5 cm^{-1} to $\nu(W=O_t)$, the peak at 875.6 cm^{-1} to $\nu(W=O_{b-x}-W)$, and the broad peak at 658.4 cm^{-1} to $\nu(W-O_{b-yz}-W)$, and speculate the peak at 361.6 cm^{-1} to be $\nu(W-OH_2)$. The peaks between $200-350 \text{ cm}^{-1}$ are assigned to the bending modes of $\delta(W-O-W)$ and $\delta(O-W-O)$ and the peaks lower than 200 cm^{-1} are assigned to lattice modes.¹⁵

The force constants of the assigned stretching modes against the W–O bond lengths are compared to literature data and the empirical relation in **Figure 4.11** and show good agreements.

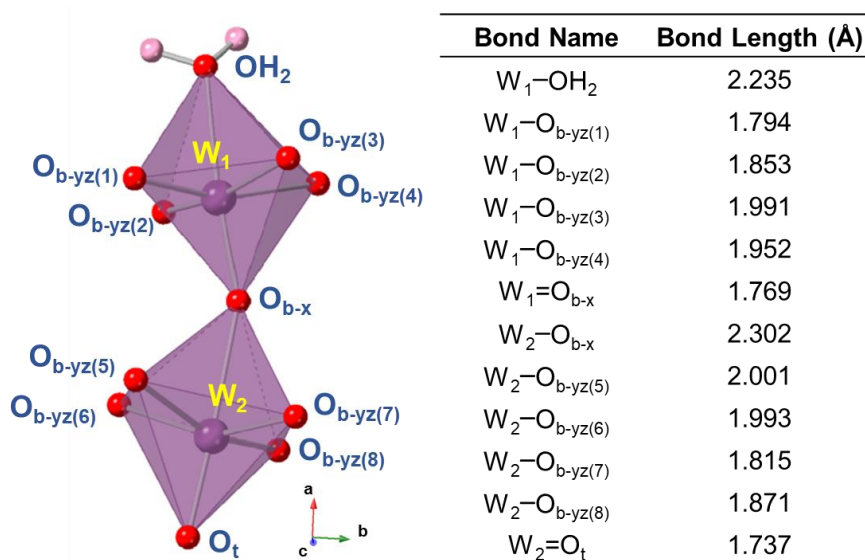


Figure 4.10. Bond lengths obtained from real-space refinement of $D_2W_2O_7$ from neutron PDF.

The double-bond was used to emphasize the exceptionally short bonds according to literature convention.¹⁵ neutron PDF refinement courtesy of Hsiu-Wen Wang.

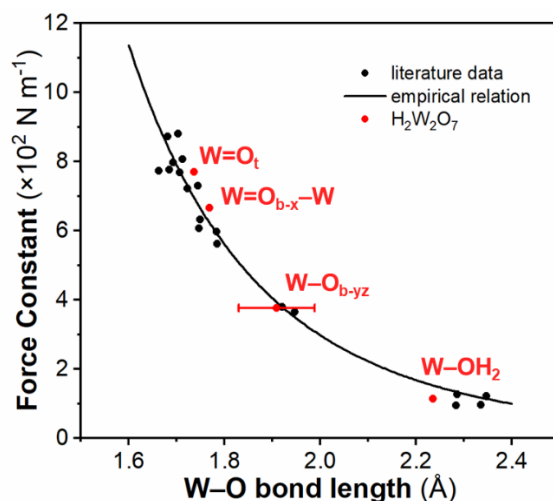


Figure 4.11. Correlation between the force constant and W–O bond length. The literature data are obtained from reference.¹⁵ The solid curve is from equation 4.2. For $\text{H}_2\text{W}_2\text{O}_7$ data points, W–O bond lengths are obtained from neutron PDF refinement and force constants are calculated from the assigned Raman peak positions using equation 4.6.

Electrochemical characterization

Electrochemical characterization of $\text{H}_2\text{W}_2\text{O}_7$ was carried out by cyclic voltammetry in a 3 M H_2SO_4 electrolyte. According to the prior report, electrochemical proton insertion into $\text{H}_2\text{W}_2\text{O}_7$ can be described as:¹⁵⁴



This results in a theoretical capacity of $0.5 e^-/\text{H}^+$ per W, or 62 mAh g^{-1} . The voltammograms in **Figure 4.12** shows the presence of a reversible redox couple with a half-wave potential ($E_{1/2}$) of -0.245 V vs. Ag/AgCl and a peak-to-peak separation (ΔE_p) of $51 \pm 2 \text{ mV}$ at 1 mV s^{-1} . The single set of well-defined redox peaks with a small peak-to-peak separation indicates that proton insertion in $\text{H}_2\text{W}_2\text{O}_7$ involves a first-order phase transformation and is not pseudocapacitive in nature. At lower sweep rates a low Coulombic efficiency (**Figure 4.13**) is attributed to the presence of a parasitic process, the hydrogen evolution reaction (HER). The Coulombic efficiency approaches

1.0 at higher sweep rates as HER is then kinetically prohibited. A lower cathodic potential limit was utilized at higher sweep rates due to decreased HER current and increased electrode polarization.

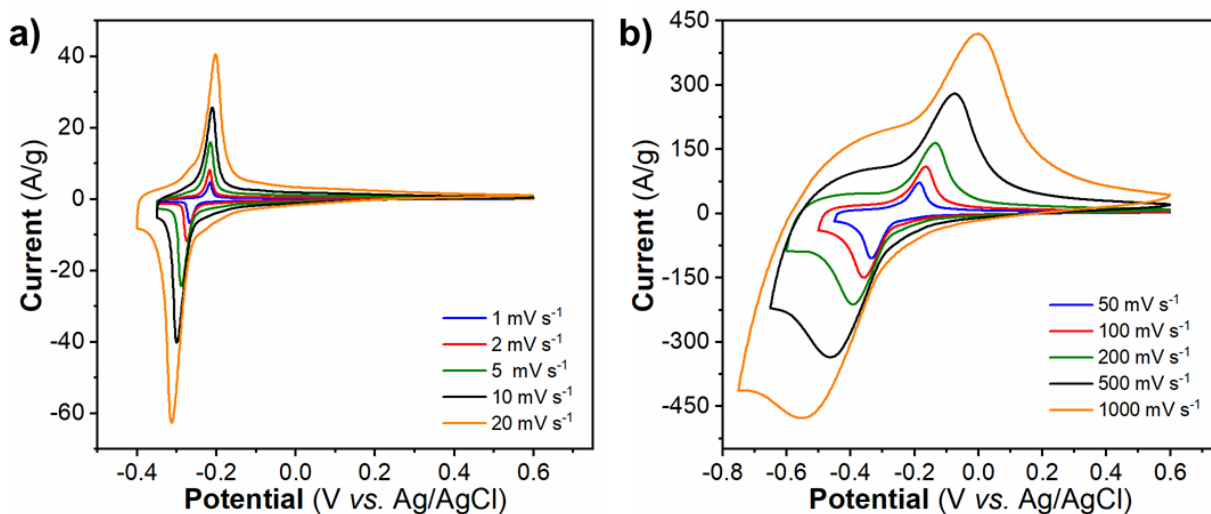


Figure 4.12. Cyclic voltammograms of $\text{H}_2\text{W}_2\text{O}_7$ in 3 M H_2SO_4 from a) 1 – 20 mV s^{-1} and b) 50 – 1000 mV s^{-1} .

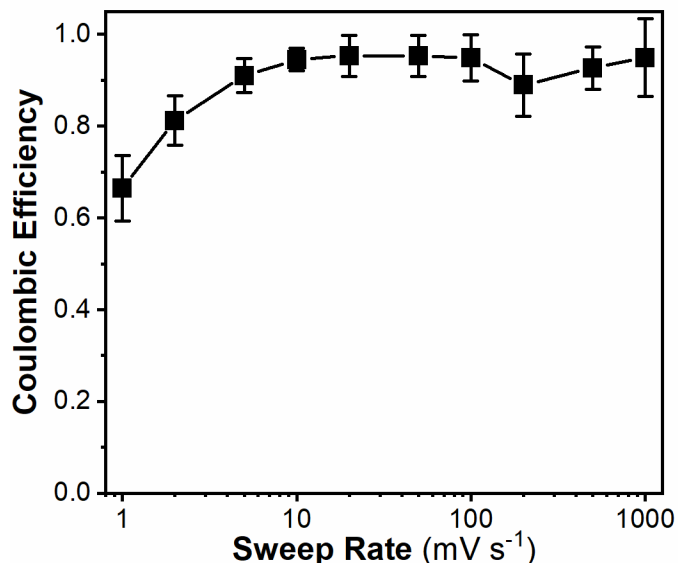


Figure 4.13. Coulombic efficiency of $\text{H}_2\text{W}_2\text{O}_7$ in 3 M H_2SO_4 from 1 to 1,000 mV s^{-1} , corresponding to the cyclic voltammograms in **Figures 4.12**. Error bars represent the standard deviation obtained from measurements performed on three separate electrodes.

The energy storage performance of $\text{H}_2\text{W}_2\text{O}_7$ was assessed by calculating the anodic specific capacity in **Figure 4.14** from 1 to 1000 mV s^{-1} . $\text{H}_2\text{W}_2\text{O}_7$ showed a specific capacity of $\sim 70 \text{ mAh g}^{-1}$ at 1 mV s^{-1} (~ 16 -min charge/discharge time) and retained 80% capacity at 1,000 mV s^{-1} (~ 1.5 -sec charge/discharge time). This indicates that nearly all of the theoretical capacity of $\text{H}_2\text{W}_2\text{O}_7$ can be accessed even at 100 mV s^{-1} (~ 11 sec discharging time). Usually, this type of rate capability is only seen in pseudocapacitive materials such as $\text{WO}_3 \cdot \text{H}_2\text{O}$,¹³⁸ which had 86% capacity retention at 1,000 mV s^{-1} but almost half of the capacity as compared to $\text{H}_2\text{W}_2\text{O}_7$. In addition, the $\text{WO}_3 \cdot \text{H}_2\text{O}$ had the kinetic advantage of a much smaller particle size, $\sim 200 \text{ nm}$ in diameter and 10 nm in thickness,¹⁵⁵ than the micron-sized $\text{H}_2\text{W}_2\text{O}_7$. This comparison showcases the high-power capability of $\text{H}_2\text{W}_2\text{O}_7$ in large particle sizes, which are beneficial for volumetric capacity. WO_3 obtained via dehydration of $\text{H}_2\text{W}_2\text{O}_7$ has the same particle size (**Figures 4.2c and 4.2d**) but

significantly worse energy storage performance, with $\sim 22 \text{ mAh g}^{-1}$ at 1 mV s^{-1} and 20% capacity retention at $1,000 \text{ mV s}^{-1}$. These results highlight the benefits of the metastable $\text{H}_2\text{W}_2\text{O}_7$ derived from selective etching: lower water content and larger particle size than $\text{WO}_3 \cdot \text{H}_2\text{O}$ obtained via direct synthesis leads to higher capacity, while the presence of a structural water network leads to better kinetics than WO_3 with the same particle size.

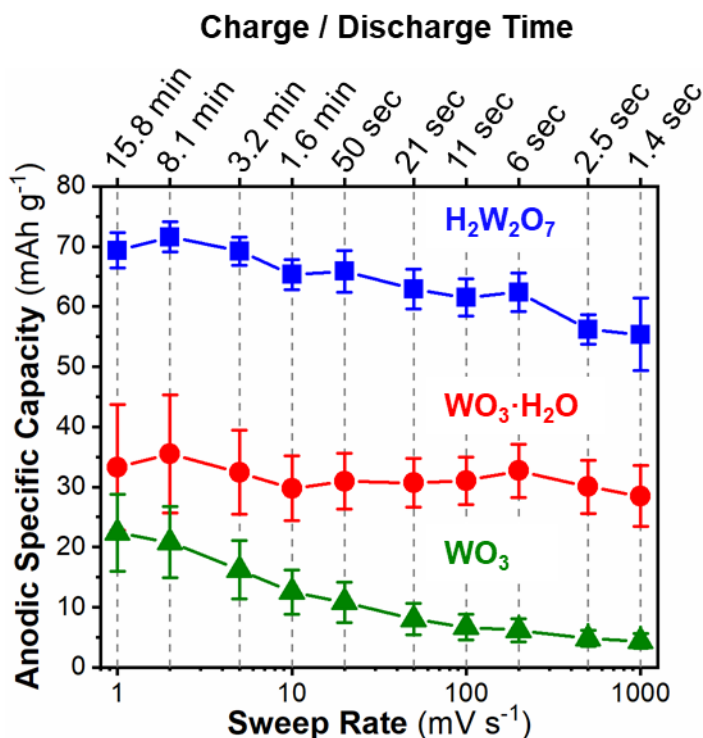


Figure 4.14. Anodic specific capacity as a function of sweep rate and the corresponding discharging time, comparing $\text{H}_2\text{W}_2\text{O}_7$, $\text{WO}_3 \cdot \text{H}_2\text{O}$, and WO_3 . The average values and standard error are obtained from three electrodes of each composition.

The kinetics of proton insertion in $\text{H}_2\text{W}_2\text{O}_7$ were quantified by tracking the relationship between peak current (i_p) and sweep rate (ν) from 1 to 1000 mV s^{-1} , as shown in **Figure 4.15**:⁶⁰

$$i_p \propto a\nu^b \quad (4.8)$$

where, a and b are constants. The boundary conditions for the “ b -value” are 0.5 for semi-infinite diffusion limited kinetics and 1 for surface-controlled kinetics.⁶⁰ The b -value of $\text{H}_2\text{W}_2\text{O}_7$ is 0.64 ($R^2 = 0.9975$) and falls in-between these boundary conditions. One convention for interpreting the b -value is to assume that the current is composed of a linear combination of semi-infinite diffusion-limited and capacitive processes.¹⁵⁶ We estimate low capacitive contributions from double layer and pseudocapacitive processes in $\text{H}_2\text{W}_2\text{O}_7$ due to the small capacitive background relative to the proton de/insertion peak currents and lack of mirror-image symmetry. The presence of both features would be indicative of surface-limited/capacitive behavior.¹ The kinetic limitation is more likely to be diffusion within a finite space.^{62,157}

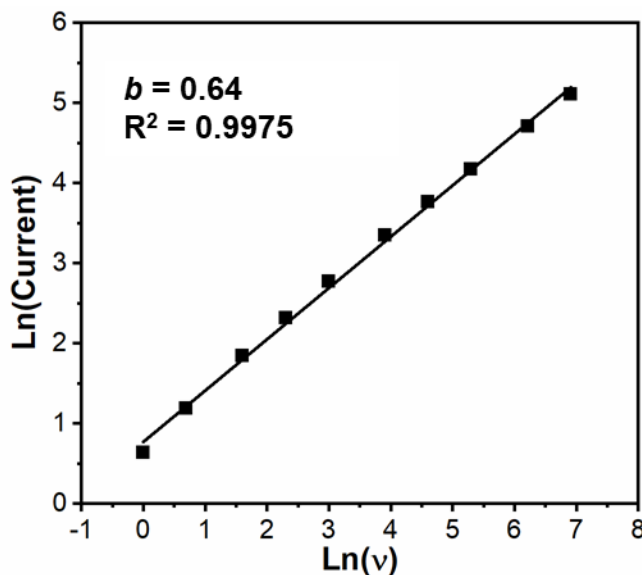


Figure 4.15. Sweep rate dependence of the anodic peak current in log scale for b -value determination from 1 – 1000 mV s^{-1} .

According to the theory developed by Aoki, Tokuda, and Matsuda,¹⁵⁷ i_p from a finite diffusion process would have the following dependence on v :

$$i_p = 0.446(n^3 F^3 D / RT)^{1/2} C^* \nu^{1/2} \tanh(0.56(nFl^2 / RTD)^{1/2} \nu^{1/2} + 0.05nFl^2 \nu / RTD) \quad (4.9)$$

where n is the number of electrons involved in the reaction, R is the ideal gas constant, T is temperature, F is Faraday's constant, l is the diffusion distance, D is the diffusion coefficient, and C^* is the initial concentration of the redox active species. A b -value of 0.64 just approximates the complicated relationship between i_p and ν . Another indication of finite diffusion comes from the ΔE_p of 51 mV at 1 mV s⁻¹, which is even smaller than the thermodynamic ΔE_p of a reversible single-electron redox couple in solution (57 mV, or 2.22 RT/F at 25 °C).¹⁵⁸ This thermodynamic value of ΔE_p is obtained based on a semi-infinite linear diffusion assumption, where the diffusion distance, l , is much greater than the theoretical diffusion length:^{159,160}

$$l \gg \sqrt{Dt} \quad (4.10)$$

where t is the diffusion time. Both the b -value and ΔE_p suggest that equation 4.10 no longer holds. Semi-infinite diffusion typically applies to many micron-sized battery materials at charge/discharge timescales of minutes/seconds. This analysis implies that proton insertion in H₂W₂O₇ must occur with a large diffusion coefficient, which will be investigated in a future study.

To determine the suitability of H₂W₂O₇ for long-term energy storage, we performed extended cycling in 3 M H₂SO₄ at 20 mV s⁻¹ between -0.365 – 0.1 V vs. Ag/AgCl (~23-sec charge/discharge time). The voltammograms for every 1,000th cycle up to 100,000 cycles are shown in **Figure 4.16a**. Most voltammograms looked the same with slight potential shifts except for the first cycle after start and restart, which presented a more prominent HER current. It indicated that after the first cycle intercalation was more energetically favorable than the Tafel step of HER. We did not investigate the mechanism of abnormal first cycle behavior in this study. Over the months of cycling, ΔE_p slightly increased, which might be associated with the increased

resistance in the electrical circuit due to the rusting of the metal wires in the aqueous system. The anodic capacity retention (**Figure 4.16b**) shows $\text{H}_2\text{W}_2\text{O}_7$ exhibits 89% capacity retention at 100,000 cycle, which is high for a transition metal oxide undergoing a redox reaction and approaches that of electrochemical capacitors. Of the capacity loss, about 5% was due to the 2-month immersion in the acid, which might have led to electrolyte evaporation. The Coulombic efficiency varies from 96~99% apart from the first CVs after start or restart. We note that due to the inevitable presence of HER, Coulombic efficiency is no longer a good indicator of cycle life in proton-based energy storage. The variation in Coulombic efficiency is likely due to the slight shift of redox potential, which included more or less HER current in the window.

With scalable synthesis, competitive capacity, excellent rate capability, and long cycle life, $\text{H}_2\text{W}_2\text{O}_7$ is a promising candidate as an anode material for proton-based aqueous batteries.

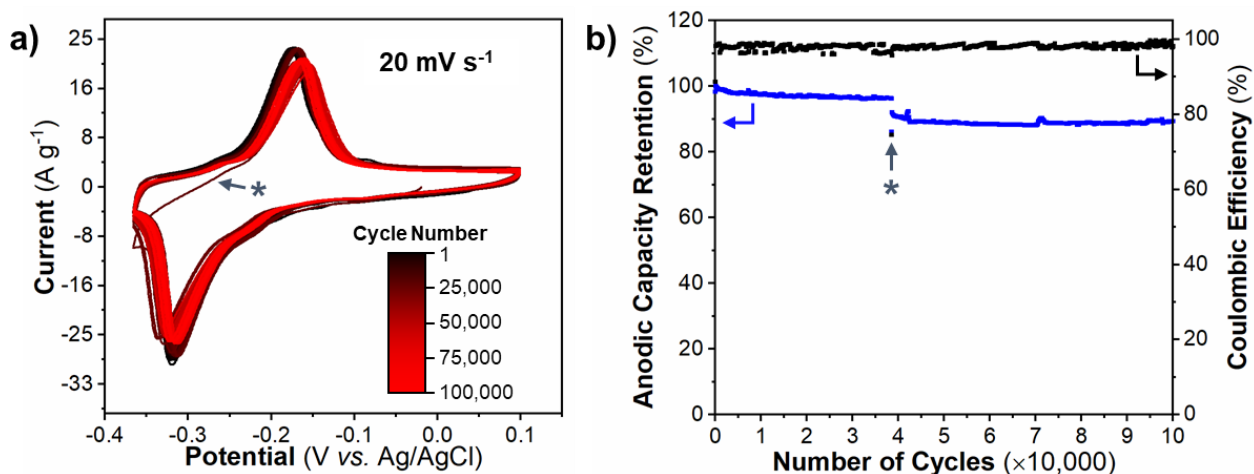


Figure 4.16. Cyclability test: a) cyclic voltammograms of $\text{H}_2\text{W}_2\text{O}_7$ at 20 mV s^{-1} to showcase the stability of this material against cycling. Presented is every 1,000th cycle out of 100,000 cycles. b) Anodic capacity retention and Coulombic efficiency as a function of cycle number for 100,000 cycles. The asterisk symbol (*) indicates the first cycle after a two-month pause of experiment due to COVID-19 outbreak.

Charge storage mechanism

The ~100% increase in capacity from $\text{WO}_3 \cdot \text{H}_2\text{O}$ to $\text{H}_2\text{W}_2\text{O}_7$ cannot be solely explained by the 3.1 wt% decrease in water content in the structure. To understand the capacity increase in $\text{H}_2\text{W}_2\text{O}_7$, we employed ex situ XRD, DFT, and in situ Raman spectroscopy to investigate the charge storage mechanism.

Ex situ XRD of a $\text{H}_2\text{W}_2\text{O}_7$ electrode cycled to -0.5 V vs. Ag/AgCl (for a capacity of $0.5 e^-$ per W) in 1 M H_2SO_4 shows the shift of both 200 and 400 peaks to higher angles (**Figure 4.17**). These shifts represent a 2.9% contraction of the interlayer at 1 proton per formula unit. After cycling back to open-circuit potential (deinsertion of $0.5 e^-$ per W), the 200 and 400 peaks returned to their original position. The ex situ XRD experiments present a reversible contraction of the interlayer spacing to accommodate electrochemical proton (de-)insertion in $\text{H}_2\text{W}_2\text{O}_7$. Due to the limited 2θ range, we cannot confirm whether the interlayer contraction comes with a phase transformation as indicated by the cyclic voltammetry peak separation. In the structurally related $\text{WO}_3 \cdot 2\text{H}_2\text{O}$, proton insertion does not change the interlayer spacing, which is indicative of a proton absorption at the equatorial bridging oxygen sites.¹³⁸ Since an interlayer contraction in $\text{H}_2\text{W}_2\text{O}_7$ was observed, we suspect the capacity increase may be due to a change of proton absorption site.

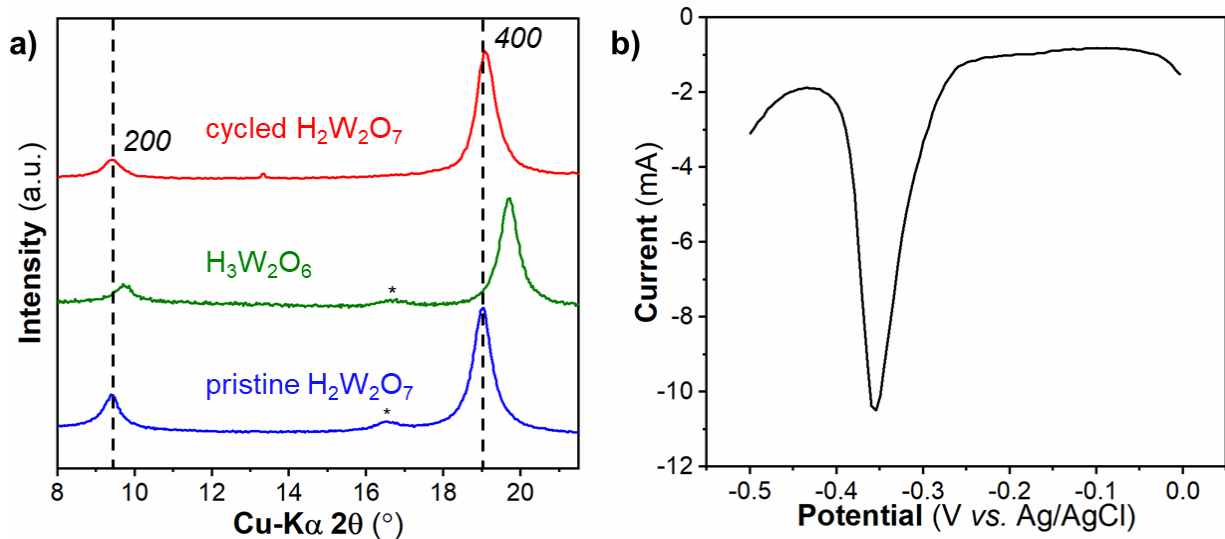


Figure 4.17. a) Ex situ XRD patterns of pristine, protonated, and cycled H₂W₂O₇ electrodes. * indicates WO₃·H₂O impurities because of selectively etching a batch of Bi₂W₂O₉ that contained Bi₂WO₆ impurities. The cycled pattern was obtained from a different electrode. b) Linear sweep voltammogram of a H₂W₂O₇ slurry electrode in 1 M H₂SO₄ cycled at 5 mV s⁻¹ to -0.5 V vs. Ag/AgCl.

DFT was used to calculate the proton absorption energy (E_{ads}) and concentrations at various oxygen sites in H_{2+x}W₂O₇. As illustrated in Figure 4.8, the potential oxygen sites include two types of bridging oxygens, the axial O_{b-x} and the equatorial O_{b-yz}, and the terminal oxygens, O_t. Because a cell containing 8 W atoms, adding one proton to the structure is equivalent to adding 0.25 protons per formula unit. The calculated E_{ads} is shown in **Figure 4.18**. At H_{2.25}W₂O₇, E_{ads} for O_t, O_{b-yz}, and O_{b-x} are, respectively, -0.49 eV, -0.55 eV, and -0.19 eV, showing that the O_{b-yz} is the most energetically favorable site and O_t has a similar but slightly higher energy. The absorption energy at O_{b-x} is significantly higher. In simulation of higher proton concentrations, generally the most energetically favorable structures from the lower proton concentrations are used. However, due to the similar absorption energy at O_{b-yz} and O_t sites at $x = 0.25$, both were used in the simulation of

the structures at $x = 0.5$. Among the combination of O_{b-yz} and O_t sites at $x = 0.5$, absorption of all protons at O_t sites becomes the most favorable. From $x = 0.5$, due to the low absorption energy at O_t sites, they are the only structure that were carried over to higher proton concentrations. At $x = 0.75$ and 1, a complete absorption at O_t sites becomes consistently the most energetically favorable. This is in contrast to the single-layer $WO_3 \cdot H_2O$, where at low proton concentrations the proton absorption site was found to be at O_t but at higher concentrations moved to O_{b-yz} due to repulsive interactions between the intercalated protons in the interlayer.^{138,161}

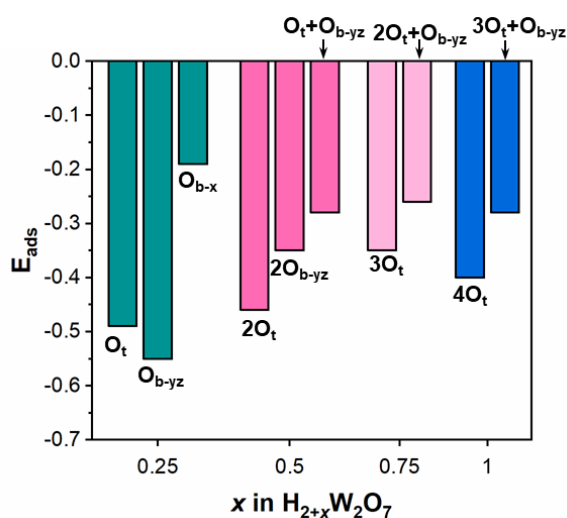


Figure 4.18. DFT-calculated proton absorption energy at various oxygen sites in $H_{2+x}W_2O_7$. O_{b-yz} , O_t , and O_{b-x} stand for equatorial bridging oxygen, terminal oxygen, and axial bridging oxygen, respectively. The integer before oxygen indicates the number of sites absorbed by proton per 8 W atoms. DFT courtesy of Yangyunli Sun and De-en Jiang.

To confirm the simulation results, we compare the calculated 200 XRD peak using the simulated structures to the ex situ XRD patterns shown in **Figure 4.19**. The increased absorption at O_t sites shows a continuous contraction of interlayer spacing. Surprisingly, the absorption at O_{b-yz} sites causes a comparatively greater interlayer contraction at $x \leq 0.75$. At $x = 1$, proton absorption

at $4O_t$ and $3O_t+O_{b-yz}$ leads to a similar interlayer contraction of 2.5% and 1.9%, respectively. Compared to the 2.9% contraction observed experimentally, the simulated structure with O_t absorption captures the extent of interlayer contraction. Therefore, we hypothesize that O_t is the most probable absorption site in $H_2W_2O_7$ and the difference of proton absorption sites is likely the main reason behind the capacity increase in $H_2W_2O_7$. In addition, Lin et al. predicted a fast diffusion pathway formed by the zigzag O_t sites in the interlayer of $WO_3 \cdot H_2O$.¹⁶¹ The O_t absorption sites in $H_2W_2O_7$ may provide protons with access to this pathway, leading to the high power capability observed in this material. This will be a subject of investigation in our future studies.

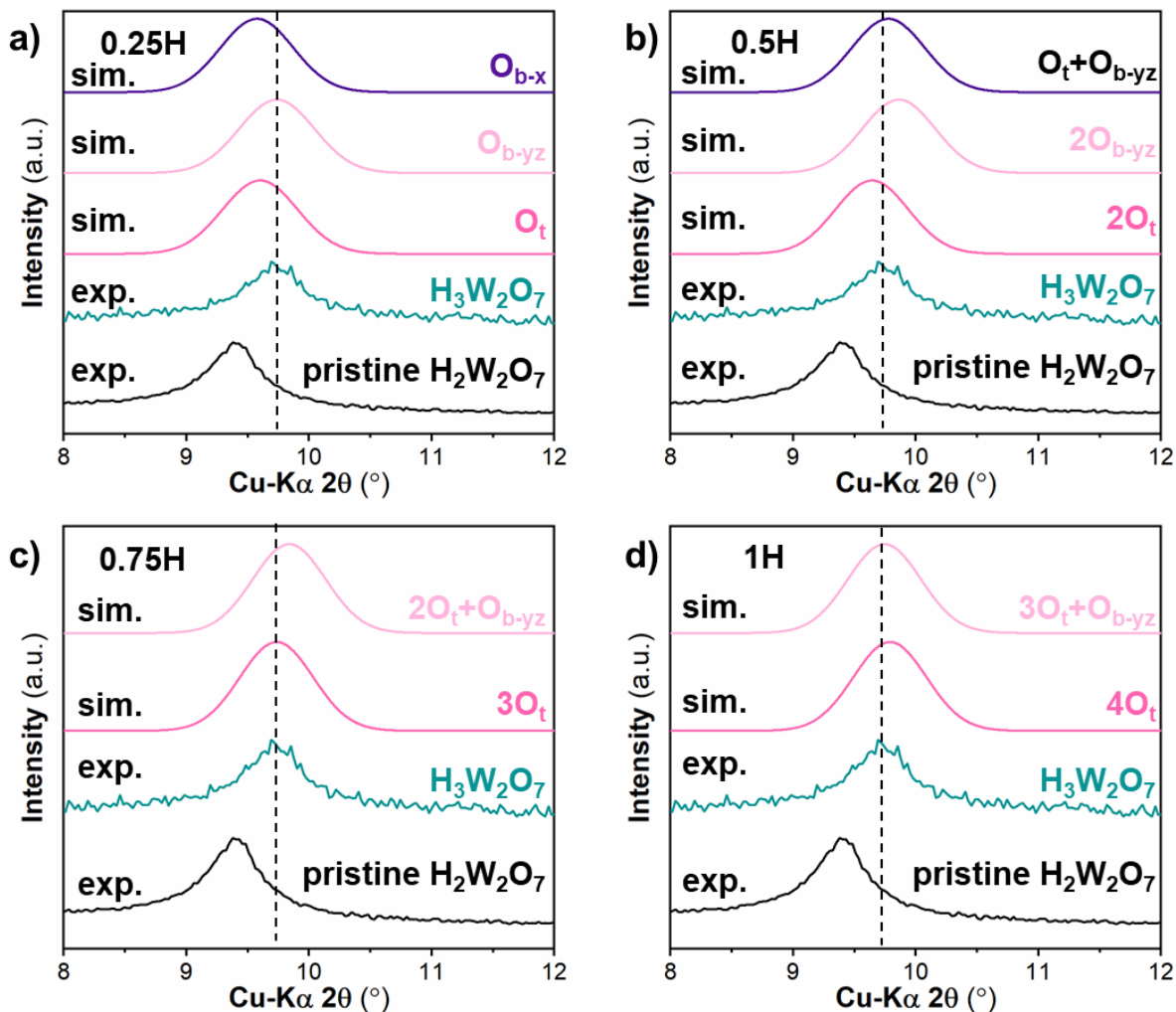


Figure 4.19. Comparison of 200 XRD peak calculated from the DFT-calculated structures to the ex situ experimental data for $\text{H}_{2+x}\text{W}_2\text{O}_7$ at various proton concentrations. a) $x = 0.25$, b) $x = 0.5$, c) $x = 0.75$, and d) $x = 1$. In the figures, “sim.” and “exp.” stand for simulated and experimental, respectively. A gaussian function was used for the shape of the simulated pattern. DFT courtesy of Yangyunli Sun and De-en Jiang.

We further investigate the changes of local structural change with in situ Raman spectroscopy. **Figure 4.20** shows the Raman spectra of $\text{H}_{2+x}\text{W}_2\text{O}_7$ as a function of proton concentrations along with linear sweep voltammograms and the optical micrographs of the

electrode at the corresponding potentials. At a proton concentration as small as $x = 0.1$, we observe the extinction of the $\nu(\text{W}-\text{O}_{\text{b-yz}}-\text{W})$ peak at 650 cm^{-1} and a blue coloration, which is characteristic to tungsten oxides.¹⁶² At $x = 0.2$, which is still before the onset of the redox peak, a new peak at 850 cm^{-1} appears and the electrode darkened to a purplish color. The redox peak is where majority of the charge is stored. At this stage, all peaks greater than 500 cm^{-1} disappeared and the electrode turned orange. This orange color was observed in $\text{Na}_{0.8}\text{WO}_3$ but is noticed for the first time due to the electrochemical ion insertion into tungsten oxides from an aqueous electrolyte.¹⁶³ Between $x = 0$ and 1.1 , the $\nu(\text{W}-\text{OH}_2)$ peak at 362 cm^{-1} gradually shifts to 440 cm^{-1} . The anodic scan demonstrates that reversible changes in Raman spectra and color. At $x = 0.5$, the spectrum is similar to the one at $x = 0.2$ and the color turns from orange back to purple. When the electrode was cycled back to the open-circuit potential, both the Raman spectrum and the color resumed their pristine states.

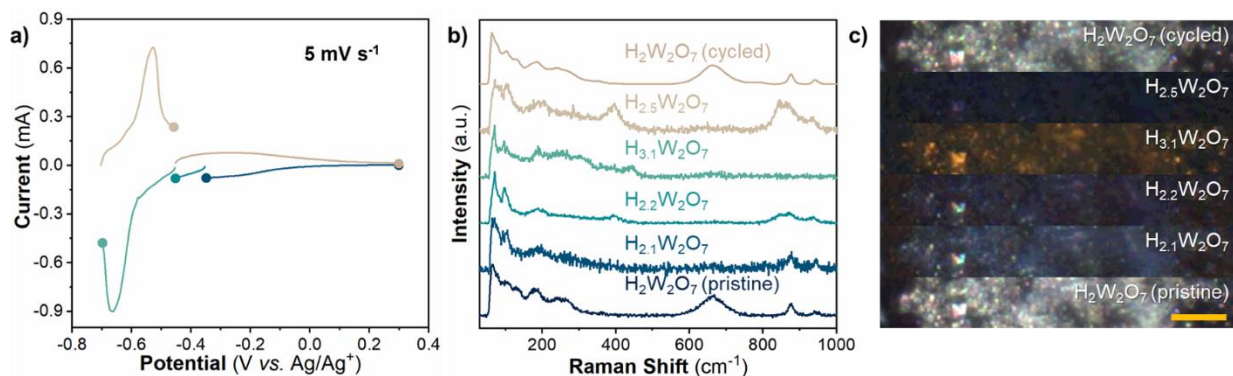


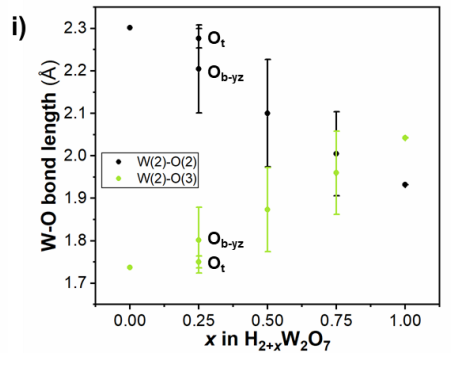
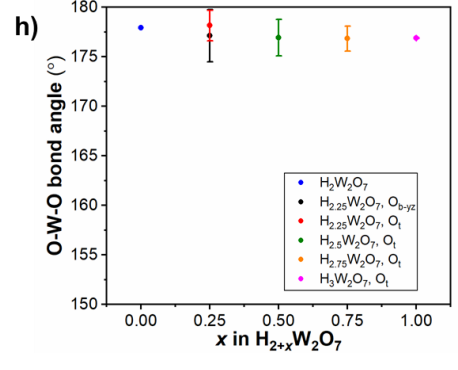
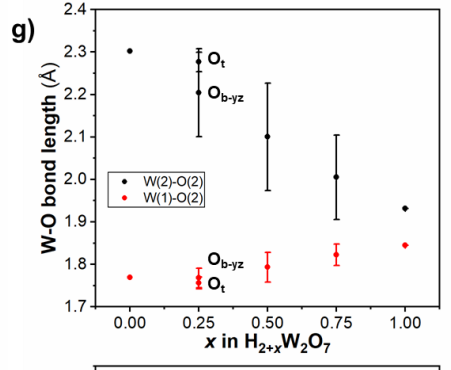
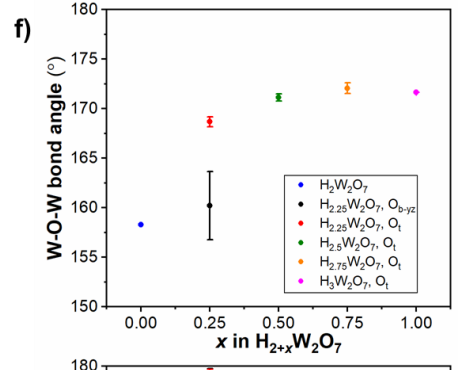
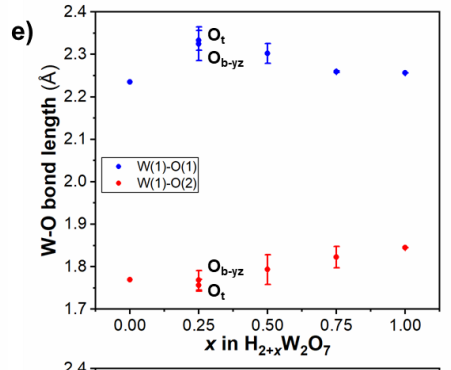
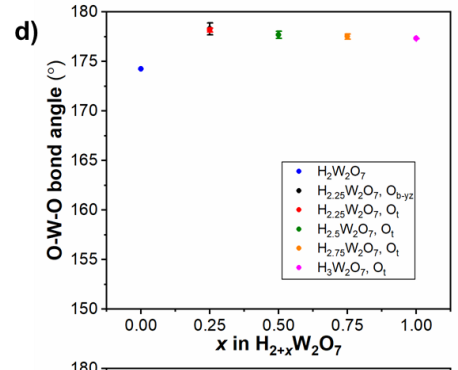
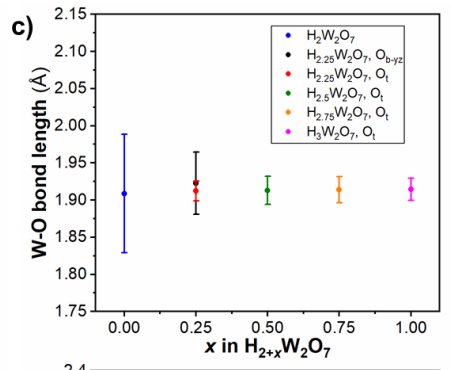
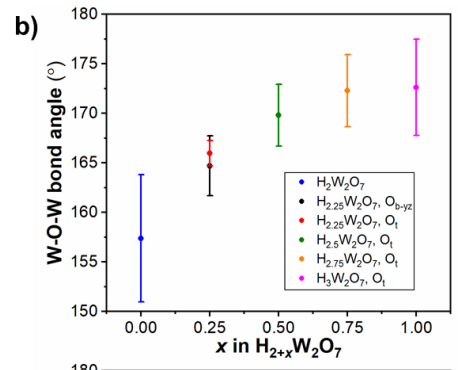
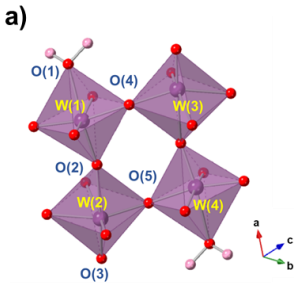
Figure 4.20. Physical characterization of the proton insertion mechanism in $\text{H}_2\text{W}_2\text{O}_7$. a) Linear sweep voltammograms of a $\text{H}_2\text{W}_2\text{O}_7$ slurry electrode in $1\text{ M H}_2\text{SO}_4$ cycled at 5 mV s^{-1} between -0.7 and 0.3 V vs. Ag pseudo-reference. b) In situ Raman spectra of $\text{H}_{2+x}\text{W}_2\text{O}_7$ as a function of proton insertion, x . The spectra were taken at the terminal potentials of the linear sweep

voltammograms. c) Optical micrographs of the same electrode showing the multicolor electrochromism of $\text{H}_{2+x}\text{W}_2\text{O}_7$. Scale bar = 10 μm .

The multicolor electrochromism in tungsten oxides was explained by the electronic band structure and shift of Fermi levels upon ion insertion by Goodenough.¹⁶⁴ The reason for $\text{H}_2\text{W}_2\text{O}_7$ to achieve the same color as $\text{Na}_{0.8}\text{WO}_3$ but with 0.3 fewer e^- s per W is worth further investigation. For in situ Raman spectra, we propose two hypotheses to explain their evolution. The first hypothesis is based on the semiconductor-to-metal transition, which happens upon ion insertion in tungsten oxides.¹⁶³ As metallic conductivity is associated with materials that have no Raman activity, this could be one reason that we lose the Raman peaks.^{14,165} The second hypothesis is based on the classical theory of the Raman effect, which states that a Raman mode is only active when there is a change in polarizability. Polarizability refers to the ease of distorting electrons by an electric field and is associated with the bond length. In **Figure 4.21**, we summarize the W–O bond lengths and angles of the refined pristine $\text{H}_2\text{W}_2\text{O}_7$ structure and the DFT-calculated structures at $\text{H}_{2.25}\text{W}_2\text{O}_7$, $\text{H}_{2.5}\text{W}_2\text{O}_7$, $\text{H}_{2.75}\text{W}_2\text{O}_7$, and $\text{H}_3\text{W}_2\text{O}_7$. For the equatorial W– $\text{O}_{\text{b-yz}}$ bond, we find that upon proton insertion the standard deviation of bond lengths reduces significantly from 0.08 Å to 0.02 Å, while the average bond lengths stay steady at around 1.91 Å. In the asymmetric stretching of W– $\text{O}_{\text{b-yz}}$ –W, one bond will be stretched and become more polarizable while the other bond will be compressed and be less polarizable. In the case of bonds with similar lengths, the change of polarizability in the longer bond can be offset by the change of polarizability of the shorter bond, leading to almost no changes in the overall polarizability. Therefore, we hypothesize that the extinction of the $\nu(\text{W}-\text{O}_{\text{b-yz}}-\text{W})$ peak may be due to the loss of changes in polarizability of the W– $\text{O}_{\text{b-yz}}$ –W bonds upon proton insertion. The new peak at 850 cm^{-1} is attributed to the variation of O–W=O $_{\text{b-x}}$ bond due to the proton absorption at the O_t site. Between $x = 0.2$ and 1, the blue shift

of $\nu(\text{W}-\text{OH}_2)$ is attributed to the shortening of $\text{W}-\text{OH}_2$ bond. At $\text{H}_3\text{W}_2\text{O}_7$, the differences among the axial bonds have significantly decreased. However, the four axial bonds are still $\sim 1 \text{ \AA}$ different from each other according to the simulation. It is difficult to analyze polarizability changes so the conclusion that the extinction of the peaks between 800 and 1000 cm^{-1} is due to the polarizability offset is speculative. We plan to further study the vibrational dynamics with ex situ inelastic neutron scattering (INS) on $\text{H}_2\text{W}_2\text{O}_7$ in the future, as INS is not sensitive to material conductivity and can provide detailed information on proton absorption sites.¹³⁸

Figure 4.21. Bond angle and length statistics of DFT-calculated structures of $\text{H}_{2+x}\text{W}_2\text{O}_7$ at various proton concentrations. a) four corner-sharing tungsten oxide octahedra with a few tungsten and oxygen atoms labeled for illustration purpose. The statistics for the following bond angles and lengths are presented: b) equatorial W–O–W bond angles [including W(1)–O(4)–W(3) and W(2)–O(5)–W(4)], c) equatorial W–O bond lengths [including W(1)–O(4), W(3)–O(4), W(2)–O(5), W(4)–O(5),], d) axial O(1)–W(1)–O(2) bond angles, e) axial W(1)–O(1) and W(1)–O(2) bond lengths, f) axial W(1)–O(2)–W(2) bond angles, g) axial W(1)–O(2) and W(2)–O(2) bond lengths, h) axial O(2)–W(2)–O(3) bond angles, and i) W(2)–O(2) and W(2)–O(3) bond lengths. The error bars stand for standard deviations of the measurements performed on 8 tungsten-oxide octahedra. At $x = 0.25$, both the absorptions at O_t and $\text{O}_{b\text{-}yz}$ sites are considered and at other concentrations only O_t absorption is considered. DFT courtesy of Yangyunli Sun and De-en Jiang.



4.4 Conclusions

In summary, we performed comprehensive structural and electrochemical characterizations of $\text{H}_2\text{W}_2\text{O}_7$ obtained by selective etching of $\text{Bi}_2\text{W}_2\text{O}_9$. $\text{H}_2\text{W}_2\text{O}_7$ is a layered material consisting of bilayer corner-sharing tungsten octahedra with space group $P112_1/n$. It can store $\sim 70 \text{ mAh g}^{-1}$ at 1 mV s^{-1} (~ 16 -min discharging time) and maintain $\sim 80\%$ capacity at $1,000 \text{ mV s}^{-1}$ (~ 1.5 -s discharging time). The cycle life at 20 mV s^{-1} is well beyond 100,000 cycles. While the kinetics are limited by finite-space diffusion, the power capability and cycle life of $\text{H}_2\text{W}_2\text{O}_7$ are competitive to electrochemical capacitors. The high capacity is attributed to proton absorption at the terminal oxygen site. In addition to the high-power energy storage capabilities, $\text{H}_2\text{W}_2\text{O}_7$ exhibits a multicolor electrochromism that is easily accessible in acidic electrolytes. These results render $\text{H}_2\text{W}_2\text{O}_7$ a promising material for energy storage and electrochromic applications. This material highlights selective etching as a method to prepare metastable transition metal oxides that cannot be obtained by traditional means. Moving forward, we plan to investigate the fast transport property and vibrational dynamics in $\text{H}_2\text{W}_2\text{O}_7$.

Chapter 5: Cathode Materials for Rechargeable Magnesium Batteries

The success of electrochemical energy storage in powering portable electronic devices and electric vehicles is in large part due to the ease with which small, monovalent cations are able to undergo charge-transfer and diffusion into a solid-state electrode. Electrochemical energy storage based on protons (H^+) and lithium ions (Li^+) has resulted in commercially available Ni-metal hydride and Li-ion batteries. The development of next-generation energy storage devices focuses on improving their energy density, power density, lifetime, cost, safety, and sustainability. Several avenues are actively pursued, primarily: moving beyond intercalation reactions,^{51,166} pursuing other monovalent ion chemistries, such as Na^+ ;^{167,168} moving beyond liquid electrolytes;¹⁶⁹ and pursuing multivalent cation chemistries.¹⁷⁰ Of the various possibilities for multivalent energy storage, that of non-aqueous magnesium (Mg^{2+}) is the most advanced. In general, multivalent energy storage holds the promise of increasing the energy density over Li^+ -based devices by replacing the low volumetric density graphite anode (777 mAh cm^{-3}) with a alkaline earth metal anode ($3,833 \text{ mAh cm}^{-3}$ for Mg). In the case of Mg^{2+} storage, there are added benefits from the increased terrestrial abundance of Mg^{2+} and better safety due to the lower reactivity of alkaline earth metals as compared to alkali metals as summarized in **Table 5.1**.¹⁷¹

Table 5.1. Comparisons of magnesium and lithium ion for energy storage applications in the areas of ionic radius, voltage vs. standard hydrogen electrode, abundance, and volumetric and gravimetric capacity.¹⁷²

Characteristics	Mg	Li
Pauling Ionic Radius	65	60
Voltage vs. S.H.E.	-2.37	-3.04
Elemental abundance (ppm in earth's crust)	2.33E+04	2.00E+01
Volumetric capacity (mAh/cm ³)	3833	2046
Gravimetric capacity (mAh/g)	2205	3862

There are two primary challenges for Mg²⁺-based energy storage devices operating in non-aqueous electrolytes: (1) electrolytes that are compatible with both Mg metal anodes and Mg²⁺ cathodes and (2) high voltage and high capacity Mg²⁺ cathodes with long cycle lives.¹⁷³ Solving both challenges will require the fundamental understanding of cathode and anode interfaces. In the case of Mg metal anodes, carbonate-based electrolytes commonly used in Li⁺ battery chemistries lead to the formation of a passivating interfacial phase that prevents reversible electrodeposition and stripping of Mg²⁺.¹⁷² In insertion-based cathodes, charge-transfer at the electrode/electrolyte interface requires an activation energy that is related to the desolvation energy of the cation.^{69,174} The higher charge density of Mg²⁺ relative to Li⁺ means that Mg²⁺ exhibits a larger desolvation energy.¹⁷⁵ A recent combined computational and experimental study of Mg²⁺ insertion into Mo₆S₈ from a magnesium chloride-based electrolyte in tetrahydrofuran showed that Mg²⁺ and Cl⁻ formed strongly bound species in the electrolyte, and that the Cl⁻ preferentially absorbed onto Mo surface sites during Mg²⁺ intercalation.¹⁷⁶ The results indicated that the success of Mo₆S₈ as a cathode material was due to its ability to dissociate Cl⁻ from Mg²⁺ at the surface. On the anode side, Cl⁻ has shown to play a role in enabling Mg deposition and stripping.^{177,178} Besides the charge-transfer step, Mg²⁺ must also undergo solid-state diffusion where its high charge density leads to increased

Coulombic interactions with the electrode and the need for rapid redistribution of the 2+ charge.¹⁰⁶ Both of these factors result in cathodes that exhibit shorter cycle life, slower rate capabilities and higher hysteresis (difference between potential for insertion vs. de-insertion) than what is observed for monovalent cation storage. The ability to undergo multi-electron redox also limits the capacity of most multivalent cathodes, so that typically less than 1 e^- is stored per redox site, similar to monovalent chemistries. Due to the relatively high potential of the Mg anode (-2.38 V vs. SHE) as compared to Li (-3.04 V vs. SHE), it is therefore important to find high potential cathodes to obtain reasonable energy densities. Typical capacity and potential values of cathode materials under consideration for Mg and Mg^{2+} batteries are summarized in **Figure 5.1**. The structure-property relationships of these materials are discussed in the rest of this chapter.

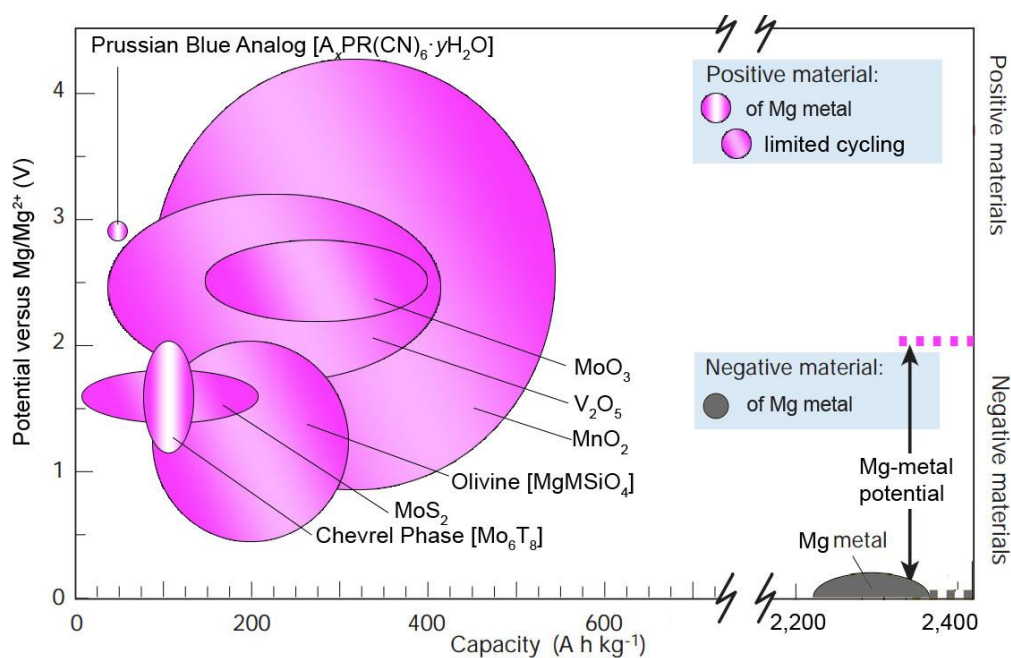


Figure 5.1. Voltage versus capacity for magnesium metal and cathode materials for magnesium ion under currently active investigations.¹⁶⁻³⁴

Chevrel phases

Chevrel phases of the Mo_6T_8 family ($\text{T} = \text{S}$, or/and Se) are the most studied cathode materials for magnesium.¹⁷² As shown in **Figure 5.2a**, its structure contains clusters of octahedra of six molybdenum ions inside cubes of eight sulfur or/and selenium. It can reversibly intercalate two magnesium ions per formula unit as indicated by the two plateaus in the galvanostatic charge/discharge curve in **Figure 5.2b**. Figure 5.2b summarizes the long cycle life, reasonable capacity and relatively low potential of Mo_6S_8 . The success of this structure was attributed to three main reasons. First of all, the molybdenum metal clusters are able to rapidly distribute the two electrons associated with each magnesium ions and maintain local charge neutrality. Secondly, the existence of 12 closely-spaced vacant sites per cluster enables fast diffusion of magnesium ions. At last but not least, the high electronic conductivity leads to fast kinetics.³⁶ The presence of sulfur provides structure stability but leads to the relatively low reduction potential.

Note that this material cannot be synthesized directly. To synthesize Mo_6S_8 , a $\text{Cu}_2\text{Mo}_6\text{S}_8$ precursor has to be made first with high temperature solid state hydrothermal³⁵ or molten salt¹⁷⁹ methods and then Mo_6S_8 can be obtained after acid leaching in 6 M HCl for nine days to remove Cu.

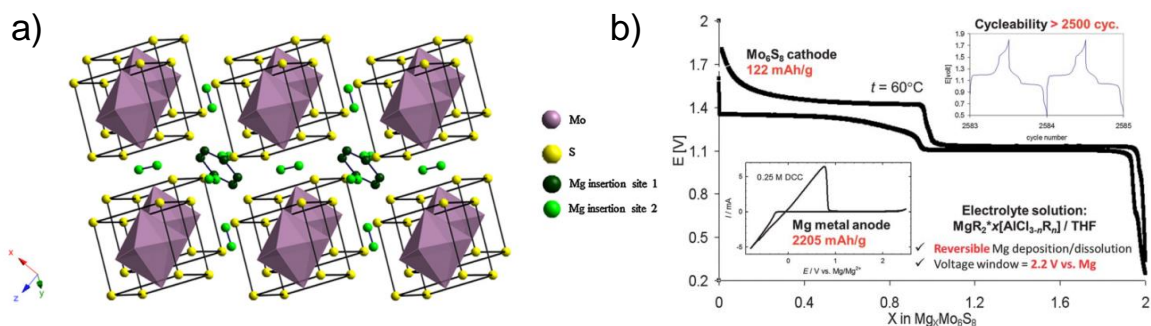


Figure 5.2. a) Crystal structure of Chevrel phase Mo_6S_8 ;³⁵ b) a performance summary of a Mg-rechargeable battery prototype using a Mo_6S_8 cathode and a magnesium metal anode.³⁶

Prussian Blue analogue

Prussian Blue analogues have a general formula of $A_xPR(CN)_6 \cdot yH_2O$, where A represents an interstitial cation like Mg^{2+} and P and R are transition metal elements like Mn, Fe, Co, Ni, and Cu. As illustrated in **Figure 5.3**, they are framework structures that contain octahedra with alternating P and R transition metal ions in their centers, at the corners of which they are connected by $(C\equiv N)^-$ anions. This connection creates large empty sub-cubes that have edge lengths greater than 1 nm.

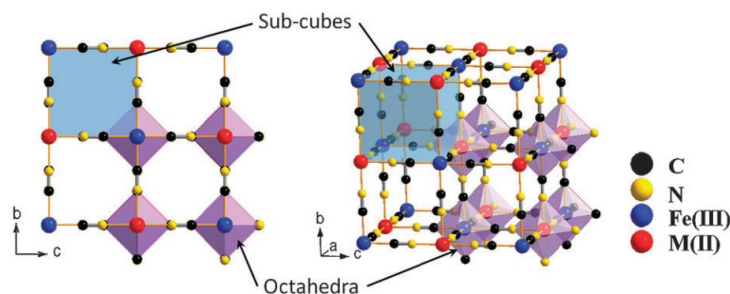


Figure 5.3. Framework structure of Prussian blue analogue.³⁷

The stable structure and large empty sub-cubes allow easy and fast insertion of magnesium ions which result in long cycle life and good rate capability. In one study,²⁹ $KNiFe(CN)_6 \cdot yH_2O$ was cycled in aqueous Mg^{2+} cells. It showed a high half-charge reaction potential of 0.6V vs. SHE (2.97 V vs. Mg/Mg^{2+}) and after 2000 cycles it can retain a capacity 16 mAh g^{-1} or 50 mAh g^{-1} if 20 mM of Ni^{2+} was added to suppress the partial solubility of the material. The success of reversible divalent Mg^{2+} insertion was not fully elucidated. However, it was attributed to the presence of water to shield electrostatic interaction during diffusion, fast distribution of charges with ordered vacancies and host ions, additional diffusion pathways provided by ferricyanide vacancies that are $\sim 5 \text{ \AA}$ in diameter. $KNiFe(CN)_6 \cdot yH_2O$ can be synthesized by a coprecipitation

method by adding aqueous nickel nitrate and potassium ferricyanide to deionized (DI) water at 80 °C.

1D tunneled or olivine structure

Hollandite and todorokite MnO_2 contain 1D tunnels formed by 2×2 and 3×3 edge-sharing MnO_6 octahedra, illustrated in **Figures 5.4a** and **5.4b**. Hollandite MnO_2 exhibits capacity ranging from 85-310 mAh g^{-1} at an operating potential of 1.7 V vs. Mg/Mg^{2+} in literature but significant capacity fade of about 50% in the initial cycles were reported due to collapse of hollandite tunnels.^{21,23,180} Todorokite MnO_2 only has one report on Mg^{2+} and showed an initial capacity of 85 mAh g^{-1} at operating potential of 1.4 V vs. Mg/Mg^{2+} .¹⁸¹ While hollandite MnO_2 is commercially available, todorokite MnO_2 can be synthesized by oxidizing Mn(OH)_2 with NaMnO_4 followed by aging.

Olivine structure transition metal silicates are formed by corner-sharing transition metal oxide (Fe, Co, or Mn) octahedra and silicate tetrahedra as shown in **Figure 5.4c**. The transition metal in this structure was proved to be capable of transferring two electrons to maintain local charge neutrality. A range of capacity from 95 to 300 mAh g^{-1} at operating potential of 1.6 V vs. Mg/Mg^{2+} were reported.²⁶ MgFeSiO_4 and MgMnSiO_4 were able to cycle for at least 20 cycles with >90% capacity retention and MgCoSiO_4 was cycled to 200 cycles with >50% capacity fade. Transition metal silicates can be obtained by water-based solution chemistry, sol-gel, or molten salt methods.

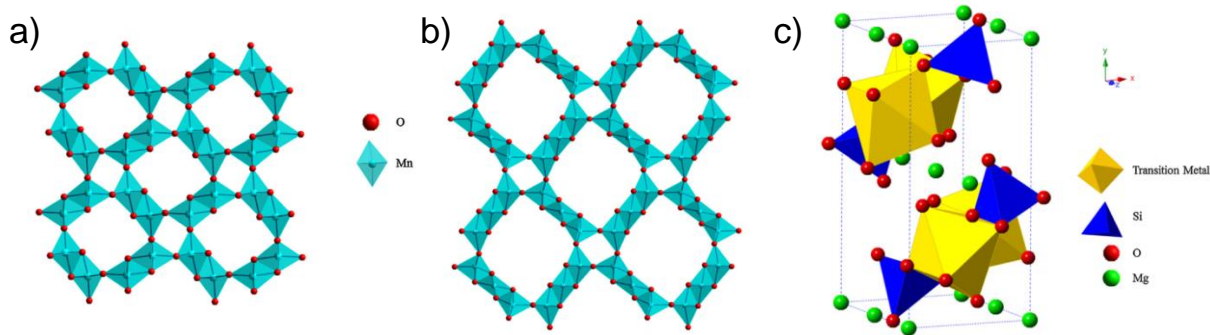


Figure 5.4. 1D tunneled/olivine structures: a) hollandite MnO_2 ,³⁸ b) todorokite MnO_2 ,³⁹ and c) transition metal silicates.⁴⁰

2D layered structure

2D transition metal oxides and sulfides have rich structural chemistry. As illustrated in **Figure 5.5**, orthorhombic V_2O_5 consists of a group of corner-sharing pyramids, orthorhombic MoO_3 contains double chains of edge-sharing octahedra, and MoS_2 and birnessite MnO_2 are stacked by edge-sharing octahedra. 2D layered structures provide two dimensional pathways for cations to insert and extract and are the structures of the most prevalent cathode materials in rechargeable lithium-ion batteries. When it comes to magnesium ion based batteries, the cycle life of these materials is significantly shortened. The oxides were hardly ever cycled to over 35 cycles and only one report showed MoS_2 being cycled for 50 cycles with a reversible capacity of 170 mAh g^{-1} at an operating voltage of 1.5 V vs Mg/Mg^{2+} .

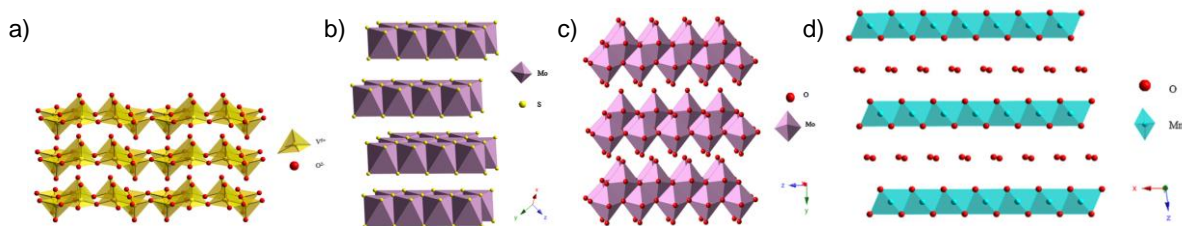


Figure 5.5. 2D layered structures: a) orthorhombic V_2O_5 ,⁴¹ b) MoS_2 ,⁴² c) orthorhombic MoO_3 ,⁴³ and d) birnessite MnO_2 .⁴⁴

A more comprehensive compilation of 2D transition metal oxides and sulfides' performances are displayed in **Table 5.2**. Compared to Chevrel phases and Prussian Blue analogues, these materials generally have higher operating voltage and can achieve higher specific capacities when the structures are tuned properly. Introduction of water to the structure or electrolyte, doping with anions with less ionicity, and nanosizing are proved to effectively increase the specific capacity. Both the oxides and sulfides suffer from structural instability.³⁶ While in the oxides the electrostatic interaction is too strong, in the sulfides the weak metal-sulfide bonds are susceptible to structural damage during electrochemical cycling.

Table 5.2. A compilation of the operating voltage, specific capacity, and quantitative cycle life of orthorhombic V₂O₅, MoS₂, orthorhombic MoO₃, and birnessite MnO₂.

	V ₂ O ₅	MoS ₂	MoO ₃	birnessite MnO ₂
Voltage (V vs. Mg/Mg ²⁺)	1.70-3.2	1.5-2.2	1.1-2.8	1.4-4.2
Specific capacity (mAh g ⁻¹)	40-420	2-213	143-400	109
Cycle life	≤35	≤50	≤10	≤25
References	16, 17, 18,27	32, 33, 182	18, 19, 20,34	180

Structural water as a strategy for improvements

One intriguing strategy for improving the electrochemical intercalation of Mg²⁺ into oxides is to utilize interlayer structural water, as was first demonstrated by Novák, et al. with hydrated vanadium bronzes.¹⁰³ It was found that structural water was necessary for high Mg²⁺ capacity in

these materials. Similar results were obtained with the electrochemical cycling of birnessite (δ) MnO_2 and amorphous MnO_2 in non-aqueous Mg^{2+} electrolytes that also contained water.^{101,183} The hypothesis driving this concept is that the structural water will provide a ‘shield’ between the diffusing Mg^{2+} cation and the host structure, thus minimizing their Coulombic interactions and leading to lower activation energies for diffusion. In addition, first principles calculations using density functional theory found that in V_2O_5 xerogels, the co-intercalation of water from the electrolyte can increase the voltage by ~ 150 mV as compared to a dry electrolyte.¹⁸⁴ The concept of utilizing structural water is a very intriguing way to tune materials for multivalent energy storage. Thus far, only the behavior of interlayer structural water has been examined. Moreover, in the case of birnessite MnO_2 and V_2O_5 , the interlayer water can be present over a wide composition range¹⁸⁵ and can include the presence of other cations during synthesis, such as K^+ .¹⁸⁶ To understand the role of structural water on Mg^{2+} storage in transition metal oxides, it is beneficial to consider the behavior of crystalline transition metal oxides containing well-defined structural water. One such family of oxides is based on WO_3 , which has two related hydrated and layered crystalline phases, $\text{WO}_3 \cdot \text{H}_2\text{O}$ and $\text{WO}_3 \cdot 2\text{H}_2\text{O}$.

Chapter 6: Electrochemical Mg²⁺ Insertion in WO₃ and WO₃·H₂O

6.1 Introduction

The room-temperature polymorph of WO₃ is the monoclinic (γ) phase, which consists of a distorted ReO₃ structure of corner-sharing WO₆ octahedra.¹⁸⁷ The layered hydrated crystalline phases also contain corner-sharing octahedra, but these are composed of layers of WO₅(H₂O) in WO₃·H₂O, where the water is bound directly to the tungsten through a primary bond; in the case of WO₃·2H₂O, a second type of structural water molecule is located in the interlayer and the water is bound to the oxygen through a secondary bond.¹⁸⁸ The crystal structures of these three phases (WO₃ and WO₃· n H₂O, $n = 1, 2$) are shown in **Figure 6.1**. For a 1 e^- redox, the theoretical gravimetric capacity of WO₃, WO₃·H₂O and WO₃·2H₂O is, respectively, 116, 107, and 100 mAh g⁻¹. Relatively little has been reported on the electrochemical behavior of crystalline WO₃ with Mg²⁺ despite the fact that WO₃ has been shown to intercalate many different monovalent cations, such as H⁺, Li⁺, and Na⁺.¹⁸⁹ Recently, multivalent storage of Ca²⁺ in WO₃ has been studied by high-resolution transmission electron microscopy (HR-TEM).¹⁹⁰ The first report of Mg²⁺ insertion into WO₃ was in 1978 when an amorphous WO₃ thin film was intercalated with Mg²⁺ from an MgCl₂ electrolyte in a water/glycerol solvent.¹⁹¹ The thin film reportedly showed reversible electrochromism, but no electrochemical cycling data was reported. Later, Gregory, et al.¹⁹ reported the formation of Mg_{0.5}WO₃ (capacity of 116 mAh g⁻¹) and an open-circuit potential of 2.16 V (vs. Mg/Mg²⁺). The capacity was calculated from chemical insertion and the electrochemical results were reported as similar, although no electrochemical cycling was shown. Later, Bruce et al.¹⁹² found that the chemical insertion of Mg²⁺ must be dependent on the Mg²⁺ precursor as in their study, the maximum Mg²⁺ content was equivalent to Mg_{0.08}WO₃ (18.5 mAh

g^{-1}). De La Cruz, et al.¹⁹³ reported the chemical insertion of Mg^{2+} into metastable hexagonal WO_3 for a maximum composition of $\text{Mg}_{0.15}\text{WO}_3$ (34.7 mAh g^{-1}).

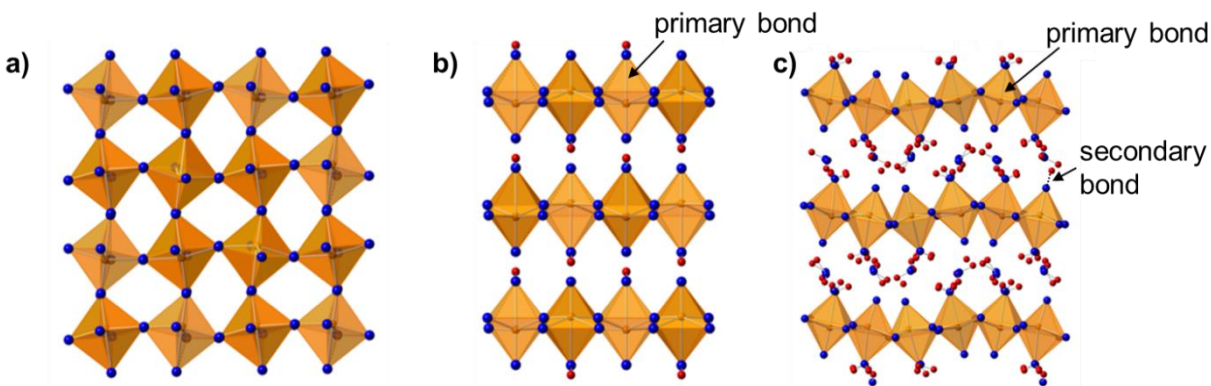


Figure 6.1. Crystal structures of a) monoclinic WO_3 , b) orthorhombic $\text{WO}_3 \cdot \text{H}_2\text{O}$, and c) monoclinic $\text{WO}_3 \cdot 2\text{H}_2\text{O}$.

Here, the electrochemical insertion of Mg^{2+} in WO_3 and $\text{WO}_3 \cdot n\text{H}_2\text{O}$ is reported in a Mg^{2+} non-aqueous electrolyte. The electrochemical behavior is correlated with ex situ Raman spectroscopy, X-ray diffraction (XRD), and energy dispersive spectrometry (EDS) to determine the type of energy storage mechanism (conversion or insertion). The kinetics of Mg^{2+} storage are compared with those for Li^+ storage in a non-aqueous electrolyte. It is found that all three phases can reversibly undergo Mg^{2+} insertion, which is evident by reversible electrochromism (blue coloration) of the electrodes and retention of the WO_3 or $\text{WO}_3 \cdot n\text{H}_2\text{O}$ structure during cycling as indicated by Raman spectroscopy. The insertion of Mg^{2+} in WO_3 was further validated by ex situ XRD and EDS. Moreover, the kinetics of Mg^{2+} storage increase while the capacity for Mg^{2+} decreases due to the presence of structural water. These results identify the electrochemical

behavior of WO_3 and its hydrated phases in a Mg^{2+} non-aqueous electrolyte, demonstrate the interaction between kinetics and available capacity in hydrated oxide phases that store ions via insertion, and the electrochemical stability of different types of structural water.

6.2 Experimental Methods

Physical Characterization

Raman spectroscopy was performed on a WITec alpha300M confocal Raman microscope with a frequency doubled Nd:YAG laser with a wavelength of 532 nm. All reported spectra were calibrated with a silicon wafer to match its characteristic peak at 520 cm^{-1} . Ex situ XRD of the WO_3 slurry electrodes was measured on a PANalytical Empyrean diffractometer with Cu $K\alpha$ radiation ($\lambda = 1.54 \text{ \AA}$). EDS and high-angle annular dark field (HAADF) imaging were performed on a probe aberration-corrected FEI Titan 80-300 scanning transmission electron microscope (STEM) equipped with a SuperX EDS system. Scanning electron microscopy (SEM) of thin film electrodes before and after electrochemical cycling was performed on a field emission FEI Verios 460L. Ex situ characterization of materials intercalated with Mg^{2+} required that the materials were protected from the ambient atmosphere. For ex situ Raman spectroscopy, the electrodes were encapsulated in a glass container and sealed with vacuum grease inside an argon filled glovebox. The ex situ XRD and STEM samples were prepared in the glovebox and kept in a sealed argon-filled jar until the moment of transfer into the instruments. During ex situ XRD measurement, the magnesiated WO_3 electrode was kept in a nitrogen environment in an Anton Paar XRK 900 chamber.

Electrode Preparation

Both slurry and thin-film electrodes were utilized for electrochemical characterization. The slurry electrodes consisted of 80 wt.% active material, 10 wt.% acetylene black (Alfa Aesar), and

10 wt.% polyvinylidene fluoride (PVDF, Arkema Kynar[®] KV 900). The powders were mixed with *n*-methyl-2-pyrrolidone (NMP) and cast onto a stainless steel foil current collector with a mass loading of $\sim 1 \text{ mg cm}^{-2}$. The thin-film electrodes were fabricated by drop-casting the WO_3 and $\text{WO}_3 \cdot n\text{H}_2\text{O}$ from ethanol solutions (5 mg mL^{-1}) onto a 1 cm^2 area of an air plasma-cleaned stainless steel foil current collector with a mass loading of $\sim 100 \text{ } \mu\text{g cm}^{-2}$. Electrodes were heated at $120 \text{ }^\circ\text{C}$ (WO_3 and $\text{WO}_3 \cdot \text{H}_2\text{O}$) or $50 \text{ }^\circ\text{C}$ ($\text{WO}_3 \cdot 2\text{H}_2\text{O}$) before transfer into the glovebox.

Electrochemical Characterization:

Three-electrode cyclic voltammetry was utilized to characterize the energy storage behavior of WO_3 and $\text{WO}_3 \cdot n\text{H}_2\text{O}$. The electrochemical cell consisted of an activated carbon counter electrode, a polished Ag wire as the pseudoreference electrode (Alfa Aesar, 99.999%), and either a thin film or slurry working electrode as described above. The electrolyte was $0.1 \text{ M Mg}(\text{ClO}_4)_2$ (Sigma Aldrich, $\geq 99.0\%$, $\leq 8\%$ water) in anhydrous acetonitrile (ACN) (Acros Organics, 99.9%). All chemicals were used as received. The potential of the working electrode vs. Mg/Mg^{2+} was determined by using ferrocene/ferrocenium (Fc/Fc^+) as an internal standard.¹⁹⁴ In these measurements, the electrolyte consisted of $\sim 0.001 \text{ M}$ ferrocene and $0.1 \text{ M Mg}(\text{ClO}_4)_2$ in ACN electrolyte at a sweep rate of 0.5 or 0.1 mV s^{-1} (**Figure 6.2** and **Table 6.1**). For the Li^+ insertion experiments, the electrochemical cell consisted of 1 M LiClO_4 in propylene carbonate (PC) electrolyte, and Li metal foils served as the counter and reference electrodes. All electrochemical experiments were performed in an argon filled glovebox with H_2O and O_2 levels of $< 1 \text{ ppm}$. Cyclic voltammetry was performed using a potentiostat (BioLogic VMP3) at sweep rates from $0.1 - 20$ (or 100 , for Li^+ electrolyte studies) mV s^{-1} . For ex situ experiments, the working electrode was cycled using linear sweep voltammetry at a 1 mV s^{-1} sweep rate.

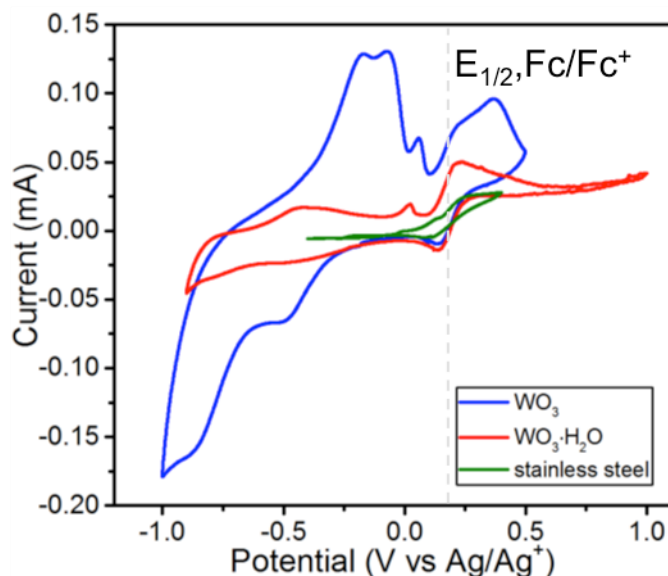


Figure 6.2. CVs at 0.5 mV s^{-1} of WO_3 , $\text{WO}_3 \cdot \text{H}_2\text{O}$, and stainless steel in a 0.001 M ferrocene and 0.1 M $\text{Mg}(\text{ClO}_4)_2$ in acetonitrile (ACN) electrolyte. The pseudoreference electrode was an Ag wire and the counter electrode was activated carbon. The dashed line indicates the half-wave potential of Fc/Fc^+ ($E_{1/2, \text{Fc}/\text{Fc}^+}$) vs. Ag/Ag^+ .

To calibrate the potential vs. Fc/Fc^+ , the half-wave potentials ($E_{1/2}$) of WO_3 (peaks 2/2' in Figure 6.5) and $\text{WO}_3 \cdot \text{H}_2\text{O}$ and $\text{WO}_3 \cdot 2\text{H}_2\text{O}$ (peaks 4/4' in Figure 6.5) were first calculated vs. Ag/Ag^+ and then this was used to convert the potential to vs. Mg/Mg^{2+} :

$$E_{1/2}(\text{vs. Fc}/\text{Fc}^+) = E_{1/2}(\text{vs. Ag}/\text{Ag}^+) - E_{1/2, \text{Fc}/\text{Fc}^+}(\text{vs. Ag}/\text{Ag}^+) \quad (6.1)$$

$$E_{1/2}(\text{vs. Mg}/\text{Mg}^{2+}) = E_{1/2}(\text{vs. Fc}/\text{Fc}^+) + E_{1/2, \text{Fc}/\text{Fc}^+}(\text{vs. Mg}/\text{Mg}^{2+}) \quad (6.2)$$

where $E_{1/2, \text{Fc}/\text{Fc}^+}(\text{vs. Mg}/\text{Mg}^{2+})$ was determined as 2.61 V in **Table 6.1**. This calibration method assumes that the half-wave potentials don't change with sweep rate and that the introduction of a small amount of ferrocene doesn't change the solvation of Mg^{2+} or block the surface of the electrode.

Table 6.1. Half-wave potentials of ferrocene/ferrocenium (Fc/Fc^+ ; $E_{1/2, \text{Fc}/\text{Fc}^+}$) measured in non-aqueous electrolytes and referenced to Mg/Mg^{2+} . To convert $E_{1/2, \text{Fc}/\text{Fc}^+}$ to its potential vs. Mg/Mg^{2+} , an average value of 2.61 V was utilized.

$E_{1/2, \text{Fc}/\text{Fc}^+}$	vs. Mg/Mg^{2+}	Electrolyte	Year	Ref
0.624 V vs. SHE	2.994	ACN	2000	1
3.42 V vs. Li/Li^+	2.745	ACN	1969	2
3.25 V vs. Li/Li^+	2.575	EC:DMC and PC	2009	3
2.5 V vs. Mg/Mg^{2+}	2.5	$\text{Mg}(\text{CB}_{11}\text{H}_{12})_2/\text{tetraglyme}$	2015	4
0.087 V vs. Ag/Ag^+	2.574	0.1 M AgNO_3 , 0.01 M TBAP, 1 M $\text{Mg}(\text{ClO}_4)_2$, ACN/Ag	2015	5
3.287 V vs. Li/Li^+	2.617	0.1 M AgNO_3 , 0.01 M TBAP, $\text{Mg}(\text{ClO}_4)_2$, ACN/Ag	2015	6
3.254 V vs. Li/Li^+	2.584	1 M $\text{LiPF}_6/1:1$ EC:EMC	2009	7
2.26 V vs. Mg/Mg^{2+}	2.26	0.5 M $\text{Mg}(\text{ClO}_4)_2/\text{ACN}$	2013	8
Average \pm Std Dev:	2.61 ± 0.19			

Abbreviations: SHE = standard hydrogen electrode, ACN = acetonitrile, EC = ethylene carbonate, DMC = dimethyl carbonate, PC = propylene carbonate, EMC = ethyl methyl carbonate, TBAP = tetrabutylammonium perchlorate

References for Table 6.1

- (1) Pavlishchuk, V.; Addison A. Conversion Constants for Redox Potentials Measured Versus Different Reference Electrodes in Acetonitrile Solutions at 25°C. *Inorg. Chim. Acta.* **2000**, 298, 97–102.
- (2) Charlot, G.; Trémillon, B. *Chemical Reactions in Solvents and Melts*; Pergamon, 1969; pp 344.

- (3) Ruch, P.; Cericola, D.; Hahn, M.; Kötz, R.; Wokaun, A. On The Use of Activated Carbon as a Quasi-Reference Electrode in Non-Aqueous Electrolyte Solutions. *J. Electroanal. Chem.* **2009**, *636*, 128–131.
- (4) Tutusaus, O.; Mohtadi, R.; Arthur, T.S.; Mizuno, F.; Nelson, E.G.; Sevryugina, Y.V. An Efficient Halogen-Free Electrolyte for Use in Rechargeable Magnesium Batteries. *Angew. Chem. – Int. Edit.* **2015**, *54*, 7900–7904.
- (5) Arthur, T.S.; Kato, K.; Germain, J.; Guo, J.; Glans, P-A.; Liu, Y.S.; Holmes, D.; Fan, X.; Mizuno, F. Amorphous V_2O_5 – P_2O_5 as High-Voltage Cathodes for Magnesium Batteries. *Chem. Commun.* **2015**, *51*, 15657–15660.
- (6) Mizuno, F.; Zhang, R.; Germain, J.; Kato, K.; Arthur, T.S. Vanadium Oxide Based Amorphous Cathode Materials for Rechargeable Magnesium Battery. U.S. Patent 20,150,132,650 A1, May 14, 2015.
- (7) Laoire, C.O.; Plichta, E.; Hendrickson, M.; Mukerjee, S.; Abraham, K.M. Electrochemical Studies of Ferrocene in a Lithium Ion Conducting Organic Carbonate Electrolyte. *Electrochim. Acta.* **2009**, *54*, 6560–6564.
- (8) Gershinsky, G.; Yoo, H.D.; Gofer, Y.; Aurbach, D. Electrochemical and spectroscopic analysis of Mg^{2+} intercalation into thin film electrodes of layered oxides: V_2O_5 and MoO_3 . *Langmuir.* **2013**, *29* (34), 10964–10972.

6.3 Results & Discussions

The WO_3 and $WO_3 \cdot nH_2O$ obtained via Freedman's method result in rectangular platelet-like particles of $\sim 100 - 200$ nm in width and ~ 20 nm in thickness (**Figure 6.3**). The platelets are oriented so that in the hydrated structures, the layers are parallel to the surface (perpendicular to

the [010] direction). The obtained materials are crystalline and phase-pure, as evident from Raman spectra (**Figure 6.4**). It should be noted that the laser power must be controlled due to the possibility for dehydration of $\text{WO}_3 \cdot 2\text{H}_2\text{O}$ and $\text{WO}_3 \cdot \text{H}_2\text{O}$ to WO_3 . The hydrated phases can be readily distinguished from the anhydrous phase by the presence of the peak associated with stretching of the terminal $\text{W}=\text{O}$ [$\nu(\text{W}=\text{O})$] at $\sim 950 \text{ cm}^{-1}$.¹⁴⁹ Moreover, $\text{WO}_3 \cdot 2\text{H}_2\text{O}$ can be distinguished from $\text{WO}_3 \cdot \text{H}_2\text{O}$ by the increased separation of the bridging oxygen stretching modes [$\nu(\text{O}-\text{W}-\text{O})$] at $\sim 660 \text{ cm}^{-1}$ and the shift of all vibration modes to slightly higher wavenumbers.¹⁵

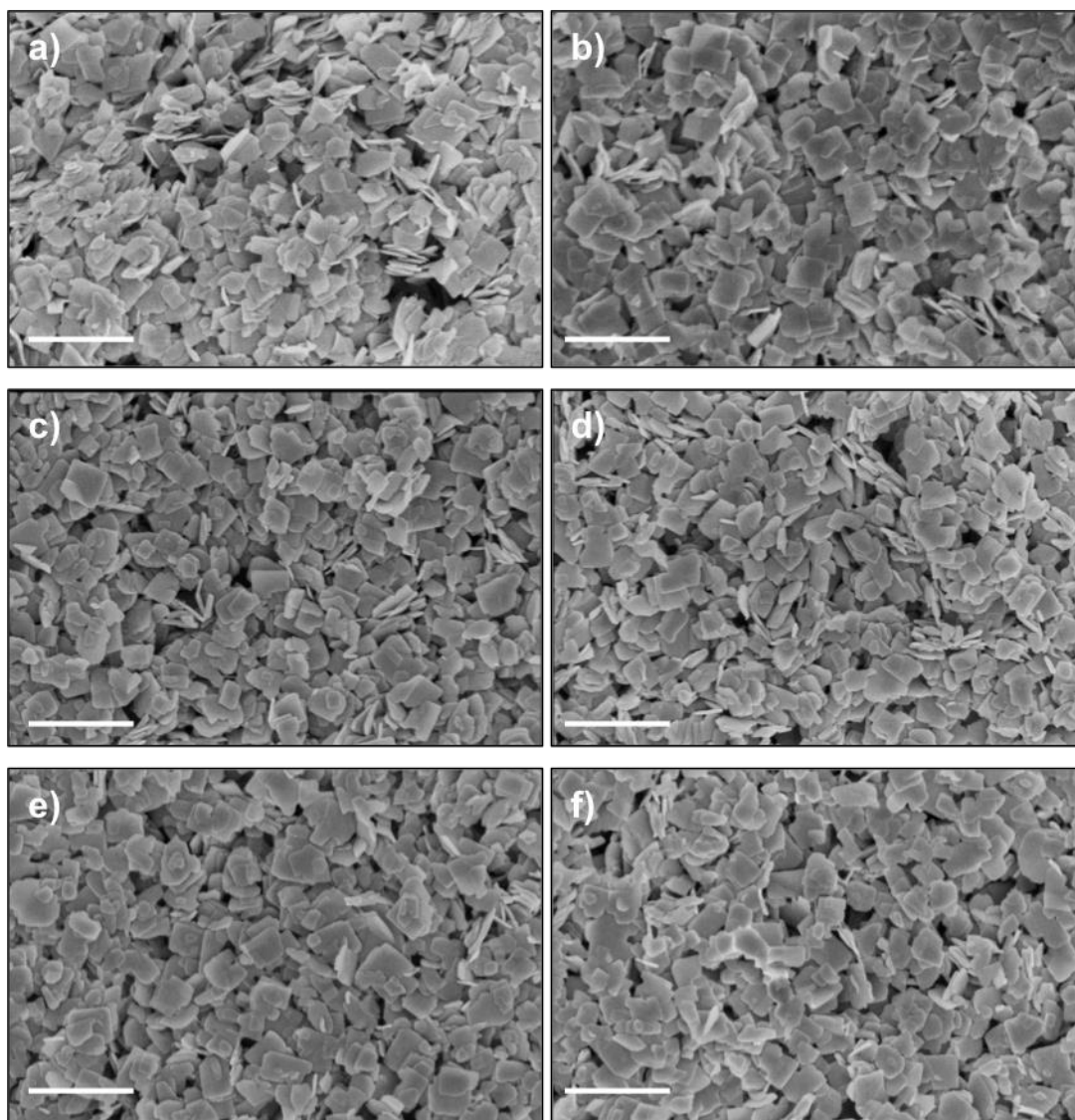


Figure 6.3. SEM micrographs of thin film electrodes before (a, c, e) and after (b, d, f) cycling in 0.1 M $\text{Mg}(\text{ClO}_4)_2$ in ACN electrolyte: a & b) WO_3 , c & d) $\text{WO}_3 \cdot \text{H}_2\text{O}$, e & f) $\text{WO}_3 \cdot 2\text{H}_2\text{O}$. The particle morphology is similar for all materials before cycling and there is no apparent change in particle morphology after electrochemical cycling. Scale bar = 500 nm. SEM micrographs courtesy of Shelby Boyd.

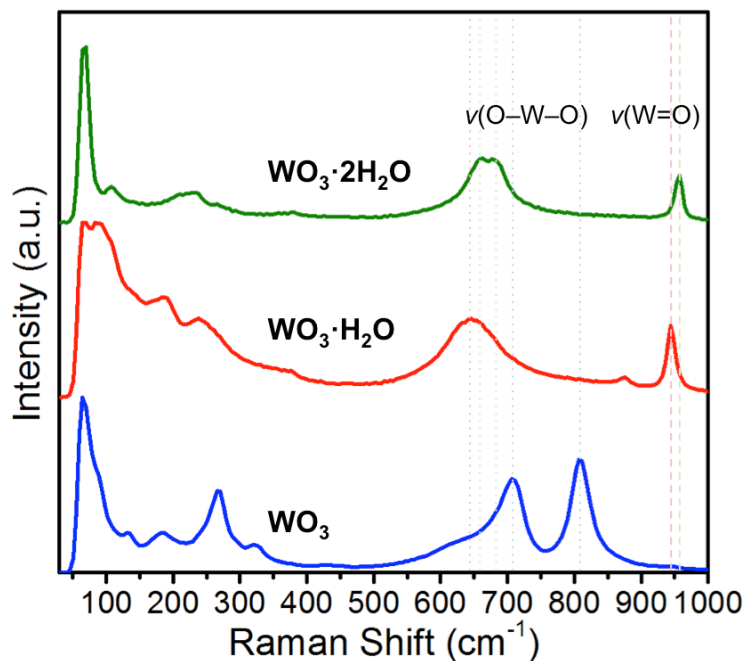


Figure 6.4. Raman spectra of the as-synthesized $\text{WO}_3 \cdot 2\text{H}_2\text{O}$, $\text{WO}_3 \cdot \text{H}_2\text{O}$, and WO_3 powders showing the phase purity of each material as highlighted by the positions of the terminal and bridging oxygen stretching modes.

The electrochemical behavior of WO_3 and $\text{WO}_3 \cdot n\text{H}_2\text{O}$ was characterized in a three-electrode cell with both thin film and slurry electrodes. The thin film electrodes are useful for identifying whether the materials exhibit electrochromism during Mg^{2+} storage. Such important visual information is hidden in slurry electrodes that utilize carbon black. Also, the thin film electrodes minimize the contributions of electrode additives such as carbon black as well as possible kinetic limitations from the inhomogeneity of the slurry architecture. In the case of Mg^{2+} storage in oxides, there are generally two mechanisms that can occur: insertion or conversion to a suboxide or metal. The competition between these two mechanisms was recently reviewed by Canepa, et al.⁵⁴ In WO_3 , the insertion reaction can be written as:



As noted above, prior research has shown that the Mg content (x) can vary between 0.08 and 0.50 depending on the method of magnesiation.^{19,192}

The complete conversion reaction of WO_3 to W^0 can be written as:



The thermodynamic potential for the conversion of WO_3 can be calculated using the Gibbs free energy at standard conditions (ΔG°) for bulk WO_3 ($-763.45 \text{ kJ mol}^{-1}$) and MgO ($-569.57 \text{ kJ mol}^{-1}$),¹⁹⁵ and the relationship between the Gibbs free energy change of the reaction, $\Delta G^\circ_{\text{rxn}}$, and the potential (E°):

$$\Delta G^\circ_{\text{rxn}} = -zFE^\circ \quad (6.5)$$

where z is the number of electrons transferred in the electrochemical reaction (here, $z = 6$) and F is the Faraday constant ($96,485 \text{ C mol}^{-1}$). Using the equation above, it is found that the thermodynamic potential for the conversion reaction of WO_3 with Mg is 1.63 V (vs. Mg/Mg²⁺). It should be noted that in the case of metal oxides undergoing a conversion reaction with Li, the actual potential is $\sim 1 \text{ V}$ lower than the thermodynamic value.¹⁹⁶ It is important to consider the energy storage mechanism of Mg²⁺ in oxides because the type of mechanism can lead to very different kinetics, cell potentials, and energy efficiencies. In the case of Mg²⁺ storage in tunnel-structured $\alpha\text{-MnO}_2$, the conversion reaction to amorphous MnO_x and MgO was shown to be highly favorable due to the structural instability induced by Mg²⁺ insertion and high thermodynamic stability of MgO .¹⁹⁷ In the layered birnessite MnO_2 with water either in the structure or electrolyte, it was found that an insertion mechanism occurs in an aqueous Mg²⁺ electrolyte but a conversion

mechanism with the formation of MnOOH, MnO, and Mg(OH)₂ was found during cycling in a non-aqueous electrolyte.¹⁹⁸ On the other hand, using Raman spectroscopy and X-ray diffraction, a Mg²⁺ intercalation mechanism in non-aqueous electrolytes was shown for thin films of the layered oxides V₂O₅ and MoO₃.¹⁸

The cyclic voltammograms (CVs) of the thin film electrodes of WO₃ and WO₃·*n*H₂O at 0.5 and 10 mV s⁻¹ (*t* = 57 min or 170 sec) are shown in **Figure 6.5**. The potential of the thin films was measured using Fc/Fc⁺ as an internal redox couple, and then converted to the potential vs. Mg/Mg²⁺ (**Figure 6.1**). It was necessary to use an internal redox couple due to the variability of the Ag pseudoreference electrode. A survey of the literature (**Table 6.1**) found that the half-wave potential of Fc/Fc⁺ can vary from 2.26 to 2.994 V vs. Mg/Mg²⁺ depending on the measurement conditions. As a result, an average value of 2.61 V was utilized; even then, it is cautioned that there is at least a 0.19 V standard deviation for the potentials reported vs. Mg/Mg²⁺.

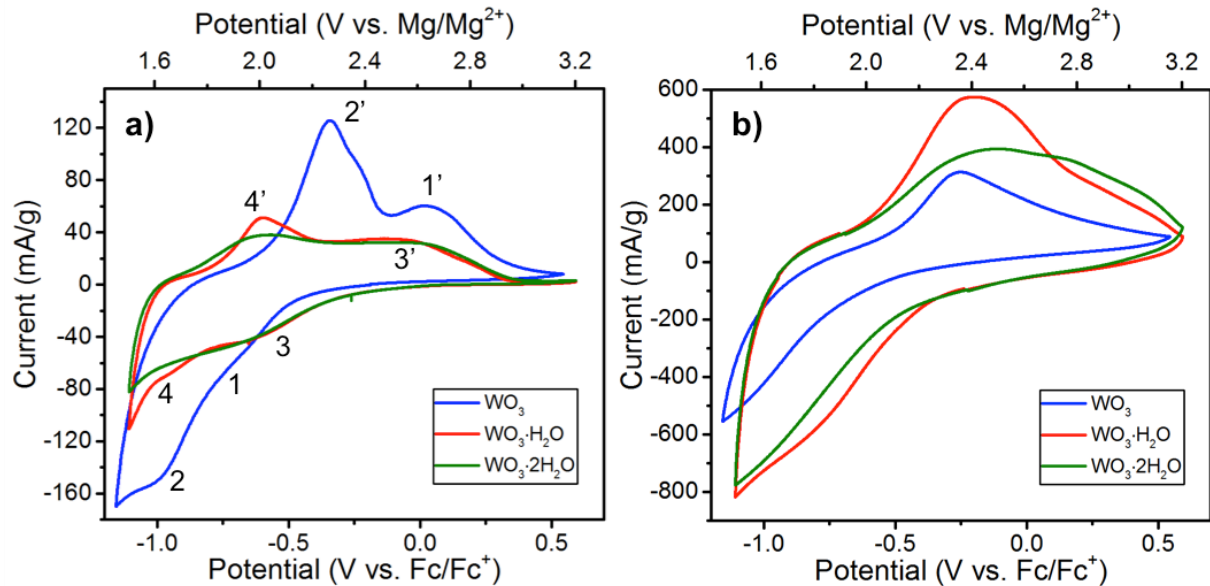


Figure 6.5. CVs of thin film electrodes of WO_3 , $\text{WO}_3 \cdot \text{H}_2\text{O}$, and $\text{WO}_3 \cdot 2\text{H}_2\text{O}$ in $0.1 \text{ Mg}(\text{ClO}_4)_2$ in ACN at a) 0.5 mV s^{-1} and b) 10 mV s^{-1} . All materials undergo reversible storage of Mg^{2+} , with the highest capacity observed in WO_3 . However, the rate capability of the hydrated phases is better, as evidence by their higher current at 10 mV s^{-1} . The numbers in (a) are the redox peak pair positions whose ΔE_{peak} is noted in the main text.

At a sweep rate of 0.5 mV s^{-1} , the electrochemical response differs based on whether the material contains structural water or not. WO_3 exhibits redox peaks that are the most well defined of the three materials. The peak voltage separation (ΔE_{peak}) for the two peaks labeled 1 and 1' is $\sim 0.68 \text{ V}$ and for 2 and 2' is $\sim 0.70 \text{ V}$. The capacity of the hydrated phases at this sweep rate is lower than that of WO_3 and the shape of the CVs of the two hydrated phases is very similar. The redox peaks are broader than in the case of WO_3 , indicating more dispersion in the Mg^{2+} energy storage potentials. ΔE_{peak} for the two peaks labeled 3 and 3' is $\sim 0.52 \text{ V}$ and for 4 and 4' is $\sim 0.39 \text{ V}$. This

indicates that the hydrated materials exhibit lower voltage hysteresis than WO_3 . The materials all exhibit charge storage between ~ 1.5 and 3.2 V vs. Mg/Mg^{2+} , which is higher than the calculated thermodynamic potential for complete conversion of WO_3 to W^0 . Cycling the materials to lower potentials (not shown) led to low Coulombic efficiency and poor reversibility; it is possible that in this potential range, the conversion reaction dominates but is not very reversible due to the electrode architecture and/or particle morphology. At 10 mV s^{-1} , all three materials exhibit increased polarization despite the thin film architecture. However, the hydrated materials now exhibit higher capacity than WO_3 . The capacity and Coulombic efficiency of the thin film electrodes are shown in **Figure 6.6**. At the slowest sweep rate measured of 0.1 mV s^{-1} , the highest capacity is obtained with WO_3 which stores 75 mAh g^{-1} ($\text{Mg}_{0.32}\text{WO}_3$) with a Coulombic efficiency of $\sim 80\%$. As the sweep rate increases, the hydrated phases exhibit better capacity retention so that by 5 mV s^{-1} , their capacity is larger than that of WO_3 . There is not a significant difference between the capacities of the two hydrated phases, although $\text{WO}_3 \cdot 2\text{H}_2\text{O}$ exhibits better Coulombic efficiency for all sweep rates tested.

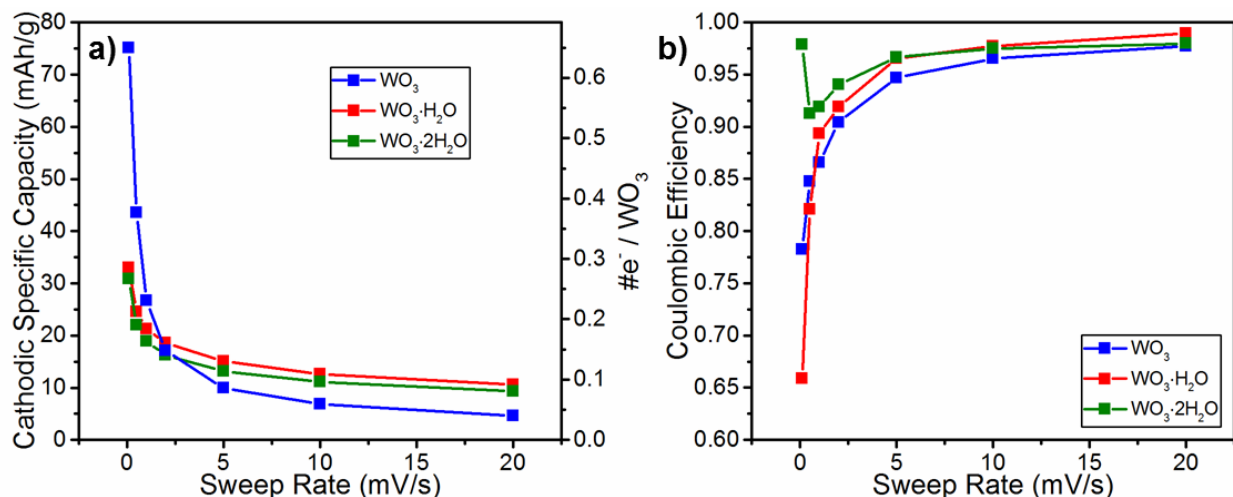


Figure 6.6. Capacity and Coulombic efficiency of Mg^{2+} storage in thin film electrodes of WO_3 , $\text{WO}_3 \cdot \text{H}_2\text{O}$, and $\text{WO}_3 \cdot 2\text{H}_2\text{O}$: a) capacity and number of e^- per WO_3 vs. sweep rate and b) Coulombic efficiency vs. sweep rate. The high capacity of WO_3 quickly declines as the sweep rate is increased above 0.1 mV s^{-1} from 75 mAh g^{-1} to less than 10 mAh g^{-1} at 20 mV s^{-1} . The Coulombic efficiency tends to improve as the sweep rate increases likely due to decreasing effects of parasitic reactions.

During electrochemical cycling, it was noted that all three thin film electrodes exhibit reversible electrochromism. The optical images of this effect are shown in the insets of **Figures 6.7, 6.8, and 6.9**. Upon magnesium storage, the thin films exhibit the characteristic blue color of lightly-doped tungsten bronzes.¹⁸⁹ The non-uniformity of the coloration is due to the inhomogeneity of the thin film electrodes, which are composed of $100 - 200 \text{ nm}$ platelet particles drop-cast from solution. The intensity of the color is correlated to the amount of stored Mg^{2+} so that WO_3 exhibits the deepest blue coloration of the three materials. Scanning electron micrographs of the thin film electrodes before and after electrochemical cycling are shown in

Figure 6.3. For all materials there are no significant changes noted in the size or morphology of the platelets.

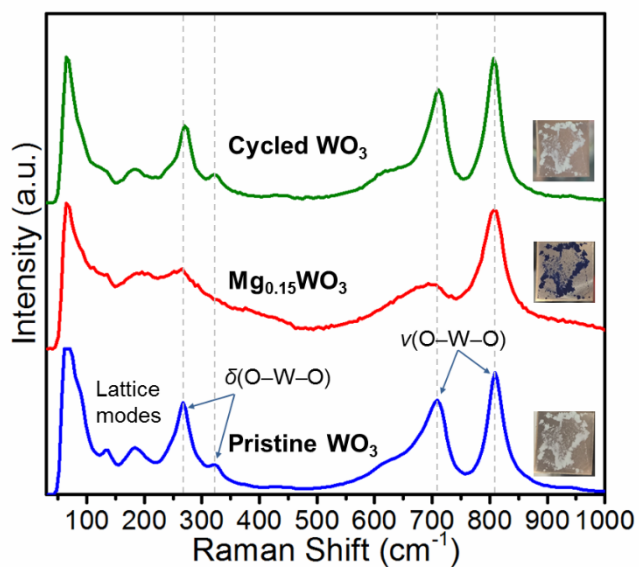


Figure 6.7. Ex situ Raman spectra of a thin film electrode of WO₃ at three different stages: as-synthesized (pristine), magnesiated, and cycled. There is no change in the structure after Mg²⁺ storage. The optical images of the thin film electrodes in the inset show the reversible electrochromism of the WO₃ with Mg²⁺.

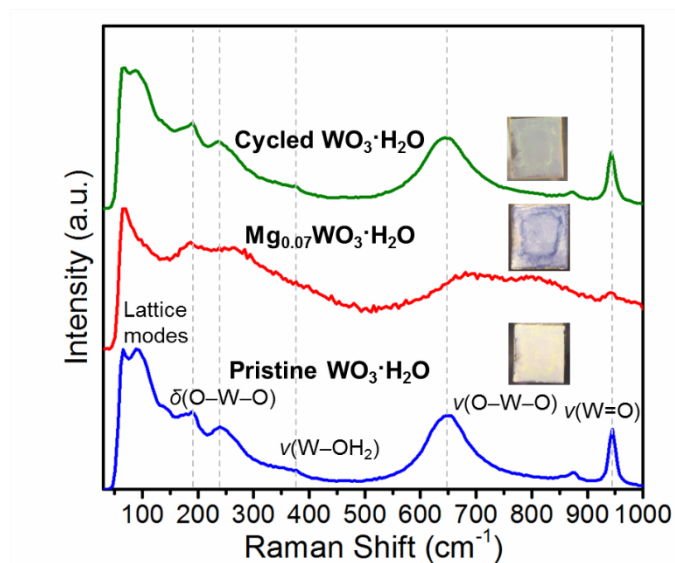


Figure 6.8. Ex situ Raman spectra of the thin film electrodes of WO₃·H₂O at three different stages: as-synthesized (pristine), magnesiated, and cycled. There is no change in the local structure after Mg²⁺ storage. The optical images of the thin film electrodes in the inset show the reversible electrochromism of the WO₃·H₂O with Mg²⁺.

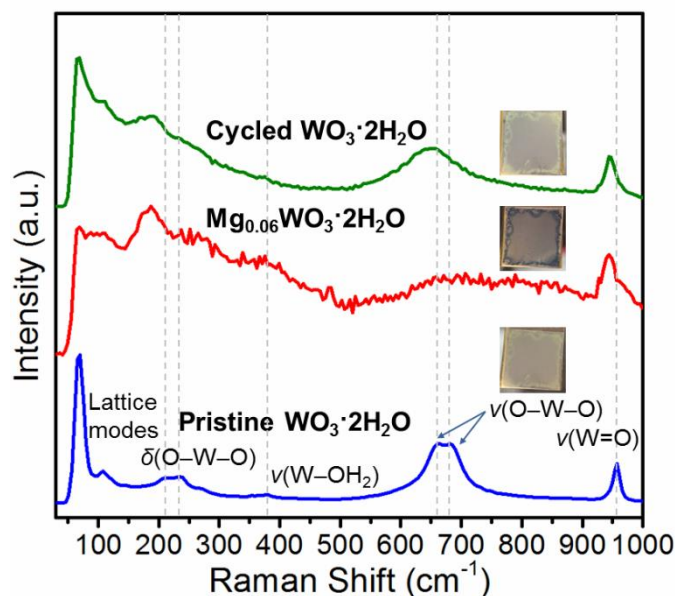


Figure 6.9. Ex situ Raman spectra of the thin film electrodes of $\text{WO}_3 \cdot 2\text{H}_2\text{O}$ at three different stages: as-synthesized (pristine), magnesiated, and cycled. After Mg^{2+} storage, the structure transforms to $\text{WO}_3 \cdot \text{H}_2\text{O}$ as indicated by the shift of the $\text{W}=\text{O}$ and $\text{O}-\text{W}-\text{O}$ stretching modes to lower wavenumbers. The optical images of the thin film electrodes in the inset show the reversible electrochromism of the $\text{WO}_3 \cdot 2\text{H}_2\text{O}$ with Mg^{2+} .

Ex situ Raman spectroscopy of the WO_3 and $\text{WO}_3 \cdot n\text{H}_2\text{O}$ thin films (Figures 6.7, 6.8, and 6.9) was performed at three stages: as-synthesized, upon Mg^{2+} storage, and after 1 cycle at 1 mV s^{-1} . As-synthesized monoclinic WO_3 (Figure 6.7) exhibits prominent bridging oxygen stretching [$\nu(\text{O}-\text{W}-\text{O})$] and bending [$\delta(\text{O}-\text{W}-\text{O})$] modes. Upon Mg^{2+} storage, these modes are still visible (most prominently, the stretching modes) but the intensity is decreased. This has been observed in other tungsten bronzes and attributed to the increased absorption of the now blue-colored particles.¹⁹⁹ Upon scan reversal back to the open-circuit potential, the Raman modes of the monoclinic WO_3 are regained with no apparent changes in peak position or the intensity ratios.

The as-synthesized $\text{WO}_3 \cdot \text{H}_2\text{O}$ (Figure 6.8) contains several prominent Raman modes from stretching of the terminal $\text{W}=\text{O}$ bond [$\nu(\text{W}=\text{O})$] and stretching and bending of the bridging oxygens. Upon Mg^{2+} storage, the intensity of the Raman spectrum becomes significantly decreased for the same reason as in WO_3 since the monohydrate also exhibits electrochromism. With sweep reversal, all Raman modes of the $\text{WO}_3 \cdot \text{H}_2\text{O}$ are regained including the terminal $\text{W}=\text{O}$ mode. This indicates that the $\text{WO}_3 \cdot \text{H}_2\text{O}$ does not lose structural water during the first cycle. Lastly, the main difference between the Raman spectrum of $\text{WO}_3 \cdot 2\text{H}_2\text{O}$ (Figure 6.9) and that of $\text{WO}_3 \cdot \text{H}_2\text{O}$ is that the bridging oxygen stretching and bending modes and the terminal $\text{W}=\text{O}$ stretch are shifted to higher wavenumbers. As in the other materials, the intensity of the Raman peaks decreases significantly upon Mg^{2+} storage in $\text{WO}_3 \cdot 2\text{H}_2\text{O}$ due to the increased absorption of the blue film. However, even at this point it is evident that the $\text{W}=\text{O}$ stretch moves to lower wavenumbers. With Mg^{2+} removal, the Raman results indicate that $\text{WO}_3 \cdot 2\text{H}_2\text{O}$ loses the interlayer structural water during cycling and forms $\text{WO}_3 \cdot \text{H}_2\text{O}$. To determine whether this change was due to electrochemical cycling or via exposure to the non-aqueous electrolyte, a $\text{WO}_3 \cdot 2\text{H}_2\text{O}$ thin film electrode was allowed to rest for 10 hours in 0.1 M $\text{Mg}(\text{ClO}_4)_2$ in ACN electrolyte. Upon removal from the electrolyte, the material showed a transformation to $\text{WO}_3 \cdot \text{H}_2\text{O}$ as determined by Raman spectroscopy (**Figure 6.10**).

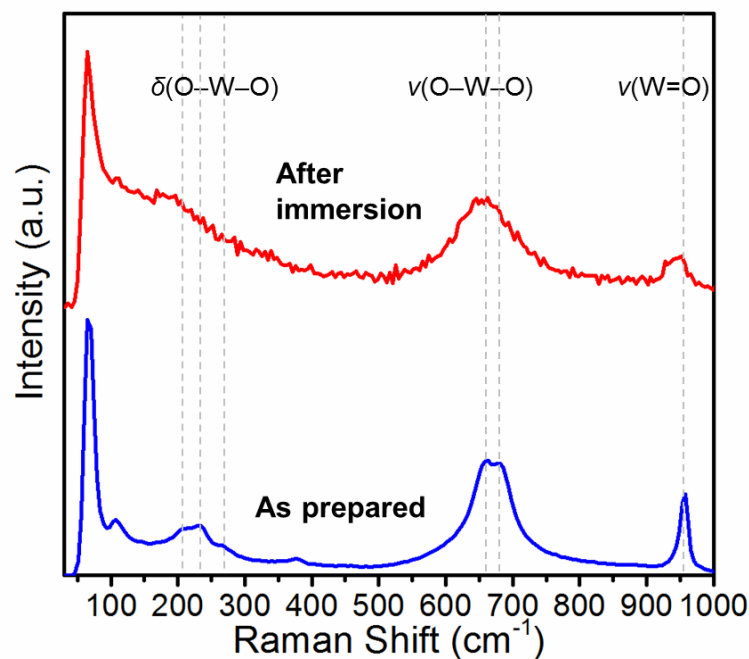


Figure 6.10. Raman spectra of a $\text{WO}_3 \cdot 2\text{H}_2\text{O}$ thin film electrode before and after immersion in 0.1 M $\text{Mg}(\text{ClO}_4)_2$ in ACN electrolyte for 10 hours. The shift of the bridging and terminal oxygen stretching and deformation modes to lower wavenumbers indicates the formation of $\text{WO}_3 \cdot \text{H}_2\text{O}$ and the removal of interlayer water from the structure.

Since WO_3 exhibited the highest amount of Mg^{2+} storage, ex situ XRD, EDS, and HAADF imaging were performed on WO_3 to give insights into the long-range order and chemical composition as a result of electrochemical cycling. The three stages of WO_3 characterized with ex situ XRD were as-synthesized, upon Mg^{2+} storage, and after 50 cycles at 0.1 mV s^{-1} . As shown in **Figure 6.11**, the XRD patterns of the slurry electrodes made of as-synthesized and cycled WO_3 match well with monoclinic WO_3 (ICDD PDF 04-005-4272) and indicate the retention of crystallinity after cycling. Upon Mg^{2+} storage, the XRD pattern corresponds to a cubic structure, which is similar to the patterns of WO_3 intercalated with H^+ , Li^+ , and Na^+ .^{200,201}

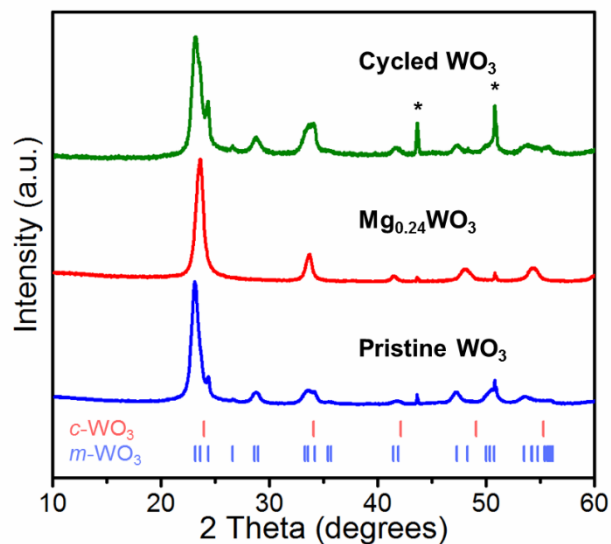


Figure 6.11. Ex situ XRD patterns of WO₃ slurry electrodes at three different stages: as-synthesized (pristine), magnesiated, and cycled. The asterisk symbol indicates the diffraction peak of the stainless steel substrate, which also served as an internal reference. The *m*-WO₃ reference pattern at the bottom corresponds to ICDD PDF 04-005-4272 (monoclinic γ -WO₃) and the *c*-WO₃ reference pattern corresponds to ICDD PDF 00-041-0905 (cubic WO₃). Ex situ XRD courtesy of Ching-Chang Chung.

The presence of Mg²⁺ in the WO₃ upon Mg²⁺ storage was determined by ex situ EDS. In **Figure 6.12b**, the Mg signal was clearly observed in WO₃ upon Mg²⁺ storage while no noticeable Mg signal is observed in the as-synthesized (Figure 6.12a) or cycled (Figure 6.12c) WO₃. A small amount of sodium was observed in the as-synthesized WO₃; the sodium may come from the Na₂WO₄ precursor used for synthesis. The Cu and C signals came from the carbon-coated Cu TEM grid. The HAADF images in Figure 6.12 support the observation from the SEM images that the particle morphology was maintained throughout cycling. The electrochromism, maintenance of particle morphology and crystallinity, and presence of Mg all point to an insertion-type energy

storage mechanism in WO_3 in non-aqueous Mg^{2+} electrolytes. Since $\text{WO}_3 \cdot \text{H}_2\text{O}$ and $\text{WO}_3 \cdot 2\text{H}_2\text{O}$ exhibit a lower capacity for Mg^{2+} along with reversible electrochromism and maintenance of morphology and crystallinity, it is thus concluded that these materials also store Mg^{2+} by an insertion mechanism.

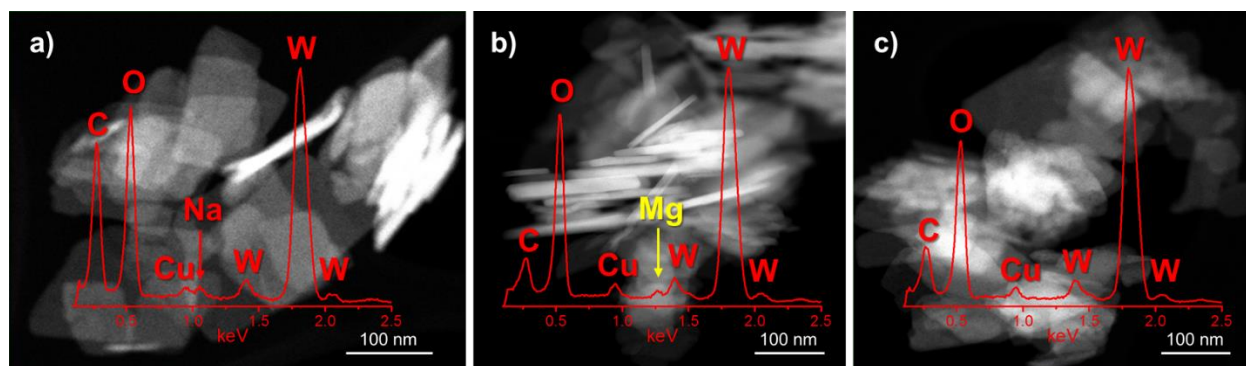


Figure 6.12. HAADF images overlaid with EDS patterns of WO_3 at three different stages: a) as-synthesized (pristine), b) magnesiated ($\text{Mg}_{0.18}\text{WO}_3$), and c) cycled. The HAADF images represent the regions where the EDS patterns were collected. The Cu and C signals came from the carbon-coated Cu TEM grids. HAADF-STEM courtesy of Yang Liu.

In order to understand the kinetics of energy storage, the electrochemical behavior of WO_3 and $\text{WO}_3 \cdot \text{H}_2\text{O}$ was compared between Mg^{2+} and Li^+ non-aqueous electrolytes. The CVs at 0.5 mV s^{-1} and cathodic capacity as a function of sweep rate for the two materials in both electrolytes are shown in **Figure 6.13**. Several interesting trends emerge from this comparison, which converts all Mg^{2+} electrolyte CVs to the Li/Li^+ reference scale. First, it is noted that the onset of insertion occurs at a potential slightly lower for Mg^{2+} than for Li^+ in WO_3 , but that the onset of insertion is approximately the same for both ions in $\text{WO}_3 \cdot \text{H}_2\text{O}$. It has previously been observed that the Mg^{2+}

insertion potential can be either the same or even higher than that for Li^+ insertion.²⁰² Second, it is observed that in both Li^+ and Mg^{2+} , the CVs become more capacitive and the hysteresis between anodic and cathodic peaks smaller due to the presence of structural water. Third, in both electrolytes, the capacity decreases with the presence of structural water suggesting that structural water limits the number of available ion storage sites. The behavior of thin films of $\text{WO}_3 \cdot n\text{H}_2\text{O}$ in LiClO_4 in PC electrolyte was reported by Livage, et al.²⁰³⁻²⁰⁶ where it was noted that as the structural water content increased, the coloration switching time decreased. Furthermore, it was also hypothesized that the adsorption of PC molecules at the surface of the hydrated oxides (as indicated by infrared spectroscopy) could lead to easier diffusion of Li^+ from the electrolyte to the electrode.²⁰⁴ Similar results are obtained with Li^+ storage in WO_3 and $\text{WO}_3 \cdot \text{H}_2\text{O}$ slurry-based electrodes (mass loading of $\sim 1 \text{ mg cm}^{-1}$) reported here. The rapid turnover from the cathodic to anodic sweep at 2 V in the Li^+ electrolyte for $\text{WO}_3 \cdot \text{H}_2\text{O}$ indicates very good kinetics, and the fact that no concentration gradient has developed in the interior of the electrode, unlike in the case of the anhydrous phase.

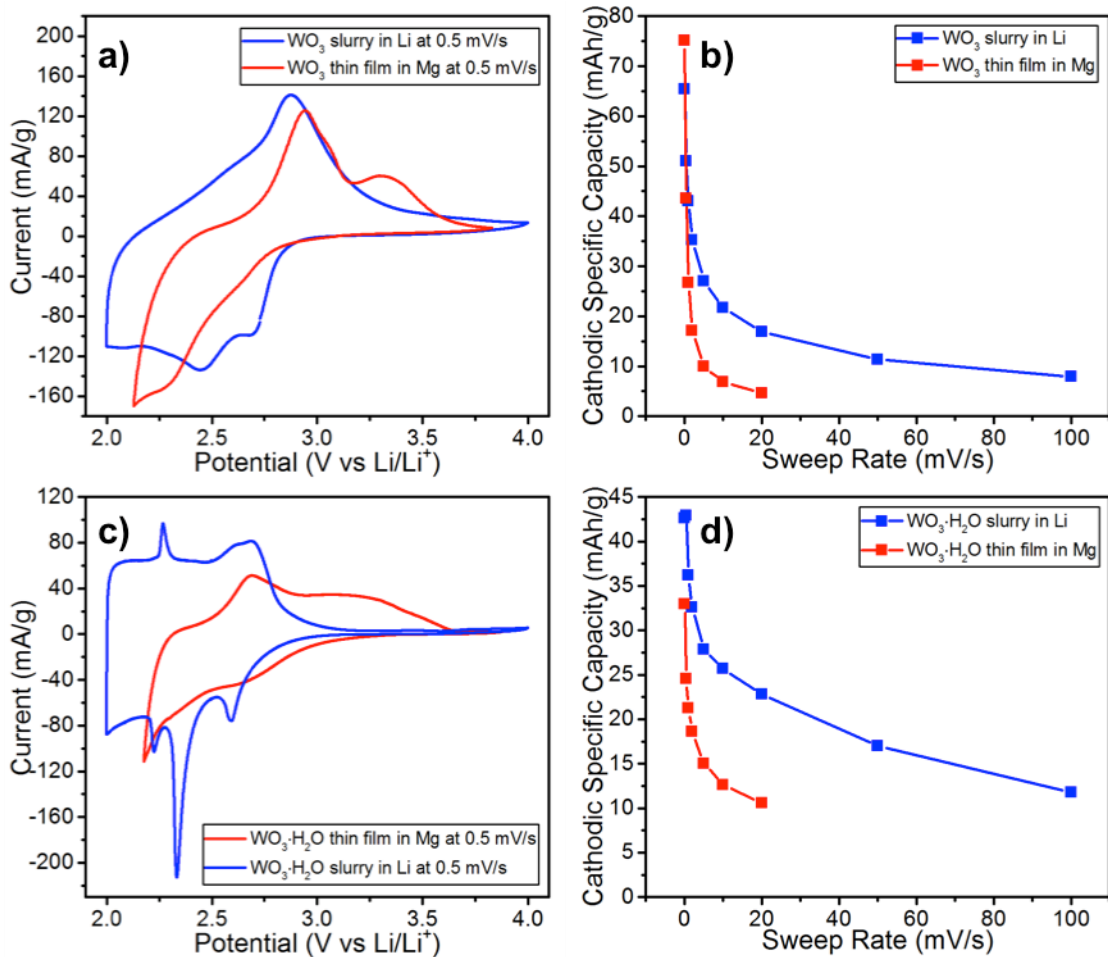


Figure 6.13. CVs at 0.5 mV s⁻¹ and the cathodic capacity of thin film and slurry electrodes cycled in non-aqueous Mg²⁺ and Li⁺ electrolytes, respectively: a, b) WO₃ and c, d) WO₃·H₂O.

The kinetics of the CVs with Mg²⁺ are generally more sluggish than with Li⁺, indicated by the peak voltage hysteresis for all materials. This follows the understanding of Mg²⁺ insertion as more kinetically hindered than Li⁺ insertion. The kinetics of ion insertion in these materials for both electrolytes can be further quantified using the relationship between the peak current, i_{peak} , and the sweep rate, v :

$$i_{peak} = av^b \quad (6.6)$$

where a and b are constants. The limiting values for b are 0.5 (semi-infinite diffusion-limited as defined by the Randles-Sevcik Equation) and 1 (interfacially limited or capacitive response).¹¹³ The results of this analysis for both Mg^{2+} and Li^+ storage are shown in **Figure 6.14**; the CVs from 0.5 to 20 mV s^{-1} used to determine the b -values are shown in **Figures 6.15** and **6.16**. In the case of WO_3 , the b -value is ~ 0.5 for both Mg^{2+} and Li^+ insertion, indicating a semi-infinite diffusion limited response of the peak anodic current. It should be noted that the quality of the linear fit in Mg^{2+} is not ideal ($r^2 = 0.9128$) likely due to the variability in peak current between cycles. On the other hand, for $\text{WO}_3 \cdot \text{H}_2\text{O}$, the b -values are 0.8 and 0.9 for, respectively, Mg^{2+} and Li^+ insertion. This suggests an insertion process that is predominantly interface-limited, or pseudocapacitive, since the charge storage occurs due to a redox reaction.

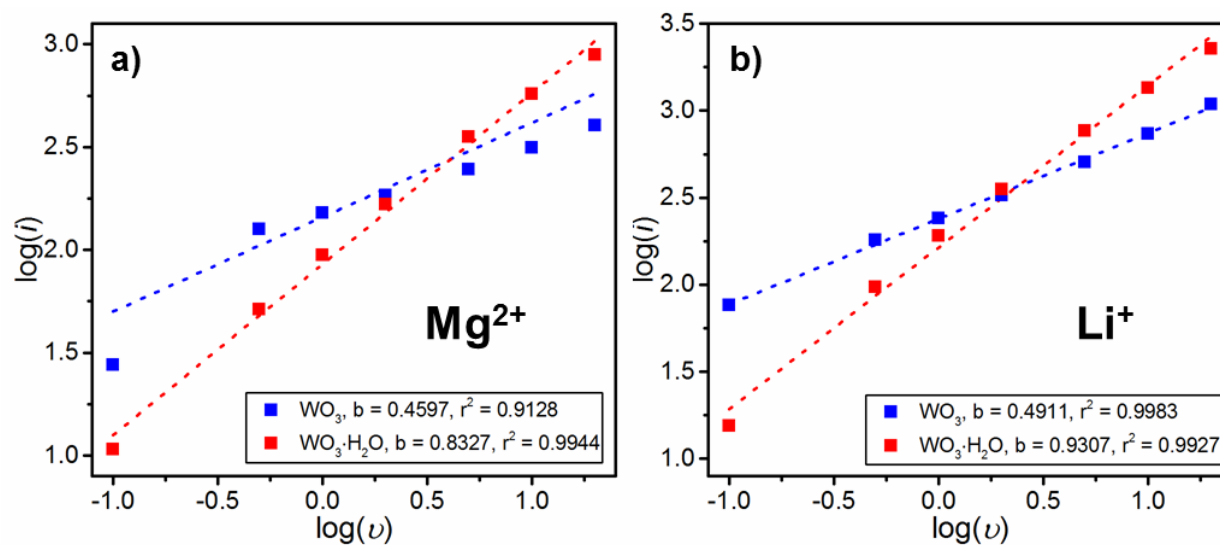


Figure 6.14. Determination of the sweep rate dependence of the anodic peak current (b value) from 0.1 to 20 mV s^{-1} for WO_3 and $\text{WO}_3 \cdot \text{H}_2\text{O}$ a) thin film electrodes in Mg^{2+} and b) slurry electrodes in Li^+ non-aqueous electrolytes. The CVs for these data points are shown in Figures 6.15 and 6.16.

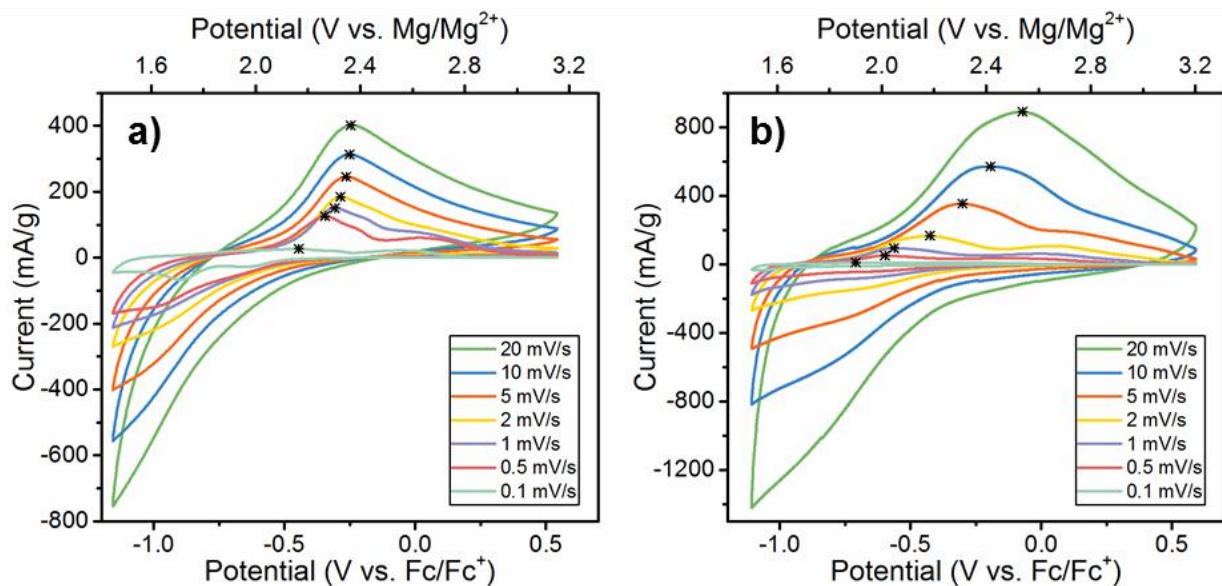


Figure 6.15. CVs from 0.1 – 20 mV s^{-1} for a) WO_3 and b) $\text{WO}_3 \cdot \text{H}_2\text{O}$ in 0.1 M $\text{Mg}(\text{ClO}_4)_2$ in ACN electrolyte. The * indicates the variation of the peak current with sweep rate utilized to determine the “ b -value” in Figure 6.14a.

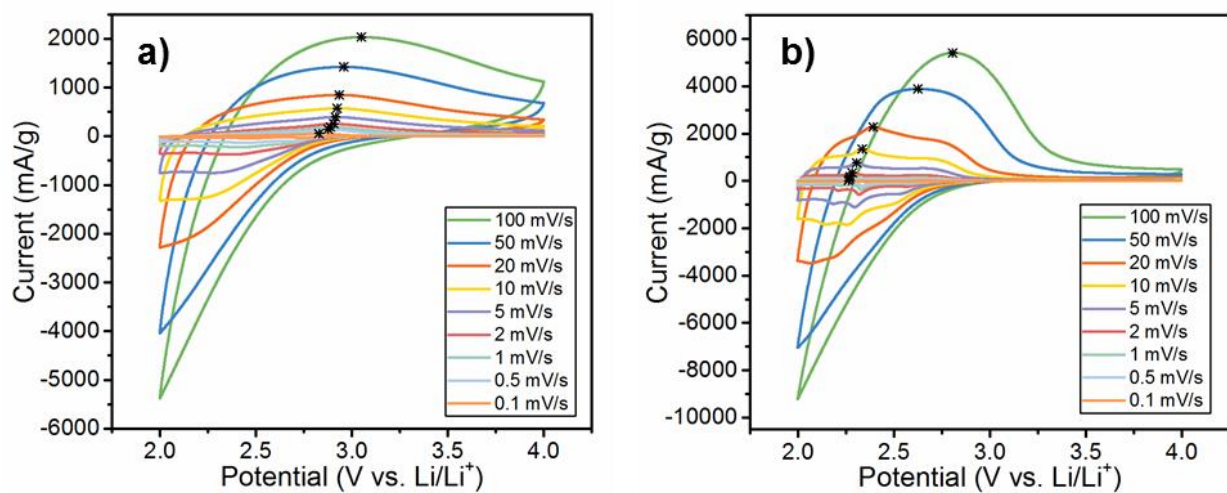


Figure 6.16. CVs from 0.1 – 100 mV s^{-1} for a) WO_3 and b) $\text{WO}_3 \cdot \text{H}_2\text{O}$ in 1 M LiClO_4 in PC electrolyte. Only anodic peaks from 0.1 – 20 mV s^{-1} were used for kinetics analysis. The * indicates the variation of the peak current with sweep rate utilized to determine the “ b -value” in Figure 6.14b.

As the highest capacity was obtained with anhydrous WO_3 , a slurry electrode of WO_3 was constructed and cycled at 0.1 mV s^{-1} for 50 cycles to determine the cycling stability at slow rates. Slurry electrodes provide a good architecture for testing long-term cycling stability by providing high porosity and a binder to keep the active material on the electrode. The CV and capacity (**Figure 6.17**) indicate that the material undergoes continuous variation in its response but a steady capacity of $\sim 70 \text{ mAh g}^{-1}$ (corresponding to $\sim \text{Mg}_{0.30}\text{WO}_3$) can be maintained throughout. Part of the shift in potential with cycling was due to the drift of the pseudoreference electrode with time. The sharp jump in capacity at cycle 37 was due to repositioning of the working electrode in the three-neck flask to ensure the entire area was submerged. After 50 cycles, Raman spectroscopy shows that the peaks associated with the monoclinic structure are retained. There is a slight shift to lower wavenumbers, which could indicate a lengthening of the W-O bonds after cycling.¹¹⁷ As mentioned previously, the XRD pattern of the ‘cycled’ WO_3 shown in Figure 6.11 indicates the maintenance of the monoclinic structure after 50 cycles.

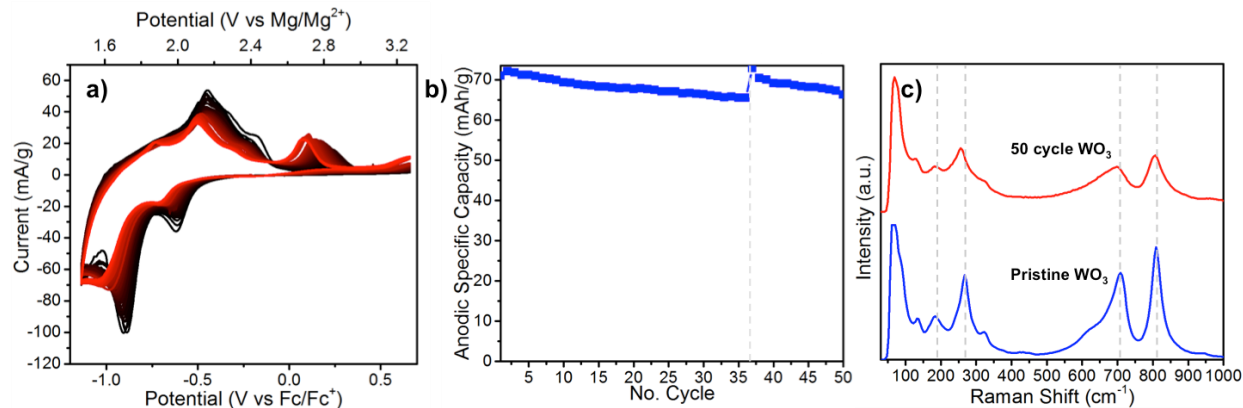


Figure 6.17. Performance of a slurry electrode of WO_3 in Mg^{2+} electrolyte: a) cyclic voltammetry at 0.1 mV s^{-1} with color gradually changing from black to red as the cycle number increases and b) capacity vs. cycle number (after cycle 36, the working electrode was adjusted to immerse the entire active area into the electrolyte), and c) Raman spectra of the electrode before and after 50 cycles at 0.1 mV s^{-1} .

Lastly, this study focused on the effect of structural water on the electrochemical behavior of $\text{WO}_3 \cdot n\text{H}_2\text{O}$ in a non-aqueous Mg^{2+} electrolyte that was used ‘as-received’. It should be noted that for mechanisms involving Mg^{2+} insertion, an interesting question under active study is the role of adsorbed water in the electrolyte. Water is typically present in commercially available magnesium perchlorate salts and can also be intentionally added to the electrolyte. As noted in the introduction, one active hypothesis is that water could be used to improve the kinetics of Mg^{2+} insertion. There is experimental and theoretical evidence for different mechanisms in these ‘wet’ electrolytes, including co-intercalation of Mg^{2+} and H_2O ^{183,184} and co-insertion of Mg^{2+} and H^+ .^{207,208} In the latter mechanism, a significant portion of the energy storage capacity has been attributed to H^+ storage particularly when the capacity is high. Future investigations of Mg^{2+} storage in WO_3 and $\text{WO}_3 \cdot \text{H}_2\text{O}$ will include the systematic variation of the water content in the

non-aqueous electrolyte to determine whether water co-insertion or protons participate in the energy storage mechanism.

6.4 Conclusions

The electrochemical storage of Mg^{2+} in thin film electrodes of crystalline WO_3 and $\text{WO}_3 \cdot n\text{H}_2\text{O}$ is based upon reversible insertion. In the 0.1 M $\text{Mg}(\text{ClO}_4)_2$ in ACN electrolyte, the maximum capacity (75 mAh g^{-1}) was obtained with anhydrous WO_3 for the storage of 0.3 Mg^{2+} or $0.6 e^-$ per WO_3 . Most of this capacity ($\sim 70 \text{ mAh g}^{-1}$) could be sustained for at least 50 cycles. The maximum capacity decreased by approximately half in $\text{WO}_3 \cdot \text{H}_2\text{O}$ and $\text{WO}_3 \cdot 2\text{H}_2\text{O}$, but the kinetics improved from a semi-infinite diffusion process to one primarily limited by the interface (pseudocapacitive). Ex situ Raman spectroscopy showed that WO_3 and $\text{WO}_3 \cdot \text{H}_2\text{O}$ maintained their structures after electrochemical cycling, but that the interlayer water of $\text{WO}_3 \cdot 2\text{H}_2\text{O}$ is removed upon exposure to the non-aqueous electrolyte which leads to a transformation to $\text{WO}_3 \cdot \text{H}_2\text{O}$. It was further shown via ex situ XRD that WO_3 undergoes a reversible phase transition (monoclinic to cubic) during Mg^{2+} storage, and ex situ EDS showed that Mg is present in the magnesiated material. For their application as cathode materials in Mg-ion batteries utilizing an Mg anode, the compatibility of WO_3 and its hydrated phases with practical magnesium electrolyte remains to be examined. In addition, the role of the electrolyte water content on the energy storage mechanism of Mg^{2+} in tungsten oxides requires further investigation (Chapter 7). These results demonstrate the possibility of utilizing tungsten oxides for multivalent energy storage based upon insertion, the effect of structural water on the kinetics of Mg^{2+} storage in these materials, and the stability of different types of structural water in non-aqueous electrolytes.

Chapter 7: Effect of Water in a Non-Aqueous Electrolyte on Electrochemical Mg²⁺

Insertion into WO₃

7.1 Introduction

One big challenge for Mg²⁺ as compared to Li⁺ insertion is the higher solvation enthalpy of the former, which leads to higher desolvation energy and thus higher charge-transfer resistance at the electrochemical interface.³⁶ One strategy for mitigating the strong host lattice/Mg²⁺ interaction and high Mg²⁺ desolvation energy is the introduction of a highly polar solvent such as water into the non-aqueous Mg electrolyte or cathode material.³⁶ The water is hypothesized to serve dual purposes: it may co-insert into the electrode with Mg²⁺ thus negating the need for desolvation, and once inside the structure, it may screen the interaction between the Mg²⁺ and the host lattice.^{101,184} This concept has been utilized for V₂O₅,^{27,184,209} VOPO₄,²¹⁰ birnessite MnO₂,^{101,183} and spinel MgMn₂O₄ cycled in non-aqueous Mg electrolytes with added water.²¹¹ While the presence of water in the non-aqueous electrolyte would lead to the surface passivation of a Mg anode,²⁰⁷ there are strategies to mitigate this problem. For example, Son, et al. developed an artificial interphase for Mg anodes that could prevent their passivation in ‘wet’ non-aqueous electrolytes.²¹²

It is important to fully understand the mechanism by which water interacts with Mg²⁺ in non-aqueous electrolytes and affects electrochemical insertion kinetics into oxides. Novák et al. investigated the electrochemical intercalation of Mg²⁺ into V₂O₅ from a Mg(ClO₄)₂ in acetonitrile (CH₃CN) electrolyte with different water contents, and found the maximum capacity at ~ 0.3 M and 1 M of water in electrolytes with 0.5 and 1 M of the Mg salt, respectively.²¹³ Sai et al. used thermodynamic modeling and first principles calculations to show that the co-intercalation of water and Mg²⁺ into a V₂O₅ xerogel (V₂O₅·nH₂O) increased the intercalation voltage and improved

intercalation kinetics due to the electrostatic shielding effect of water.¹⁸⁴ Subsequently, solid-state nuclear magnetic resonance (SS-NMR),²⁰⁷ inductively coupled plasma (ICP), and X-ray structure analysis^{208,214} suggested that a significant amount of the capacity in V_2O_5 was due to proton intercalation. Song et al. found that the maximum capacity was achieved in 0.1 M $Mg(ClO_4)_2$ in propylene carbonate with 0.6 M added water.¹⁹ Their follow-up study attributed the capacity improvement to the formation of a $Mg(OH)_2$ interphase and charge-screening of co-inserted water.²¹⁵ These studies suggest that the role of water in non-aqueous electrolytes may be more complex than originally hypothesized, affecting not only the kinetics of the insertion mechanism but also the charged species responsible for the energy storage capacity.

In the last chapter, we investigated the role of structural water in tungsten oxide on Mg^{2+} insertion from a non-aqueous Mg electrolyte, 0.1 M $Mg(ClO_4)_2$ in CH_3CN . We found that both monoclinic WO_3 and orthorhombic $WO_3 \cdot H_2O$ exhibit reversible charge storage in this electrolyte. WO_3 exhibited the highest capacity (~ 75 mAh g^{-1}) but $WO_3 \cdot H_2O$ had the best rate capability.¹⁵⁵ While this prior work indicated the participation of Mg^{2+} in the energy storage mechanism, we could not exclude the role of protons or water co-insertion. Here, we utilize WO_3 as a model insertion host to investigate how the presence of water in the non-aqueous electrolyte affects the electrochemical energy storage mechanism. To do this, we systematically varied the water concentration in 0.1 M $Mg(ClO_4)_2$ in CH_3CN and characterized the electrode and electrolyte properties with physical and electrochemical techniques. Using cyclic voltammetry, we demonstrated that the most reversible insertion kinetics were found at a water concentration of 0.6 M H_2O . Solution proton nuclear magnetic resonance (1H NMR) was used to study the solvation structure of the water in $Mg(ClO_4)_2$ in CD_3CN to probe for the presence of free protons. Ex situ X-ray diffraction (XRD), scanning electron microscopy-energy dispersive spectrometry (SEM-

EDS), X-ray photoelectron spectroscopy (XPS), and transmission electron microscopy (TEM) were used to further probe the energy storage mechanism by investigating the structure, morphology, composition, and surface of the WO_3 after reduction in electrolytes with different water contents. Our results suggest that the improvement of insertion kinetics in WO_3 are likely due to an enhancement of Mg^{2+} surface diffusion at higher water concentrations. This study provides new insights into the role of water during ion insertion in non-aqueous electrolytes.

7.2 Experimental Methods

Control of Water Concentration in the Electrolyte

The electrolytes were prepared by dissolving as-received $\text{Mg}(\text{ClO}_4)_2$ (Sigma-Aldrich, $\geq 99.1\%$, $\leq 2.5\%$ water) in CH_3CN (Acros Organics, 99.9%) or CD_3CN (Sigma-Aldrich, ≥ 99.8 atom % D). Water concentration was controlled by drying the electrolyte over molecular sieves and subsequently adding DI water in a glovebox with water and oxygen level < 0.5 ppm. Karl-Fischer titration (Mettler Toledo C20S Coulometric titrator) revealed that the as-prepared 0.1 M $\text{Mg}(\text{ClO}_4)_2$ in CH_3CN contained 900 – 1000 ppm water, of which *ca.* 200 ppm came from the as-received CH_3CN and the rest from the crystal water in the $\text{Mg}(\text{ClO}_4)_2$ salt. Note that the ppm unit used here is obtained directly from the titrator and is mass-based ($\mu\text{g g}^{-1}$). The electrolytes were dried with 3\AA molecular sieves (Sigma-Aldrich) for at least two days. The water concentration after this treatment ranged from 0.1 to 31 ppm. The addition of DI water was performed with 10 μL and 1000 μL micropipettes (Eppendorf). In a typical process, water concentrations were measured before and after the addition of 10 μL water to determine how much more was needed to achieve the targeted water ratio. The targeted water concentrations were estimated based on 2232.42 ppm per 0.1 M of water. The conversion from mg L^{-1} to $\mu\text{g g}^{-1}$ was done with the density

of the as-prepared 0.1 M $\text{Mg}(\text{ClO}_4)_2$ in CH_3CN , which was 0.81 g mL^{-1} . Water was present in the glovebox in a septum vial, and the water level of the glovebox was closely monitored during these experiments to ensure it never went above 0.5 ppm.

Physical Characterization

^1H NMR spectra of the electrolytes were collected at a regulated temperature of $24.0 \text{ }^\circ\text{C}$ on a Varian VNMR500 spectrometer using pw90, a recycle delay of 25 seconds, and 32 transients at the Center for Nanophase Materials Sciences at Oak Ridge National Laboratory. Ex situ XRD of WO_3 slurry electrodes was measured on a PANalytical Empyrean diffractometer with $\text{Cu K}\alpha$ radiation ($\lambda = 1.54 \text{ \AA}$). Ex situ EDS spectra were collected on a FEI Verios 460L field-emission scanning electron microscope with an Oxford X-Max 50 mm^2 Silicon Drift Detector. Ex situ TEM was performed on a ThermoFisher Talos F200X field-emission scanning transmission electron microscope operating at 200 kV with a SuperX EDS system. The sample for ex situ TEM was moved from a thin film WO_3 electrode on stainless steel substrate to a Lacey carbon grid by a bamboo stick. Ex situ XPS was performed on a SPECS System with a PHOIBOS 150 Analyzer. Materials for ex situ characterization were protected from the ambient atmosphere. The ex situ XRD and SEM samples were kept in a sealed argon-filled jar until the moment of transfer into the instruments. During ex situ XRD measurement, the WO_3 electrodes were kept in a nitrogen environment in an Anton Paar XRK 900 holder. The XRD single-peak fitting was performed with the Line-Profile Analysis Software (LIPRAS).⁴⁶ Electron trajectories were simulated with the CASINO software package.²¹⁶

Electrode Preparation

Both slurry and thin-film electrodes were utilized for electrochemical characterization. The slurry electrodes consisted of 80 wt.% WO_3 , 10 wt.% acetylene black (Alfa Aesar), and 10 wt.%

polyvinylidene fluoride (PVDF, Arkema Kynar[®] KV 900). The powders were mixed with *n*-methyl-2-pyrrolidone (NMP, Sigma-Aldrich) and cast onto a stainless steel foil (304 steel, 0.1 mm thick, Fisher) current collector with a mass loading of $\sim 1 \text{ mg cm}^{-2}$. The thin-film electrodes were fabricated by drop-casting the WO_3 and $\text{WO}_3 \cdot \text{H}_2\text{O}$ powders from ethanol solutions (5 mg mL^{-1}) onto a 1 cm^2 area of an air plasma-cleaned stainless steel foil or gold-plate glass current collector. Details about the electrodes for each ex situ physical characterization are shown in **Figure 7.1**.

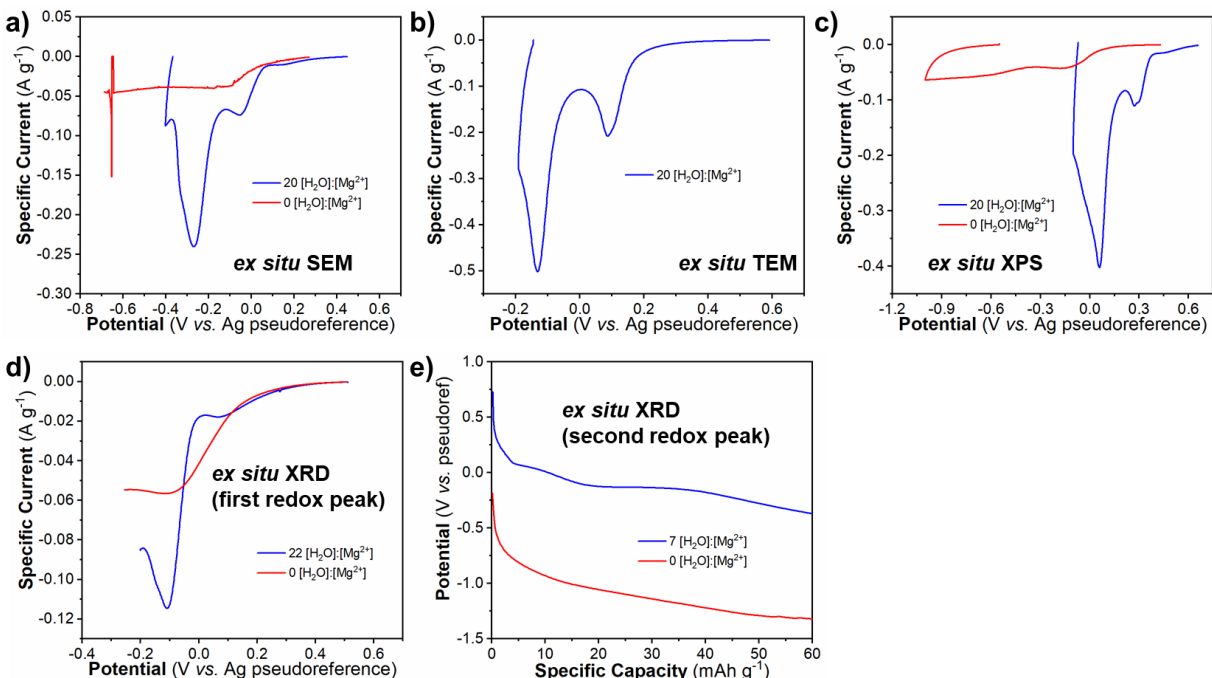


Figure 7.1. CVs at 0.5 mV s^{-1} and galvanostatic discharge curves at 1C of WO_3 electrodes in $0.1 \text{ M Mg}(\text{ClO}_4)_2$ in CH_3CN with various water concentrations for ex situ physical characterization. a) CVs of 5 mg cm^{-2} electrodes on stainless steel substrates for ex situ SEM, b) CV of a $100 \mu\text{g cm}^{-2}$ thin film electrode for ex situ TEM, c) CVs of $200 \mu\text{g cm}^{-2}$ electrodes on gold-plated glass substrate for ex situ XPS, d) CVs of slurry electrodes (mass between 1 and 3 mg cm^{-2}) on stainless steel substrates cycled just below the first redox for ex situ XRD, and e) galvanostatic discharge curves of slurry electrodes (mass between 1 and 3 mg cm^{-2}) on stainless steel substrates to obtain 60 mAh g^{-1} in both electrodes, which is equivalent to cycling beyond the second redox peak in cyclic voltammetry. Note that the potential ranges in the CVs shifted from one to another. This was caused by the potential shift of the Ag pseudoreference electrode.

Electrochemical Characterization

Three-electrode cyclic voltammetry was used to characterize the energy storage behavior of WO_3 and $\text{WO}_3 \cdot \text{H}_2\text{O}$. The electrochemical cell consisted of a glass 50 mL three-neck flask, an activated carbon counter electrode, a polished Ag wire as the pseudoreference electrode (Alfa Aesar, 99.999%), and either a thin film or slurry working electrode as described above. The electrolyte was 0.1 M $\text{Mg}(\text{ClO}_4)_2$ in CH_3CN with various water concentrations. All electrochemical experiments were performed in an argon filled glovebox with H_2O and O_2 levels of < 0.5 ppm. Cyclic voltammetry was performed using a potentiostat (BioLogic VMP3) at sweep rates from 0.1 – 100 mV s^{-1} . For most ex situ physical characterization except the tetragonal to cubic phase transformation in ex situ XRD, the working electrode was cycled using linear sweep voltammetry at a 0.5 mV s^{-1} sweep rate. For the tetragonal to cubic phase transformation in ex situ XRD, a galvanostatic discharge test was used at a 1C discharge rate to cycle electrodes to 60 mAh g^{-1} . All electrochemical characterizations for the ex situ physical characterizations are shown in Figure 7.1 with detailed mass and condition of the electrodes.

7.3 Results & Discussions

To probe the effects of water in 0.1 M $\text{Mg}(\text{ClO}_4)_2$ in CH_3CN on the electrochemical insertion behavior of WO_3 , we added water to the electrolyte, measured water concentration with Karl-Fischer titration, and performed cyclic voltammetry. The resulting cyclic voltammograms (CVs) are shown in **Figure 7.2**. The water concentration is presented as a ratio of H_2O to Mg^{2+} because the electrochemical response was previously correlated with the number of water molecules solvating Mg^{2+} .^{213,217} Upon cathodic polarization (reduction), the WO_3 electrodes underwent a color change from pale yellow to blue (**Figure 7.3**). The color change was reversible

upon anodic polarization (oxidation). These optical changes are similar to those observed for Na_xWO_3 and are indicative of the successful electrochemical reduction of the WO_3 due to ion insertion.¹⁸⁹ To quantify the change in electrochemical response, we calculated the redox peak voltage separation (ΔE_p) between cathodic peak 2 and anodic peak 2'. At 1 mV s^{-1} , ΔE_p decreased from 1.4 V at “0 water” to 0.3 V at $\sim 6 [\text{H}_2\text{O}]:[\text{Mg}^{2+}]$. The width of cathodic peaks 1 and 2 also decreased between “0 water” and $\sim 6 [\text{H}_2\text{O}]:[\text{Mg}^{2+}]$. Beyond $6 [\text{H}_2\text{O}]:[\text{Mg}^{2+}]$, both ΔE_p and peak width remained similar, with ΔE_p showing a slight increase to 0.4 V at $\sim 19 [\text{H}_2\text{O}]:[\text{Mg}^{2+}]$. A smaller ΔE_p indicates faster kinetics of the electrochemical reaction.²¹⁸ Therefore, the addition of moderate amounts of water to the non-aqueous electrolyte appears to have a positive impact on the insertion kinetics, with the optimal effect at $\sim 6 [\text{H}_2\text{O}]:[\text{Mg}^{2+}]$. Above $\sim 1 [\text{H}_2\text{O}]:[\text{Mg}^{2+}]$, an irreversible current wave appeared at the cathodic turnover potential. The improvement of insertion kinetics is also shown in $\text{WO}_3 \cdot \text{H}_2\text{O}$ (**Figure 7.4**). Since the capacity of WO_3 is higher, further investigation into the mechanism of kinetic improvement focused only on WO_3 .

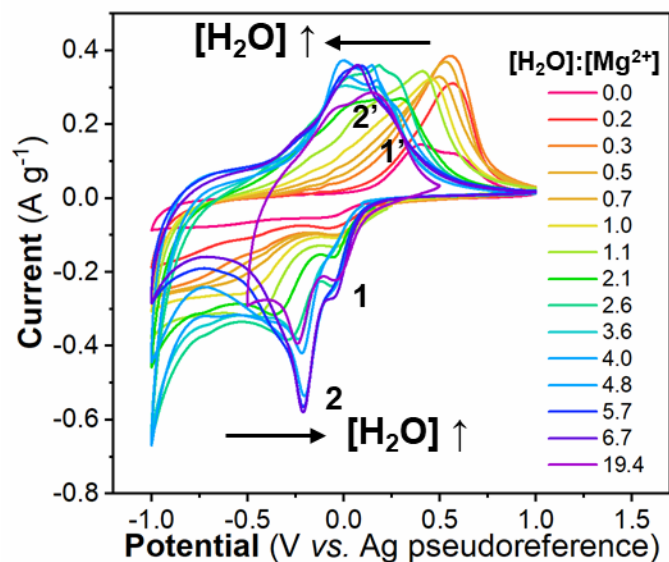


Figure 7.2. Cyclic voltammograms of WO_3 in $0.1 \text{ M Mg}(\text{ClO}_4)_2$ in CH_3CN with various added water concentrations in the electrolyte at a sweep rate of 1 mV s^{-1} . Arrows indicate the direction of redox peak shift with increased water concentration. 1/1' and 2/2' represent two sets of redox peaks associated with the energy storage process in WO_3 . A fresh WO_3 electrode was used for each water concentration.

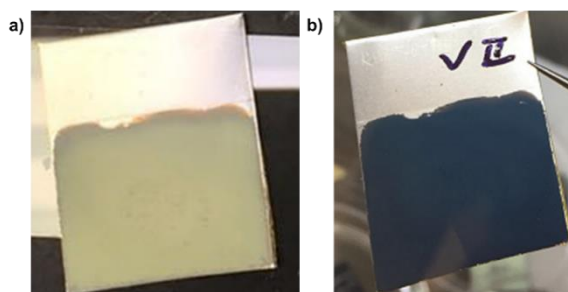


Figure 7.3. Photographs of 25 mg WO_3 dropcast on $2.5 \text{ cm} \times 3 \text{ cm}$ stainless steel substrate in the a) pristine state and b) after reduction in $0.1 \text{ M Mg}(\text{ClO}_4)_2$ in CH_3CN with $0 \text{ [H}_2\text{O]:[Mg}^{2+}]$ at 20 mV s^{-1} .

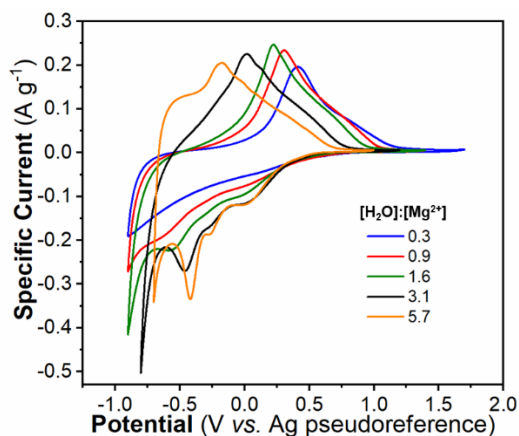


Figure 7.4. CVs of $\text{WO}_3 \cdot \text{H}_2\text{O}$ at 1 mV s^{-1} in $0.1 \text{ M Mg}(\text{ClO}_4)_2$ in CH_3CN with various added concentrations of water.

We quantified the rate performance of WO_3 by tracking the anodic specific capacity at selected water concentrations as a function of sweep rate, shown in **Figure 7.5**. The anodic specific capacity was selected because the CVs indicate no irreversible oxidative processes that would overestimate the capacity calculations. At a sweep rate of 0.1 mV s^{-1} , all electrodes showed specific capacities from $\sim 60 - 80 \text{ mAh g}^{-1}$ ($\sim 0.5 - 0.7 e^-$ per WO_3) indicating that the energy storage process does not involve multivalent redox. The variation in capacity is attributed to side reactions as shown in the CV comparisons in **Figure 7.6**. Like the trend of ΔE_p and peak width, the rate performance of WO_3 is dependent on water concentration. At 100 mV s^{-1} , the rate capability increased with water concentration up to 21% at $\sim 6 [\text{H}_2\text{O}]:[\text{Mg}^{2+}]$, and then decreased with the addition of more water. Surprisingly, WO_3 had similarly poor performance at 100 mV s^{-1} in the electrolytes with 0 and $\sim 19 [\text{H}_2\text{O}]:[\text{Mg}^{2+}]$, retaining $\sim 2 - 3\%$ of the initial capacity at 0.1 mV s^{-1} . The performance in the dry electrolyte agrees with the slow kinetics indicated by the large ΔE_p . However, while ΔE_p was similar at ~ 6 and $\sim 19 [\text{H}_2\text{O}]:[\text{Mg}^{2+}]$, the rate performance degraded more significantly at higher water concentration. Comparison of the CVs in $19 [\text{H}_2\text{O}]:[\text{Mg}^{2+}]$

electrolyte at 1 mV s^{-1} in Figure 7.2 and at 0.1 and 0.5 mV s^{-1} in **Figure 7.6f** shows that prior electrochemical cycling at slow rates affects ΔE_p . Cycling at 0.1 mV s^{-1} leads to a wider ΔE_p at 0.5 mV s^{-1} than what is observed at 1 mV s^{-1} , which had no prior electrochemical cycling. Therefore, we suspect that the performance degradation could be due to process(es) at slow sweep rates that impede electrochemical insertion on subsequent cycles. Overall, both ΔE_p and rate capability trends suggest that the electrochemical insertion kinetics of WO_3 improve upon the addition of water to the electrolyte up to a concentration of ~ 6 $[\text{H}_2\text{O}]:[\text{Mg}^{2+}]$.

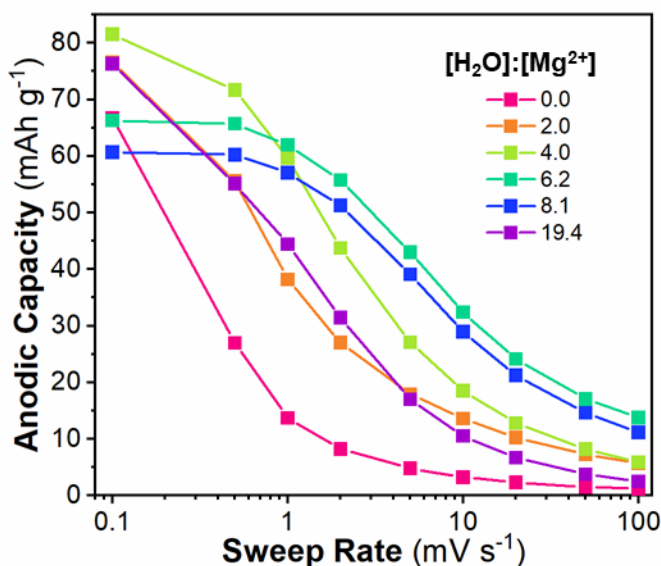


Figure 7.5. Anodic capacity as a function of sweep rate for selected cyclic voltammograms in Figure 7.2.

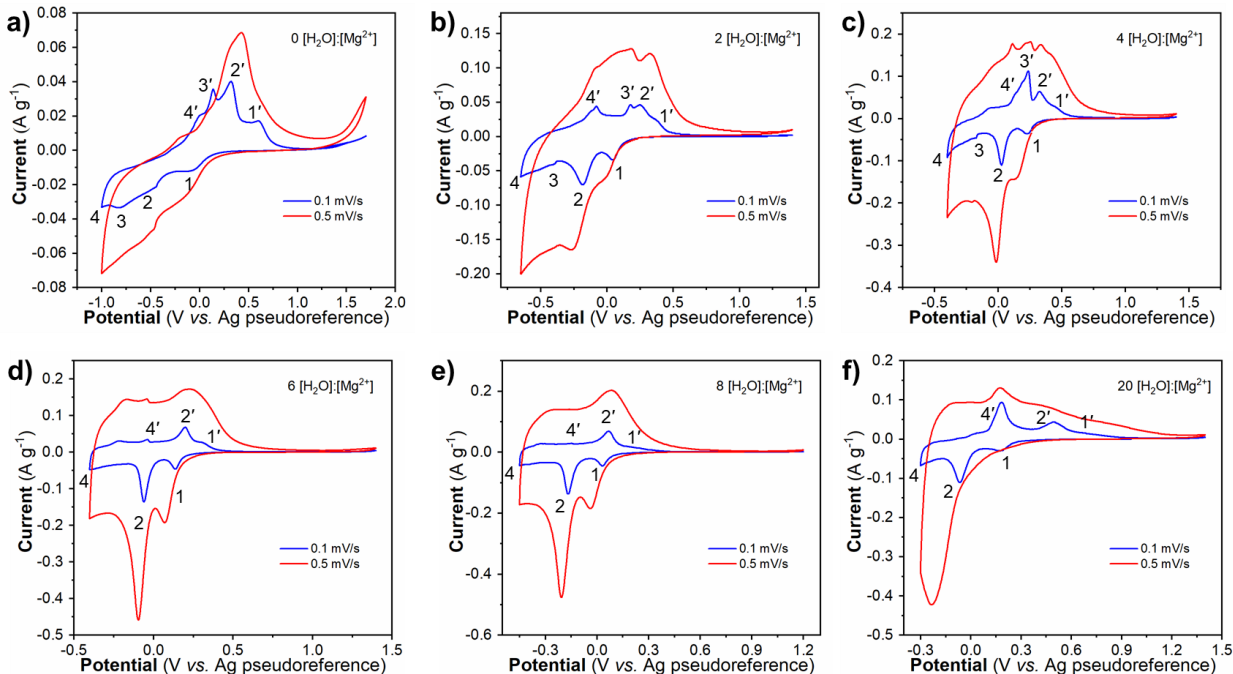


Figure 7.6. Cyclic voltammograms (CVs) of WO_3 at 0.1 and 0.5 mV s^{-1} in 0.1 M $\text{Mg}(\text{ClO}_4)_2$ in acetonitrile (CH_3CN) with various concentrations of added water for $[\text{H}_2\text{O}]:[\text{Mg}^{2+}]$ of a) 0, b) 2, c) 4, d) 6, e) 8, and f) 20. In the figures, 1/1', 2/2', 3/3', and 4/4' indicate the likely electrochemical redox couples. Each cyclic voltammetry experiment was conducted in a fresh electrolyte with a fresh WO_3 electrode.

Another way to quantify the kinetics of the energy storage mechanism is to evaluate the rate of cathodic capacity increase at 1 mV s^{-1} , which is the slope in **Figure 7.7**. The rate of capacity increase gradually rises with water concentration when it is below $2.6 [\text{H}_2\text{O}]:[\text{Mg}^{2+}]$. While the electrochemical kinetics improve at higher water concentrations, the rise in the rate of capacity increase is minor. Note that $2.6 [\text{H}_2\text{O}]:[\text{Mg}^{2+}]$ is equivalent to 0.5 % (v/v) of H_2O in the electrolyte. At such a low concentration, water will preferentially solvate Mg^{2+} ion in CH_3CN solutions.^{219,220} The cathodic capacity higher than $\sim 60 \text{ mAh g}^{-1}$ in Figure 7.7 is due to unidentified parasitic reactions.

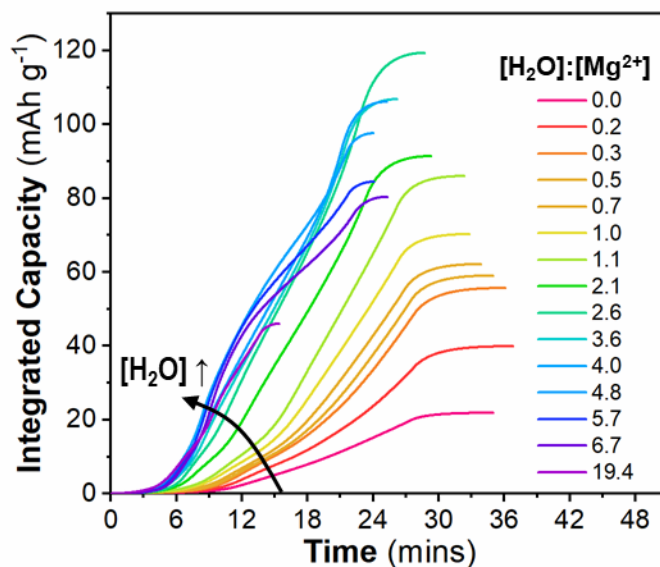
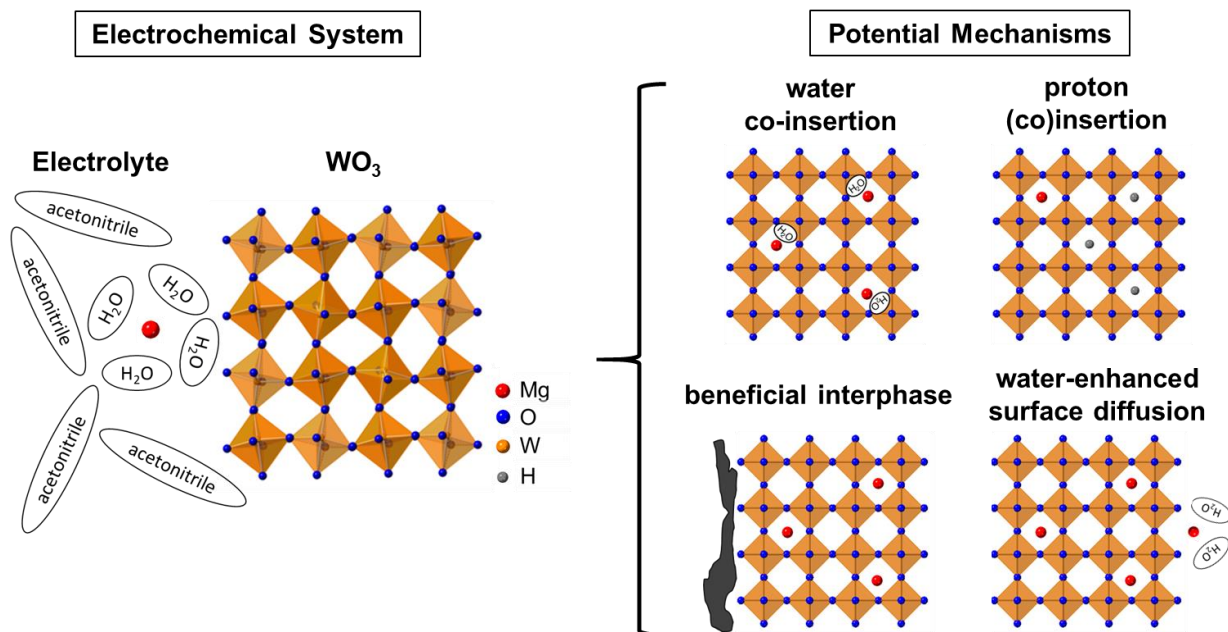


Figure 7.7. Integrated capacity of the cathodic cycle versus time calculated from the CVs in Figure 7.2.

To analyze the potential mechanisms by which water in the non-aqueous electrolyte improves electrochemical insertion kinetics, we assume that ideal ion insertion occurs as follows: solvated ions in the electrolyte will diffuse towards the electrode surface, partially desolvate, adsorb onto the surface, diffuse on the surface to an insertion site while partially solvated, and finally insert into the electrode.^{7,69,221} Several hypotheses have been proposed regarding the improvement of insertion kinetics in the presence of water in a non-aqueous Mg electrolyte. The four most likely ones are summarized in **Scheme 7.1** and listed below:



Scheme 7.1. Illustration of the electrochemical system in this study and the potential mechanisms by which water in the non-aqueous electrolyte could improve electrochemical insertion kinetics.

1. **Water co-insertion:** Mg^{2+} ions are preferentially and strongly solvated by water and carry part of the water solvation shell into the electrode. The co-inserted water is hypothesized to effectively screen the charge of Mg^{2+} ions as they diffuse through the material. Insertion kinetics are improved due to a lowered diffusion barrier.^{27,36,101,222}
2. **Proton (co)insertion:** The insertion kinetics and capacity are improved if a proton source such as water is present in the electrolyte since the insertion of H^+ is more facile than Mg^{2+} .^{207,214,223}
3. **Beneficial interphase:** The addition of water leads to the formation of a beneficial interphase on the surface of the electrode that increases insertion kinetics by decreasing the charge-transfer activation energy. For example, a $\text{Mg}(\text{OH})_2$ containing interphase could form in the presence of water in the electrolyte.²¹⁵

4. **Water-enhanced surface diffusion:** Water may lower the energy barrier of Mg^{2+} surface diffusion on WO_3 , as was demonstrated in the case of Li^+ insertion into LiFePO_4 .¹²

We investigated each of these potential mechanisms with ex situ techniques and discuss the results in the following sections.

Possibility of Water Co-insertion

We examined the possibility of water co-insertion with ex situ XRD. If the kinetic improvement was a result of water co-insertion, ex situ XRD would reveal a shift in the interplanar spacing at higher water concentrations due to the change of inserted species from Mg^{2+} to water-solvated Mg^{2+} . We controlled the electrochemical charging to obtain the same electrode state of charge in dry and wet electrolytes. Two states of charge were selected: cycled just beyond the first cathodic peak (peak 1; $e_{0.09}\text{WO}_3$, 10 mAh g^{-1}) and cycled beyond the second cathodic peak (peak 2; $e_{0.52}\text{WO}_3$, 60 mAh g^{-1}) in the CVs. Here, e represents the number of electrons stored per WO_3 . Comparison of the ex situ XRD patterns to the reference patterns (**Figure 7.8**) shows that the WO_3 goes through a monoclinic to tetragonal phase transformation upon cycling to just beyond the first cathodic peak. Cycling to beyond the second cathodic peak leads to a second phase transformation from the tetragonal to cubic structure. The insertion of Mg^{2+} into WO_3 from dry and wet electrolytes resulted in virtually the same XRD patterns at both states of charge, and thereby very similar interplanar spacings. Based on these findings, water co-insertion is unlikely to occur in this material.

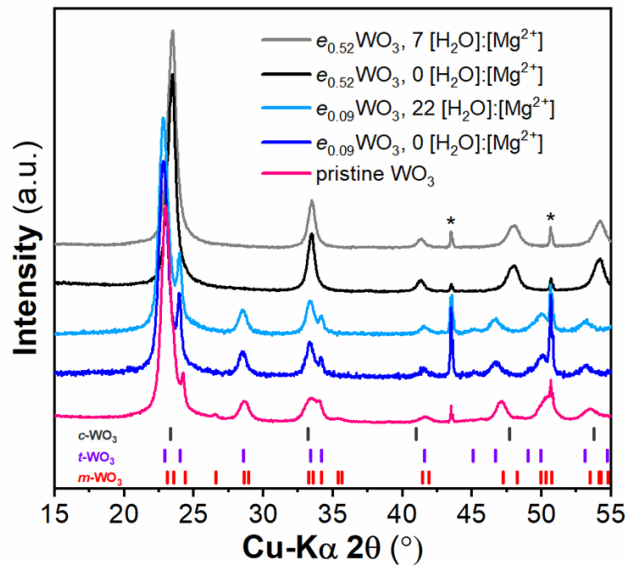


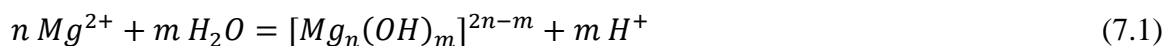
Figure 7.8. Ex situ XRD patterns of WO_3 slurry electrodes, comparing the pristine electrode to the ones reduced in electrolytes with different water concentrations. The asterisk (*) indicates peaks from the stainless-steel substrates. $m\text{-WO}_3$ reference pattern is from PDF 04-005-4272 (monoclinic $\gamma\text{-WO}_3$); $t\text{-WO}_3$ reference pattern is from PDF 00-050-1750 (tetragonal $\text{Na}_{0.1}\text{WO}_3$); the $c\text{-WO}_3$ reference pattern is from PDF 01-075-0293 (cubic $\text{Na}_{0.3}\text{WO}_3$).⁴⁵

Possibility of Proton (Co)insertion

We explored the possibility of proton (co)insertion by searching for the presence of protons in the electrolyte and in the reduced WO_3 . We investigated whether “free” protons existed in the electrolyte with proton nuclear magnetic resonance ($^1\text{H-NMR}$) and studied whether protons were in the reduced WO_3 indirectly via ex situ XRD and elemental analysis using ex situ scanning electron microscopy – energy dispersive spectrometry (ex situ SEM-EDS).

When it comes to proton (co)insertion in non-aqueous electrolytes, it is first necessary to determine the source of the protons. The literature presents two hypotheses. The first one is the

hydrolysis of water due to the presence of Mg^{2+} . Mg^{2+} is a Lewis acid with a pKa of 11.2 in aqueous solutions,²²⁴ and protons may be generated via the following equation:



The second hypothesis suggests that electrochemical side reactions of water or other hydrogen-containing solvents produce protons.²¹⁴ For example, protons were proposed to form during hydroxide formation and oxidation of surface hydroxyl groups in the presence of water.²²⁵ While the hunt for a proton source is not a trivial task, we investigated the first hypothesis with 1H -NMR of the 0.1 M $Mg(ClO_4)_2$ in CD_3CN with various water concentrations. If an appreciable number of “free” protons exist due to the hydrolysis of Mg^{2+} , we should see a peak in the 1H -NMR spectra ascribed to their presence.

The 1H -NMR spectra are presented in **Figure 7.9a**. At each water concentration, only two major set of peaks are visible. The pentet peak at 1.94 ppm was assigned to the residual CD_2HCN in CD_3CN , while the singlet peak, which grew and shifted upfield with water concentration, was assigned to protons from water. All of the water molecules, both free and interacting with Mg^{2+} , are in dynamic exchange on the NMR timescale leading to only one observable broad peak for water. No other peaks existed in the spectra that could be assigned to “free” protons in the electrolyte. As more water was added to the electrolyte, the chemical shift moved upfield, from ca. 5.0 ppm to ca. 3.4 ppm, as the influence of the Lewis acid-base interaction between Mg^{2+} and water decreased relative to the bulk water solvated in the system. Free water at low concentration generally occurs at ca. 2.13 ppm in CD_3CN ,²²⁶ but can shift downfield to ca. 2.5 ppm at higher concentrations (**Figure 7.9b**). The trend of chemical shift shows that at higher water concentrations, the OH bond in water is strengthened and the hydrolysis of Mg^{2+} is less favorable.²²⁷ The lack of “free” protons and less favorable hydrolysis indicate that the electrolyte

itself is not a proton source. If proton (co)insertion does occur, the protons would have to come from electrochemical side reactions involving the electrolyte and electrode.

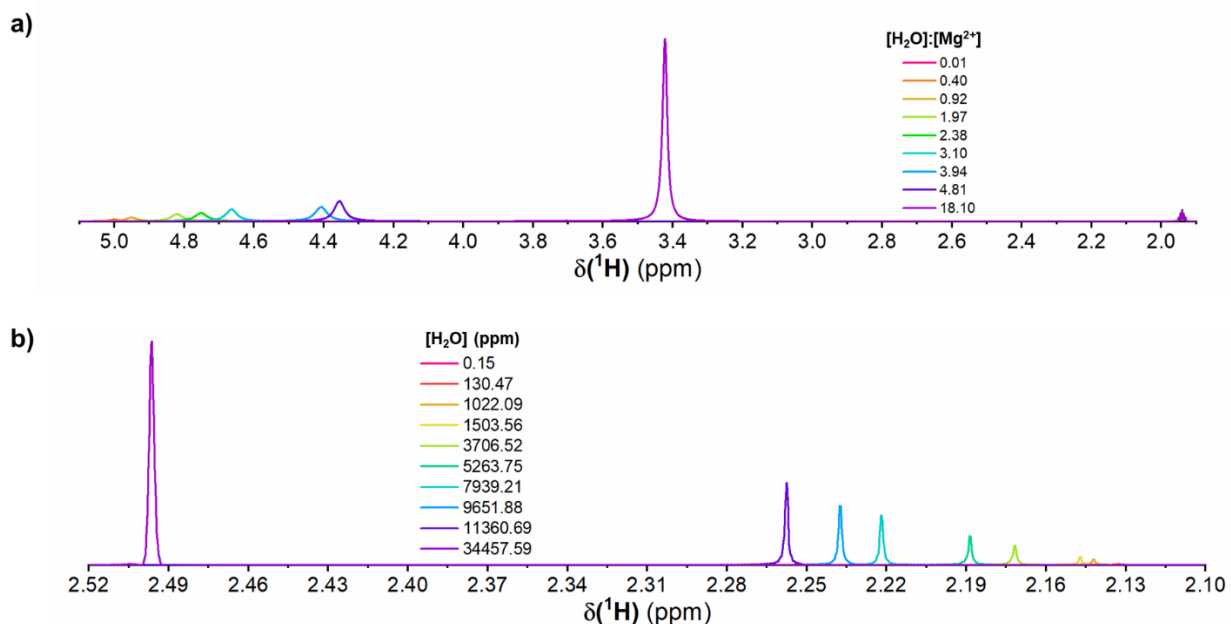


Figure 7.9. a) ¹H-NMR spectra of 0.1 M Mg(ClO₄)₂ in CD₃CN with various concentrations of added water. b) ¹H-NMR spectra of CD₃CN with various concentrations of added water. NMR courtesy of Peter V. Bonnesen.

We investigated proton (co)insertion in WO₃ with structural and elemental analysis. XRD was used since different inserted species can lead to different changes in the lattice parameters of the host.²¹⁴ The lattice parameter depends on the electrostatic attraction between the oxygen anions and intercalants as well as on the steric effect of the intercalants. We calculated the *a*-lattice parameter of cubic *e*_{0.52}WO₃ in the dry and wet electrolytes using single-peak fitting of the 200

reflection (**Figure 7.10**), and obtained $a = 3.810 \text{ \AA}$ and 3.796 \AA for 0 and 7 $[\text{H}_2\text{O}]:[\text{Mg}^{2+}]$, respectively. These values were compared to data available in the International Centre for Diffraction Data (ICDD) Powder Diffraction File (PDF) database on other cubic $M_x\text{WO}_3$ ($M = \text{H}, \text{Li}, \text{Na}, \text{and Ca}$), as shown in **Figure 7.11**.⁴⁵ For a large cation like Na^+ , the lattice parameter increases with the amount of Na^+ which indicates that the steric effect dominates the host response. On the other hand, in both H_xWO_3 and Li_xWO_3 , the lattice parameter decreases with increasing ion content indicative of a greater effect of the electrostatic attraction between the oxygen anions and the inserted species.

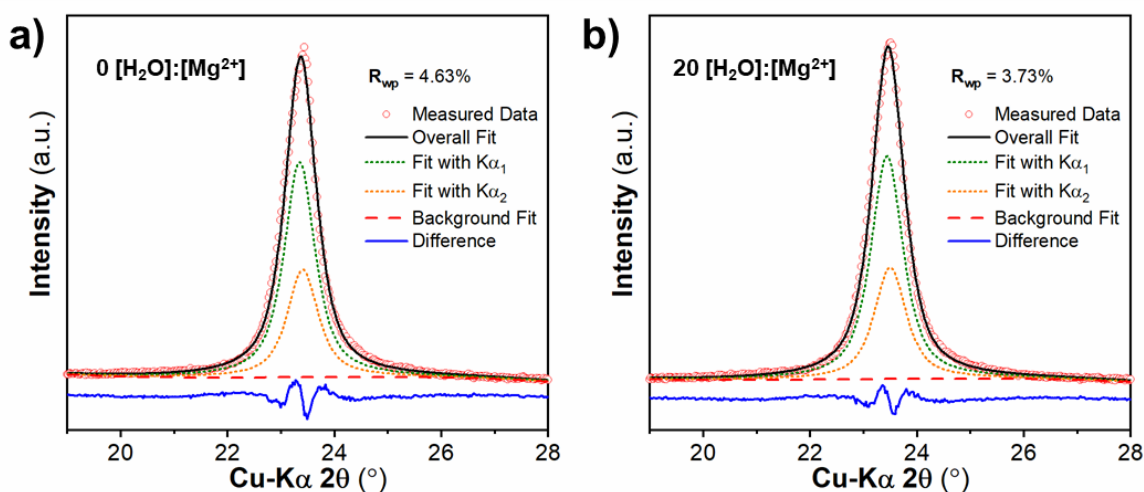


Figure 7.10. Single-peak fitting of the 200 reflection in the XRD patterns of $e_{0.52}\text{WO}_3$ shown in Figure 7.8, for a) $0 [\text{H}_2\text{O}]:[\text{Mg}^{2+}]$ and b) $20 [\text{H}_2\text{O}]:[\text{Mg}^{2+}]$. The data was fitted with Line-Profile Analysis Software (LIPRAS).⁴⁶ The fit was performed with a combination of $\text{Cu-K}\alpha_1$ and $\text{Cu-K}\alpha_2$ using Pseudo-Voigt peak shape function. The background was fit with a polynomial function and refined during the peak fitting process.

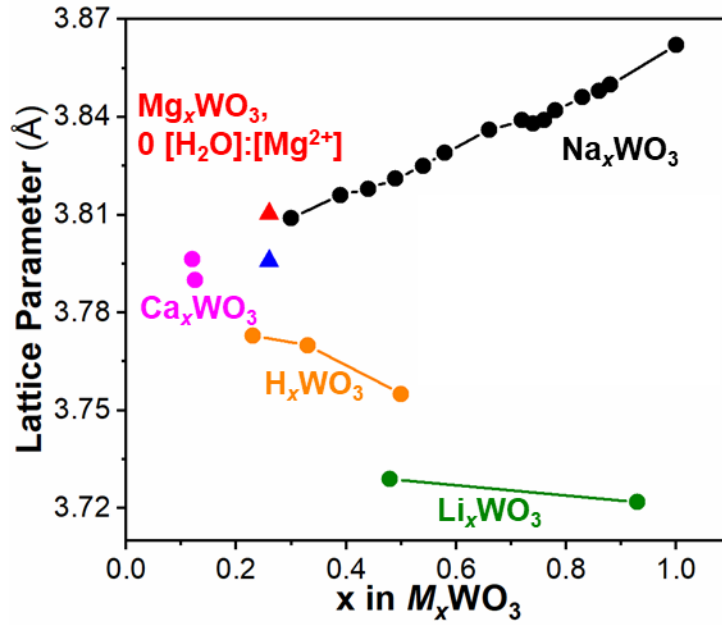


Figure 7.11. Lattice parameter comparison of cubic Mg_xWO_3 to published data (Table 7.1) on cubic M_xWO_3 ($M = H, Li, Na, \text{ and } Ca$). Assuming pure Mg^{2+} insertion, x in Mg_xWO_3 was assumed as half of the stored charge.

Table 7.1. The ICDD PDF numbers of the $M_x\text{WO}_3$ used in **Figure 7.11**.⁴⁵

Formula	PDF Number	Formula	PDF Number
$\text{H}_{0.23}\text{WO}_3$	00-042-1260	$\text{Na}_{0.66}\text{WO}_3$	01-080-7968
$\text{H}_{0.33}\text{WO}_3$	00-023-1449	$\text{Na}_{0.72}\text{WO}_3$	01-075-0235
$\text{H}_{0.5}\text{WO}_3$	00-006-0707	$\text{Na}_{0.74}\text{WO}_3$	01-075-0234
$\text{Li}_{0.48}\text{WO}_3$	04-006-7122	$\text{Na}_{0.76}\text{WO}_3$	01-075-0233
$\text{Li}_{0.93}\text{WO}_3$	01-075-0244	$\text{Na}_{0.78}\text{WO}_3$	01-075-0232
$\text{Na}_{0.3}\text{WO}_3$	01-075-0293	$\text{Na}_{0.83}\text{WO}_3$	01-075-0231
$\text{Na}_{0.39}\text{WO}_3$	01-075-0241	$\text{Na}_{0.86}\text{WO}_3$	01-075-0230
$\text{Na}_{0.44}\text{WO}_3$	01-075-0240	$\text{Na}_{0.88}\text{WO}_3$	01-075-0229
$\text{Na}_{0.49}\text{WO}_3$	01-075-0239	Na_1WO_3	00-005-0367
$\text{Na}_{0.54}\text{WO}_3$	01-075-0238	$\text{Ca}_{0.12}\text{WO}_3$	04-013-6573
$\text{Na}_{0.58}\text{WO}_3$	01-075-0237	$\text{Ca}_{0.125}\text{WO}_3$	04-001-9097

When reduced in a dry electrolyte, $a = 3.810 \text{ \AA}$ for $e_{0.52}\text{WO}_3$, a 0.03% difference from $\text{Na}_{0.3}\text{WO}_3$ and 1.5% greater than the published value for $\text{H}_{0.5}\text{WO}_3$. For the sake of comparison, a significant increase in cation content from $\text{Na}_{0.3}\text{WO}_3$ to Na_1WO_3 , only led to a 1.4% increase in the a -lattice parameter. After reduction in a wet electrolyte, $a = 3.796 \text{ \AA}$ for $e_{0.52}\text{WO}_3$, which is only 0.37% smaller than the lattice parameter of the electrode reduced in the dry electrolyte. Our results show 1) the increase of lattice parameter upon cation insertion, and 2) the difference between the lattice constants of WO_3 reduced in dry vs. wet electrolytes is more likely to represent a slightly different amount of cation insertion, rather than different inserting species altogether.

Therefore, while some amount of proton co-insertion could be present, ex situ XRD indicates that the lattice parameter changes are not consistent with only proton insertion.

Elemental analysis was performed with ex situ SEM-EDS to probe the chemical nature of the inserted species. Since protons are undetectable by this technique, the proton content was assessed indirectly by comparing the Mg concentration in the reduced electrodes via SEM-EDS to the cathodic charge calculated from electrochemistry. To assess whether SEM-EDS was able to sample the bulk of the electrode, we used a Monte Carlo algorithm to simulate the electron trajectories and X-ray intensities (**Figure 7.12**).²¹⁶ Estimating the density of the WO₃ thin film electrodes as 1.2 g cm⁻³,²²⁸ the simulation shows that the majority of the Mg K-edge X-rays come from within 2 μm but can also reach as deep as 6 μm. Under the same density assumption, our 5 mg cm⁻² electrode is about 4.2 μm thick. This shows the efficacy of SEM-EDS as a quantitative elemental analysis tool for determining Mg content in the bulk of the WO₃ electrodes. For ex situ SEM-EDS, we maintained the same sweep rate and insertion time in both dry and wet electrolytes to see if the improved electrochemical kinetics were due to more proton insertion at higher water concentrations. The ex situ SEM-EDS spectra of the reduced WO₃ in comparison to a control sample are shown in **Figure 7.13a**. As expected, the control sample showed no intensity for the Mg K-edge at 1.25 keV. There was Mg K-edge intensity in the *e*_{0.28}WO₃ from the dry electrolyte, and higher intensity in the *e*_{0.53}WO₃ from the 20 [H₂O]:[Mg²⁺] electrolyte. We note that the presence of Mg and lack of particle morphology change was also found via scanning transmission electron microscopy – energy dispersive spectrometry (STEM-EDS) mapping (*vide infra*).

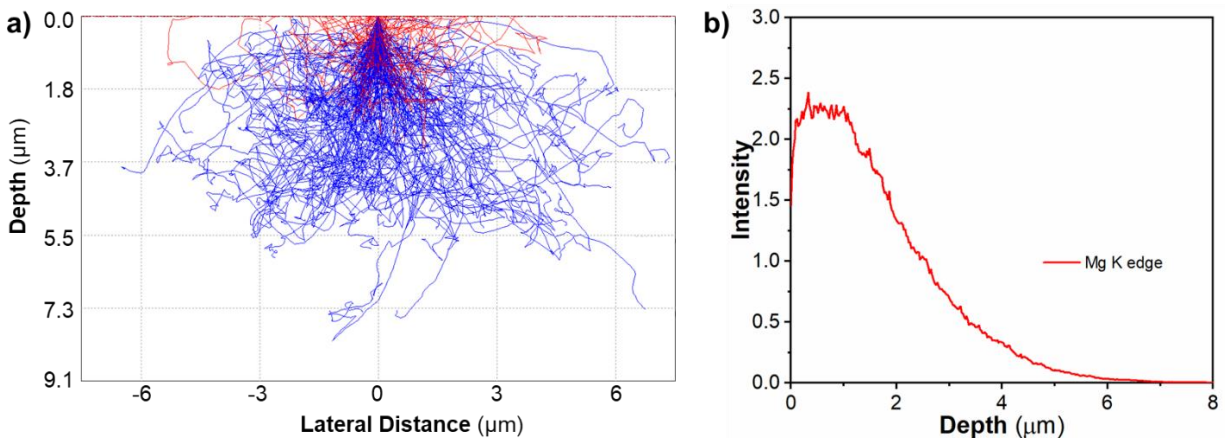


Figure 7.12. Electron trajectory and X-ray intensity simulation of a 20 kV electron beam on a Mg_xWO_3 film. a) Electron trajectory as a function of depth and width. The red trajectories represent back-scattered electrons and the blue trajectories are for electrons that did not back scatter. b) The intensity of the Mg K-edge X-ray generated as a function of depth.

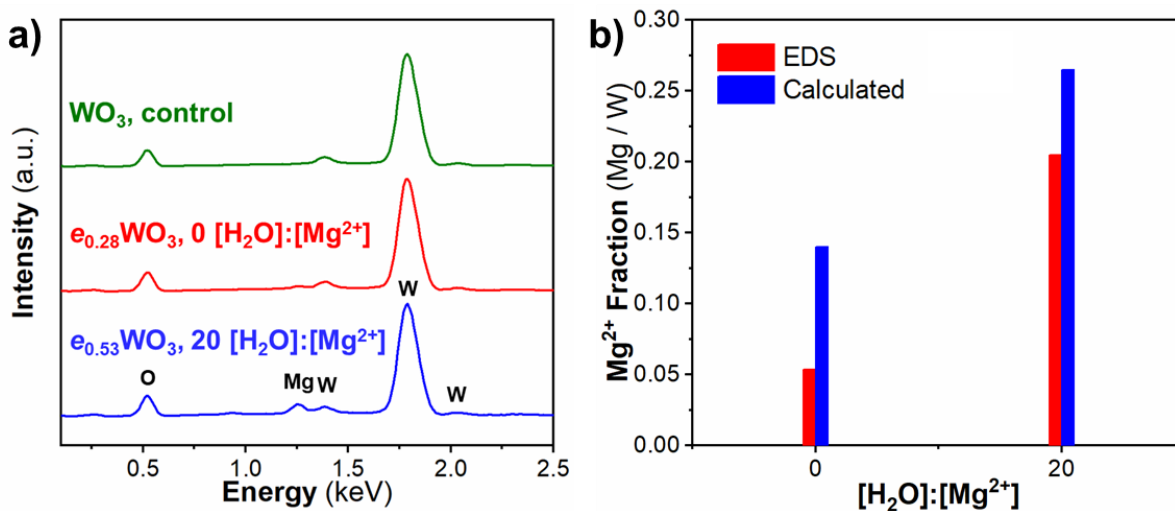


Figure 7.13. a) EDS of WO_3 thin film electrodes, comparing a control sample immersed in the dry Mg electrolyte to the ones reduced in electrolytes with different water concentrations. b) Bar charts comparing the fraction of Mg^{2+} obtained from EDS and cyclic voltammetry (calculated) assuming that all charge storage was only due to Mg^{2+} insertion. EDS courtesy of Shelby Boyd.

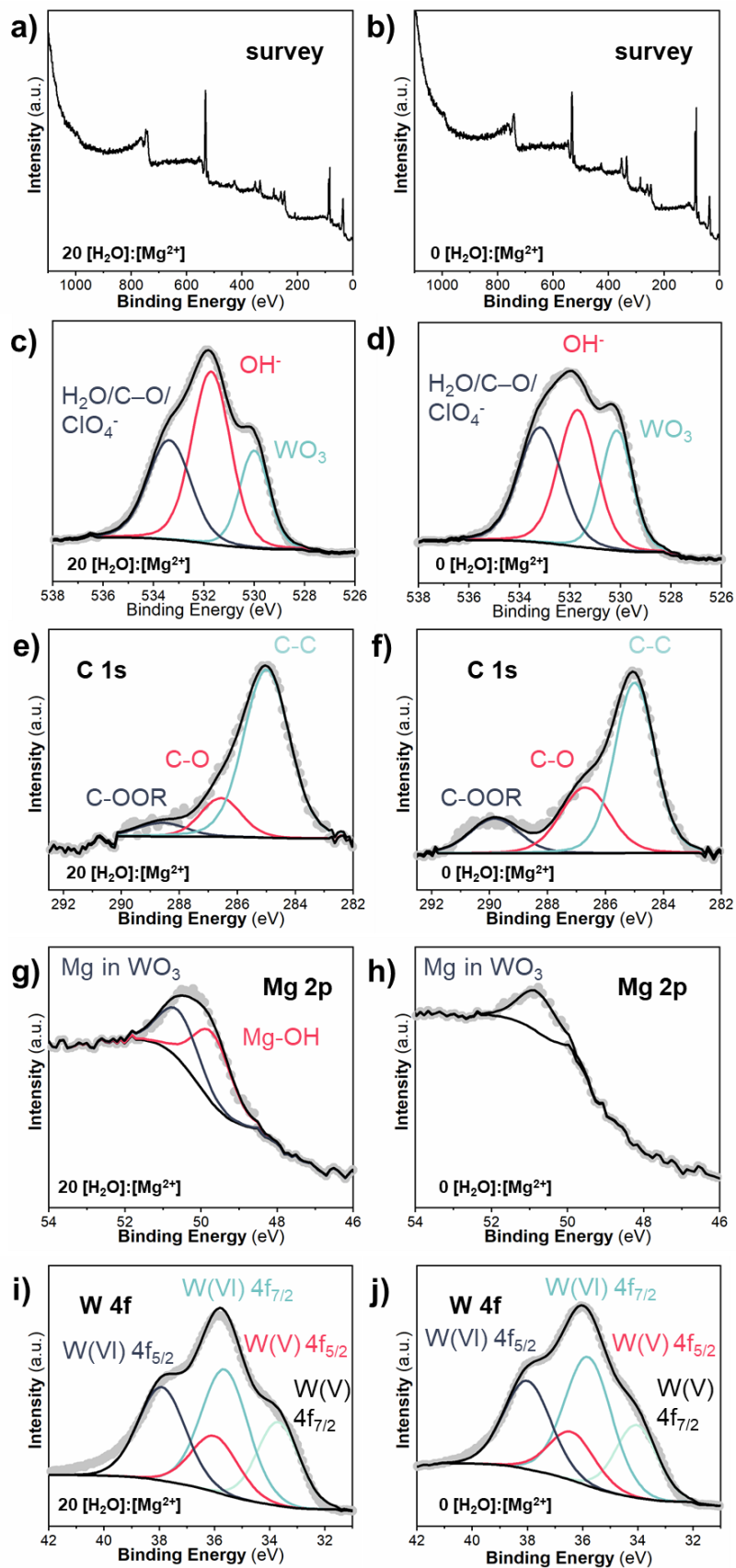
We quantified the fraction of Mg^{2+} from the EDS spectra and compared it to the electrochemical charge in WO_3 assuming all charge storage was due to Mg^{2+} insertion (**Figure 7.13b**). This comparison shows two important results. First, WO_3 reduced in the wet electrolyte has about 4 times the Mg concentration as its counterpart in the dry electrolyte. This indicates that for the same rate and time allowed for electrochemical insertion, the extra capacity in the wet electrolyte was due to Mg^{2+} , rather than proton co-insertion. The second result is that in both electrolytes, the Mg^{2+} concentration obtained from EDS cannot account for all the electrochemical charge. While experimental error and electrochemical side reactions could contribute to this difference, we are not able to entirely exclude the possibility of proton co-insertion. If the difference was due to proton co-insertion, it would appear that proton co-insertion was more dominant in the dry electrolyte, which is counter to the idea that decomposition of additional water in the electrolyte provides a source of protons. In summary, ex situ XRD and SEM-EDS indicates that while proton co-insertion is possible, Mg^{2+} insertion is present and improvement of insertion kinetics with additional water cannot be ascribed to proton co-insertion. Further, $^1\text{H-NMR}$ of the electrolytes suggests that if proton co-insertion were to happen, it would originate from the electrolysis of water.

Formation of a Beneficial Interphase

The possibility of beneficial interphase formation was investigated using ex situ XPS and TEM to probe its physical existence and chemical nature. The ex situ XPS spectra of WO_3 reduced in Mg electrolytes with 0 and 20 $[\text{H}_2\text{O}]:[\text{Mg}^{2+}]$ are presented in **Figure 7.14**. In the O 1s region, the peaks were assigned to lattice oxygen at 530.1 eV, OH^- or $\text{C}=\text{O}$ at 531.9 eV, and water, C-O, or ClO_4^- at 533.2 eV. Since the only variable in the two electrolytes was water concentration, the

increased intensity at 531.9 eV from dry to wet electrolyte was likely due to more OH⁻ on the surface. This is supported by the comparison of the Mg 2p region in **Figures 7.14g** and **7.14h**, where a peak at 49.9 eV can be assigned to Mg-OH in the wet electrolyte but not in the dry. The C 1s region in **Figures 7.14e** and **7.14f** shows that WO₃ reduced in the dry electrolyte had more C-OOR and C-O groups on the surface. Together, these results show that WO₃ reduced in dry vs. wet electrolytes had different surface compositions, with comparatively more carbonaceous species in the dry electrolyte and more Mg and OH⁻ groups in the wet electrolyte.

Figure 7.14. Survey and high resolution XPS spectra of WO_3 reduced in Mg electrolytes with 0 and 20 $[\text{H}_2\text{O}]:[\text{Mg}^{2+}]$. a,b) survey scans. c,d) O 1s spectra, the fitted peaks are $\text{H}_2\text{O}/\text{C}-\text{O}/\text{ClO}_4^-$ (533.2 eV), OH^- or $\text{C}=\text{O}$ (531.9 eV), and WO_3 (530.1 eV). e,f) C 1s spectra, the fitted peaks are C-C (285 eV), C-O (286.5 eV), and COOR (289 eV). g,h) Mg 2p spectra, the fitted peaks are Mg in WO_3 (50.8 eV) and Mg-OH (49.9 eV). i,j) W 4f spectra, the fitted peaks are W(V) $4f_{7/2}$ (34.1 eV), W(V) $4f_{5/2}$ (36.5 eV), W(VI) $4f_{7/2}$ (35.9 eV), and W(VI) $4f_{5/2}$ (38.1 eV). XPS courtesy of Fred Stevie.



To determine if these different chemical signatures were due to the presence of an interphase layer, we performed TEM on WO_3 reduced in a 20 $[\text{H}_2\text{O}]:[\text{Mg}^{2+}]$ electrolyte. An high-resolution transmission electron microscopy (HRTEM) micrograph of a reduced WO_3 particle that was partly on zone is shown in **Figure 7.15a**. The crystal lattice fringes did not extend to the surface, indicating the potential presence of an amorphous surface film with a thickness of 1.1 nm. Fast Fourier transformation (FFT) of the surface region also showed the lack of crystalline features, in contrast to the inner region of the particle. However, among the tens of WO_3 particles surveyed, this was the only one with an identifiable amorphous region. STEM-EDS mapping was used to examine if there was any chemical enrichment at the surface. The results are shown in **Figure 7.15b** together with a high-angle annular dark-field (HAADF) STEM micrograph of the side-view of a group of WO_3 particles. The elemental distribution of Mg, W, and O appears homogeneous across the eight WO_3 particles, and there is no obvious surface enrichment of Mg. Together, ex situ XPS and TEM show that while the surface chemistry changes depending upon the water concentration in the electrolyte, we could not identify the formation of any appreciable interphase layer.

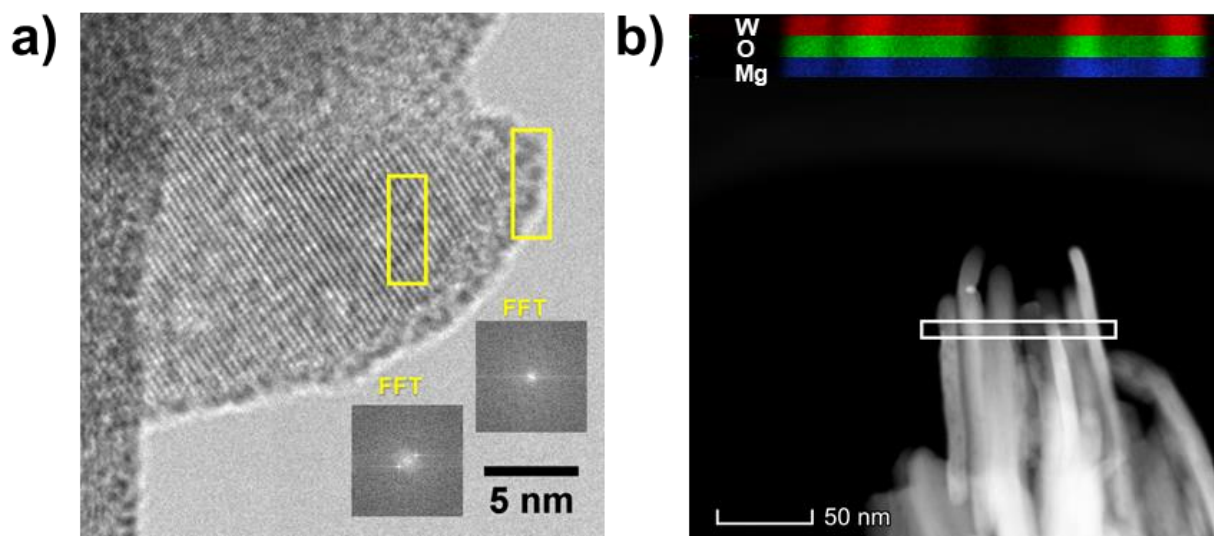


Figure 7.15. a) HRTEM micrograph of a WO_3 particle reduced in Mg electrolytes with 20 $[\text{H}_2\text{O}]:[\text{Mg}^{2+}]$. The inset shows the FFT results and the corresponding regions in yellow boxes. b) HAADF-STEM micrograph and STEM-EDS mapping of a group of WO_3 particles “on edge” reduced in Mg electrolyte with 20 $[\text{H}_2\text{O}]:[\text{Mg}^{2+}]$. The white box indicates the region of STEM-EDS mapping.

Possibility of Water-enhanced Surface Diffusion

The experimental evidence so far has not supported the water co-insertion or beneficial interphase formation hypotheses. While some proton co-insertion is possible, it does not appear dominant in the highest water content electrolyte. The final hypothesis we consider is the role of water on surface diffusion. It is challenging to experimentally measure surface diffusivity during electrochemical ion insertion. Therefore, in this section, we discuss the hypothesis of water-enhanced surface diffusion based on findings in the literature in comparison to our existing

experimental data to show that surface diffusion of Mg^{2+} ion was likely enhanced by water in the electrolyte.

The addition of water was proposed to enhance ion surface diffusion on transition metal oxides in multiple systems, including LiFePO_4 , FeO , and WO_3 . For example, the bulk Li^+ diffusivity in LiFePO_4 is $1\text{--}6 \times 10^{-16} \text{ cm}^2 \text{ s}^{-1}$,^{79,229} and Li et al. found that water-enhanced surface diffusion of Li^+ on LiFePO_4 was at least four orders of magnitude higher ($> 10^{-12} \text{ cm}^2 \text{ s}^{-1}$).¹² Scanning tunneling microscopy showed that the presence of water led to faster proton hopping on a $\text{FeO}(111)$ surface.²³⁰ The density-functional theory (DFT)-calculated energy barrier for proton hopping with or without water mediation was 0.19 eV and 1.02 eV, respectively. Given the exponential dependence of the diffusivity on the activation energy, this is equivalent to a 10^{14} difference at room temperature.

Water-enhanced surface diffusion of protons on WO_3 was intensively studied in the context of hydrogen spillover.^{80,231–233} In hydrogen spillover, hydrogen gas is passed over a mixture of Pt and oxides. Hydrogen gas dissociates into protons and electrons at the Pt surface, and the protons and electrons will diffuse to the oxide surface and eventually insert into the bulk.⁸⁰ It was found that on WO_3 , this process occurred significantly faster upon the addition of water vapor.²³² The rate of hydrogen uptake in WO_3 increased with water vapor pressure until a monolayer of water formed on the surface. A recent DFT calculation of hydrogen spillover showed that for a $\text{WO}_3(001)$ surface, the energy barrier for a proton to hop from one terminal oxygen site to another was reduced by 2.8 eV upon the addition of water, from 2.91 eV without water to 0.11 eV with the mediation of water.²³³ The energy barrier for bulk proton diffusion in WO_3 was 0.23 eV. Based on these differences in energy barriers at room temperature, the surface diffusivity with water is about 100 times higher than the bulk diffusivity and 10^{47} times higher than surface diffusivity without water.

One common trait among the simulations of surface ion hopping processes is that water behaves like a “swing” to bridge the gap between ion adsorption sites. While no simulation has been performed for Mg^{2+} surface diffusion on WO_3 , we hypothesize that a similar enhancement could apply leading to faster surface diffusion of Mg^{2+} in the presence of water.

There are two ways in which our experimental results are in agreement with the water-enhanced surface diffusion hypothesis. The first is the similarity between the hydrogen uptake rate at different water pressures in hydrogen spillover and the capacity increase rate, or charge uptake rate, at different water concentrations in our experiments (Figure 7.7). In our electrochemical system, water molecules preferentially solvate Mg^{2+} and together diffuse to the surface of WO_3 . When the concentration of water in the electrolyte is $< 2.6 [\text{H}_2\text{O}]:[\text{Mg}^{2+}]$, the charge uptake rate increases with water concentration similar to hydrogen spillover. The charge uptake rate slows at water concentrations beyond $2.6 [\text{H}_2\text{O}]:[\text{Mg}^{2+}]$, which could be due to the formation of a monolayer of water on the surface that reduces the benefit of further water addition. Another similarity is that Li^+ insertion in LiFePO_4 gradually transitioned from a solid solution-dominated process to a phase separation-dominated process with faster surface diffusivity from the presence of water. This phenomenon is reflected in the CVs in Figure 7.2 – with more water added to the electrolyte up to $6 [\text{H}_2\text{O}]:[\text{Mg}^{2+}]$, the redox peak width decreased. Well-defined redox peaks in a CV during ion insertion are indicative of a first-order phase transformation. The optimal water concentration of $6 [\text{H}_2\text{O}]:[\text{Mg}^{2+}]$ is likely the result of a tradeoff between improved surface diffusion and electrochemical side reactions. Further investigation is required to fully understand why faster surface diffusion would lead to improved insertion kinetics in a Mg^{2+} non-aqueous electrolyte. This hypothesis could explain the electrochemical behavior and agree with all physical characterization results.

7.4 Conclusions

In this work, we investigated the electrochemical reduction of WO_3 in 0.1 M $\text{Mg}(\text{ClO}_4)_2$ in ACN with various water concentrations. We observed the following correlations between the electrochemical behavior and water concentration: the charge uptake rate was significantly improved with increasing water concentration from 0 to 2.6 $[\text{H}_2\text{O}]:[\text{Mg}^{2+}]$. Above that concentration, the electrochemical kinetics continued to increase until about 6 $[\text{H}_2\text{O}]:[\text{Mg}^{2+}]$. Above 6 $[\text{H}_2\text{O}]:[\text{Mg}^{2+}]$, the rate performance of WO_3 deteriorated. Four mechanisms were proposed to explain the electrochemical behavior, namely, water co-insertion, proton (co)insertion, beneficial interphase formation, and water-enhanced surface diffusion. The possibility of each was investigated with ex situ physical characterizations and electrochemical characterization. Ex situ XRD, SEM-EDS, and STEM-EDS suggested the dominance of Mg^{2+} insertion in the charge storage process. The possibility of proton co-insertion was not excluded but could not explain the difference in insertion kinetics at higher water concentrations. Ex situ XPS and TEM suggested the different kinetic behavior occurred before the development of any significant interphase formation. Ex situ XPS also showed the development of Mg and OH^- species on the surface of WO_3 reduced in the 20 $[\text{H}_2\text{O}]:[\text{Mg}^{2+}]$ electrolyte. Improvement of the insertion kinetics due to water-enhanced surface diffusion appears the most consistent with our electrochemical characterization and ex situ physical and chemical characterization.

Further work is needed to understand the impact of surface diffusion on electrochemical insertion kinetics. An interesting future study would be to vary the WO_3 particle size and observe the rate of charge uptake in non-aqueous Mg electrolytes with different water concentrations. In larger particles, the contribution from surface diffusion should be smaller. As a result, in these electrodes water addition might not lead to significant insertion kinetic improvements. Also,

considering that water is detrimental to Mg deposition/stripping at the anode, one future direction is to find other solvents or electrolyte additives that promote surface diffusion of Mg^{2+} .

Chapter 8: Conclusions

This dissertation centered around the effect of water on the kinetics of electrochemical ion insertion using tungsten oxides as model structures.

In the first study, we investigated the mechanism behind the fast proton insertion kinetics of $\text{WO}_3 \cdot 2\text{H}_2\text{O}$. Operando AFM dilatometry and ex situ XRD suggested the role of structural water in $\text{WO}_3 \cdot 2\text{H}_2\text{O}$ was to minimize the mechanical deformation during ion insertion, which contributed to the fast kinetics. Inspired by the role of structural water, one future direction might be to look for other structural motifs that could minimize insertion-induced deformation. The deformation rate from operando AFM correlated well to the current induced by the electrochemical ion insertion. This relationship opens up an opportunity for studying electrochemical reactions via their mechanical deformation. Exciting directions include investigation of the heterogeneity of electrochemical insertion as a function of rate and surface location, measurement of a single particle electrochemomechanical response, and separating the insertion response from other competing electrochemical processes such as side reactions associated with electrolyte breakdown.

In the second study, the concept of structural water as a motif for fast insertion kinetics inspired the synthesis of $\text{H}_2\text{W}_2\text{O}_7$ from selective ion etching to improve the energy storage performance of $\text{WO}_3 \cdot n\text{H}_2\text{O}$. Comprehensive structural characterization determined that the crystal structure of $\text{H}_2\text{W}_2\text{O}_7$ had similar bonding environment as $\text{WO}_3 \cdot \text{H}_2\text{O}$. The main differences were 1) $\text{H}_2\text{W}_2\text{O}_7$ was monoclinic and $\text{WO}_3 \cdot \text{H}_2\text{O}$ was orthorhombic and 2) the single-layer tungsten oxide octahedra in $\text{WO}_3 \cdot \text{H}_2\text{O}$ were replaced with bi-layer tungsten oxide octahedra in $\text{H}_2\text{W}_2\text{O}_7$. These differences led to 100% higher capacity with proton insertion in $\text{H}_2\text{W}_2\text{O}_7$, which was attributed to a change of ion intercalation site. The ion insertion kinetics changed from surface-limited in $\text{WO}_3 \cdot \text{H}_2\text{O}$ to finite-space diffusion-limited in $\text{H}_2\text{W}_2\text{O}_7$. However, the material was still

able to deliver 80% of its capacity within one-minute charge/discharge time and could last for over 100,000 cycles. $\text{H}_2\text{W}_2\text{O}_7$ also possessed a multi-color electrochromism in acidic electrolyte. This material demonstrated the applicability of using structural water as a material design strategy and the use of selective ion etching to synthesize metastable materials with attractive energy storage properties. Future directions include investigating the dynamics of proton transport via neutron scattering, investigating the electronic structure changes that determine the electrochromism in $\text{H}_2\text{W}_2\text{O}_7$, and synthesizing other transition metal oxides using the selective ion etching approach.

The third study investigated the ion insertion behavior of $\text{WO}_3 \cdot 2\text{H}_2\text{O}$, $\text{WO}_3 \cdot \text{H}_2\text{O}$, and WO_3 in a non-aqueous Mg^{2+} electrolytes. $\text{WO}_3 \cdot 2\text{H}_2\text{O}$ spontaneously lost its lattice water in the non-aqueous electrolyte but the water of coordination in $\text{WO}_3 \cdot \text{H}_2\text{O}$ remained stable during electrochemical cycling. Both $\text{WO}_3 \cdot \text{H}_2\text{O}$ and WO_3 could insert Mg^{2+} ions from the non-aqueous electrolyte. As in proton insertion, the Mg^{2+} ion insertion kinetics were faster in $\text{WO}_3 \cdot \text{H}_2\text{O}$ than WO_3 .

In the fourth study, we found that Mg^{2+} ion insertion kinetics in $\text{WO}_3 \cdot \text{H}_2\text{O}$ and WO_3 could be improved by adding trace amounts of water to the non-aqueous electrolyte. Four potential hypotheses for this phenomenon were tested: water co-insertion, proton (co)insertion, formation of a beneficial interphase, and water-enhanced surface diffusion. Water co-insertion was rejected due to the lack of steric effect in ex situ XRD. Proton (co)insertion was not likely due to a greater amount of Mg insertion from wet electrolyte suggested by elemental analyses. Formation of an interphase was not significant according to surface analysis. The experimental evidence left water-enhanced surface diffusion as the most probable hypothesis. However, it should be noted that we lacked direct experimental evidence to support this hypothesis. Future work may include synthesizing WO_3 particles of different sizes to compare the surface effect, simulation with force-

field modeling to examine how water could change the phase transformation kinetics in WO_3 , and in situ X-ray absorption spectroscopy to visualize the phase transformation dynamics.

REFERENCES

- (1.) Fleischmann, S.; Mitchell, J. B.; Wang, R.; Zhan, C.; Jiang, D.; Presser, V.; Augustyn, V. Pseudocapacitance : From Fundamental Understanding to High Power Energy Storage Materials. *Chem. Rev.* **2020**.
- (2.) Abruña, H. D.; Kiya, Y.; Henderson, J. C. Batteries and Electrochemical Capacitors. *Phys. Today* **2008**, 61, 43–47.
- (3.) Manthiram, A.; Murugan, A. V.; Sarkar, A.; Muraliganth, T. Nanostructured Electrode Materials for Electrochemical Energy Storage and Conversion. *Energy Environ. Sci.* **2008**, 1, 621–638.
- (4.) Winter, M.; Brodd, R. J. What Are Batteries, Fuel Cells, and Supercapacitors? *Chem. Rev.* **2004**, 104, 4245–4269.
- (5.) Gogotsi, Y.; Penner, R. M. Energy Storage in Nanomaterials - Capacitive, Pseudocapacitive, or Battery-Like? *ACS Nano* **2018**, 12, 2081–2083.
- (6.) Wang, J.; Polleux, J.; Lim, J.; Dunn, B. Pseudocapacitive Contributions to Electrochemical Energy Storage in TiO₂ (Anatase) Nanoparticles. *J. Phys. Chem. C* **2007**, 111, 14925–14931.
- (7.) Okumura, T.; Fukutsuka, T.; Matsumoto, K.; Orikasa, Y.; Arai, H.; Ogumi, Z.; Uchimoto, Y. Lithium-Ion Transfer Reaction at the Interface between Partially Fluorinated Insertion Electrodes and Electrolyte Solutions. *J. Phys. Chem. C* **2011**, 115, 12990–12994.
- (8.) Bard, A. J.; Inzelt, G.; Scholz, F. *Electrochemical Dictionary*; Springer Science & Business Media, **2008**.
- (9.) Angerstein-Kozłowska, H.; Conway, B. E.; Sharp, W. B. A. The Real Condition of Electrochemically Oxidized Platinum Surfaces Part I. Resolution of Component Processes.

- Electroanal. Chem. Interfacial Electrochem.* **1973**, 43, 9–36.
- (10.) Conway, B. E. Transition from “Supercapacitor” to “Battery” Behavior in Electrochemical Energy Storage. *J. Electrochem. Soc.* **1991**, 138, 1539–1548.
- (11.) Conway, B. E. The Electrochemical Behavior of Ruthenium Oxide (RuO₂) as a Material for Electrochemical Capacitors. In *Electrochem. Supercapacitors*; **1999**; pp 259–297.
- (12.) Li, Y.; Chen, H.; Lim, K.; Deng, H. D.; Lim, J.; Fraggedakis, D.; Attia, P. M.; Lee, S. C.; Jin, N.; Moškon, J.; Guan, Z.; Gent, W. E.; Hong, J.; Yu, Y. S.; Gaberšček, M.; Islam, M. S.; Bazant, M. Z.; Chueh, W. C. Fluid-Enhanced Surface Diffusion Controls Intraparticle Phase Transformations. *Nat. Mater.* **2018**, 17, 915–922.
- (13.) Zhao, K.; Pharr, M.; Vlassak, J. J.; Suo, Z. Fracture of Electrodes in Lithium-Ion Batteries Caused by Fast Charging. *J. Appl. Phys.* **2010**, 108, 073517.
- (14.) Mitchell, J. B.; Lo, W. C.; Genc, A.; Lebeau, J.; Augustyn, V. Transition from Battery to Pseudocapacitor Behavior via Structural Water in Tungsten Oxide. *Chem. Mater.* **2017**, 29, 3928–3937.
- (15.) Daniel, M. F.; Desbat, B.; Lassegues, J. C.; Gerand, B.; Figlarz, M. Infrared and Raman Study of WO₃ Tungsten Trioxides and WO₃·xH₂O Tungsten Trioxide Hydrates. *J. Solid State Chem.* **1987**, 67, 235–247.
- (16.) Inamoto, M.; Kurihara, H.; Yajima, T. Vanadium Pentoxide-Based Composite Synthesized Using Microwave Water Plasma for Cathode Material in Rechargeable Magnesium Batteries. *Materials* **2013**, 6, 4514–4522.
- (17.) Lee, S. H.; Dileo, R. A.; Marschilok, A. C.; Takeuchi, K. J.; Takeuchi, E. S. Sol Gel Based Synthesis and Electrochemistry of Magnesium Vanadium Oxide : A Promising Cathode Material for Secondary Magnesium Ion Batteries. *ECS Electrochem. Lett.* **2014**, 3, A87–

A90.

- (18.) Gershinsky, G.; Yoo, H. D.; Gofer, Y.; Aurbach, D. Electrochemical and Spectroscopic Analysis of Mg^{2+} Intercalation into Thin Film Electrodes of Layered Oxides: V_2O_5 and MoO_3 . *Langmuir* **2013**, 29, 10964–10972.
- (19.) Gregory, T. D. T.; Hoffman, R. R. J.; Winterton, R. C. R. Nonaqueous Electrochemistry of Magnesium Applications to Energy Storage. *J. Electrochem. Soc.* **1990**, 137, 2–7.
- (20.) Spahr, M. E.; Haas, O. Electrochemical Insertion of Lithium, Sodium, and Magnesium Molybdenum(VI) Oxide. **1995**, 54, 346–351.
- (21.) Zhang, R.; Yu, X.; Nam, K. W.; Ling, C.; Arthur, T. S.; Song, W.; Knapp, A. M.; Ehrlich, S. N.; Yang, X. Q.; Matsui, M. $\alpha\text{-MnO}_2$ as a Cathode Material for Rechargeable Mg Batteries. *Electrochem. Commun.* **2012**, 23, 110–113.
- (22.) Yuan, C.; Zhang, Y.; Pan, Y.; Liu, X.; Wang, G.; Cao, D. Investigation of the Intercalation of Polyvalent Cations (Mg^{2+} , Zn^{2+}) into $\lambda\text{-MnO}_2$ for Rechargeable Aqueous Battery. *Electrochim. Acta* **2014**, 116, 404–412.
- (23.) Rasul, S.; Suzuki, S.; Yamaguchi, S.; Miyayama, M. Synthesis and Electrochemical Behavior of Hollandite MnO_2 /Acetylene Black Composite Cathode for Secondary Mg-Ion Batteries. *Solid State Ionics* **2012**, 225, 542–546.
- (24.) NuLi, Y.; Zheng, Y.; Wang, Y.; Yang, J.; Wang, J. Electrochemical Intercalation of Mg^{2+} in 3D Hierarchically Porous Magnesium Cobalt Silicate and Its Application as an Advanced Cathode Material in Rechargeable Magnesium Batteries. *J. Mater. Chem.* **2011**, 21, 12437–12443.
- (25.) Li, Y.; Nuli, Y.; Yang, J.; Yiliner, T.; Wang, J. MgFeSiO_4 Prepared via a Molten Salt Method as a New Cathode Material for Rechargeable Magnesium Batteries. *Chinese Sci.*

- Bull.* **2011**, 56, 386–390.
- (26.) NuLi, Y.; Yang, J.; Li, Y.; Wang, J. Mesoporous Magnesium Manganese Silicate as Cathode Materials for Rechargeable Magnesium Batteries. *Chem. Commun.* **2010**, 46, 3794.
- (27.) Novák, P.; Scheifele, W.; Joho, F.; Haas, O. Electrochemical Insertion of Magnesium into Hydrated Vanadium Bronzes. *J. Electrochem. Soc.* **1995**, 142, 2544.
- (28.) Aurbach, D.; Suresh, G. S.; Levi, E.; Mitelman, A.; Mizrahi, O.; Chusid, O.; Brunelli, M. Progress in Rechargeable Magnesium Battery Technology. *Adv. Mater.* **2007**, 19, 4260–4267.
- (29.) Wang, R. Y.; Wessells, C. D.; Huggins, R. A.; Cui, Y. Highly Reversible Open Framework Nanoscale Electrodes for Divalent Ion Batteries. *Nano Lett.* **2013**, 13, 5748–5752.
- (30.) Mizuno, Y.; Okubo, M.; Hosono, E.; Kudo, T.; Oh-ishi, K.; Okazawa, A.; Kojima, N.; Kurono, R.; Nishimura, S.; Yamada, A. Electrochemical Mg^{2+} Intercalation into a Bimetallic CuFe Prussian Blue Analog in Aqueous Electrolytes. *J. Mater. Chem. A* **2013**, 1, 13055.
- (31.) Aurbach, D.; Lu, Z.; Schechter, A.; Gofer, Y.; Gizbar, H.; Turgeman, R.; Cohen, Y.; Moshkovich, M.; Levi, E. Prototype Systems for Rechargeable Magnesium Batteries. *Nature* **2000**, 407, 724–727.
- (32.) Li, X.-L.; Li, Y.-D. MoS_2 Nanostructures: Synthesis and Electrochemical Mg^{2+} Intercalation. *J. Phys. Chem. B* **2004**, 108, 13893–13900.
- (33.) Liu, Y.; Jiao, L.; Wu, Q.; Du, J.; Zhao, Y.; Si, Y.; Wang, Y.; Yuan, H. Sandwich-Structured Graphene-like MoS_2/C Microspheres for Rechargeable Mg Batteries. *J. Mater. Chem. A* **2013**, 1, 5822–5826.
- (34.) Pandey, G. P.; Agrawal, R. C.; Hashmi, S. A. Magnesium Ion-Conducting Gel Polymer

- Electrolytes Dispersed with Fumed Silica for Rechargeable Magnesium Battery Application. *J. Solid State Electrochem.* **2011**, 15, 2253–2264.
- (35.) Levi, E.; Lancry, E.; Mitelman, A.; Aurbach, D.; Ceder, G.; Morgan, D.; Isnard, O. Phase Diagram of Mg Insertion into Chevrel Phases, $Mg_xMo_6T_8$ (T = S, Se). 1. Crystal Structure of the Sulfides. *Chem. Mater.* **2006**, 18, 5492–5503.
- (36.) Yoo, H. D.; Shterenberg, I.; Gofer, Y.; Gershinsky, G.; Pour, N.; Aurbach, D. Mg Rechargeable Batteries: An on-Going Challenge. *Energy Environ. Sci.* **2013**, 6, 2265–2279.
- (37.) Lu, Y.; Wang, L.; Cheng, J.; Goodenough, J. B. Prussian Blue: A New Framework of Electrode Materials for Sodium Batteries. *Chem. Commun.* **2012**, 48, 6544.
- (38.) Miura, H. The Crystal Structure of Hollandite. *Mineral. J.* **1986**, 13, 119–129.
- (39.) Post, J.; Bish, D. Rietveld Refinement of the Todorokite Structure. *Am. Miner.* **1988**, 73, 861–869.
- (40.) Chatterjee, S.; Sengupta, S.; Saha-Dasgupta, T.; Chatterjee, K.; Mandal, N. Site Preference of Fe Atoms in $FeMgSiO_4$ and $FeMg(SiO_3)_2$ Studied by Density Functional Calculations. *Phys. Rev. B* **2009**, 79, 1–8.
- (41.) Enjalbert, R.; Galy, J. A Refinement of the Structure of V_2O_5 . *Acta Cryst.* **1986**, C42, 1467–1469.
- (42.) Bell, R. E.; Herfert, R. E. Preparation and Characterization of a New Crystalline Form of Molybdenum Disulfide. *J. Am. Chem. Soc.* **1957**, 79, 3351–3354.
- (43.) Sitepu, H. Texture and Structural Refinement Using Neutron Diffraction Data from Molybdite (MoO_3) and Calcite ($CaCO_3$) Powders and a Ni-Rich $Ni_{50.7}Ti_{49.30}$ Alloy. *Powder Diffr.* **2009**, 24, 315–326.
- (44.) Post, J. E.; Veblen, D. R. Crystal Structure Determinations of Synthetic Sodium,

- Magnesium, and Potassium Birnessite Using TEM and the Rietveld Method. *Am. Mineral.* **1990**, 75, 477–489.
- (45.) Gates-Rector, S.; Blanton, T. The Powder Diffraction File: A Quality Materials Characterization Database. *Powder Diffr.* **2019**, 34, 352–360.
- (46.) Esteves, G.; Ramos, K.; Fancher, C. M.; Jones, J. L. *LIPRAS: Line-Profile Analysis Software*; **2017**.
- (47.) Poushter, J.; Bell, J.; Carle, J.; Cuddington, D.; Deane, C.; Devlin, K.; Drake, B.; Keegan, M.; Kent, D.; Parker, B.; Poushter, J.; Schwarzer, S.; Simmons, K.; Smith, B.; Stokes, B.; Wike, R.; Zainbulbhai, H. *Cell Phones in Africa : Communication Lifeline*; **2015**.
- (48.) Coast, E. Population Trends in Developing Countries. In *The Arnold companion to development studies*; **2002**; pp 360–367.
- (49.) Dunn, B.; Kamath, H.; Tarascon, J.-M. Electrical Energy Storage for the Grid: A Battery of Choices. *Science* **2011**, 334, 928–935.
- (50.) Lu, M.; Beguin, F.; Frackowiak, E. *Supercapacitors: Materials, Systems, and Applications*; Wiley-VCH, **2013**.
- (51.) Cabana, J.; Monconduit, L.; Larcher, D.; Palacín, M. R. Beyond Intercalation-Based Li-Ion Batteries: The State of the Art and Challenges of Electrode Materials Reacting through Conversion Reactions. *Adv. Mater.* **2010**, 22, E170–E192.
- (52.) Gür, T. M. Review of Electrical Energy Storage Technologies, Materials and Systems: Challenges and Prospects for Large-Scale Grid Storage. *Energy Environ. Sci.* **2018**, 11, 2696–2767.
- (53.) Smith, P. F.; Takeuchi, K. J.; Marschilok, A. C.; Takeuchi, E. S. Holy Grails in Chemistry: Investigating and Understanding Fast Electron/Cation Coupled Transport within Inorganic

- Ionic Matrices. *Acc. Chem. Res.* **2017**, 50, 544–548.
- (54.) Canepa, P.; Sai Gautam, G.; Hannah, D. C.; Malik, R.; Liu, M.; Gallagher, K. G.; Persson, K. A.; Ceder, G. Odyssey of Multivalent Cathode Materials: Open Questions and Future Challenges. *Chem. Rev.* **2017**, 117, 4287–4341.
- (55.) Lee, B.-S.; Wu, Z.; Petrova, V.; Xing, X.; Lim, H.-D.; Liu, H.; Liu, P. Analysis of Rate-Limiting Factors in Thick Electrodes for Electric Vehicle Applications. *J. Electrochem. Soc.* **2018**, 165, A525–A533.
- (56.) Bard, A. J.; Faulkner, L. R. *Electrochemical Methods: Fundamentals and Applications*; John Wiley & Sons, **2000**.
- (57.) Conway, B. E. Similarities and Differences between Supercapacitors and Batteries for Storing Electrical Energy. In *Electrochem. Supercapacitors Sci. Fundam. Technol. Appl.*; **1999**; pp 11–31.
- (58.) Ji, H.; Zhao, X.; Qiao, Z.; Jung, J.; Zhu, Y.; Lu, Y.; Zhang, L. L.; MacDonald, A. H.; Ruoff, R. S. Capacitance of Carbon-Based Electrical Double-Layer Capacitors. *Nat. Commun.* **2014**, 5.
- (59.) Trasatti, S.; Petrii, O. A. Real Surface Area Measurements in Electrochemistry. *J. Electroanal. Chem.* **1992**, 327, 353–376.
- (60.) Lindström, H.; Södergren, S.; Solbrand, A.; Rensmo, H.; Hjelm, J.; Hagfeldt, A.; Lindquist, S. E. Li⁺ Ion Insertion in TiO₂ (Anatase). 2. Voltammetry on Nanoporous Films. *J. Phys. Chem. B* **1997**, 101, 7717–7722.
- (61.) Liu, T. -C.; Pell, W. G.; Conway, B. E.; Roberson, S. L. Behavior of Molybdenum Nitrides as Materials for Electrochemical Capacitors Comparison with Ruthenium Oxide. *J. Electrochem. Soc.* **1998**, 145, 1882–1888.

- (62.) Aoki, K.; Tokuda, K.; Matsuda, H. Theory of Linear Sweep Voltammetry with Finite Diffusion Space Part II. Totally Irreversible and Quasi-Reversible Cases. *J. Electroanal. Chem. Interfacial Electrochem.* **1984**, 160, 33–45.
- (63.) Ko, J. S.; Sassin, M. B.; Rolison, D. R.; Long, J. W. Deconvolving Double-Layer, Pseudocapacitance, and Battery-like Charge-Storage Mechanisms in Nanoscale LiMn_2O_4 at 3D Carbon Architectures. *Electrochim. Acta* **2018**, 275, 225–235.
- (64.) Brezesinski, T.; Wang, J.; Polleux, J.; Dunn, B.; Tolbert, S. H. Templated Nanocrystal-Based Porous TiO_2 Films for next-Generation Electrochemical Capacitors. *J. Am. Chem. Soc.* **2009**, 131, 1802–1809.
- (65.) Brezesinski, T.; Wang, J.; Senter, R.; Brezesinski, K.; Dunn, B.; Tolbert, S. H. On the Correlation between Mechanical Flexibility, Nanoscale Structure, and Charge Storage in Periodic Mesoporous CeO_2 Thin Films. *ACS Nano* **2010**, 4, 967–977.
- (66.) Brezesinski, K.; Wang, J.; Haetge, J.; Reitz, C.; Steinmueller, S. O.; Tolbert, S. H.; Smarsly, B. M.; Dunn, B.; Brezesinski, T. Pseudocapacitive Contributions to Charge Storage in Highly Ordered Mesoporous Group V Transition Metal Oxides with Iso-Oriented Layered Nanocrystalline Domains. *J. Am. Chem. Soc.* **2010**, 132, 6982–6990.
- (67.) Shao, H.; Lin, Z.; Xu, K.; Taberna, P. L.; Simon, P. Electrochemical Study of Pseudocapacitive Behavior of $\text{Ti}_3\text{C}_2\text{T}_x$ MXene Material in Aqueous Electrolytes. *Energy Storage Mater.* **2019**, 18, 456–461.
- (68.) Opitz, M.; Yue, J.; Wallauer, J.; Smarsly, B.; Roling, B. Mechanisms of Charge Storage in Nanoparticulate TiO_2 and $\text{Li}_4\text{Ti}_5\text{O}_{12}$ Anodes: New Insights from Scan Rate-Dependent Cyclic Voltammetry. *Electrochim. Acta* **2015**, 168, 125–132.
- (69.) Bruce, P. G.; Saidi, M. Y. The Mechanism of Electrointercalation. *J. Electroanal. Chem.*

- 1992**, 322, 93–105.
- (70.) Levi, M. D.; Aurbach, D. Simultaneous Measurements and Modeling of the Electrochemical Impedance and the Cyclic Voltammetric Characteristics of Graphite Electrodes Doped with Lithium. *J. Phys. Chem. B* **1997**, 101, 4630–4640.
- (71.) Bard, A. J.; Inzelt, G.; Scholz, F. *Electrochemical Dictionary*; Springer Science & Business Media, **2008**.
- (72.) Grahame, D. C. The Electrical Double Layer and the Theory of Electrocapillarity. *Chem. Rev.* **1947**, 41, 441–501.
- (73.) Bockris, J. O.; Devanathan, M. A. V.; Müllen, K. On the Structure of Charged Interfaces. *Proc. R. Soc. A* **1963**, 274, 55–79.
- (74.) Tsai, W. Y.; Come, J.; Zhao, W.; Wang, R.; Feng, G.; Prasad Thapaliya, B.; Dai, S.; Collins, L.; Balke, N. Hysteretic Order-Disorder Transitions of Ionic Liquid Double Layer Structure on Graphite. *Nano Energy* **2019**, 60, 886–893.
- (75.) Conway, B. E.; Gileadi, E. Kinetic Theory of Pseudo-Capacitance and Electrode Reactions at Appreciable Surface Coverage. *Trans. Faraday Soc.* **1962**, 58, 2493–2509.
- (76.) Bazant, M. Z. Thermodynamic Stability of Driven Open Systems and Control of Phase Separation by Electro-Autocatalysis. *Faraday Discuss.* **2017**, 199, 423–463.
- (77.) Levi, M. D.; Aurbach, D. Frumkin Intercalation Isotherm - a Tool for the Description of Lithium Insertion into Host Materials: A Review. *Electrochim. Acta* **1999**, 45, 167–185.
- (78.) Conway, B. E.; Angerstein-Kozłowska, H. Electrochemical Study of Multiple-State Adsorption in Monolayers. *Acc. Chem. Res.* **1981**, 14, 49–56.
- (79.) Dathar, G. K. P.; Sheppard, D.; Stevenson, K. J.; Henkelman, G. Calculations of Li-Ion Diffusion in Olivine Phosphates. *Chem. Mater.* **2011**, 23, 4032–4037.

- (80.) Levy, R. B.; Boudart, M. Kinetics and Mechanism of Spillover. *J. Catal.* **1974**, 32, 304–314.
- (81.) Attias, R.; Salama, M.; Hirsch, B.; Gofer, Y.; Aurbach, D. Solvent Effects on the Reversible Intercalation of Magnesium-Ions into V₂O₅ Electrodes. *ChemElectroChem* **2018**, 5, 3514–3524.
- (82.) Bashian, N. H.; Zhou, S.; Zuba, M.; Ganose, A. M.; Stiles, J. W.; Ee, A.; Ashby, D. S.; Scanlon, D. O.; Piper, L. F. J.; Dunn, B.; Melot, B. C. Correlated Polyhedral Rotations in the Absence of Polarons during Electrochemical Insertion of Lithium in ReO₃. *ACS Energy Lett.* **2018**, 3, 2513–2519.
- (83.) Gerhard, N.; Tuijin, C. *Self-Diffusion and Impurity Diffusion in Pure Metals: Handbook of Experimental Data*; Pergamon, **2009**.
- (84.) Markevich, E.; Levi, M. D.; Aurbach, D. Comparison between Potentiostatic and Galvanostatic Intermittent Titration Techniques for Determination of Chemical Diffusion Coefficients in Ion-Insertion Electrodes. *J. Electroanal. Chem.* **2005**, 580, 231–237.
- (85.) Ho, C.; Raistrick, I. D.; Huggins, R. A. Application of A-C Techniques to the Study of Lithium Diffusion in Tungsten Trioxide Thin Films. *J. Electrochem. Soc.* **1980**, 127, 343–350.
- (86.) Black, J. M.; Feng, G.; Fulvio, P. F.; Hillesheim, P. C.; Dai, S.; Gogotsi, Y.; Cummings, P. T.; Kalinin, S. V.; Balke, N. Strain-Based In Situ Study of Anion and Cation Insertion into Porous Carbon Electrodes with Different Pore Sizes. *Adv. Energy Mater.* **2014**, 4, 1300683.
- (87.) Mukhopadhyay, A.; Sheldon, B. W. Deformation and Stress in Electrode Materials for Li-Ion Batteries. *Prog. Mater. Sci.* **2014**, 63, 58–116.
- (88.) Wang, R.; Mitchell, J. B.; Gao, Q.; Tsai, W. Y.; Boyd, S.; Pharr, M.; Balke, N.; Augustyn,

- V. Operando Atomic Force Microscopy Reveals Mechanics of Structural Water Driven Battery-to-Pseudocapacitor Transition. *ACS Nano* **2018**, 12, 6032–6039.
- (89.) Cogswell, D. A.; Bazant, M. Z. Coherency Strain and the Kinetics of Phase Separation in LiFePO₄ Nanoparticles. *ACS Nano* **2012**, 6, 2215–2225.
- (90.) Schweidler, S.; De Biasi, L.; Schiele, A.; Hartmann, P.; Brezesinski, T.; Janek, J. Volume Changes of Graphite Anodes Revisited: A Combined Operando X-Ray Diffraction and in Situ Pressure Analysis Study. *J. Phys. Chem. C* **2018**, 122, 8829–8835.
- (91.) Koerver, R.; Zhang, W.; De Biasi, L.; Schweidler, S.; Kondrakov, A. O.; Kolling, S.; Brezesinski, T.; Hartmann, P.; Zeier, W. G.; Janek, J. Chemo-Mechanical Expansion of Lithium Electrode Materials-on the Route to Mechanically Optimized All-Solid-State Batteries. *Energy Environ. Sci.* **2018**, 11, 2142–2158.
- (92.) Woodford, W. H.; Carter, W. C.; Chiang, Y. M. Design Criteria for Electrochemical Shock Resistant Battery Electrodes. *Energy Environ. Sci.* **2012**, 5, 8014–8024.
- (93.) Ohzuku, T. T.; Ueda, A.; Yamamoto, N. Zero-Strain Insertion Material of Li[Li_{1/3}Ti_{5/3}]O₄ for Rechargeable Lithium Cells. *J. Electrochem. Soc.* **1995**, 142, 1431–1435.
- (94.) Verde, M. G.; Baggetto, L.; Balke, N.; Veith, G. M.; Seo, J. K.; Wang, Z.; Meng, Y. S. Elucidating the Phase Transformation of Li₄Ti₅O₁₂ Lithiation at the Nanoscale. *ACS Nano* **2016**, 10, 4312–4321.
- (95.) Griffith, K. J.; Wiaderek, K. M.; Cibin, G.; Marbella, L. E.; Grey, C. P. Niobium Tungsten Oxides for High-Rate Lithium-Ion Energy Storage. *Nature* **2018**, 559, 556–563.
- (96.) Tavassol, H.; Jones, E. M. C.; Sottos, N. R.; Gewirth, A. A. Electrochemical Stiffness in Lithium-Ion Batteries. *Nat. Mater.* **2016**, 15, 1182–1187.
- (97.) Schiffer, Z. J.; Cannarella, J.; Arnold, C. B. Strain Derivatives for Practical Charge Rate

- Characterization of Lithium Ion Electrodes. *J. Electrochem. Soc.* **2016**, 163, A427–A433.
- (98.) Reichman, B.; Bard, A. J. The Electrochromic Process at WO₃ Electrodes Prepared by Vacuum Evaporation and Anodic Oxidation of W. *J. Electrochem. Soc.* **1979**, 126, 583–591.
- (99.) Judeinstein, P.; Livage, J. Role of the Water Content on the Electrochromic Properties of WO₃·nH₂O Thin Films. *Mater. Sci. Eng. B3* **1989**, 3, 129–132.
- (100.) Kattouf, B.; Frey, G. L.; Siegmann, A.; Ein-Eli, Y. Enhanced Reversible Electrochromism via in Situ Phase Transformation in Tungstate Monohydrate. *Chem. Commun.* **2009**, 7396–7398.
- (101.) Nam, K. W.; Kim, S.; Lee, S.; Salama, M.; Shterenberg, I.; Gofer, Y.; Kim, J.-S.; Yang, E.; Park, C. S.; Kim, J.-S.; Seok-Soo, L.; Chang, W.-S.; Doo, S.-G.; Jo, Y. N.; Jung, Y.; Aurbach, D.; Choi, J. W. The High Performance of Crystal Water Containing Manganese Birnessite Cathodes for Magnesium Batteries. *Nano Lett.* **2015**, 15, 4071–4079.
- (102.) Kundu, D.; Adams, B. D.; Duffort, V.; Vajargah, S. H.; Nazar, L. F. A High-Capacity and Long-Life Aqueous Rechargeable Zinc Battery Using a Metal Oxide Intercalation Cathode. *Nat. Energy* **2016**, 1, 16119.
- (103.) Novák, P.; Scheifele, W.; Joho, F.; Haas, O. Electrochemical Insertion of Magnesium into Hydrated Vanadium Bronzes. *J. Electrochem. Soc.* **1995**, 142, 2544–2550.
- (104.) Augustyn, V.; Gogotsi, Y. 2D Materials with Nanoconfined Fluids for Electrochemical Energy Storage. *Joule* **2017**, 1, 443–452.
- (105.) Huang, J. Y.; Zhong, L.; Wang, C. M.; Sullivan, J. P.; Xu, W.; Zhang, L. Q.; Mao, S. X.; Hudak, N. S.; Liu, X. H.; Subramanian, A.; Fan, H.; Qi, L.; Kushima, A.; Li, J. In Situ Observation of the Electrochemical Lithiation of a Single SnO₂ Nanowire Electrode.

- Science* **2010**, 330, 1515–1520.
- (106.) Levi, E.; Levi, M. D.; Chasid, O.; Aurbach, D. A Review on the Problems of the Solid State Ions Diffusion in Cathodes for Rechargeable Mg Batteries. *J. Electroceramics* **2009**, 22, 13–19.
- (107.) Pharr, M.; Zhao, K.; Wang, X.; Suo, Z.; Vlassak, J. J. Kinetics of Initial Lithiation of Crystalline Silicon Electrodes of Lithium-Ion Batteries. *Nano Lett.* **2012**, 12, 5039–5047.
- (108.) Come, J.; Black, J. M.; Lukatskaya, M. R.; Naguib, M.; Beidaghi, M.; Rondinone, A. J.; Kalinin, S. V.; Wesolowski, D. J.; Gogotsi, Y.; Balke, N. Controlling the Actuation Properties of MXene Paper Electrodes upon Cation Intercalation. *Nano Energy* **2015**, 17, 27–35.
- (109.) Hantel, M. M.; Presser, V.; Kötzt, R.; Gogotsi, Y. In Situ Electrochemical Dilatometry of Carbide-Derived Carbons. *Electrochem. Commun.* **2011**, 13, 1221–1224.
- (110.) Jäckel, N.; Dargel, V.; Shpigel, N.; Sigalov, S.; Levi, M. D.; Daikhin, L.; Aurbach, D.; Presser, V. In Situ Multi-Length Scale Approach to Understand the Mechanics of Soft and Rigid Binder in Composite Lithium Ion Battery Electrodes. *J. Power Sources* **2017**, 371, 162–166.
- (111.) Freedman, M. L. The Tungstic Acids. *J. Am. Chem. Soc.* **1959**, 81, 3–8.
- (112.) Granqvist, C. G. *Handbook of Inorganic Electrochromic Materials*; Elsevier, **1995**.
- (113.) Bard, A. J.; Faulkner, L. R. *Electrochemical Methods: Fundamentals and Applications*; John Wiley & Sons, Inc.: New York, **2001**.
- (114.) Strømme Mattsson, M. Cation Intercalation in Sputter-Deposited W Oxide Films. *Phys. Rev. B - Condens. Matter Mater. Phys.* **1998**, 58, 11015–11022.
- (115.) Zhong, Q.; Dahn, J. R.; Colbow, K. Lithium Intercalation into WO₃ and the Phase Diagram

- of Li_xWO_3 . *Phys. Rev. B* **1992**, 46, 2554–2560.
- (116.) Ampe, B.; Leroy, J. M.; Thomas, D.; Tridot, G. Contribution to Study of Systems Tungsten-Oxygen and Tungsten-Vanadium-Oxygen. *Rev. Chim. Miner.* **1968**, 5, 801.
- (117.) Guéry, C.; Choquet, C.; Dujeancourt, F.; Tarascon, J. M.; Lassègues, J. C. Infrared and X-Ray Studies of Hydrogen Intercalation in Different Tungsten Trioxides and Tungsten Trioxide Hydrates. *J. Solid State Electrochem.* **1997**, 1, 199–207.
- (118.) Righettoni, M.; Tricoli, A.; Pratsinis, S. E. Thermally Stable, Silica-Doped $\epsilon\text{-WO}_3$ for Sensing of Acetone in the Human Breath. *Chem. Mater.* **2010**, 22, 3152–3157.
- (119.) Lin, H.; Zhou, F.; Liu, C.-P.; Ozolins, V. Non-Grotthuss Proton Diffusion Mechanism in Tungsten Oxide Dihydrate from First-Principles Calculations. *J. Mater. Chem. A* **2014**, 2, 12280–12288.
- (120.) Laurinavichute, V. K.; Yu.Vassiliev, S.; Khokhlov, A. A.; Plyasova, L. M.; Molina, I. Y.; Tsirlina, G. A. Electrodeposited Oxotungstate Films: Towards the Molecular Nature of Recharging Processes. *Electrochim. Acta* **2011**, 56, 3530–3536.
- (121.) Pugolovkin, L. V; Cherstiouk, O. V; Plyasova, L. M.; Molina, I. Y.; Kardash, T. Y.; Stonkus, O. A.; Yatsenko, D. A.; Kaichev, V. V; Tsirlina, G. A. Electrodeposited Non-Stoichiometric Tungstic Acid for Electrochromic Applications: Film Growth Modes, Crystal Structure, Redox Behavior and Stability. *Appl. Surf. Sci.* **2016**, 388, 786–793.
- (122.) Dickens, P. G.; Kay, S. A.; Crouch-Baker, S.; Claridge, D. A. Thermochemistry of the Hydrogen Insertion Compounds Formed by the Molybdic and Tungstic Acids $\text{H}_x\text{MO}_3 \cdot n\text{H}_2\text{O}$ (M=Mo, N=1; M=W, N=1,2). *Solid State Ionics* **1987**, 23, 9–14.
- (123.) Granqvist, C. G. Electrochromic Tungsten Oxide Films: Review of Progress 1993–1998. *Sol. Energy Mater. Sol. Cells* **2000**, 60, 201–262.

- (124.) Uppuluri, R.; Sen Gupta, A.; Rosas, A. S.; Mallouk, T. E. Soft Chemistry of Ion-Exchangeable Layered Metal Oxides. *Chem. Soc. Rev.* **2018**, 47, 2401–2430.
- (125.) Schaak, R. E.; Mallouk, T. E. Perovskites by Design: A Toolbox of Solid-State Reactions. *Chem. Mater.* **2002**, 14, 1455–1471.
- (126.) Naguib, M.; Gogotsi, Y. Synthesis of Two-Dimensional Materials by Selective Extraction. *Acc. Chem. Res.* **2015**, 48, 128–135.
- (127.) Anasori, B.; Lukatskaya, M. R.; Gogotsi, Y. 2D Metal Carbides and Nitrides (MXenes) for Energy Storage. *Nat. Rev. Mater.* **2017**, 2.
- (128.) Anasori, B.; Gogotsi, Y. *2D Metal Carbides and Nitrides (MXenes) Structure, Properties and Applications*; Springer Nature Switzerland AG, **2019**.
- (129.) Xia, Y.; Mathis, T. S.; Zhao, M.; Anasori, B.; Dang, A.; Zhou, Z.; Cho, H.; Gogotsi, Y.; Yang, S. Thickness-Independent Capacitance of Vertically Aligned Liquid-Crystalline MXenes. *Nature* **2018**, 557.
- (130.) Lukatskaya, M. R.; Kota, S.; Lin, Zi.; Zhao, M.-Q.; Shpigel, N.; Levi, M. D.; Halim, J.; Taberna, P.-L.; Barsoum, M. W.; Simon, P.; Gogotsi, Y. Ultra-High-Rate Pseudocapacitive Energy Storage in Two-Dimensional Transition Metal Carbides. *Nat. Energy* **2017**, 2, 17105.
- (131.) Perez, A. J.; Beer, R.; Lin, Z.; Salager, E.; Taberna, P. L.; Abakumov, A. M.; Simon, P.; Tarascon, J. M. Proton Ion Exchange Reaction in Li_3IrO_4 : A Way to New $\text{H}_{3+x}\text{IrO}_4$ Phases Electrochemically Active in Both Aqueous and Nonaqueous Electrolytes. *Adv. Energy Mater.* **2018**, 8, 1–11.
- (132.) Zhang, R.; Pearce, P. E.; Pimenta, V.; Cabana, J.; Li, H.; Alves Dalla Corte, D.; Abakumov, A. M.; Rouse, G.; Giaume, D.; Deschamps, M.; Grimaud, A. First Example of Protonation

- of Ruddlesden–Popper Sr_2IrO_4 : A Route to Enhanced Water Oxidation Catalysts. *Chem. Mater.* **2020**, 32, 3499–350.
- (133.) Sanjaya Ranmohotti, K. G.; Josepha, E.; Choi, J.; Zhang, J.; Wiley, J. B. Topochemical Manipulation of Perovskites: Low-Temperature Reaction Strategies for Directing Structure and Properties. *Adv. Mater.* **2011**, 23, 442–460.
- (134.) Kendall, K. R.; Navas, C.; Thomas, J. K.; Zur Loye, H. C. Recent Developments in Oxide Ion Conductors: Aurivillius Phases. *Chem. Mater.* **1996**, 8, 642–649.
- (135.) Schaak, R. E.; Mallouk, T. E. Exfoliation of Layered Rutile and Perovskite Tungstates. *Chem. Commun.* **2002**, 2, 706–707.
- (136.) Kudo, M.; Ohkawa, H.; Sugimoto, W.; Kumada, N.; Liu, Z.; Terasaki, O.; Sugahara, Y. A Layered Tungstic Acid $\text{H}_2\text{W}_2\text{O}_7 \cdot n\text{H}_2\text{O}$ with a Double-Octahedral Sheet Structure: Conversion Process from an Aurivillius Phase $\text{Bi}_2\text{W}_2\text{O}_9$ and Structural Characterization. *Inorg. Chem.* **2003**, 42, 4479–4484.
- (137.) KIM, E.; SUZUKI, S.; MIYAYAMA, M. Electrode Properties of Layered Tungsten-Based Oxides for Electrochemical Capacitors. *J. Ceram. Soc. Japan* **2014**, 122, 426–429.
- (138.) Mitchell, J. B.; Geise, N. R.; Paterson, A. R.; Osti, N. C.; Sun, Y.; Fleischmann, S.; Zhang, R.; Madsen, L. A.; Toney, M. F.; Jiang, D. E.; Kolesnikov, A. I.; Mamontov, E.; Augustyn, V. Confined Interlayer Water Promotes Structural Stability for High-Rate Electrochemical Proton Intercalation in Tungsten Oxide Hydrates. *ACS Energy Lett.* **2019**, 2805–2812.
- (139.) Neufeind, J.; Feygenson, M.; Carruth, J.; Hoffmann, R.; Chipley, K. K. Nuclear Instruments and Methods in Physics Research B The Nanoscale Ordered Materials Diffractometer NOMAD at the Spallation Neutron Source SNS. *Nucl. Instruments Methods Phys. Res. Sect. B Beam Interact. with Mater. Atoms* **2012**, 287, 68–75.

- (140.) Soper, A. K.; Barney, E. R. Extracting the Pair Distribution Function from White-Beam X-Ray Total Scattering Data Research Papers. *J. Appl. Crystallogr.* **2011**, 44, 714–726.
- (141.) Soper, A. K. Inelasticity Corrections for Time-of-Flight and Fixed Wavelength Neutron Diffraction Experiments. *Mol. Phys.* **2009**, 107, 1667–1684.
- (142.) Farrow, C. L.; Juhas, P.; Liu, J. W.; Bryndin, D.; Božin, E. S.; Bloch, J.; Proffen, T.; Billinge, S. J. L. PDFfit2 and PDFgui : Computer Programs for Studying Nanostructure in Crystals. *J. Phys. Condens. Matter* **2007**, 19, 335219–335225.
- (143.) Toby, B. H.; Dreele, R. B. Von. GSAS-II : The Genesis of a Modern Open-Source All Purpose Crystallography Software Package. *J. Appl. Crystallogr.* **2013**, 46, 544–549.
- (144.) Kresse, G.; Furthmüller, J. Efficient Iterative Schemes for Ab Initio Total-Energy Calculations Using a Plane-Wave Basis Set. *Phys. Rev. B* **1996**, 54, 11169–11186.
- (145.) Perdew, J. P.; Burke, K.; Ernzerhof, M. Generalized Gradient Approximation Made Simple. *Phys. Rev. Lett.* **1996**, 77, 3865–3868.
- (146.) Blöchl, P. E. Projector Augmented-Wave Method. *Phys. Rev. B* **1994**, 50, 17953–17979.
- (147.) Grimme, S.; Antony, J.; Ehrlich, S.; Krieg, H. A Consistent and Accurate Ab Initio Parametrization of Density Functional Dispersion Correction (DFT-D) for the 94 Elements H-Pu. *J. Chem. Phys.* **2010**, 132, 154104.
- (148.) White, C. E.; Provis, J. L.; Proffen, T.; Riley, D. P.; Van Deventer, J. S. J. Combining Density Functional Theory (DFT) and Pair Distribution Function (PDF) Analysis to Solve the Structure of Metastable Materials: The Case of Metakaolin. *Phys. Chem. Chem. Phys.* **2010**, 12, 3239–3245.
- (149.) Gotić, M.; Ivanda, M.; Popović, S.; Musić, S. Synthesis of Tungsten Trioxide Hydrates and Their Structural Properties. *Mater. Sci. Eng. B Solid-State Mater. Adv. Technol.* **2000**, 77,

- 193–201.
- (150.) Szymanski, J. T.; Roberts, A. C. The Crystal Structure of Tungstite, $\text{WO}_3 \cdot \text{H}_2\text{O}$. *Can. Mineral.* **1984**, 22, 681–688.
- (151.) Hoda, S. N.; Chang, L. L. Y. Phase Relations in the System Bi_2O_3 - WO_3 . *J. Am. Ceram. Soc.* **1974**, 57, 323–326.
- (152.) Seguin, L.; Figlarz, M.; Cavagnat, R.; Lassègues, J.-C. Infrared and Raman Spectra of MoO_3 Molybdenum Trioxides and $\text{MoO}_3 \cdot x\text{H}_2\text{O}$ Molybdenum Trioxide Hydrates. *Spectrochim. Acta Part A Mol. Biomol. Spectrosc.* **1995**, 51, 1323–1344.
- (153.) Brown, I. D.; Wu, K. K. Empirical Parameters for Calculating Cation–Oxygen Bond Valences. *Acta Crystallogr. Sect. B Struct. Crystallogr. Cryst. Chem.* **1976**, 32, 1957–1959.
- (154.) Kim, E.; Suzuki, S.; Miyayama, M. Electrode Properties of Layered Tungsten-Based Oxides for Electrochemical Capacitors. *J. Ceram. Soc. Japan* **2014**, 122, 426–429.
- (155.) Wang, R.; Chung, C.-C.; Liu, Y.; Jones, J. L.; Augustyn, V. Electrochemical Intercalation of Mg^{2+} into Anhydrous and Hydrated Crystalline Tungsten Oxides. *Langmuir* **2017**, 33, 9314–9323.
- (156.) Wang, J.; Polleux, J.; Lim, J.; Dunn, B. Pseudocapacitive Contributions to Electrochemical Energy Storage in TiO_2 (Anatase) Nanoparticles. *J. Phys. Chem. C* **2007**, 111, 14925–14931.
- (157.) Aoki, K.; Tokuda, K.; Matsuda, H. Theory of Linear Sweep Voltammetry with Finite Diffusion Space. *J. Electroanal. Chem. Interfacial Electrochem.* **1983**, 146, 417–424.
- (158.) Elgrishi, N.; Hammon, K.; McCarthy, B.; Eisenhart, T.; Dempsey, J. A Practical Beginner's Guide to Cyclic Voltammetry. *J. Chem. Educ.* **2018**, 95, 197–206.
- (159.) Nicholson, R. S.; Shain, I. Theory of Stationary Electrode Polarography: Single Scan and

- Cyclic Methods Applied to Reversible, Irreversible, and Kinetic Systems. *Anal. Chem.* **1964**, 36, 706–723.
- (160.) Reinmuth, W. H. Theory of Diffusion Limited Charge-Transfer Processes in Electroanalytical Techniques. *Anal. Chem.* **1962**, 34, 1446–1454.
- (161.) Lin, H.; Zhou, F.; Liu, C.-P.; Ozoliņš, V. Non-Grotthuss Proton Diffusion Mechanism in Tungsten Oxide Dihydrate from First-Principles Calculations. *J. Mater. Chem. A* **2014**, 2, 12280.
- (162.) Granqvist, C. G. Electrochromic Oxides: A Bandstructure Approach. *Sol. Energy Mater. Sol. Cells* **1994**, 32, 369–382.
- (163.) Dickens, P. G.; Whittingham, M. S. S. The Tungsten Bronzes and Related Compounds. *Q. Rev. Chem. Soc.* **1968**, 22, 30–44.
- (164.) Goodenough, J. B. Transition-Metal Oxides with Metallic Conductivity. *Bull. Soc. Chim. Fr.* **1965**, 4, 1200–1207.
- (165.) Baddour-Hadjean, R.; Pereira-Ramos, J. P. Raman Microspectrometry Applied to the Study of Electrode Materials for Lithium Batteries. *Chem. Rev.* **2010**, 110, 1278–1319.
- (166.) Bruce, P. G.; Freunberger, S. a; Hardwick, L. J.; Tarascon, J.-M. Li-O₂ and Li-S Batteries with High Energy Storage. *Nat. Mater.* **2012**, 11, 19–29.
- (167.) Whitacre, J. F. F.; Tevar, A.; Sharma, S. Na₄Mn₉O₁₈ as a Positive Electrode Material for an Aqueous Electrolyte Sodium-Ion Energy Storage Device. *Electrochem. Commun.* **2010**, 12, 463–466.
- (168.) Kundu, D.; Talaie, E.; Duffort, V.; Nazar, L. F. The Emerging Chemistry of Sodium Ion Batteries for Electrochemical Energy Storage. *Angew. Chemie - Int. Ed.* **2015**, 54, 3432–3448.

- (169.) Janek, J.; Zeier, W. G. A Solid Future for Battery Development. *Nat. Energy* **2016**, *1*, 16141.
- (170.) Muldoon, J.; Bucur, C. B.; Gregory, T. Quest for Nonaqueous Multivalent Secondary Batteries: Magnesium and Beyond. *Chem. Rev.* **2014**, *114*, 11683–11720.
- (171.) Muldoon, J.; Bucur, C. B.; Oliver, A. G.; Sugimoto, T.; Matsui, M.; Kim, H. S.; Allred, G. D.; Zajicek, J.; Kotani, Y. Electrolyte Roadblocks to a Magnesium Rechargeable Battery. *Energy Environ. Sci.* **2012**, *5*, 5941–5950.
- (172.) Huie, M. M.; Bock, D. C.; Takeuchi, E. S.; Marschilok, A. C.; Takeuchi, K. J. Cathode Materials for Magnesium and Magnesium-Ion Based Batteries. *Coord. Chem. Rev.* **2015**, *287*, 15–27.
- (173.) Bucur, C. B.; Gregory, T.; Oliver, A. G.; Muldoon, J. Confession of a Magnesium Battery. *J. Phys. Chem. Lett.* **2015**, *6*, 3578–3591.
- (174.) Xu, K. “Charge-Transfer” Process at Graphite/Electrolyte Interface and the Solvation Sheath Structure of Li^+ in Nonaqueous Electrolytes. *J. Electrochem. Soc.* **2007**, *154*, A162–A167.
- (175.) Lapidus, S. H.; Rajput, N.; Qu, X.; Chapman, K. W. Solvation Structure and Energetics of Electrolytes for Multivalent Energy Storage. *Phys. Chem. Chem. Phys.* **2014**, *16*, 21941–21945.
- (176.) Wan, L. F.; Perdue, B. R.; Apblett, C. A.; Prendergast, D. Mg Desolvation and Intercalation Mechanism at the Mo_6S_8 Chevrel Phase Surface. *Chem. Mater.* **2015**, *27*, 5932–5940.
- (177.) Canepa, P.; Gautam, G. S.; Malik, R.; Jayaraman, S.; Rong, Z.; Zavadil, K. R.; Persson, K.; Ceder, G. Understanding the Initial Stages of Reversible Mg Deposition and Stripping in Inorganic Nonaqueous Electrolytes. *Chem. Mater.* **2015**, *27*, 3317–3325.
- (178.) See, K. A.; Chapman, K. W.; Zhu, L.; Wiaderek, K. M.; Borkiewicz, O. J.; Barile, C. J.;

- Chupas, P. J.; Gewirth, A. A. The Interplay of Al and Mg Speciation in Advanced Mg Battery Electrolyte Solutions. *J. Am. Chem. Soc.* **2015**, jacs.5b10987.
- (179.) Lancry, E.; Levi, E.; Mitelman, A.; Malovany, S.; Aurbach, D. Molten Salt Synthesis (MSS) of $\text{Cu}_2\text{Mo}_6\text{S}_8$ -New Way for Large-Scale Production of Chevrel Phases. *J. Solid State Chem.* **2006**, 179, 1879–1882.
- (180.) Rasul, S.; Suzuki, S.; Yamaguchi, S.; Miyayama, M. High Capacity Positive Electrodes for Secondary Mg-Ion Batteries. *Electrochim. Acta* **2012**, 82, 243–249.
- (181.) Kumagai, N.; Komaba, S.; Sakai, H.; Kumagai, N. Preparation of Todorokite-Type Manganese-Based Oxide and Its Application as Lithium and Magnesium Rechargeable Battery Cathode. *J. Power Sources* **2001**, 97–98, 515–517.
- (182.) Liang, Y.; Feng, R.; Yang, S.; Ma, H.; Liang, J.; Chen, J. Rechargeable Mg Batteries with Graphene-like MoS_2 Cathode and Ultrasmall Mg Nanoparticle Anode. *Adv. Mater.* **2011**, 23, 640–643.
- (183.) Song, J.; Noked, M.; Gillette, E.; Duay, J.; Rubloff, G.; Lee, S. B. Activation of a MnO_2 Cathode by Water-Stimulated Mg^{2+} Insertion for a Magnesium Ion Battery. *Phys. Chem. Chem. Phys.* **2015**, 17, 5256–5264.
- (184.) Sai Gautam, G.; Canepa, P.; Richards, W. D.; Malik, R.; Ceder, G. Role of Structural H_2O in Intercalation Electrodes: The Case of Mg in Nanocrystalline Xerogel- V_2O_5 . *Nano Lett.* **2016**, 16, 2426–2431.
- (185.) Mansour, A. N.; Dallek, S.; Smith, P. H.; Baker, W. M. Thermogravimetry and X-Ray Absorption Spectroscopy Study of Heated $\text{V}_2\text{O}_5 \cdot n\text{H}_2\text{O}$ Aerogels and Ambigels. *J. Electrochem. Soc.* **2002**, 149, A1589–A1597.
- (186.) Brousse, T.; Toupin, M.; Dugas, R.; Athouël, L.; Crosnier, O.; Bélanger, D. Crystalline

- MnO₂ as Possible Alternatives to Amorphous Compounds in Electrochemical Supercapacitors. *J. Electrochem. Soc.* **2006**, 153, A2171–A2180.
- (187.) Zheng, H.; Ou, J. Z.; Strano, M. S.; Kaner, R. B.; Mitchell, A.; Kalantar-Zadeh, K. Nanostructured Tungsten Oxide - Properties, Synthesis, and Applications. *Adv. Funct. Mater.* **2011**, 21, 2175–2196.
- (188.) Li, Y. M.; Hibino, M.; Miyayama, M.; Kudo, T. Proton Conductivity of Tungsten Trioxide Hydrates at Intermediate Temperature. *Solid State Ionics* **2000**, 134, 271–279.
- (189.) Granqvist, C. G. Bulk Crystalline Tungsten Oxide. In *Handbook of Inorganic Electrochromic Materials*; Elsevier, Ed.; Amsterdam, **2002**; pp 19–27.
- (190.) He, Y.; Gu, M.; Xiao, H.; Luo, L.; Shao, Y.; Gao, F.; Du, Y.; Mao, S. X.; Wang, C. Atomistic Conversion Reaction Mechanism of WO₃ in Secondary Ion Batteries of Li, Na, and Ca. *Angew. Chemie - Int. Ed.* **2016**, 55, 6244–6247.
- (191.) Colton, R. J.; Guzman, A. M.; Rabalais, J. W. Electrochromism in Some Thin-Film Transition-Metal Oxides Characterized by X-Ray Electron Spectroscopy. *J. Appl. Phys.* **1978**, 49, 409–416.
- (192.) Bruce, P. G.; Krok, F.; Nowinski, J.; Gibson, V. C.; Tavakkoli, K. Chemical Intercalation of Magnesium into Solid Hosts. *J. Mater. Chem.* **1991**, 1, 705.
- (193.) De La Cruz, A. M.; Torres-Martínez, L. M.; García-Alvarado, F. Synthesis and Characterization of H-Mg_xWO₃ and Mg_xW₁₈O₄₉ and Their Intercalation with Lithium. *Solid State Ionics* **1996**, 84, 181–188.
- (194.) Gagné, R. R.; Koval, C. A.; Lisensky, G. C. Ferrocene as an Internal Standard for Electrochemical Measurements. *Inorg. Chem.* **1980**, 19, 2854–2855.
- (195.) Latimer, W. M. *The Oxidation States of the Elements and Their Potentials in Aqueous*

- Solutions*, 2nd Ed.; Prentice Hall: New York, **1952**.
- (196.) Poizot, P.; Laruelle, S.; Grugeon, S.; Tarascon, J.-M. Rationalization of the Low-Potential Reactivity of 3d-Metal-Based Inorganic Compounds toward Li. *J. Electrochem. Soc.* **2002**, *149*, A1212–A1217.
- (197.) Ling, C.; Zhang, R.; Arthur, T. S.; Mizuno, F. How General Is the Conversion Reaction in Mg Battery Cathode: A Case Study of the Magnesium of α -MnO₂. *Chem. Mater.* **2015**, *27*, 5799–5807.
- (198.) Sun, X.; Duffort, V.; Mehdi, B. L.; Browning, N. D.; Nazar, L. F. Investigation of the Mechanism of Mg Insertion in Birnessite in Nonaqueous and Aqueous Rechargeable Mg-Ion Batteries. *Chem. Mater.* **2016**, *28*, 534–542.
- (199.) Granqvist, C. G. Tungsten Oxide Films: Ion Intercalation/Deintercalation Studied by Physical Techniques. In *Handbook of Inorganic Electrochromic Materials*; Elsevier: Amsterdam, **1995**; pp 111–137.
- (200.) Wiseman, P. J.; Dickens, P. G. Neutron Diffraction Studies of Cubic Tungsten Bronzes. *J. Solid State Chem.* **1976**, *17*, 91–100.
- (201.) Glemser, O.; Naumann, C. Kristallisierte Wolframblauverbindungen; Wasserstoffanaloga Der Wolframbronzen H_xWO₃. *Z. anorg. allg. Chem.* **1951**, *265*, 288–302.
- (202.) Levi, E.; Gofer, Y.; Aurbach, D. On the Way to Rechargeable Mg Batteries: The Challenge of New Cathode Materials. *Chem. Mater.* **2010**, *22*, 860–868.
- (203.) Judeinstein, P.; Livage, J. Electrochromic Properties of Sol-Gel Derived WO₃ Coatings. *Proc. SPIE* **1990**, *1328*, 344–351.
- (204.) Judeinstein, P.; Livage, J.; Judeinstein, P.; Livage, J. Role of the Water Content on the Electrochromic Properties of WO₃·nH₂O Thin Films. *Mater. Sci. Eng. B3* **1989**, *3*, 129–

- (205.) Livage, J.; Guzman, G. Aqueous Precursors for Electrochromic Tungsten Oxide Hydrates. *Solid State Ionics* **1996**, 84, 205–211.
- (206.) Judeinstein, P.; Livage, J. Electrochemical Mechanisms in Tungsten Oxide Thin Films. *J. Chim. Phys. Physico-Chimie Biol.* **1993**, 90, 1137–1147.
- (207.) Sa, N.; Wang, H.; Prof, D. L.; Lipson, A. L.; Key, B.; Liu, M.; Feng, Z.; Fister, T. T.; Ren, Y.; Sun, C.; Vaughey, J. T.; Fenter, P. A.; Persson, K. A.; Burrell, A. K. Is Alpha-V₂O₅ a Cathode Material for Mg Insertion Batteries? *J. Power Sources* **2016**, 323, 44–50.
- (208.) Lim, S.; Lee, J.; Kwak, H. H.; Heo, J. W.; Chae, M. S.; Ahn, D.; Jang, Y. H.; Lee, H.; Hong, S. Unraveling the Magnesium-Ion Intercalation Mechanism in Vanadium Pentoxide in a Wet Organic Electrolyte by Structural Determination. *Inorg. Chem.* **2017**, 56, 7668–7678.
- (209.) Sa, N.; Kinnibrugh, T. L.; Wang, H.; Sai Gautam, G.; Chapman, K. W.; Vaughey, J. T.; Key, B.; Fister, T. T.; Freeland, J. W.; Proffitt, D. L.; Chupas, P. J.; Ceder, G.; Barenjo, J. G.; Bloom, I. D.; Burrell, A. K. Structural Evolution of Reversible Mg Insertion into a Bilayer Structure of V₂O₅·nH₂O Xerogel Material. *Chem. Mater.* **2016**, 28, 2962–2969.
- (210.) Ji, X.; Chen, J.; Wang, F.; Sun, W.; Ruan, Y.; Miao, L.; Jiang, J.; Wang, C. Water Activated VOPO₄ for Magnesium Ion Batteries. *Nano Lett.* **2018**, 18, 6441–6448.
- (211.) Yin, J.; Brady, A. B.; Takeuchi, E. S.; Marschilok, A. C.; Takeuchi, K. J. Magnesium-Ion Battery-Relevant Electrochemistry of MgMn₂O₄: Crystallite Size Effects and the Notable Role of Electrolyte Water Content. *Chem. Commun.* **2017**, 53, 3665–3668.
- (212.) Son, S. B.; Gao, T.; Harvey, S. P.; Steirer, K. X.; Stokes, A.; Norman, A.; Wang, C.; Cresce, A.; Xu, K.; Ban, C. An Artificial Interphase Enables Reversible Magnesium Chemistry in Carbonate Electrolytes. *Nat. Chem.* **2018**, 10, 532–539.

- (213.) Novák, P.; Desilverstro, J. Electrochemical Insertion of Magnesium in Metal Oxides and Sulfides from Aprotic Electrolytes. *J. Electrochem. Soc.* **1993**, 140, 140–144.
- (214.) Verrelli, R.; Black, A. P.; Pattanathummasid, C.; Tchitchekova, D. S.; Ponrouch, A.; Oró-Solé, J.; Frontera, C.; Bardé, F.; Rozier, P.; Palacín, M. R. On the Strange Case of Divalent Ions Intercalation in V_2O_5 . *J. Power Sources* **2018**, 407, 162–172.
- (215.) Sahadeo, E.; Song, J.; Gaskell, K.; Kim, N.; Rubloff, G.; Lee, S. B. Investigation of the Water-Stimulated Mg^{2+} Insertion Mechanism in an Electrodeposited MnO_2 Cathode Using X-Ray Photoelectron Spectroscopy. *Phys. Chem. Chem. Phys.* **2018**, 2517–2526.
- (216.) Drouin, D.; Couture, A. R.; Joly, D.; Tastet, X.; Aimez, V.; Gauvin, R. CASINO V2.42 - A Fast and Easy-to-Use Modeling Tool for Scanning Electron Microscopy and Microanalysis Users. *Scanning* **2007**, 29, 92–101.
- (217.) Song, J.; Noked, M.; Gillette, E.; Duay, J.; Rubloff, G.; Lee, S. B. Activation of a MnO_2 Cathode by Water-Stimulated Mg^{2+} Insertion for a Magnesium Ion Battery. *Phys. Chem. Chem. Phys.* **2015**, 17, 5256–5264.
- (218.) Nicholson, R. S. Theory and Application of Cyclic Voltammetry for Measurement of Electrode Reaction Kinetics. *Anal. Chem.* **1965**, 37, 1351–1355.
- (219.) Cha, J.-N.; Cheong, B.-S.; Cho, H.-G. Solvation of $Mg(ClO_4)_2$ in Deuterated Acetonitrile Studied by Means of Vibrational Spectroscopy. *J. Phys. Chem. A* **2001**, 105, 1789–1796.
- (220.) Covington, A. D.; Covington, A. K. Nuclear Magnetic Resonance Studies of Preferential Solvation. *J. Chem. Soc., Faraday Trans. 1* **1989**, 85, 2827–2834.
- (221.) Nakayama, M.; Ikuta, H.; Uchimoto, Y.; Wakihara, M. Study on the AC Impedance Spectroscopy for the Li Insertion Reaction of $Li_xLa_{1/3}NbO_3$ at the Electrode-Electrolyte Interface. *J. Phys. Chem. B* **2003**, 107, 10603–10607.

- (222.) Mao, M.; Gao, T.; Hou, S.; Wang, C. A Critical Review of Cathodes for Rechargeable Mg Batteries. *Chem. Soc. Rev.* **2018**, 47, 8804–8841.
- (223.) Bohnke, C.; Bohnke, O. Impedance Analysis of Amorphous WO₃ Thin Films in Hydrated LiClO₄-Propylene Carbonate Electrolytes. *Solid State Ionics* **1990**, 39, 195–204.
- (224.) Hawkes, S. J. All Positive Ions Give Acid Solutions in Water. *J. Chem. Educ.* **2009**, 73, 516.
- (225.) Suárez-Herrera, M. F.; Costa-Figueiredo, M.; Feliu, J. M. Voltammetry of Basal Plane Platinum Electrodes in Acetonitrile Electrolytes: Effect of the Presence of Water. *Langmuir* **2012**, 28, 5286–5294.
- (226.) Fulmer, G. R.; Miller, A. J. M.; Sherden, N. H.; Gottlieb, H. E.; Nudelman, A.; Stoltz, B. M.; Bercaw, J. E.; Goldberg, K. I. NMR Chemical Shifts of Trace Impurities: Common Laboratory Solvents, Organics, and Gases in Deuterated Solvents Relevant to the Organometallic Chemist. *Organometallics* **2010**, 29, 2176–2179.
- (227.) Adrian-scotto, M.; Vasileva, D.; Mallet, G.; Vasilescu, D. About Hydration of Mg²⁺: A Quantum DFT Study. *Internet Electron. J. Mol. Des.* **2004**, 3, 400–411.
- (228.) Raj, K. Effect of WO₃ Powder Particle Shape , Size and Bulk Density , on the Grain Size and Grain Size Distribution of Tungsten Metal Powder. *Met. Powder Rep.* **2016**, 71, 285–287.
- (229.) Liu, H.; Choe, M.; Enrique, R. A.; Orvan, B.; Zhou, L.; Liu, T.; Thornton, K.; Grey, C. P. Effects of Antisite Defects on Li Diffusion in LiFePO₄ Revealed by Li Isotope Exchange. *J. Phys. Chem. C* **2017**, 121, 12025–12036.
- (230.) Merte, L. R.; Peng, G.; Bechstein, R.; Rieboldt, F.; Farberow, C. A.; Grabow, L. C.; Kudernatsch, W.; Wendt, S.; Lægsgaard, E.; Mavrikakis, M.; Besenbacher, F. Water-

- Mediated Proton Hopping on an Iron Oxide Surface. *Science* **2012**, 336, 889–894.
- (231.) Vondrák, J.; Bludská, J. The Role of Water in Hydrogen Insertion into WO_3 . *Solid State Ionics* **1994**, 68, 317–323.
- (232.) Boudart, M.; Vannice, M. A.; Benson, J. E. Adlineation, Portholes and Spillover. *Zeitschrift für Phys. Chemie* **1968**, 64, 171–177.
- (233.) Xi, Y.; Zhang, Q.; Cheng, H. Mechanism of Hydrogen Spillover on $\text{WO}_3(001)$ and Formation of H_xWO_3 ($x = 0.125, 0.25, 0.375, \text{ and } 0.5$). *J. Phys. Chem. C* **2014**, 118, 494–501.

APPENDICES

Appendix A – Derivation of Ambipolar Diffusivity and Conductivity for Ion Insertion Processes

The derivation below is adapted from Dr. Sossina Haile's lecture on the ambipolar diffusion for n-type oxygen permeation membrane for the ion insertion case. For the diffusion of charged species, A^{n+} , in the lattice, we consider both the gradients of chemical potential and electrical potential as the driving force. From Fick's first law, we have

$$J_i = -D_i \frac{dc_i}{dx} \quad (\text{A.1})$$

where, J_i is the flux of the charged specie i , c_i is its concentration, and x is the distance. From Ohm's law, we have

$$J_i = -\sigma_i \frac{dV}{dx} \quad (\text{A.2})$$

where, σ_i is the conductivity of the charged specie i . Assume each charged specie carries n charges, then

$$J_i^{charge} = nF J_i^{mass} \quad (\text{A.3})$$

The total flux is the sum of both flux relationships,

$$J_i^{mass} = -D_i \frac{dc_i}{dx} - \frac{\sigma_i}{nF} \frac{dV}{dx} \quad (\text{A.4})$$

To convert the concentration gradient into chemical potential gradient, we assume the charged specie in the material is regarded as an ideal solution,

$$\mu = \mu_0 + RT \ln a = \mu_0 + RT \ln \left(\frac{c}{c_0} \right) \quad (\text{A.5})$$

where, μ_0 is the chemical potential at standard conditions, R is the ideal gas constant, T is temperature, a is activity, and c_0 is the standard concentration. Taking the derivative on both side and applying the mathematical relationship of $dc = cd[\ln(c)]$ give us:

$$\frac{d\mu}{dc} = \frac{RT}{c} \quad (\text{A.6})$$

$$\frac{dc}{dx} = \frac{c}{RT} \frac{d\mu}{dx} \quad (\text{A.7})$$

Plugging equation A.7 into equation A.4 gives us:

$$J_i^{mass} = -\frac{D_i c_i}{RT} \frac{d\mu_i}{dx} - \frac{\sigma_i}{nF} \frac{dV}{dx} \quad (\text{A.8})$$

Nernst-Einstein equation correlates conductivity to diffusivity by

$$D_i = \frac{RT}{(nF)^2} \frac{\sigma_i}{c_i} \quad (\text{A.9})$$

Combining equations A.8 and A.9 gives us the drift-diffusion equation:

$$J_i^{mass} = -\frac{\sigma_i}{(nF)^2} \left(\frac{d\mu_i}{dx} + nF \frac{dV}{dx} \right) \quad (\text{A.10})$$

Because equation A.10 is for charged species, we need to combine the fluxes of electron and ion to achieve a neutral transport. Due to charge neutrality, the fluxes of electron and ion satisfy:

$$J_{e^-}^{mass} = n J_{A^{n+}}^{mass} \quad (\text{A.11})$$

For simplicity, from now on $J^{mass} \equiv J$. We consider the drift diffusion for both e^- and A^{n+} ,

$$J_{A^{n+}} = -\frac{\sigma_{A^{n+}}}{(nF)^2} \left(\frac{d\mu_{A^{n+}}}{dx} + nF \frac{dV}{dx} \right) \quad (\text{A.12})$$

$$J_{e^-} = -\frac{\sigma_{e^-}}{F^2} \left(\frac{d\mu_{e^-}}{dx} - F \frac{dV}{dx} \right) \quad (\text{A.13})$$

We can eliminate the dV/dx term by reorganizing equations A.12 and A.13 into dV/dx as a function of the other terms.

$$\frac{dV}{dx} = \frac{1}{nF} \left[-\frac{(nF)^2}{\sigma_{A^{n+}}} J_{A^{n+}} - \frac{d\mu_{A^{n+}}}{dx} \right] \quad (\text{A.14})$$

$$\frac{dV}{dx} = \frac{1}{F} \left(\frac{F^2}{\sigma_{e^-}} J_{e^-} + \frac{d\mu_{e^-}}{dx} \right) \quad (\text{A.15})$$

Equating equations A.14 and A.15 gives

$$\frac{1}{F} \left(\frac{F^2}{\sigma_{e^-}} J_{e^-} + \frac{d\mu_{e^-}}{dx} \right) = \frac{1}{nF} \left[-\frac{(nF)^2}{\sigma_{A^{n+}}} J_{A^{n+}} - \frac{d\mu_{A^{n+}}}{dx} \right] \quad (\text{A.16})$$

Using equation A.11, we can reorganize equation A.16 into

$$J_A = J_{A^{n+}} = -\frac{1}{(nF)^2} \left(\frac{1}{\sigma_{e^-}} + \frac{1}{\sigma_{A^{n+}}} \right)^{-1} \left(\frac{d\mu_{A^{n+}}}{dx} + n \frac{d\mu_{e^-}}{dx} \right) \quad (\text{A.17})$$

The ambipolar conductivity, $\tilde{\sigma}$, can be defined as

$$\tilde{\sigma} = \left(\frac{1}{\sigma_{e^-}} + \frac{1}{\sigma_{A^{n+}}} \right)^{-1} = \frac{\sigma_{e^-} \sigma_{A^{n+}}}{\sigma_{e^-} + \sigma_{A^{n+}}} \quad (\text{A.18})$$

Then,

$$J_A = -\frac{\tilde{\sigma}}{(nF)^2} \left(\frac{d\mu_{A^{n+}}}{dx} + n \frac{d\mu_{e^-}}{dx} \right) \quad (\text{A.19})$$

To arrive at the form like the Fick's first law, we need to convert chemical potential back to concentration. Using the chain rule, we can get

$$\frac{d\mu}{dx} = \frac{d\mu}{dc} \frac{dc}{dx} \quad (\text{A.20})$$

Using equation A.5 and the mathematical relationship of $dc = cd[\ln(c)]$, we can get

$$\frac{d\mu}{dc} = \frac{RT}{c} \frac{d(\ln a)}{d(\ln c)} \quad (\text{A.21})$$

Combining equations A.19, A.20, and A.21 results in

$$J_A = -\frac{\tilde{\sigma}}{(nF)^2} \left[\frac{RT}{c_{A^{n+}}} \frac{d(\ln a_{A^{n+}})}{d(\ln c_{A^{n+}})} \frac{dc_{A^{n+}}}{dx} + \frac{nRT}{c_{e^-}} \frac{d(\ln a_{e^-})}{d(\ln c_{e^-})} \frac{dc_{e^-}}{dx} \right] \quad (\text{A.22})$$

The mass and charge balances give

$$dc_A = dc_{A^{n+}} \quad (\text{A.23})$$

$$dc_A = dc_{e^-}/n \quad (\text{A.24})$$

Then,

$$J_A = -\frac{RT\tilde{\sigma}}{(nF)^2} \left[\frac{d(\ln a_{A^{n+}})}{d(\ln c_{A^{n+}})} \frac{1}{c_{A^{n+}}} + \frac{d(\ln a_{e^-})}{d(\ln c_{e^-})} \frac{n^2}{c_{e^-}} \right] \frac{dc_A}{dx} \quad (\text{A.25})$$

Equation A.25 is in the form of Fick's first law. We can then obtain the ambipolar diffusivity,

$$\tilde{D} = -\frac{RT\tilde{\sigma}}{(nF)^2} \left[\frac{d(\ln a_{A^{n+}})}{d(\ln c_{A^{n+}})} \frac{1}{c_{A^{n+}}} + \frac{d(\ln a_{e^-})}{d(\ln c_{e^-})} \frac{n^2}{c_{e^-}} \right] \quad (\text{A.26})$$

At dilute solution limit, activity is equal to concentration, and equation A.26 can be simplified as

$$\tilde{D} = -\frac{RT\tilde{\sigma}}{(nF)^2} \left(\frac{1}{c_{A^{n+}}} + \frac{n^2}{c_{e^-}} \right) = -\frac{RT}{(nF)^2} \left(\frac{1}{\sigma_{e^-}} + \frac{1}{\sigma_{A^{n+}}} \right)^{-1} \left(\frac{1}{c_{A^{n+}}} + \frac{n^2}{c_{e^-}} \right) \quad (\text{A.27})$$

Appendix B – Matlab Code for Performance Analysis of Cyclic Voltammograms

Function of the code: export cathodic specific capacity, anodic specific capacity, Coulombic efficiency, rate capability, and number of electrons transferred per formula unit as a function of sweep rates in one text file with the name end in “_analysis.txt”.

Input file: “.mpt” files generated by Bio-Logic potentiostats. If the files are generated by other brand potentiostats, the “Load file” section needs to be modified.

How to use: If you don’t have a “.m” file to execute this code already, copy and paste the code below into a blank Matlab script and save it. Put the “.m” file and the “.mpt” files in the same folder. Open the “.m” file and check the precautions below to adapt the code to your own experiment. Execute the “.m” file. Some error and debugging may be expected. If the “.m” is successfully executed, you should see one text file that contains what was explained in the function.

Precautions: Update the variable *mass* and *MW* for your experiment. The line “CC(any(CC(:,3)==1 | CC(:,3)==3,2), :) = [];” means that cycle 1 and 3 are removed so that only the 2nd cycle is analyzed. You may want to adapt this line for the number of cycles you run at each sweep rate and which cycle you would like to analyze.

Code:

```
% INTRODUCTION
% 1. Please put the '.mpt' files you want to analyze in the same folder as
% this file.
% 2. Update the mass and molecular weight
% 3. Click 'Run'
% 4. You should expect a text file that contains the analyzed outcome

mass = 0.63*(58.06/(58.06+9.68+589.76*0.05))/1000; %mass of the electrode
(unit: g)
MW = 183.84*2+16*6+18; % molecular weight of your sample

% Load files
allFiles = dir( '*.mpt' );% get the information all .mpt file in the current
folder
```

```

allNames = {allFiles(~[allFiles.isdir]).name};% get the names of the .mpt
files
Num_El = numel(allNames);% count the number of files in the folder
Ewe = NaN(Num_El,1);% create a matrix to contain working electrode potential
I = NaN(Num_El,1);% create a matrix to contain current
Cath_Cap = NaN(Num_El,1);% create a matrix to contain cathodic capacity
Anod_Cap = NaN(Num_El,1);% create a matrix to contain anodic capacity
sweep_rates = NaN(Num_El,1);% create a matrix to sweep rates
for i = 1:1:Num_El% a for loop function to extract data from each .mpt file
    % To find out headerlines and sweep rate
    textFileName = char(allNames(i)); % convert the name of the i-th file
into a string format readable by Matlab
    fileID = fopen(textFileName,'rt');% open the i-th file for getting
headerline and sweep rate infos
    D = textscan(fileID,'%s','Delimiter','\n');% scan the text in the i-th
file and save to D
    fclose(fileID);% close the file
    Headerlines_Num = str2num(D{1}{2}(19))*10+str2num(D{1}{2}(20));% Find the
number of headerlines in the 2nd row of D{1} which are stored in the 19th and
20th positions and convert the string format to a number format
    % find the sweep rate
    for sweep_rate_finder = 1:Headerlines_Num
        Sweep_Rate_Line = D{1}{sweep_rate_finder};
        Sweep_Rate_Key = 'dE/dt          ';
        Sweep_Rate_Index = strfind(Sweep_Rate_Line, Sweep_Rate_Key);
        if Sweep_Rate_Index == 1
            sweep_rate(i) = sscanf(Sweep_Rate_Line(Sweep_Rate_Index(1) +
length(Sweep_Rate_Key):end), '%g', 1);% scan the line that stores the sweep
rate data from the position that the Sweep_Rate_Key ends to where the line
ends. The number is stored in the i-th position in the sweep_rate matrix.
        end
    end
    % to read the columns
    fileID = fopen(textFileName,'rt');% open the i-th file for getting actual
data
    C = textscan(fileID,'%d %d %d %d %d %f %f %f %f %d %f
%f','Headerlines',Headerlines_Num);% obtain data
    fclose(fileID);% close the file
    CC = [double(C{8}),double(C{9}),double(C{10}), (double(C{6})-
12000)/3600];% save contained working electrode potential, current, cycle
number, and time
    CC(any(CC(:,3)==1 | CC(:,3)==3,2),:) = [];% delete cycle number 1 and 3
    if i == 1% for the first time running the loop
        Ewe = CC(:,1);% obtain working electrode potential
        I = CC(:,2)/mass;% obtain specific current
    else% other runs
        % the following lines are able to concatenate matrices even if they
        % have different sizes
        Size_File = numel(CC(:,1));% get the size of the file
        Size_Mat = numel(Ewe(:,1));% get the size of the current matrix
containing the previous data
        Max = max(Size_File, Size_Mat);% get the larger one of the two sizes
above
        Ewe = [[Ewe;NaN(abs(Max - Size_Mat),i-1)], [CC(:,1);NaN(abs(Max -
Size_File),1)]]; % Concatenate matrices
        I = [[I;NaN(abs(Max - Size_Mat),i-1)], [CC(:,2)/mass;NaN(abs(Max -
Size_File),1)]]; % Concatenate matrices

```

```

    end% end if
    % for calculating cathodic and anodic capacities
    It_neg = [CC(CC(:,2)<0,4),CC(CC(:,2)<0,2)];% Get time and current that is
less than 0
    It_pos = [CC(CC(:,2)>=0,4),CC(CC(:,2)>=0,2)];% Get time and current that
is greater than or equal to 0
    Cath_Cap(i) = abs(trapz(It_neg(:,1), It_neg(:,2))/mass);% integration to
find cathodic capacity
    Anod_Cap(i) = abs(trapz(It_pos(:,1), It_pos(:,2))/mass);% integration to
find anodic capacity
    sweep_rates(i) = sweep_rate(i);% this line is stupid.
end

for i = 0:length(sweep_rates)% sort capacities from small sweep rate to large
j = 2;
while j <= length(sweep_rates)
    if sweep_rates(j-1,1) > sweep_rates(j,1)
        temp = sweep_rates(j-1,1);
        sweep_rates(j-1,1) = sweep_rates(j,1);
        sweep_rates(j,1) = temp;
        temp_Cath_Cap = Cath_Cap(j-1);
        temp_Anod_Cap = Anod_Cap(j-1);
        Cath_Cap(j-1) = Cath_Cap(j);
        Anod_Cap(j-1) = Anod_Cap(j);
        Cath_Cap(j) = temp_Cath_Cap;
        Anod_Cap(j) = temp_Anod_Cap;
    end
    j=j+1;
end
end

% calculate Coulombic efficiency, number of electrons stored, and rate
% capability
Coulombic_Efficiency = Anod_Cap./Cath_Cap;
e_stored_Cath = Cath_Cap * MW / 96485.3329 * 3.6;
e_stored_Anod = Anod_Cap * MW / 96485.3329 * 3.6;
rate_capability_Cath = Cath_Cap / max(Cath_Cap);
rate_capability_Anod = Anod_Cap / max(Anod_Cap);

%text file output
Name = char(allNames(1));
New_fileName = strrep(Name, Name(end-13:end), '_analysis.txt');% create new
file names
fileID = fopen(char(New_fileName), 'w');% create a file
A = [sweep_rates,Cath_Cap,Anod_Cap,Coulombic_Efficiency,
e_stored_Cath,e_stored_Anod,rate_capability_Cath,rate_capability_Anod];%
create a matrix to contain the data to be exported
fprintf(fileID,'%10s\t%18s\t%24s\t%20s\t%14s\t%12s\t%27s\t%25s\r\n','Sweep
Rate','Cathodic Specific Capacity', 'Anodic Specific Capacity', 'Coulombic
Efficiency', '#e in Cathodic', '#e in Anodic', 'Rate Capability in Cathodic',
'Rate Capability in Anodic');% Name of the columns
fprintf(fileID,'%s\t%s\t%s\t%s\t%s\t%s\t%s\t%s\r\n','mV/s', 'mAh/g', 'mAh/g',
'', '', '', '', '');% units of the columns
fprintf(fileID,'%10.1f\t%19.5f\t%25.5f\t%21.5f\t%22.5f\t%20.5f\t%28.5f\t%26.5
f\r\n',A');% data exported
fclose(fileID);% close the file

```

Appendix C – Matlab Code for *b*-Value Analysis of Cyclic Voltammograms

Function of the code: export $\log(v)$, $\log(\text{anodic peak current})$, the fitted $\log(v)$, the fitted $\log(\text{anodic peak current})$, and *b*-value in one text file with the name end with “_log_b.txt” and export the selected cycles of cyclic voltammograms at various sweep rates and the peak current and potential used for *b*-value analysis in another text file with the name end with “_E_I.txt”.

Input file: “.mpt” files generated by Bio-Logic potentiostats. If the files are generated by other brand potentiostats, the “Load file” section needs to be modified.

How to use: If you don’t have a “.m” file to execute this code already, copy and paste the code below into a blank Matlab script and save it. Put the “.m” file and the “.mpt” files in the same folder. Open the “.m” file and check the precautions below to adapt the code to your own experiment. Execute the “.m” file. Some error and debugging may be expected. If the “.m” is successfully executed, you should see two text files that contain what was explained in the function.

Precautions: Update the variable *mass* and *MW* for your experiment. The line “CC(any(CC(:,3)==1 | CC(:,3)==3,2), :) = [];” means that cycle 1 and 3 are removed so that only the 2nd cycle is analyzed. You may want to adapt this line for the number of cycles you run at each sweep rate and which cycle you would like to analyze.

Code:

```
clear all
%%
mass = 0.96*(58.06/(58.06+9.68+589.76*0.05))/1000; %mass of the electrode
(unit: g)

% Load files
allFiles = dir( '*.mpt' );% get the information all .mpt file in the current
folder
allNames = {allFiles(~[allFiles.isdir]).name};% get the names of the .mpt
files
Num_El = numel(allNames);% count the number of files in the folder
Ewe = NaN(Num_El,1);% create a matrix to contain working electrode potential
I = NaN(Num_El,1);% create a matrix to contain current
```

```

sweep_rates = NaN(Num_El,1);% create a matrix to sweep rates

for i = 1:1:Num_El% a for loop function to extract data from each .mpt file
    % To find out headerlines and sweep rate
    textFileName = char(allNames(i)); % convert the name of the i-th file
into a string format readable by Matlab
    fileID = fopen(textFileName,'rt');% open the i-th file for getting
headerline and sweep rate infos
    D = textscan(fileID,'%s','Delimiter','\n');% scan the text in the i-th
file and save to D
    fclose(fileID);% close the file
    Headerlines_Num = str2num(D{1}{2}(19))*10+str2num(D{1}{2}(20));% Find the
number of headerlines in the 2nd row of D{1} which are stored in the 19th and
20th positions and convert the string format to a number format
    % find the sweep rate
    for sweep_rate_finder = 1:Headerlines_Num
        Sweep_Rate_Line = D{1}{sweep_rate_finder};
        Sweep_Rate_Key = 'dE/dt          ';
        Sweep_Rate_Index = strfind(Sweep_Rate_Line, Sweep_Rate_Key);
        if Sweep_Rate_Index == 1
            sweep_rates(i) = sscanf(Sweep_Rate_Line(Sweep_Rate_Index(1) +
length(Sweep_Rate_Key):end), '%g', 1);% scan the line that stores the sweep
rate data from the position that the Sweep_Rate_Key ends to where the line
ends. The number is stored in the i-th position in the sweep_rate matrix.
        end
    end
    % to read the columns
    fileID = fopen(textFileName,'rt');% open the i-th file for getting actual
data
    C = textscan(fileID,'%d %d %d %d %d %f %f %f %f %d %f
%f','Headerlines',Headerlines_Num);% obtain data
    fclose(fileID);% close the file
    CC = [double(C{8}),double(C{9}),double(C{10}), (double(C{6})-
12000)/3600];% save contained working electrode potential, current, cycle
number, and time
    CC(any(CC(:,3)==3 | CC(:,3)==1,2), :) = [];% delete cycle number 1 and 3
    if i == 1% for the first time running the loop
        Ewe = CC(:,1);% obtain working electrode potential
        I = CC(:,2);% obtain specific current
        E_I = [CC(:,1),CC(:,2)/mass];
    else% other runs
        % the following lines are able to concatenate matrices even if they
        % have different sizes
        Size_File = numel(CC(:,1));% get the size of the file
        Size_Mat = numel(Ewe(:,1));% get the size of the current matrix
containing the previous data
        Max = max(Size_File, Size_Mat);% get the larger one of the two sizes
above
        Ewe = [[Ewe;NaN(abs(Max - Size_Mat),i-1)], [CC(:,1);NaN(abs(Max -
Size_File),1)]]; % Concatenate matrices
        I = [[I;NaN(abs(Max - Size_Mat),i-1)], [CC(:,2);NaN(abs(Max -
Size_File),1)]]; % Concatenate matrices
        E_I = [[E_I;NaN(abs(Max - Size_Mat),2*(i-
1))], [CC(:,1),CC(:,2)/mass;NaN(abs(Max - Size_File),2)]]; % Concatenate
matrices
    end% end if
end

```

```

%%
% Num_Rates = numel(unique(sweep_rates));
% Samples = unique(Water_Mg_Ratio);
% Num_Samples = numel(unique(Water_Mg_Ratio));
for i = 1:Num_El
    % for allocating data
    [Max_I,Max_Loc] = max(I(:,i));
    Max_E = Ewe(Max_Loc,i);
    Max_sort(i,:)=[sweep_rates(i) Max_E Max_I];
    % for calculating b
    Log_for_b(i,:) = [log(sweep_rates(i)) log(Max_I)];
end
% for calculating b
p = polyfit(Log_for_b(:,1),Log_for_b(:,2),1);
slope = p(1);
intercept = p(2);
fit = [Log_for_b(1,1), Log_for_b(1,1) * slope +
intercept;Log_for_b(Num_El,1), Log_for_b(Num_El,1) * slope + intercept];
% b(i,:) = [Samples(i) B(2)];

%% text file output
% b value
Name = char(allNames(1));
New_fileName = strrep(Name, Name(end-13:end), '_log_b.txt');% create new file
names
fileID = fopen(char(New_fileName), 'w');% create a file
resized_fit = [fit;nan(numel(Log_for_b(:,1))-2,2)];
resized_b = [p(1);nan(numel(Log_for_b(:,1))-1,1)];
% A = {Log_for_b(:,1),Log_for_b(:,2),fit(:,1),fit(:,2),p(2)};% create a
matrix to contain the data to be exported
A = [Log_for_b,resized_fit,resized_b];% create a matrix to contain the data
to be exported
fprintf(fileID, '%10s\t%18s\t%24s\t%20s\t%14s\r\n', 'Log(v)', 'Log(I)', 'fitted
Log(v)', 'fitted Log(I)', 'b value');% Name of the columns
fprintf(fileID, '%s\t%s\t%s\t%s\t%s\r\n', '', '', '', '', '');% units of the
columns
fprintf(fileID, '%10.5f\t%19.5f\t%25.5f\t%21.5f\t%22.5f\r\n',A');% data
exported
fclose(fileID);% close the file

% potential and current
value_holder = [];
New_fileName = strrep(Name, Name(end-13:end), '_E_I.txt');% create new file
names
fileID = fopen(char(New_fileName), 'w');% create a file
resized_Peaks = [Max_sort(:,2:3);nan(numel(E_I(:,1))-
numel(Max_sort(:,1)),2)];
EI_and_Peaks = [E_I,resized_Peaks];
for i = 1:Num_El+1
    if i ~= Num_El+1
        fprintf(fileID, '%s\t%s\t', 'Potential', 'Current');
    else
        fprintf(fileID, '%s\t%s\r\n', 'Potential', 'Current');
    end
end
end

```

```

for i = 1:Num_El+1

    if i ~= Num_El+1
        fprintf(fileID, '%s\t%s\t', 'V', 'mA');
    else
        fprintf(fileID, '%s\t%s\r\n', 'V', 'mA');
    end
end
for i = 1:Num_El+1

    if i ~= Num_El+1
        fprintf(fileID, '%s\t%s\t', [num2str(sweep_rates(i)), '
mV/s'], [num2str(sweep_rates(i)), ' mV/s']);
    else
        fprintf(fileID, '%s\t%s\r\n', 'Peak Potentials', 'Peak Current');
    end
end
for i = 1:Num_El+1

    if i ~= Num_El+1
        value_holder = [value_holder, '%.4f\t%.4f\t'];
    else
        value_holder = [value_holder, '%.4f\t%.4f\r\n'];
    end
end

fprintf(fileID, value_holder, EI_and_Peaks');
fclose(fileID);% close the file

```

Appendix D – Matlab Code for Cyclability Analysis of Cyclic Voltammetry Experiments

Function of the code: extract and export the capacity and the cyclic voltammograms every n^{th} cycle in two separate text files.

Input file: “.mpt” files generated by Bio-Logic potentiostats. If the files are generated by other brand potentiostats, the “Load file” section needs to be modified.

How to use: If you don't have a “.m” file to execute this code already, copy and paste the code below into a blank Matlab script and save it. Put the “.m” file and the “.mpt” file in the same folder. Open the “.m” file and check the precautions below to adapt the code to your own experiment. Execute the “.m” file. Some error and debugging should be expected. If the “.m” is successfully executed, you should see two text files that contain the capacity and cyclic voltammogram data.

Precautions: the number of headerlines in the “textscan” function may vary from file to file. Update the variable *mass*, *MW*, *Gap* (this is the every n^{th} cycle to be extracted of your choice) for your experiment.

Code:

```
mass = 0.53*(58.06/(58.06+9.68+589.76*0.05))e-3; %mass of the electrode
MW = 183.84*2+16*6+18; % molecular weight of your sample

% Load files
allFiles = dir( '*.mpt' );% get all .mpt file in the current folder
allNames = {allFiles(~[allFiles.isdir]).name};% get the names

Ewe = NaN(1,13);% create a matrix to contain working electrode potential
I = NaN(1,13);% create a matrix to contain current
Cath_Cap = NaN(13,1);% create a matrix to contain cathodic capacity
Anod_Cap = NaN(13,1);% create a matrix to contain anodic capacity
textFileName = char(allNames);% change data type to character
fileID = fopen(textFileName,'rt');% open a file
C = textscan(fileID,'%d %d %d %d %d %f %f %f %f %f %d %f
%f','Headerlines',63);% obtain data
fclose(fileID);% close the file
CC = [double(C{9}),... % potential
      double(C{10}),... % current
      double(C{11}),... % cycle no.
      double(C{7})/3600];% time
%% Capacity and Coulombic Efficiency Calculation
Gap = 100;% calculate every 100 cycles
```

```

for i = 1:Gap:max(CC(:,3))
    It = [CC(CC(:,3) == i,4), ...% time
          CC(CC(:,3) == i,2)];% current
    It_neg = [It(It(:,2)<0,1), It(It(:,2)<0,2)];
    It_pos = [It(It(:,2)>=0,1), It(It(:,2)>=0,2)];
    Cath_Cap((i-1)/100+1) = abs(trapz(It_neg(:,1), It_neg(:,2))/mass);%
Calculate Cathodic capacity
    Anod_Cap((i-1)/100+1) = abs(trapz(It_pos(:,1), It_pos(:,2))/mass);%
Calculate Anodic capacity
end

%text file output
Num = 1:Gap:max(CC(:,3));
Coulombic_Efficiency = Anod_Cap./Cath_Cap;
e_stored_Cath = Cath_Cap * MW / 96485.3329 * 3.6;
e_stored_Anod = Anod_Cap * MW / 96485.3329 * 3.6;
Cath_Capacity_Retention = Cath_Cap/max(Cath_Cap(:));
Anod_Capacity_Retention = Anod_Cap/max(Anod_Cap(:));

fileName = [date, ' cyclability analysis.txt'];
fileID = fopen(char(fileName), 'w');
A = [Num',Cath_Cap,Anod_Cap,Coulombic_Efficiency,
e_stored_Cath,e_stored_Anod, Cath_Capacity_Retention,
Anod_Capacity_Retention];
fprintf(fileID, '%10s\t%18s\t%24s\t%20s\t%21s\t%19s\t%27s\t%25s\r\n', 'No.
Cycle', 'Cathodic Specific Capacity', 'Anodic Specific Capacity', 'Coulombic
Efficiency', '#e Stored in Cathodic', '#e Stored in Anodic', 'Capacity
Rentention in Cathodic', 'Capacity Rentention in Anodic');
fprintf(fileID, '%s\t%13s\t%29s\t%s\t%s\t%s\t%s\t%s\r\n', ' ', 'mAh/g',
'mAh/g', ' ', ' ', ' ', ' ', ' ');
fprintf(fileID, '%10.1f\t%19.5f\t%25.5f\t%21.5f\t%22.5f\t%20.5f\t%28.5f\t%26.5
f\r\n', A');
fclose(fileID);

%% extract CVs
CV_Gap = 1000;% get CV every 1000 cycles

for i = 1:CV_Gap:max(CC(:,3))
    E_I(:, (i-1)/(CV_Gap/2)+1:(i-1)/(CV_Gap/2)+2) = [CC(CC(:,3) == i,1), ...%
potential
          CC(CC(:,3) == i,2)];%current
    Label(:, (i-1)/(CV_Gap/2)+1:(i-1)/(CV_Gap/2)+2) = [i,i];
end
Label = string(Label);
%text file output
fileName = [date, ' sampled CV.txt'];
fileID = fopen(char(fileName), 'w');

% Title line
for j = 1:CV_Gap:i
    if j ~= i
        fprintf(fileID, '%s\t%s\t', 'Potential', 'Current');
    else
        fprintf(fileID, '%s\t%s\r\n', 'Potential', 'Current');
    end
end
end

```

```

% Unit line
for k = 1:CV_Gap:i
    if k ~= i
        fprintf(fileID, '%s\t%s\t', 'V\i( vs. )Ag/Ag\+(+)', 'mA');
    else
        fprintf(fileID, '%s\t%s\r\n', 'V\i( vs. )Ag/Ag\+(+)', 'mA');
    end
end

% Label line
Label_Holder = [];
for l = 1:CV_Gap:i
    if l ~= i
        Label_Holder = [Label_Holder, '%s\t%s\t'];
    else
        Label_Holder = [Label_Holder, '%s\t%s\r\n'];
    end
end
fprintf(fileID, Label_Holder, Label);

% Print dataset
Space_Holder = [];
for m = 1:CV_Gap:i
    if m ~= i
        Space_Holder = [Space_Holder, '%.5f\t%.5f\t'];
    else
        Space_Holder = [Space_Holder, '%.5f\t%.5f\r\n'];
    end
end
fprintf(fileID, Space_Holder, E_I');
fclose(fileID);

```

Appendix E – Matlab Code for Single-Spot Operando AFM Dilatometry Analysis

Function of the code: perform data cleaning, structuring, and visualization of the in situ AFM dilatometry. Apology that you will need to manually export the data by copying and pasting from the individual variables.

Input file: “.mpt” files generated by Bio-Logic potentiostats. If the files are generated by other brand potentiostats, the “Load file” section needs to be modified.

How to use: If you don’t have a “.m” file to execute this code already, copy and paste the code below into a blank Matlab script and save it. Put the “.m” file and the “.mpt” file (only one file at a time) in the same folder. Open the “.m” file and check the precautions below to adapt the code to your own experiment. Execute the “.m” file. Some error and debugging should be expected. If the “.m” is successfully executed, you should see two text files that contain what was explained in the function.

Precautions: the number of headerlines in the “textscan” function may vary from file to file. The column that hosts the dilatometry data may vary depending on your export settings.

Code:

```
%% Assumptions
% 1. background was assumed to be straight lines defined by the lowest
% deformation values in each CV cycles.
%% Code structure
% load file
% background subtraction
% deformation rate calculation
% data visualization
%% Load file
% I was analyzing one ECLab file each time
clear all
getFile = dir( '*.mpt' );% get all .txt file in the current folder
FileName = {getFile(~[getFile.isdir]).name};% get the names
textFileName = char(FileName);% change data type to character
fileID = fopen(textFileName,'rt');% open a file
% scan text, the columns and # of headerlines may be subject to change
depending on your output options
C = textscan(fileID,'%d %d %d %d %d %f %f %f %f %d %f %f %f
%[\n]', 'Headerlines',55);% obtain data
```

```

fclose(fileID);% close the file
% save contained working electrode potential, time, current and cycle
% number,and deformation
CC = [double(C{8}),double(C{9}),double(C{10}),double(C{6}), double(C{12})];
time = CC(:,4);
SGF = 251; %SG filter framelength
filt_deform = sgolayfilt(CC(:,5), 1, SGF);% Savitzky_Golay filtering

%% Get the indexes where each CV cycle starts
j_count = 1;
Cycle_Change = zeros(1,max(CC(:,3))); % CC(:,3) is cycle number
for j = 2:size(CC,1)
    if CC(j,3) == CC(j-1,3) + 1
        Cycle_Change(j_count) = j;
        j_count = j_count + 1;
    end
end
Cycle_Change(max(CC(:,3))) = size(CC,1);
%% Background subtraction
% Find peaks (in deformation) in order to determine valleys
max_holder = zeros(1,max(CC(:,3))+1);
max_time_holder = zeros(1,max(CC(:,3)));
max_displacement_holder = zeros(1,max(CC(:,3)));
max_locs = zeros(1,max(CC(:,3)));
for k = 1:max(CC(:,3))
    format long
    if k == 1
        cycle_max = max(filt_deform(1:Cycle_Change(k)-1));
        max_holder(k) = find(filt_deform(1:Cycle_Change(k)-1) ==
cycle_max,1);
        max_time_holder(k) = CC(max_holder(k),4);
        max_displacement_holder(k) = cycle_max;
        max_locs(k) = max_holder(k);
    else
        cycle_max = max(filt_deform(Cycle_Change(k-1):Cycle_Change(k)-1));
        max_holder(k) = find(filt_deform(Cycle_Change(k-1):Cycle_Change(k)-1)
== cycle_max,1);
        max_time_holder(k) = CC(Cycle_Change(k-1)+max_holder(k)-1,4);
        max_displacement_holder(k) = cycle_max;
        max_locs(k) = Cycle_Change(k-1)+max_holder(k)-1;
    end
end
% Find local minima in between peaks
min_holder = zeros(1,max(CC(:,3))+1);
min_time_holder = zeros(1,max(CC(:,3)));
min_displacement_holder = zeros(1,max(CC(:,3)));
min_locs = zeros(1,max(CC(:,3)));
for k = 1:max(CC(:,3))
    format long
    if k == 1
        cycle_min = min(filt_deform(1:max_locs(1)));
        min_holder(k) = find(filt_deform(1:max_locs(1)) == cycle_min,1);
        min_time_holder(k) = CC(min_holder(k),4);
        min_displacement_holder(k) = cycle_min;
        min_locs(k) = min_holder(k);
    else
        cycle_min = min(filt_deform(max_locs(k-1):max_locs(k)));

```

```

        min_holder(k) = find(filt_deform(max_locs(k-1):max_locs(k)) ==
cycle_min,1);
        min_time_holder(k) = CC(max_locs(k-1)+min_holder(k)-1,4);
        min_displacement_holder(k) = cycle_min;
        min_locs(k) = max_locs(k-1)+min_holder(k)-1;
    end
end
min_locs = [min_locs size(CC(:,3),1)];
min_time_holder(max(CC(:,3))+1)=CC(size(CC,1),4);
min_displacement_holder(max(CC(:,3))+1)=filt_deform(size(CC,1));
% find equations for the baseline
k = zeros(1,max(CC(:,3)));
b = zeros(2,max(CC(:,3)));
min_locs_diff = min_locs(1)-1;
for l = 1:1:max(CC(:,3))
    k(l) = (min_displacement_holder(l+1)-
min_displacement_holder(l))/(min_time_holder(l+1)-min_time_holder(l));
    b(l) = min_displacement_holder(l+1)-k(l)*min_time_holder(l+1);
    % borrow the loop to find the biggest difference btw min_locs
    min_locs_diff = [min_locs_diff, min_locs(l+1)-min_locs(l)];
end
y = zeros(1,size(CC,1));
for m = 1:max(CC(:,3))
    if m == 1
        y(1:min_locs(2)-1) =k(m) * time(1:min_locs(2)-1) + b(m);
    elseif m ~= max(CC(:,3))
        y(min_locs(m):min_locs(m+1)-1) = k(m) *
time(min_locs(m):min_locs(m+1)-1) + b(m);
    else
        y(min_locs(m):min_locs(m+1)) = k(m) * time(min_locs(m):min_locs(m+1))
+ b(m);
    end
end
Deform_Baseline_Subtracted = filt_deform - y';

% sort the data in matrices based on cycle #
deform_nobase_in_cyc = NaN(max([Cycle_Change(1) diff(Cycle_Change)]),
max(CC(:,3)));

%% d(Deformation)/dt
dDeformdx_tot = diff([eps; Deform_Baseline_Subtracted(:)].)/diff([eps;
time(:)]);

% I was using median filter to filter the deformation rate
MF = 501;
filt_dDeformdx_tot = medfilt1(dDeformdx_tot, MF, 'truncate');
Y = y';

% Re-organize the data
for cycle = 1:max(CC(:,3))
    if cycle == 1
        Ewe(:,cycle) = [CC(1:Cycle_Change(cycle),1);NaN(max([Cycle_Change(1)
diff(Cycle_Change)])-Cycle_Change(cycle),1)];% obtain working electrode
potential
    end
end

```

```

        I(:,cycle) = [CC(1:Cycle_Change(cycle),2);NaN(max([Cycle_Change(1)
diff(Cycle_Change)])-Cycle_Change(cycle),1)];% obtain specific current
        t(:,cycle) = [CC(1:Cycle_Change(cycle),4);NaN(max([Cycle_Change(1)
diff(Cycle_Change)])-Cycle_Change(cycle),1)];% time data
        deform_nobase(:,cycle) =
[Deform_Baseline_Subtracted(1:Cycle_Change(cycle));NaN(max([Cycle_Change(1)
diff(Cycle_Change)])-Cycle_Change(cycle),1)];% deformation with baseline
subtracted
        dDeformdx(:,cycle) =
[dDeformdx_tot(1:Cycle_Change(cycle));NaN(max([Cycle_Change(1)
diff(Cycle_Change)])-Cycle_Change(cycle),1)];
        filt_dDeformdx(:,cycle) =
[filt_dDeformdx_tot(1:Cycle_Change(cycle));NaN(max([Cycle_Change(1)
diff(Cycle_Change)])-Cycle_Change(cycle),1)];
        filt_deform_comp(:,cycle) =
[filt_deform(1:Cycle_Change(cycle));NaN(max([Cycle_Change(1)
diff(Cycle_Change)])-Cycle_Change(cycle),1)];
        y_comp(:,cycle) = [Y(1:Cycle_Change(cycle));NaN(max([Cycle_Change(1)
diff(Cycle_Change)])-Cycle_Change(cycle),1)];
        deform_nobase_in_cyc(:,cycle) =
[Deform_Baseline_Subtracted(1:Cycle_Change(cycle));NaN(max([Cycle_Change(1)
diff(Cycle_Change)])-Cycle_Change(cycle),1)];
    else
        Ewe(:,cycle) = [CC(Cycle_Change(cycle-
1)+1:Cycle_Change(cycle),1);NaN(max([Cycle_Change(1) diff(Cycle_Change)])-
numel(Cycle_Change(cycle-1)+1:Cycle_Change(cycle)),1)];% obtain working
electrode potential
        I(:,cycle) = [CC(Cycle_Change(cycle-
1)+1:Cycle_Change(cycle),2);NaN(max([Cycle_Change(1) diff(Cycle_Change)])-
numel(Cycle_Change(cycle-1)+1:Cycle_Change(cycle)),1)];% obtain specific
current
        t(:,cycle) = [CC(Cycle_Change(cycle-
1)+1:Cycle_Change(cycle),4);NaN(max([Cycle_Change(1) diff(Cycle_Change)])-
numel(Cycle_Change(cycle-1)+1:Cycle_Change(cycle)),1)];% time data
        deform_nobase(:,cycle) =
[Deform_Baseline_Subtracted(Cycle_Change(cycle-
1)+1:Cycle_Change(cycle));NaN(max([Cycle_Change(1) diff(Cycle_Change)])-
numel(Cycle_Change(cycle-1)+1:Cycle_Change(cycle)),1)];% deformation with
baseline subtracted
        dDeformdx(:,cycle) = [dDeformdx_tot(Cycle_Change(cycle-
1)+1:Cycle_Change(cycle));NaN(max([Cycle_Change(1) diff(Cycle_Change)])-
numel(Cycle_Change(cycle-1)+1:Cycle_Change(cycle)),1)];
        filt_dDeformdx(:,cycle) = [filt_dDeformdx_tot(Cycle_Change(cycle-
1)+1:Cycle_Change(cycle));NaN(max([Cycle_Change(1) diff(Cycle_Change)])-
numel(Cycle_Change(cycle-1)+1:Cycle_Change(cycle)),1)];
        filt_deform_comp(:,cycle) = [filt_deform(Cycle_Change(cycle-
1)+1:Cycle_Change(cycle));NaN(max([Cycle_Change(1) diff(Cycle_Change)])-
numel(Cycle_Change(cycle-1)+1:Cycle_Change(cycle)),1)];
        y_comp(:,cycle) = [Y(Cycle_Change(cycle-
1)+1:Cycle_Change(cycle));NaN(max([Cycle_Change(1) diff(Cycle_Change)])-
numel(Cycle_Change(cycle-1)+1:Cycle_Change(cycle)),1)];
        deform_nobase_in_cyc(:,cycle) =
[Deform_Baseline_Subtracted(Cycle_Change(cycle-
1)+1:Cycle_Change(cycle));NaN(max([Cycle_Change(1) diff(Cycle_Change)])-
numel(Cycle_Change(cycle-1)+1:Cycle_Change(cycle)),1)];
    end
end
end

```

```

%% Data visualization
% plot Def vs. E and I vs. E / Def vs. time
fig = figure(1);
linecolors = jet(cycle);
left_color = [0 0 0];
right_color = [0 0 0];
set(fig, 'defaultAxesColorOrder', [left_color; right_color]);
def_in_nm = filt_deform_comp*2546;
y_in_nm = y_comp*2546;
hL = zeros(cycle,1);
for o = 1:cycle
    % yyaxis left
    hL(o) = plot(t(:,o), def_in_nm(:,o), '-
', 'color', linecolors(o,:), 'linewidth', 2);
    hold on
% yyaxis right
    plot(t(:,o), y_in_nm(:,o), '-', 'color', linecolors(o,:), 'linewidth', 2);
end

xlabel('Time (sec)')
ylabel('Deformation (nm)')
legend(hL, '1', '2', '3', '4', '5', '6', '7', '8', '9', '10', '11', '12', '13', '14', '15', '
16', '17', '18', '19', '20')
hold off
neg_dDeformdx = -filt_dDeformdx*2546;

% plot derivative of Def
fig2 = figure(2);
set(fig2, 'defaultAxesColorOrder', [linecolors(2,:); linecolors(cycle-2,:)]);
[min_k, p] = min(abs(k));
yyaxis left
plot(Ewe(:,p), -filt_dDeformdx(:,p)*2546, '-
', 'color', linecolors(2,:), 'linewidth', 2)
ylabel('-d(Deformation)/dt (nm/sec)')
hold on
yyaxis right
plot(Ewe(:,p), I(:,p), '-', 'color', linecolors(cycle-2,:), 'linewidth', 2)
ylabel('Current (mA)')
xlim([-0.4 0.5])
hold off
xlabel('Potential (V {\itvs.} Ag/AgCl)')
h = legend(sprintf('WO_3, point 1, 2 mV/s, cycle %d, SGF %d, MF %d', p,
SGF, MF));
LEG = findobj(h, 'type', 'text');
set(LEG, 'FontSize', 20)

% Find integration at each time for the pth cycle
It_neg = [t(I(:,p)<0,p), I(I(:,p)<0,p)]; % Get time and current that is less
than 0
t_neg = t(I(:,p)<0,p)-min(t(I(:,p)<0,p));
It_pos = [t(I(:,p)>=0,p), I(I(:,p)>=0,p)]; % Get time and current that is
greater than or equal to 0
t_pos = t(I(:,p)>=0,p)-min(t(I(:,p)>=0,p));
Cath_Cap = NaN(size(It_neg,1),1);
Anod_Cap = NaN(size(It_pos,1),1);

```

```

for pos_count = 2:size(It_pos,1)
    Anod_Cap(pos_count) = abs(trapz(It_pos(1:pos_count,1),
It_pos(1:pos_count,2)));% integration to find anodic capacity
end
for neg_count = 2:size(It_neg,1)
    Cath_Cap(neg_count) = abs(trapz(It_neg(1:neg_count,1),
It_neg(1:neg_count,2)));% integration to find anodic capacity
end
figure (3)
plot(t_pos, (8-Anod_Cap)*4)
hold on
plot(t_pos,deform_nobase(I(:,p)>=0,p)*2546)
hold off

```